UNIVERSITY OF FORT HARE

Faculty of Science and Agriculture

University of Fort Hare
Together in Excellence

Preparation and application of plasmon metal enhanced titanium dioxide photocatalyst for the removal of organics in water

A thesis submitted in fulfilment of the requirements for the

Doctoral Degree in Chemistry

By

Pardon Nyamukamba

(Student Number: 200805439)

Supervisors: Prof Lilian Tichagwa

Prof Leslie Petrik

Prof Sampson Mamphweli

January 2016

Preface

I, Pardon Nyamukamba, declare that this work was performed in the Department of Chemistry, University of Fort Hare and University of The Western Cape from March 2013 to January 2016 under the supervision of Prof L Tichagwa, Prof L Petrik and Prof S Mamphweli.

This work has not been submitted in part or whole to any other university.

Dedications

This work is dedicated to my wife Dr Nyarai Margaret Mujuru Nyamukamba, my daughter Natalie Anopaishe, my sons Atidaishe Reynold and Anashe Daniel, my mother Beatrice and my father Livaty in appreciation of their inspiration, unconditional love and acceptance.

Acknowledgements

I am so thankful to God the Almighty who made everything possible. His unconditional endless love, support and courage helped me achieve what was required of me to complete this work.

I would like to express my sincere gratitude to my supervisors Prof Lilian Tichagwa, Prof Leslie Petrik and Prof Sampson Mamphweli for their invaluable guidance, support and fruitful conversations. My achievements in my PhD research work would not have been possible without their guidance and support.

I also extend my gratitude to my fellow chemistry postgraduate students for their support and encouragement; Dr Bunhu, Dr Oyedeji, Dr Katwire, Dr Kuvarega, Dr Mungondori, Mr Ruwuya, Mr Tavengwa, Miss Peteni, Ms Singiswa Miss Lukanji and all departmental staff who were extremely supportive and genuinely interested in my work. To my other research group members, Environmental and Nanosciences at UWC, I would like to say thank you so much for all the support and constructive comments in my reaserch. The work would not have been successful had it not been for the technical assistance offered by Mr Tshapu, Mr Mcwako, Mr Rudolph, Dr Botha, Dr Green, Miss Fameo, Mr Mutingwende and Mr Komani.

Special mention goes to Prof Catherine Ngila for allowing me to use her laboratory to do some of my work and also for her support in various ways.

I also want to thank my family, parents, brothers, sisters and all my relatives and friends who were always there for me when I needed them and for their prayers. I say thank you so much for the support and bringing the best out of me and may our good Lord richly bless you all.

It is with a deep sense of gratitude that I thank the National Research Foundation Sasol Inzalo Foundation and Govan Mbeki Research and Development for their generous financial support.

Abstract

Advanced oxidation processes are capable of removing organic compounds that cannot be removed by conventional water treatment methods. Among the oxidation processes, photo-catalysis using titanium dioxide (TiO_2) is a promising method but suffers from rapid electron-hole recombination rates and only absorbs UV light which is a small percentage (5 %) of the total solar radiation. Therefore there is a need to reduce the recombination rates and also extend the absorption of the photo-catalyst into the visible region which constitutes 55 % of the total solar radiation. The major aims of this study were to prepare plasmon metal decorated and doped TiO_2 photo-catalysts immobilized on quartz substrates and test their photo-catalytic and antimicrobial activities.

The effect of film thickness (loading) and use of different shapes of plasmon metal nanostructures was investigated. TiO_2 thin films were prepared by a sputter coating technique while plasmon metal (Au & Ag)/carbon co-doped TiO_2 by a simple sol gel process and plasmon metal films were prepared by the thermal evaporation technique. Different plasmon metal nanostructures (nanorods, dendrites, nanowires and spherical nanoparticles) were prepared using a wet chemical technique using sodium borohydride as the reducing agent. Nanocomposites of co-doped TiO_2 photo-catalyst and plasmon elements of different proportions were also prepared. The prepared photo-catalysts were coated onto etched and MPTMS (3-Mercaptopropyl trimethoxysliane) treated quartz glass substrate which is a stable support favouring easy recovery. The prepared materials were characterized by XRD, HRTEM, TEM, HRSEM, FT-IR, SEM, PIXE and TGA while the doped TiO_2 was characterized by XPS, BET, CHNS and Raman Spectroscopy.

The effect of pH of solution, presence of other contaminants and salts in solution, initial concentration of the model pollutant and type of the plasmonic elements on the photo-catalytic activity of TiO_2 towards 4-(4-sulfophenylazo)-*N*,*N*-dimethyl aniline (methyl orange) were also investigated. The selected TiO_2 photo-catalyst films were tested for antimicrobial properties. The effect of different types of plasmon elements on the antimicrobial activity of TiO_2 against *E. coli* ATCC 3695 was evaluated under both sunlight and weak UV light.

Under UV light, Ag showed the highest enhancement in photo-catalytic activity of TiO_2 than Au and Cu. The photo-catalytic activity of TiO_2 increased with an increase in Ag content to an optimum loading and then started to decrease with a further increase in loading. For Cu and Au, photo-activity activity increased with an increase in plasmon metal content. Under sunlight, Cu showed the highest enhancement of TiO_2 photo-catalytic compared to Ag and Au. The change in order of deposition showed that Au films enhanced the photo-activity better when they were deposited underneath rather than on top of TiO_2 on quartz supports but Ag films performed better in enhancing photo-activity when they were deposited on top of TiO_2. The use of bimetallic layers and three layer systems of different plasmon elements enhanced photo-catalytic activity better than the use of a monometallic layer. The presence of other organic contaminants and salts in solutions was found to reduce the photo-degradation of methyl orange due to preferential adsorption of other contaminants. When the pH was increased, the photo-catalytic activity of TiO_2 towards methyl orange was reduced. In antimicrobial studies, it was found that the plasmon elements greatly improved the antibacterial action of TiO_2

against *Escherichia coli* ATCC 3695 in water and the best antibacterial action was observed with silver/carbon co-doped TiO_2 photo-catalyst under sunlight.

The doped samples consisted of polydisperse nanoparticles which were found to be beneficial for photo-catalytic activity enhancement under sunlight. No general trend was observed on the band gap reduction with an increase in plasmon metal content. Among the Ag doped photo-catalysts, the highest photo-degradation rate constant of 2.45×10^{-3} min^{-1} was achieved by TiO_2 with a silver content of 0.5 % because it had the lowest band gap of 1.95 eV, and lowest rate constant of 1.74×10^{-3} min^{-1} was achieved with 0.7 % Ag loaded TiO_2 towards methyl orange. For the Au doped samples, the highest photo-degradation was achieved with a sample loaded with 1.0 % Au which had a photo-degradation rate constant of 3.22×10^{-3} min^{-1}. Doping with Au and Ag was found to promote anatase to rutile phase transformation, which allowed utilization of visible light but reduced the surface area of the photo-catalyst.

There was no change in band gap observed in the composite systems. The use of more than one plasmon element to prepare composites was found to be more effective in enhancing the photo-catalytic activity of TiO_2 than the use of one plasmon element only. The highest photo-degradation of 66.56 % after 5 hours under visible light irradiation was achieved by co-doped-TiO_2/Au-Ag-Cu composite system.

Durability tests showed that the selected photo-catalysts were durable and could be used for at least four times without appreciable loss of photo-catalytic activities. For instance

TiO_2 on a three layer system (TiO_2/Au-Ag-Cu) showed 95.88 % degradation of bromocresol purple after five hours and after the fourth application/cycle it decreases by only 14.9 % to 80.98 %. Leaching of the plasmon elements increased with an increase in the number of cycles and was minimal for Au and Cu. The extent of leaching was also found to depend on the position of the plasmon element relative to the photo-catalyst.

It was shown that low band gap does not always guarantee high photo-catalytic activity as some samples with high band gaps were found to have higher photo-catalytic activities than low band gap photo-catalysts. Silver was found to favour anatase to rutile phase transformation more than gold. Some secondary photo-degradation by-products of methyl orange were found. The mode in which the LC-MS is operated has an impact on the photo-degradation products that can be detected by the instrument. The study achieved its goals of enhancing the photo-catalytic activity of TiO_2 both under UV and visible light irradiation. It was proved that under UV light the plasmon elements act as electron reservoirs thereby reducing electron recombination rates and under visible light irradiation they increase TiO_2 photo-catalytic activity by both creating localized surface plasmons and reducing recombination rates.

Table of Contents

List of Tables

List of Figures

List of Abbreviations

AFM: Atomic force spectroscopy

AuNP: Gold nanoparticle

AgNP: Silver nanoparticle

BPA: Bisphenol A

BCP: Bromocresol purple

CuNP: Copper nanoparticle

CHNS: Carbon hydrogen nitrogen sulphur analyzer

DET: Direct electron transfer

DBD: Dielectric barrier discharge

DRS: Diffuse reflectance spectroscopy

EDS: Energy dispersive X-ray spectroscopy

FTIR: Fourier-transform infrared spectroscopy

HRTEM: High resolution transmission electron microscopy

HRSEM: High resolution scanning electron microscopy

ICP: Inductively coupled plasma

LC-MS: Liquid chromatography mass spectrometry

LSPR: Localized surface plasmon resonance

PIRET: Plasmonic induced resonant energy transfer

MPTMS: 3-Mercaptopropyl trimethoxysliane

MeO: Methyl orange

PIXE: Particle induced X-ray emission

TGA: Thermogravimetric analysis

THM: Trihalomethanes

UV-Vis: Ultraviolet visible spectroscopy

XRD: X-ray diffraction

Chapter 1

Introduction

1.1 Study Background and Motivation

Water purification is among the most important technologies for human life. Access to adequate and safe drinking water is vital for effective health protection but in developing countries, this is still lacking hence it remains a high priority. It has been shown that in some regions, the investments in water supply and sanitation can yield a net economic benefit since the reduction in adverse health related problems costs outweigh the costs of undertaking the interventions (WHO, 2008). The water demand is increasing due to the increase in population and according to the 2009 World Water Development report, almost half of the world population will have high water stress by 2030 (WWD., 2009). The pressure on water resources in some countries for instance South Africa, is due to limited resources as it is in a semi-arid part of the world and its average rainfall (450 mm/year) is well below the world average of 860 mm/year (NWRS., 2004). Safe drinking water is a major public health issue in developing countries and millions of people are dying every year due to preventable water related diseases. In 2012 WHO/INICEF reported that about 768 million people worldwide have no access to drinking water. These figures are expected to increase in future as a result of contamination from the discharge of pollutants into the water systems (Chong *et al*., 2010; Suarez *et al*., 2008).

The effluents from industries have an adverse impact on human health and when found in drinking water systems; they pose a threat to users and the environment. Chemicals such as pesticides and herbicides from agricultural activities also end up in rivers and lakes and some

are confirmed to be endocrine-disrupting which require removal from water systems (Akpan & Hameed., 2009). The degradation of these chemical contaminants has received increasing attention. Conventional water treatment methods such as flocculation and coagulation, ultrafiltration and adsorption using activated carbon have been used but they have a disadvantage of creating secondary pollution which requires further treatment, disposal of the solid waste and regeneration of the adsorbent in adsorption making them expensive processes (Akpan & Hameed., 2009; Tang & An., 1995). Besides the high operational costs, these methods could generate toxic secondary pollutants which can further pollute the environment (Gaya & Abdulah., 2008).

The use of chlorine for disinfection has been common in water purification as it is cheap and kills a large number of pathogens but has a big disadvantage of the possibility of chlorine reacting chemically with organic matter found in water. This can lead to the formation of carcinogens such as trihalomethanes and other chlorinated disinfection by-products (DBPs) (Fischer *et al*, 2012). Several factors including the release of these DBPs and persistent organics and the Millennium Development Goal (MGD) to reduce the proportion of the population without access to safe drinking water by 2015 means that new methods of water treatment have to be developed or efforts made to improve the existing ones. This has led to increase in research focusing on the development of alternative methods to conventional ones such as disinfection methods. The new methods include advanced oxidation processes (AOPs) which are very promising in the treatment of contaminated water. The most common AOPs include electrochemical oxidation, ozonation, UV irradiation alone or in combination with H_2O_2 and TiO_2 photo-catalysis. Among these, much attention has been given to photo-catalysis, due to its potential to degrade a wide of recalcitrant organic contaminants into harmless products at ambient temperatures (Alinsafi *et al*., 2007; Zainal *et al*., 2005).

1.2 Organic water pollutants

The list of organic contaminants that are found in water is increasing as new analytical techniques allow detection at low concentrations. The recalcitrant organic pollutants are increasing in water streams and air hence environmental laws and regulations are becoming more stringent (Gayaa *et al*, 2008). Dissolved organic pollutants give water an undesirable taste, odour or even imparts colour in drinking water. For instance, methyl tertiary butyl ether (MTBE), a gasoline additive causes water to smell oily. Industrial phenols, hydrocarbons, volatile organic compounds, *trans*-1,10-dimethyl-*trans*-9-decalol (geosmin) and 2-methyl-isoborneol (MIM) can also cause odours in the water. The use of powdered activated carbon (PAC) to remove taste and odor problems caused by geosmin and MIM requires large doses of PAC making it impractical for larger utilities. Also activated carbon can remove some organic contaminants that readily adsorbs onto it such as aromatic solvents, chlorinated aromatics, phenol and chlorophenols meaning those compounds which do not adsorb require other methods. The most reliable, effective and suitable method for removal of organic contaminants in drinking water is chemical transformation by oxidation. One such method is ozonation which is an alternative to PAC but it is expensive and can result in the formation of bromate (ozonation by-product) which is harmful and carcinogenic (USEPA. 1999) hence photo-catalysis seems to be a better option. Photo-catalysis through the generation of radicals is a promising method as the OH radicals are highly oxidizing and react rapidly with any organic contaminant in water including taste and odour imparting compounds.

1.3 Nanotechnology in water treatment

Nanotechnology has enabled water treatment to overcome most challenges that are faced by some of the existing treatment techniques. It has allowed economic utilization of unconventional water sources resulting in the expansion of the water supply. It is believed

that the nanotechnology-based techniques could lead to cheaper, more durable and more efficient water treatment technologies that could solve the problems of developing countries in the water treatment sector. The nanotechnology based water treatment methods include such techniques as the use of nano-Ag (Li *et al*., 2013), fullerene derivatives, nanofiber membranes (Feng *et al*., 2013), forward osmosis, nano-TiO_2 and the use of carbon based nano-adsorbents such as carbon nanotubes and nano-zeolites (Wang & Peng., 2010). Among these techniques, photo-catalysis has gained more interest as it is useful for pre-treatment of hazardous and non-biodegradable contaminants to increase their biodegradability and it is a polishing step to remove recalcitrant organic compounds from water. The most common photo-catalyst is titanium dioxide which is readily available and is close to being an ideal photo-catalyst because it is inexpensive, chemically stable, relatively non-toxic and the photo-generated holes are highly oxidizing (Ochiai *et al*., 2010).

Photo-catalysis using semiconductors is environmentally friendly as it degrades contaminants into harmless products such as CO_2 and water. It involves the generation of electron hole-pairs when light of energy matching or exceeding the band gap of the semiconductor is absorbed. The generated electrons and holes migrate to the surface of the semiconductor to reduce and oxidize contaminants adsorbed by the semiconductor (Ni *et al*., 2007). Due to some shortcomings of TiO_2, most current research is focused on increasing photo-catalytic reaction kinetics and photo-activity through band gap engineering of TiO_2 and increasing the lifetime of the photo-generated charge carriers.

The commercialization of nano-engineered TiO_2 photo-catalysts for water and wastewater technology strongly depends on their impact on the aqueous environment. Hence, to limit the release of TiO_2 nanoparticles into environment and for easy recovery of the photo-catalyst,

the nanoparticles need to be immobilized, for example, as a film on a substrate such as quartz. The quartz is normally etched and surface modified with adhesion promoters such as 3-Mercaptopropyl trimethoxysliane (MPTMS) to improve the adhesion of the nanoparticles. The quality of the films and the MPTMS monolayer depend on several factors such as the nature and roughness of the substrate, concentration of the adhesion promoter and cleanliness of the substrate. Previous studies proved that uniform and well-defined films of plasmon metal such as gold and silver could be formed on surface modified quartz (Park *et al*, 1999).

1.4 Problem Statement

A perfect photo-catalyst is not yet available but TiO_2 is very close to being an ideal photo-catalyst. Besides all the good properties which TiO_2 has, there are some shortcomings of which the major drawback is its inactivity in the visible region which reduces its photo-catalytic efficiency. It only absorbs in the UV region which is only about 5 % of the total solar radiation and this implies that more energy is required to supply light of appropriate wavelength, making the use of TiO_2 expensive. Hence there is a need to do some modifications of TiO_2 so that it can respond in the visible region, which is the major part of the solar radiation (55 %). The modifications include doping which results in band gap reduction and an increase in photo-catalytic activity but metal ion dopants also sometimes serve as recombination centers for charge carriers thus act against the separation of excited electron and hole pairs (Tan *et al.*, 2011). This recombination of charge carriers is a major limitation in semiconductor photo-catalysis as it results in low quantum efficiency. Also, the metal ion dopants are often not effective in aiding surface reduction and oxidation reactions (Emeline *et al.*, 2008). The co-doping of TiO_2 with both a nonmetal and transition metal is believed to be appropriate in narrowing the band gap with minimal recombination centers.

Sensitization is another way to improve TiO_2 efficiency by broadening the range of visible light response but the use of a dye to photosensitize TiO_2 results in the destruction of the dye by oxidizing holes. When used in aqueous solutions the organic dyes can also detach from the photo-catalyst surface (Kusumawardani *et al.*, 2010). The use of plasmon elements which create local electric fields which make the TiO_2 respond to visible light seem to be a better alternative. The other drawback of TiO_2 is the low life span of the electron-hole carriers which is 10 ns due to high electron-hole recombination rates. This recombination is one of the most detrimental reactions in photo-catalysis as it affects the interfacial charge transfer processes resulting in a low photon quantum efficiency of the photo-catalytic process. The recombination rates could be reduced by effective immobilization of the photocatalyst on a conductive material (Saehana *et al., 2011*) or decorating the photo-catalyst with plasmon metal nanoparticles which act as electron reservoirs. As a result it is essential to develop a photo-catalyst that works efficiently in visible light/general sunlight while it has low charge recombination.

The use of powdered TiO_2 causes a shadowing effect reducing light penetration in solutions and also requires separation of the catalyst from the treated water by filtration after the photo-degradation process. Immobilization of the photo-catalyst on a support means no filtration will be required which could effectively save costs in commercial applications, since powdered TiO_2 has a high dispersion in water which causes difficulties in separation, whereas supported photo-catalysts do not pollute the water and allow better light penetration.

1.5 Aims

- The major aim of this study is to develop thin films of plasmon metal modified TiO_2 photo-catalysts on quartz supports that are capable of utilizing UV light or visible

light and have low electron-hole recombination rates and good antimicrobial properties.

1.6 Objectives

- To prepare and characterise TiO_2 photo-catalyst and plasmon metal thin films of different thicknesses immobilized on quartz substrates
- To study the effect of the order of deposition of the thin films of plasmon elements on TiO_2 photo-catalytic activity
- To study the effect of using a bilayer of two different plasmon elements on TiO_2 photo-catalytic activity
- To study the effect of plasmon element contents/loading on TiO_2 photo-catalytic activity
- To synthesise carbon-gold co-doped TiO_2 thin films with different amounts of gold and characterise them by HRTEM, HRSEM, EDS, Raman, FT-IR, BET, XPS and DRS
- To synthesise carbon-silver co-doped TiO_2 thin films with different amounts of silver and characterise HRTEM, HRSEM, EDS, Raman, FT-IR, BET, XPS and DRS
- To synthesise, characterize and study the effect of different nanostructures of gold and silver nanoparticles on the photo-catalytic activity of TiO_2
- To evaluate the durability of the as-prepared plasmon metal decorated photo-catalysts.
- To evaluate the specificity/selectivity of the photo-catalyst towards degrading certain organic compounds, as well as their antimicrobial properties
- To determine the photo-degradation pathway of the model pollutant using LC-MS technique

1.7 Research questions

- Is it possible to prepare and characterize TiO_2 photo-catalyst and plasmon metal thin films of different thicknesses immobilized on quartz substrates?
- What are the effects of order of deposition of the thin films of plasmon elements on TiO_2 photo-catalytic activity?
- What are the effects of using bilayer systems of different plasmon elements instead of monometallic layers on TiO_2 photo-catalytic activity?
- Is it possible to synthesize carbon and gold co-doped TiO_2 thin films with different contents of gold and characterize them?
- Is it possible to synthesize carbon and silver co-doped TiO_2 thin films with different contents of silver and characterize them?
- Is it possible to synthesize plasmon metal nanostructures of different shapes and study their effects on TiO_2 photo-catalytic activity?
- How durable and how long can the prepared TiO_2 photo-catalysts be used without losing their photo-catalytic activity?
- Are the prepared TiO_2 photo-catalysts more selective towards certain organic contaminants than others?
- Is it possible to determine the nature of the photo-degradation products of methyl orange?

1.8 Scope of the study

The study investigated the feasibility and effectiveness of plasmon metal enhanced TiO_2 semiconductor photo-catalyst as an advanced oxidation treatment technology for the mineralization of methyl orange and bromocresol purple to the levels that were not

detrimental to people, animals and the environment. The performance of the photo-catalyst was also tested with addition of salts and other organics to determine the effect of the presence of other contaminants on the performance of TiO_2 photo-catalyst. Three different models of plasmon enhanced TiO_2 photo-catalytic thin film systems were prepared to solve the issue of electron-hole recombination and light absorption resulting in low quantum efficiency. The semiconductor photo-catalyst was immobilized on quartz to eliminate the possibility of post-separation of TiO_2 nanoparticles when utilized in powder form. The employed model systems were as follows:

Model I: TiO_2 films and plasmon element films deposited layer by layer on quartz. This model had two sections;

(i) plasmon element thin films deposited underneath the TiO_2 thin films. This model tried to address both the effects of noble metals on TiO_2 photo-catalytic activity and the importance of reducing leaching of the metal nanoparticles during the photo-degradation process

(ii) TiO_2 thin films underneath the plasmon metal thin films. This model tried to address the importance of the order of deposition of the thin films.

Model I tried to determine the effect of plasmon elements on the photo-catalytic activity of TiO_2 photo-catalyst when they were deposited as films that is, layer by layer.

Model II: Plasmon metal and carbon co-doped TiO_2 photo-catalyst thin films. This model tried to address the importance of using a photo-catalyst that had both low band gap and low electron-hole recombination rates. It tried to find the effect of plasmon elements on the photo-catalytic activity of TiO_2 when they were used as dopants.

Model III: Composite material of plasmon elements and doped TiO_2 photo-catalyst. This model tried to show the importance and the effect of increasing contact surface area between metal nanoparticles and TiO_2 for efficient charge separation. It tried to show the effect of plasmon elements of different structures on the photo-catalytic activity of TiO_2 when they were used as composite materials.

The three model systems above were designed to address the role played by noble metals in enhancing photo-catalytic activity due to mechanisms such as localised surface plasmon resonance, electron capturing, band gap reduction, and/or activation by visible light. The plasmon elements that were employed were Au, Cu, and Ag.

1.9 Outline of thesis

This thesis consists of eight chapters and a brief summary of the contents of each chapter is presented in this section.

Chapter 1 gives the general introduction of the study. The aims, objectives and problem statement are presented in this chapter.

Chapter 2 gives a literature review which focuses mainly on the role of nanotechnology based materials in removing organic contaminants and bacteria from water. The different approaches of enhancing the photo-catalytic activity of TiO_2 both under UV and visible light and the general mechanisms of photo-catalysis are given. The possible mechanisms through which plasmon metal elements enhance TiO_2 photo-catalytic activity are discussed. The applications of TiO_2 and plasmon elements and the different kinds of photo-catalyst supports are also given towards the end of the chapter.

Chapter 3 presents the details of the experimental procedures and characterization techniques that were employed in this study. Where possible, the photographs and schematic representations of the experimental set-up are highlighted. A list of all materials used is also given.

Chapter 4 gives characterization of plasmon metal/TiO_2 photo-catalyst thin films made according to model I and the evaluation of their photo-catalytic activity using methyl orange and in some cases bromocresol purple. A systematic study on the effect of plasmon metal nanoparticle film thicknesses (loading), order of deposition of the films and the use of different plasmon elements (Au, Ag & Cu) is presented. Possible mechanisms of enhancement of TiO_2 photo-catalyst are discussed. A discussion on the effect of both operational parameters and presence of other contaminants on the photo-degradation of methyl orange is presented.

Chapter 5 presents the characterization and photo-catalytic activity evaluation of TiO_2 semiconductor co-doped with a nonmetal (carbon) and a transition metal (Au and Ag) made according to model II. The effects of transition metal loading on the band gap, surface area, anatase to rutile phase transformation and the resulting photo-catalytic activity are explored.

Chapter 6 gives a detailed account on the preparation of different plasmon metal nanostructures such as nanowires, dendrites and nanorods made according to model III and their effect on the photo-catalytic activity of TiO_2 when combined as nanocomposites.

Chapter 7 covers the evaluation of the antimicrobial activity of the plasmon decorated TiO_2 photo-catalysts under sunlight on *E. coli* 3695.

Chapter 8 gives conclusions and recommendations for further studies.

References cited in all the chapters are given at the end.

Chapter 2

Literature Review

2.1 Introduction

Potable water is regarded as one of the most important resources and its supply for human consumption is of high importance. The availability of new, improved analytical methods coupled with deeper understanding of the adverse effects of organic pollutants has triggered the enactment of stringent drinking water standards. Hence the water needs to undergo various treatment processes to remove both pollutants and pathogenic microorganisms before it can be used by people. There are several methods that can used to remove organic pollutants from water and the choice of which treatment technology to use depends on the characteristics of the water, the types of water quality problems likely to be present and the costs.

The available water treatment methods can be grouped into two: destructive and non-destructive techniques. The non-destructive techniques include adsorption, flocculation, coagulation, filtration and sedimentation. The destructive techniques that fall under advanced oxidation processes can be divided into two groups, the non-irradiation and irradiation techniques. The non-irradiation processes include ozonation, fenton process, sonolysis and electrohydraulic discharge. Photo-catalysis which falls under the irradiation processes is one of the most promising techniques in water treatment since various chemical and microbiological pollutants in water are degraded into harmless products (CO_2 and H_2O) without chemical addition. One of the most important aspects of environmental photo-catalysis is the availability of titanium dioxide which is a multifunctional semiconductor photo-catalyst that can be used as (i) an energy catalyst in hydrogen production, (ii) an

electron transport medium in dye-sensitized solar cells and (iii) an environmental catalyst in water and air purification (Lazar *et al*., 2012).

2.2 Semiconductor photo-catalysis

Photo-catalysis is an acceleration of a reaction under the action of light in the presence of a photo-catalyst that absorbs light quanta. The process can be powered by sunlight if a suitable catalyst is employed. It has gained interest due the fact that it is capable of degrading nearly all organic contaminants into harmless products if there is complete mineralization as represented by Equation 2.1.

$$Organic\ compounds \rightarrow CO_2 + H_2O + mineral\ acids \quad \ldots\ldots\ldots\ldots (2.1)$$

Photo-catalysis started in 1972 after the discovery of photochemical water splitting into oxygen and hydrogen using TiO_2 (Fujishima & Honda, 1972). Semiconductor photo-catalysis has several advantages which include (i) environmentally friendly, (ii) no use of chemicals, (iii) the equipment involved can be operated easily and (iv) the process can use free natural sunlight thus reducing operational costs.

2.2.1 Titanium dioxide as a semiconductor

Titanium dioxide has been investigated extensively for its electrochemical and catalytic properties due to its wide applications. It exists mainly in four forms namely anatase, rutile, brookite and TiO_2(B), all of which consist of TiO_6 octahedra but differing in the distortion and manner in which they share the edges and corners as shown in Figure 2.1.

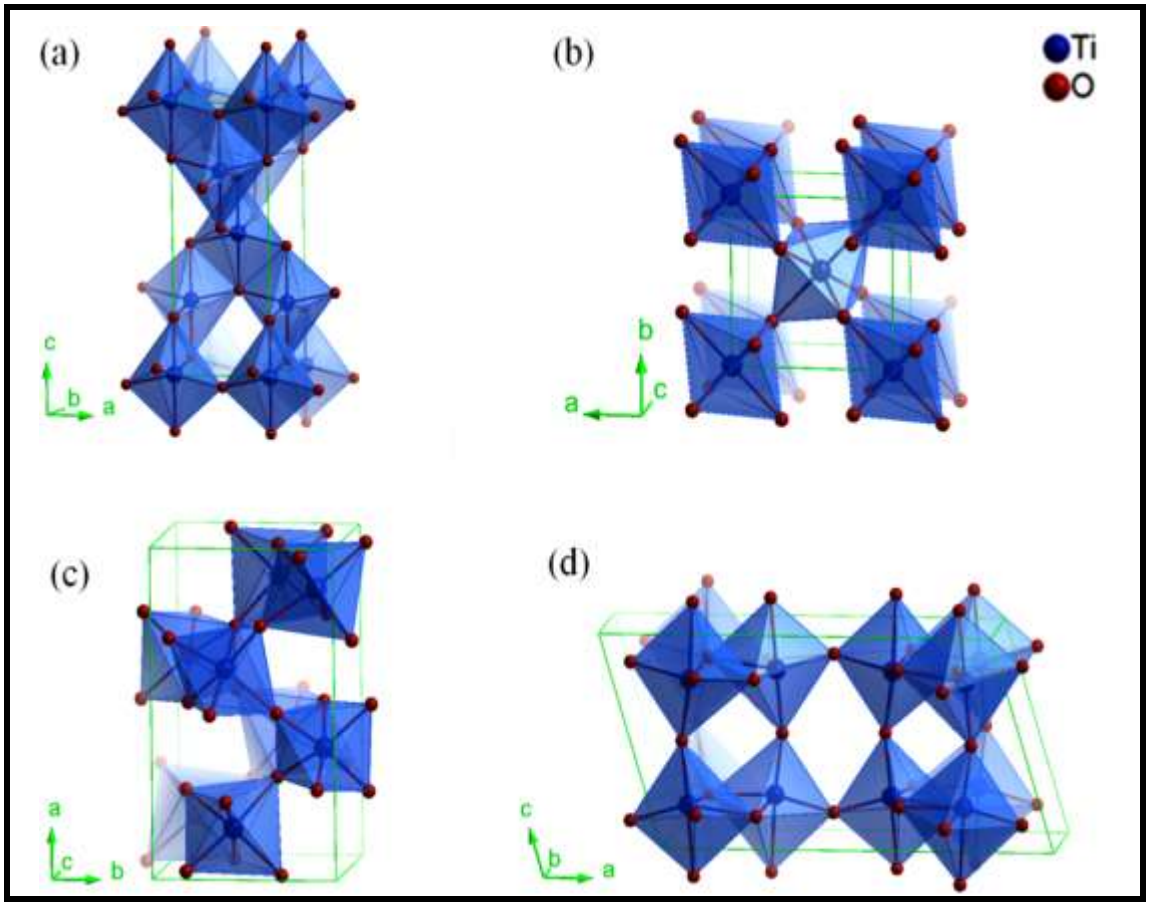

Figure 2.1: Crystalline Structures of different phases of TiO_2, (a) anatase, (b) rutile, (c) brookite and (d) TiO_2 (B), (Ma *et al*., 2014).

Brookite is not common and is less used as a catalyst when compared to anatase and rutile phases. The polymorphs have different mass densities, exhibit different photo-catalytic properties and electronic band structures due to the difference in lattice structures. The phase structure of the photo-catalyst is one of the most important factors that determine photo-catalytic performance of TiO_2.

Anatase with a band gap (E_{bg}) of 3.2 eV absorbs UV light around 387 nm and has been reported to be more catalytically active than rutile with a E_{bg} of 3.02 eV whose light absorption onset occurs around 413 nm (Emeline *et al*., 2008). The higher photo-catalytic activity of anatase is attributed to the slightly higher Fermi level, high density of localized

states and consequent high levels of adsorbed reactive species ($OH^{\bullet}$) and lower e^{-}/h^{+} recombination relative to rutile (Hanaor & Sorrell, 2011; Setiawati & Kawano, 2008). In some studies, researchers observed that a mixture of anatase (70-75 %) and rutile (25-30 %) is more photo-catalytically active than pure anatase (Muggli & Ding., 2001).

Rutile is more thermodynamically stable when compared to the anatase phase whereas anatase is kinetically stable at low temperatures (Ovenstone & Yanagisawa, 1999). The anatase phase is suitable for use as a catalyst and support (Foger & Anderson, 1996) while the rutile phase is employed for optical and electronic purposes due to its high refractive index and dielectric constant (Zhang *et al*., 1997). Rutile is obtained by annealing the other polymorphs at elevated temperatures and the mechanism of phase transformation depends on variables such as impurities, morphology and particle size of the starting anatase (Ma *et al*., 2014). The most stable crystal faces of rutile are the 100 and 101 (Ramamoorthy *et al*., 1994). Brookite does not change directly to rutile but changes into anatase first as follows:

brookite → anatase → rutile transition.

Based on band positions relative to the standard hydrogen electrode (NHE), several semiconductors such as WO_3, ZnO, ZnS, Fe_2O_3, CdS, WO_3 and $SrTiO_3$ (Figure 2.2) can be used in photo-catalysis for the photo-degradation of organics in water. In contrast with these semiconductors, TiO_2 is widely used in environmental applications and is close to being an ideal photo-catalyst because it is inexpensive, chemically stable, environmentally friendly, stable over a wide range of pH, relatively easy to produce and use, relatively nontoxic, the photo-generated holes are highly oxidizing and it has a relatively slow rate of charge carrier recombination in comparison with other semiconductors (Hanaor & Sorrell, 2011). For instance, cadmium sulphide has a small band gap of 2.42 eV but it is not desirable because it suffers from photo-corrosion resulting in the release of Cd^{2+} ions which are dangerous

pollutants (Yang, 1998). Zinc oxide also suffers from degradation during repeated photo-catalytic cycles due to pH sensitivity hence cannot be used for technical applications.

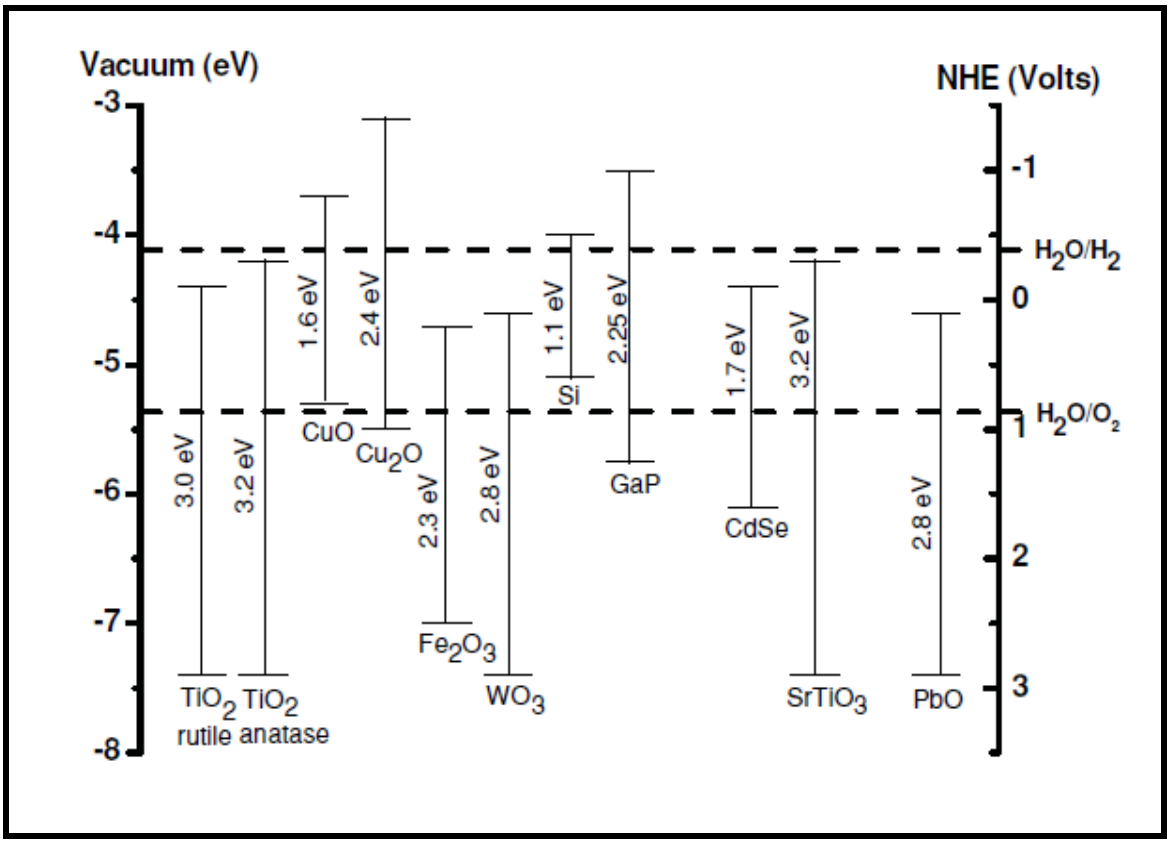

Figure 2.2: Energy band diagram and redox potentials of various metal oxide semiconductors.

The band edge position relative to NHE for the metal oxides has been reported to depend on the pH value of the solution through the same Nernstian relation as for the water redox potentials (Chen *et al*., 2012).

2.2.2 Principles of photo-catalysis

When a semiconductor photo-catalyst is irradiated with photons whose energies are equal or greater than the band-gap energy, electrons are excited resulting in the promotion of valence band (VB) electrons to the empty conduction band (CB) leaving a positive hole (h_v^+) in the

valence band. There are three possible ways in which the photo-generated electron-hole pairs may be involved and these are (Ma *et al*., 2014):

(i) Migrate to the semiconductor surface successfully

(ii) Recombine releasing heat energy or photons

(iii) Trapped by defect sites

The following reactions for the activation of TiO_2 have been widely postulated.

$$TiO_2 \xrightarrow{hv} e_{cb}^{-}(TiO_2) + h_{vb}^{+}(TiO_2) \qquad (2.2)$$

where *hv* is the energy required to transfer the excited electron from the valence band (vb) to the empty conduction band (cb). The superoxide radical is generated by the reduction of the adsorbed oxygen on the photo-catalyst as shown in equation 2.3. The superoxide ions then react with water molecules to produce hydroxyl ions (OH^-) and peroxide radicals ($^{\bullet}OOH$).

$$e^- + O_2 \longrightarrow O_2^{\bullet -} \qquad (2.3)$$

The hydroxyl radical is formed from the oxidation of adsorbed water by positive holes where it is adsorbed as OH^- as shown in equations 2.4 and 2.5.

$$H_2O_{ads} + h^+ \longrightarrow OH^{\bullet}_{ads} + H^+ \qquad (2.4)$$

$$h^+ + OH^-_{ads} \longrightarrow OH^{\bullet}_{ads} \qquad (2.5)$$

The hydroxyl radical is highly oxidizing and it attacks pollutants in the solution (Equation 2.6).

$$OH^{\bullet}_{ads} + \text{organics} \longrightarrow CO_2 + H_2O \qquad (2.6)$$

A simplified mechanism for the activation of TiO_2 photo-catalyst is shown in Figure 2.3.

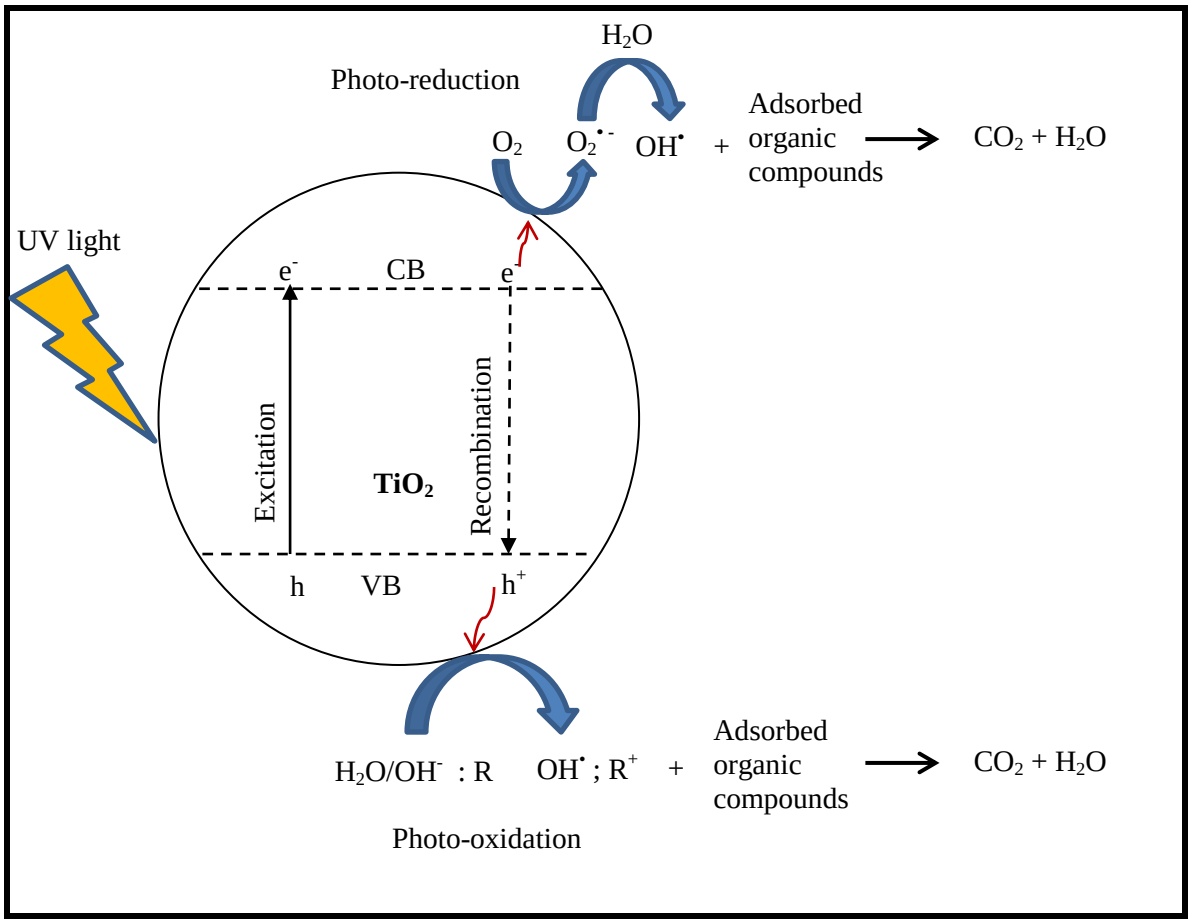

Figure 2.3: Schematic representation of the activation of TiO_2 photo-catalyst and principle of photo-catalysis.

The overall oxidation pathway can be divided into five steps (Chong *et al*., 2010; Fogler *et al*., 1999) and these are:

(i) Diffusion of the organic contaminants to the photo-catalyst surface.

(ii) Adsorption of the organic contaminants onto the photo-catalyst surface.

(iii) Photodecomposition of the adsorbed organics on the TiO_2 surface.

(iv) Desorption of products from the TiO_2 surface.

(v) Diffusion of products from the photo-catalyst surface.

From the given oxidation pathway, it can be noted that only the organic molecules that are in direct contact with the photo-catalyst surface undergo photo-catalytic degradation.

2.2.3 Preparation of titanium dioxide

There are several methods that can be used to prepare titanium dioxide nanoparticles. The available methods include solvothermal, sol-gel process, hydrothermal, sonochemical, microwave assisted, deposition method and oxidation methods. Some of these methods are discussed in detail in the following sections.

2.2.3.1 Deposition methods

The methods involve the condensation of materials in the vapour state to form a solid phase material. The deposition process is normally carried out in a vacuum chamber and if a chemical reaction takes place it is called chemical vapor deposition (CVD) and physical vapor deposition (PVD) if no reaction occurs. In CVD, there are several parameters that need to be controlled so as to have the desired material. The parameters include pressure, flow rate, gas composition, deposition temperature and geometry of the chamber. Djerdj and coworkers, (2005) prepared TiO_2 films using VCD on different substrates and they found that the nature of the substrates influence size and distribution of nanograins in the films.

2.2.3.2 Hydro/solvo-thermal methods

The solvothermal and hydrothermal methods are similar except that the solvent used in the solvothermal method is not aqueous and temperatures can be elevated much higher (Byranvand *et al*., 2013). Solvothermal method has better control of TiO_2 properties such as size and shape distributions and crystallinity than the hydrothermal method. Synthesis using these methods is usually done in autoclaves under controlled pressure and temperature. The temperature and the amount of solvent added to the autoclave determine the internal pressure produced. Several researchers have used these techniques to prepare TiO_2 nanoparticles (Yan *et al*., 2013; Gao *et al*., 2001; Mohan *et al*., 2013; Huang *et al*., 2006).

2.2.3.3 Oxidation method

The direct oxidation methods involve the formation of nanostructured TiO_2 by the oxidation of titanium metal using oxidants or anodization. Wu and co-workers produced crystalline TiO_2 nanorods by directly oxidizing titanium metal with hydrogen peroxide (Wu *et al*., 2005). Ryu et al prepared TiO_2 nanotubes by the anodization process using commercial pure titanium foil (Ryu *et al*., 2008). The process was performed in a solution of NH_4F and malonic acid using voltages between 5 and 20 V at ambient temperature (22 °C).

2.2.3.4 Sol-gel methods

A sol-gel process is the conversion of a precursor solution to an inorganic solid through polymerization reactions induced by water. It involves the formation of a colloidal suspension called a sol that is formed from hydrolysis and polymerization reactions of the precursors. The precursors are normally inorganic metal salts or metal inorganic compounds such as alkoxides. When the polymerization process is accompanied by removal of the solvent, there is a transition from the liquid sol to a solid gel phase. The method is promising

for TiO_2 synthesis or other inorganic nanomaterials when compared to other preparation methods because it allows the use of temperatures of less than 100 °C and molecular level homogeneity. One of the most attractive features of this method is the possibility to shape the resulting nanomaterial into different forms of interest such as fibers, films and monodispersed powders (Cushing *et al*., 2004).

Most metal alkoxides that are normally used in the sol-gel process are generally very reactive hence modifiers or chelating ligands such as β-diketones, carboxylic acids or other complex ligands are added to control the reactivity (Attar *et al.*, 2008). The process usually proceeds via an acid-catalyzed hydrolysis of titanium (IV) alkoxide followed by condensation. The formation of the Ti-O-Ti chains with a low water content and the formation of $Ti(OH)_4$ is favored by high rates of hydrolysis (Byranvand *et al*., 2013).

2.2.4 Parameters affecting TiO_2 efficiency

The parameters which affect the efficiency of a photo-catalytic oxidation process include initial concentration of the contaminant, light intensity and wavelength, presence of inorganic ions, temperature, pH, reactor design, catalyst loading and oxygen content (Grozescu *et al*., 2013; Mozia *et al*., 2005). Besides the parameters discussed above, the rate of free radical generation and the extent of contact between organic compounds and radicals also determine the efficiency of advanced oxidation processes. The adsorption of organic compounds on the photo-catalyst is often considered to be a prerequisite for the photo-degradation of the organics hence affecting efficiency but other studies suggest it is not required as the $OH^{\bullet}$ radicals are capable of diffusing into the solution to react with the pollutants (Para *et al*., 2002). The $OH^{\bullet}$ radicals are highly reactive hence they cannot diffuse far meaning the reactions have to take place close to the photo-catalyst surface (Minero *et al*., 1992).

2.2.5 Advantages of TiO_2 photo-catalysis

Photo-catalysis using TiO_2 photo-catalyst has several advantages and these include:

(i) Oxidation of organic pollutants in the ppb range.

(ii) Non-selective destruction organic contaminants under normal temperature and pressure.

(iii) Oxidative and reductive reactions occur simultaneously

(iv) The photo-catalyst is adaptable to specially designed reactor systems

(v) Uses oxygen as the only oxidant

(vi) Effective for inactive contaminants such as alkanes and their derivatives hence making it possible for cleaning oil spills (Heller *et al*., 1994) and dyes from industrial effluent (Kiwi *et al*., 1993).

2.2.6 Shortcomings of TiO_2 as a photo-catalyst

Besides all its advantages mentioned in the previous section, TiO_2 has disadvantages in its applications as a photo-catalyst. The major drawback is its wide band gap meaning that it only absorbs UV light which is only 5 % of the total solar spectrum. Absorption of visible light which is the major part of the solar radiation is prevented hindering efficient photo-catalysis hence a lot of effort has been made to find ways of resolving this problem. Some attempts of modifying TiO_2 to achieve efficient photo-catalysis using visible light has been made (Shar *et al*., 2002; Nyamukamba *et al*., 2012; Mungondori *et al*., 2013; Kuvarega *et al*., 2011). Another disadvantage of the use of TiO_2 as a photo-catalyst is the high recombination rates of photo-generated electron-hole pairs. It is believed that this recombination is one of the main reasons for the low efficiency of the TiO_2 photo-catalyst. The electron-hole recombination time (10^{-9} s) is shorter than the time for chemical interaction with adsorbed species which is in the range 10^{-8}–10^{-3} s (Fan *et al*, 2013). It is only the photo-generated

charges that successfully reach the semiconductor surface that participate in the photo-catalytic reactions hence efficient charge separation is the key to good photo-catalytic activity of the semiconductor. The last key challenge on the use of TiO_2 is its use as a powder. Immobilizing it on a support has been found to reduce its efficiency but when used as a powder, the filtration step is required which adds extra cost to develop commercial applications and the powder form limits the penetration of light due to the shadowing effect.

2.3 Modifications to enhance TiO_2 performance

To overcome the shortcomings which reduce the wide application of TiO_2 as a photo-catalyst, a lot of researchers have attempted to improve photo-catalytic activity using various modifications which can be categorized into three approaches, (i) quantum yield improvement which include creation of oxygen deficiencies (Nakajima *et al*., 2001), and crystal structure modifications (Zhang & Banfield, 2000) all of which affect photo-catalytic activity, (ii) Extension of light absorption from the UV region into the visible region by doping with metals and/or non-metals (iii) suppression of electron-hole recombination rates which can be achieved by deposition of plasmon elements which act as electron traps aiding separation. The modifications include noble metal loading, ion doping, anion doping, addition of electron donors, dye sensitization, coupling with low band gap semiconductors and noble metal loading (plasmon metal enhancement) which is the main focus in this study.

2.3.1 Doping

Doping is the addition of impurities in a controlled manner to intrinsic semiconductors to alter their properties**.** From the present semiconductor technologies, it is well known that the incorporation of impurities or defects into semiconductor lattices is the primary means of controlling properties of the semiconductor (Bryan *et al.*, 2005). Doping of the TiO_2 photo-

catalyst can be done using either cations or anions and to achieve maximum efficiency, the optimum dopant level should not be exceeded otherwise the photo-catalytic activity decreases (Ma *et al*., 2014). Different dopants have different electron-hole trapping capabilities on the surface or during interface charge transfer due to their different positions in the TiO_2 lattice (Shah *et al*., 2002). Doping improves physical properties such as high crystallinity, high specific surface area and promotes small crystallite size. Nyamukamba *et al*., (2012) reported that carbon and nitrogen dopants helped to control the crystallite size of nano-doped-TiO_2 and increased its surface area. High surface areas can enhance adsorption resulting in high photo-catalytic activity. It is quite clear from literature that small crystallite size which results in high surface area increases the efficiency of TiO_2 photo-catalyst but, care must be taken not to reduce the particle size below the Bohr radius of the semiconductor. This is because as the particle size decreases below the Bohr radius of the semiconductor material, the electron becomes more confined in the particle resulting in the increase in the band gap energy (quantum confinement effect) (Eustis & El-Sayed, 2006).

Both metal doping (Rahulan *et al*., 2011) and nonmetal doping (Sathish *et al*., 2005) were proved to red-shift the absorption edge to lower energies thereby enhancing the photo-catalytic activity. For years, doped TiO_2 photo-catalysts have been prepared using different methods and experimental conditions hence it is difficult to summarize optical mechanisms and photo-catalytic properties. Generally dopants are considered to reduce band gap, introduce mid-gap states (Nowotny *et al*., 2007), improve charge carrier separation and promote adsorption of reactive species such as hydroxyl radicals (Franch *et al*., 2005). The position of the incorporated heteroatom in the lattice of TiO_2 plays a major role in the band structure and there are two sites (interstitial and substitutional) which are possible for doping.

It is believed that the occupation in the substitutional position alters the band gap more effectively than doping in the interstitial position (Palanivelu *et al*., 2007).

2.3.1.1 Metal doping

When cations are used to dope TiO_2, an impurity level could be introduced in the forbidden band which acts either as an electron acceptor or donor thus allowing visible light absorption. Due to their unique d-orbital electron configuration, transition metal doping also modifies the conduction band or the valence band resulting in improved TiO_2 photo-catalytic activity (Wang *et al*., 2014). Shah and coworkers (2002) investigated the effect of doping with Nd^{3+} , Pd^{2+} , Pt^{4+} , and Fe^{3+} on the photo-catalytic degradation of 2-chlorophenol and they found that Nd^{3+} and Pd^{2+} improved TiO_2 performance, Pt^{2+} showed a very small decrease and Fe^{3+} was detrimental to the photo-degradation process (Shah *et al*., 2002). Numerous metals have been investigated and controversial results have been reported in literature and different models have been proposed to explain the phenomena. Choi and coworkers (2010) investigated the effects of doping TiO_2 with 13 metal ions and they found that all metal ions extended the absorption of TiO_2 into the visible region except Ag^{+}, Rb^{+}, Y^{3+} and La^{3+}. Li and coworkers (2007) studied the effect of doping with alkali earth metal ions (Be^{2+}, Mg^{2+}, Ca^{2+}, Sr^{2+} and Ba^{2+}) and all improved hydrogen production but only with optimum loading. The study by Wang and coworkers showed that most transition metal doping could reduce the TiO_2 band gap leading to improved photo-catalytic activity and still maintain strong redox potential (Wang *et al*., 2014). Polycrystalline TiO_2 photo-catalysts doped with Mo, Cr, W, Fe, Co, V and Cu were prepared by Di Paola and co-workers., (2002) and they found that TiO_2 doped with W was the most efficient in photo-degrading 4-nitrophenol and benzoic acid.

Although metal ion incorporation in the TiO_2 crystalline matrix was found to significantly influence photo-catalytic activity, there are some shortcomings which are controversial such as lack of reliable controllability of the doping structure, increase in charge carrier recombination rates and interfacial electron-transfer rates (Choi *et al.*, 1994: Diwald *et al.*, 2004). The controversy is partly due to the difficulty in establishing valid direct comparisons and drawing conclusions about the effect of metal ion dopant on photo-catalytic activity of TiO_2 due to different experimental conditions utilizing parameters that are inconsistent and different sample preparation methods. Choi and co-workers., (1994) concluded that the relative efficiency of the cation depended on whether it served as a recombination center or as a mediator of interfacial charge transfer. They claimed that the role played by the cation depended on (i) the concentration of the dopant, (ii) dopant distribution within the particles, (iii) dopant energy level within the lattice of the photo-catalyst, (iv) intensity of the incident light and (v) electronic configuration of the d-energy levels. Therefore the total induced changes in photo-catalytic activity are a result of the changes in the light absorption ability of the photo-catalyst, adsorption capability of substrates on the photo-catalyst surface and rate of interfacial charge transfer.

2.3.1.2 Nonmetal doping

Doping with nonmetal ions has been shown to be effective in inducing TiO_2 electronic modifications through the creation of oxygen vacancies without significant changes in the photo-catalyst's optical absorption (Rengifo-Herrera & Pulgarin., 2010). This is controversial as most researchers who studied nonmetal doping concluded that, nonmetals narrow the TiO_2 band gap resulting in the semiconductor absorbing in the visible region.

Nitrogen is one of the most studied TiO_2 dopants for shifting spectral response into the visible region. Mungondori and Tichagwa., (2013) reported that nitrogen doped TiO_2 is capable of degrading methyl orange under visible light irradiation due to reduced band gap energy. Up to date researchers have come up with several opinions to describe modification mechanism of N-doped TiO_2 which results in visible light absorption and these include;

(i) Creation of oxygen vacancies; From the series of experiments conducted by Kuznetsov & Serpone., 2006 on doping TiO_2 with N, C and S, it was proposed that the visible light activity of TiO_2 was due to oxygen vacancies formation. Ihara et al., 2003 reported that the oxygen deficient sites formed at the grain boundaries are important for prevention of re-oxidation and promotion of visible light absorption.

(ii) Band gap narrowing; It is generally considered to be an effective approach for improving visible light driven photo-catalysts. Most researchers proposed that when nitrogen is used as a dopant, it substitutes some oxygen atoms in the lattice of TiO_2 and reduces the band gap by mixing/overlapping of the N 2p and O 2p states. This is possible since the N 2p and O 2p states have energies that are very close and the atomic radius of nitrogen is similar to that of oxygen (Zhao *et al*., 2008).

(iii) Impurity energy levels; The N doped TiO_2 optical absorption red shift into the visible region was explained by means of spin-polarized GGA calculations which showed that the N 2p states were localized above the O 2p valence bands (Valentin *et al.*, 2005). Electrons are excited from the impurity energy level when illuminated with visible light. This is illustrated in Figure 2.4.

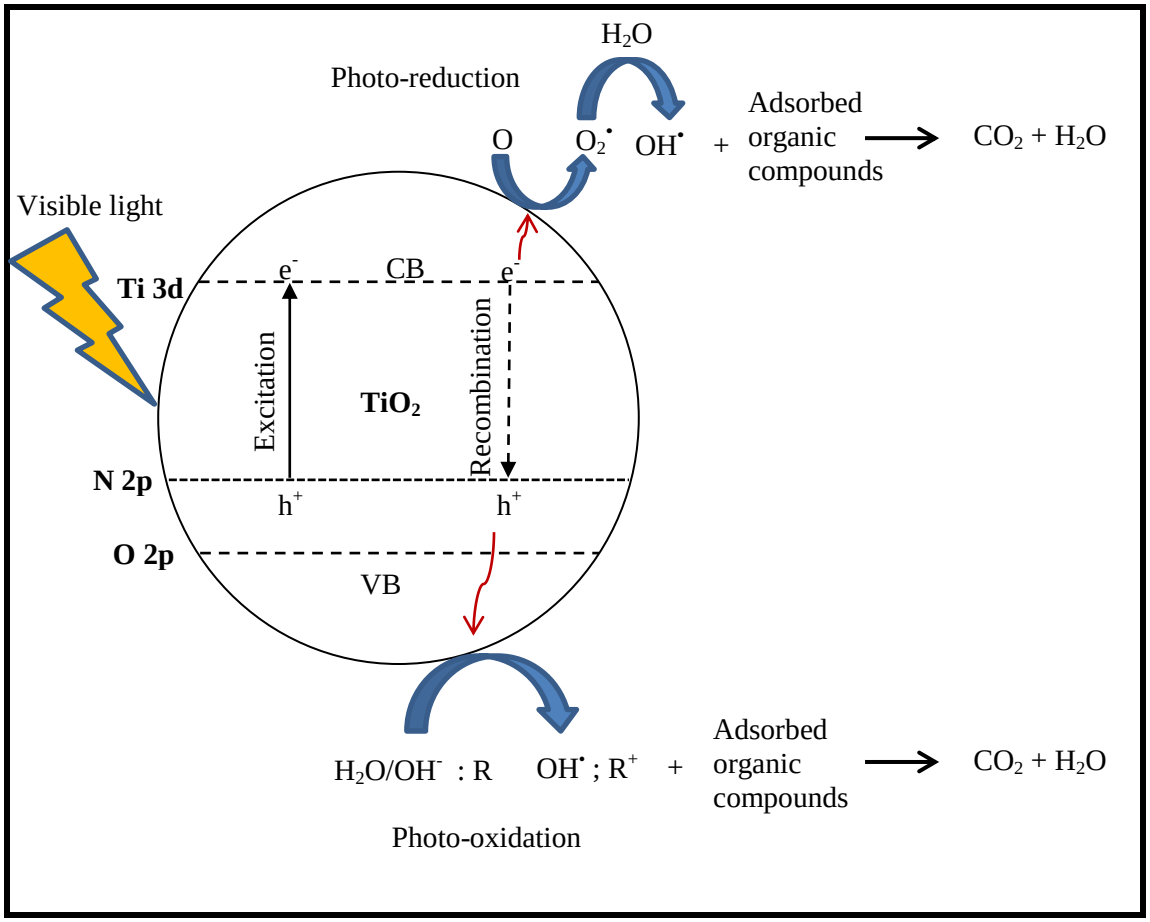

Figure 2.4: Schematic representation of visible light activation of N-doped TiO_2 photo-catalyst and photo-catalysis.

Besides nitrogen, there are other nonmetals that can be used for doping TiO_2 and these include C, I, F, P, B, S, Cl and Br. Yang *et al* co-doped TiO_2 with carbon and nitrogen and it resulted in enhanced photo-catalytic activity which they concluded as due to oxygen vacancy states and formation of Ti^{3+} species in the band structure (Yang *et al*., 2008). Co-doping of TiO_2 with carbon and nitrogen was also found to be effective in the photo-degradation of methylene blue under visible light irradiation due to the beneficial effects from both dopants (Zhang & Song., 2009; Yang *et al*.; 2008).

2.3.2 Dye sensitization

The use of sensitizers on TiO_2 to utilize visible light has been an area of interest in photochemical energy conversion and degradation of toxic substances. The sensitizers are normally quantum dots or organic dyes both of which have the disadvantage of low photo-stability and lose of the dye due to mineralization during photo-catalysis resulting in the lowering of TiO_2 efficiency or even losing its response towards visible light. The sensitizers are visible light absorbers which collect the radiation and transfer its photo-excited electrons to the semiconductor. Hirano and coworkers (2000), sensitized platinum loaded TiO_2 powder by $Ru(bpy)_3^{2+}$, tris(bipyrimidine)Ru(II) and porphines for efficient H_2 production from water. Furlong and coworkers, (1986) also achieved H_2 evolution under visible light after adsorbing tris(2,2'-bipyridine-4,4'-dicarboxylic acid)ruthenium(II) ($Ru(dcbpy)_3$) sensitizer on platinized TiO_2 particles.

The dye absorbs energy and becomes excited resulting in an electron transfer from the dye to the conduction band of the semiconductor. The injected electron reacts with surface adsorbed oxygen yielding $O_2^{\bullet}$ (Equations 2.7-2.9) leading to the reduction of organic compounds.

$$Dye + hv \longrightarrow Dye^{*} \qquad 2.7$$

$$Dye^{*} + TiO_2 \longrightarrow Dye^{\bullet+} + TiO_2(e^{-}) \qquad 2.8$$

$$TiO_2(e^{-}) + O_2 \longrightarrow TiO_2 + O_2^{\bullet-} \qquad 2.9$$

2.3.3 Coupling

Generally no single semiconductor excels in efficient light absorption for photo-catalysis hence combining two semiconductors synergistically will compensate their individuual weakness. The coupling of TiO_2 with a low band gap semiconductor results in an increase in the photo-response, efficient charge separation, increased life-time of charge carriers, and an enhanced interfacial charge transfer to adsorbed substrates resulting in enhanced photo-catalytic activity of the TiO_2 semiconductor. Under visible light illumination, the low band gap semiconductor coupled to TiO_2 is photo-excited, producing electrons that travel through the semiconductor to the non-activated TiO_2 nanoparticles. These injected electrons are then transferred to the TiO_2 surface to form a superoxide radical which attacks water producing strongly oxidising hydroxyl radicals. The common semiconductors and metal oxides that can be coupled with TiO_2 photo-catalyst include ZnO, CdS, WO_3, MnO_2, MoO_3, Bi_2S_3, SnO_2 and In_2O_3. Among these, CdS received the most attention.

Semiconductors coupled to TiO_2 also significantly reduce electron-hole recombination due to the heterojunction space between the two semiconductors which allows effective charge separation. The charge separation is due to the difference in the conduction band (CB) and valence band (VB) potentials of the two semiconductors which makes the electrons and holes move in opposite directions to accumulate on different semiconductors (Lee *et al*., 2014). For efficient charge separation, the placement of the individual semiconductor should be appropriate and the thickness of the covering semiconductor should be optimal.

Gopidas *et al*., (1990) reported that methyl blue was almost completely degraded by CdS/TiO_2 photo-catalyst under visible light irradiation. It has been reported that the use of SnO_2/TiO_2 composite system increased the photo-degradation of textile dyes by ten times

since electrons were transferred from TiO_2 CB to SnO_2 CB and holes from VB of SnO_2 to VB of TiO_2 (Vinodgopal *et al*, 1996; Wang *et al*., 2009). The photo-catalytic decomposition of 1,4-dichlorobenzene was found to increase by almost six times when TiO_2/WO_3 coupled semiconductor was used compared to pure TiO_2 (Song *et al*., 2001)

2.3.4 Plasmon metal enhancement

The recent development of surface plasmon resonance (SPR) has paved the way for an opportunity to overcome the low efficiency of semiconductor photo-catalysts. The incorporation of plasmonic nanomaterials onto semiconductors gives an alternative and promising way of improving both the photo-catalytic activity and solar energy conversion of the semiconductors. This introduction of metallic nanostructures onto a semiconductor to enhance of photo-catalytic activity by strong plasmonic effect has received attention recently (Xu *et al.*, 2013). There are several ways in which the SPR of the plasmonic materials improves the photo-catalytic activity and these include: (i) extension of light absorption to low energy, (ii) excitation of electrons in semiconductors by transfer of plasmonic energy from metal to semiconductor, (iii) increase in light scattering (iv) reduction in electron-hole recombination and (v) direct electron transfer from metal to semiconductor. The mechanisms are explained in detail in the next section.

The deposition of Au nanoparticles on TiO_2 was found to enhance the photo-catalytic activity of TiO_2 under visible light in the degradation of 2-propanol and acetic acid (Kowalka *et al*., 2010) and oxidation of alcohols to carbonyl compounds (Naya *et al*., 2010). Au nanoparticles were also deposited on other semiconductors other than TiO_2 such as ZrO_2 and SiO_2 and they showed efficient selective oxidation of hydrocarbons and other organic compounds such as CH_3OH and HCHO (Chen *et al.*, 2008). Liu *et al.*, (2011) demonstrated plasmonic

enhancement of photo-catalytic water splitting under visible light which showed up to 66 times more with addition of Au nanoparticles. Liu *et al*., (2014) also reported that the deposition of silver on TiO_2 nanosheets improved the photo-catalytic activity of TiO_2. It was found that the photo-catalytic degradation of phenol red and methyl orange was highly improved by the addition of Ag onto TiO_2 photo-catalyst under visible irradiation (Shah *et al*., 2015).

Gold and silver have photo-catalytic activities but they are lower when compared to plasmon enhanced TiO_2 where there is a synergistic interaction between the plasmon nanoparticles and TiO_2 photo-catalyst (Hintsho *et al*., 2014). The use of Au-TiO_2 composite on the degradation of Rhodamine-B was studied by Zhou *et al*., (2012) and they found that the decolourization of the contaminant was significantly enhanced by the Au nanoparticles. Gondal *et al*., (2013) prepared Au/Cu-TiO_2 nanoparticles using a sol-gel method for photo-reduction of Cr (IV) and the presence of the noble metals showed enhanced activity when compared to bare TiO_2 nanoparticles.

The use of Janus Au-TiO_2 nanostructures for hydrogen generation was reported by Seh *et al*., (2012) and they proved to be efficient plasmon-enhanced visible-light photo-catalysts due to stronger localization of plasmonic fields. (Janus particles are nanoparticles whose surfaces have at least two distinct physical properties). They found that the photo-catalytic activity of the Janus nanostructures increased with an increase in the size of the gold nanoparticles due to their stronger plasmonic near-fields.

2.3.4.1 Mechanism of enhancement

There are several possible mechanisms of TiO_2 enhancement by plasmonic metal nanostructures and these include; (i) plasmonic enhancement of light absorption and scattering, (ii) direct transfer of plasmonic energy from metal to semiconductor which is also called plasmonic induced resonant energy transfer and (iii) reduction of electron-hole recombination rates

(i) Direct electron transfer (DET)/Visible light sensitization

Xiang *et al.*, (2013) reported that when the incident photons are absorbed by gold nanoparticles, there is injection of electrons from gold into the conduction band of TiO_2 which will then be scavenged by oxygen. This happens when the metal and TiO_2 nanoparticles are in direct contact and also if there is a match of the metal electron energy level with TiO_2 conduction band. Primo *et al.*, (2011) proposed a mechanism similar to that of Xiang *et al.*, (2013) for the degradation of 2-propanol but in their mechanism the resulting positive gold oxidized 2-propanol to form the initial zero-valent metallic state. Kowalska *et al.*, (2010) also suggested a similar mechanism for gold nanoparticles (AuNPs). Gunawan and co-workers, (2009) demonstrated that when Ag-TiO_2 is exposed to light of wavelength greater than 450 nm, it results in the excitation and reverse flow of electrons from silver to TiO_2 overcoming the Schottky barrier. This absorption of visible light by noble nanoparticles to activate the photo-catalyst is an essential mechanism of plasmonic photo-catalysis as it enables the creation of active electrons and holes in TiO_2 photo-catalyst even without light absorption by TiO_2. This DET mechanism is illustrated in Figure 2.5.

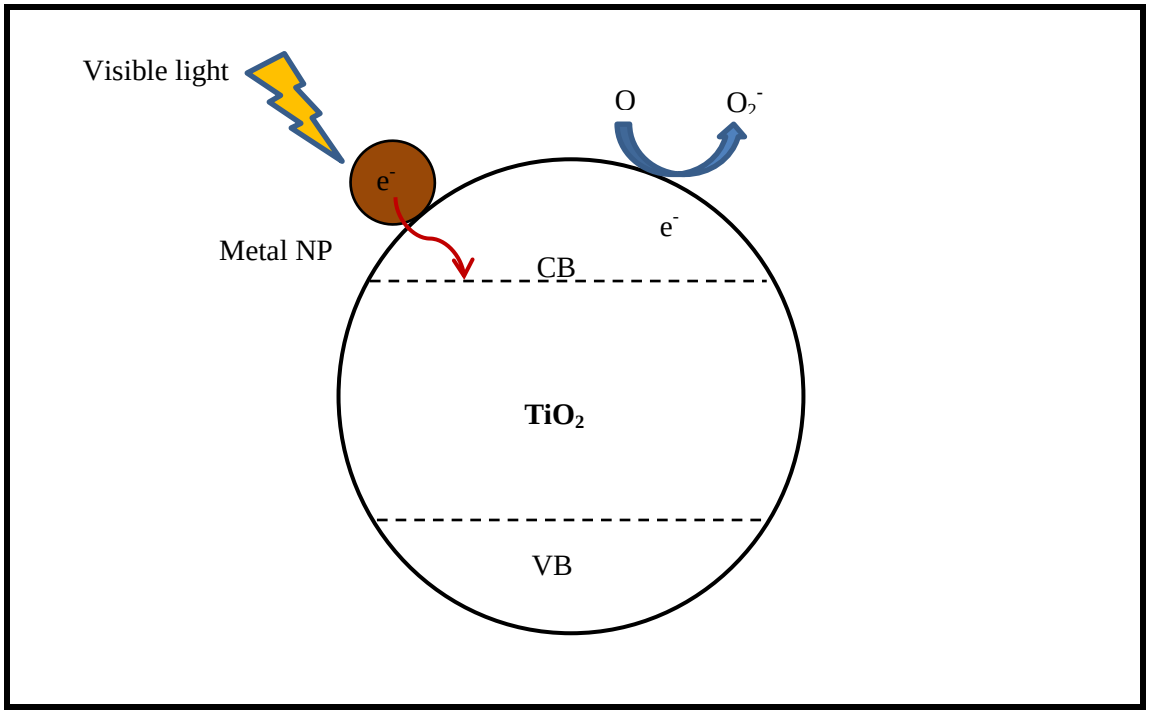

Figure 2.5: Schematic illustration of the proposed mechanism of activation of TiO_2 via direct electron transfer.

(ii) Plasmonic induced resonant energy transfer (PIRET)

PIRET involves the direct transfer of the plasmonic energy from the metal to the semiconductor resulting in charge separation in the semiconductor photo-catalyst. It allows charge transfer even below the photo-catalyst's band gap energy. PIRET was found to proceed also when the there is an insulating layer between the semiconductor and the plasmonic material (Cushing *et al.*, 2012)**.** It is a non-radiative transfer of energy from the localised surface plasmon resonance (LSPR) of the metal to the transition dipole of the semiconductor which results in the excitation of the electron in the semiconductor as illustrated in Figure 2.6a. In other words, the plasmon metal nanoparticles generate strong electric fields which strongly couple to optical transitions involving localized electronic states in TiO_2 resulting in enhanced optical absorption and generation of electron-hole pairs. Its

strength depends on the distance between the plasmonic metal and the semiconductor, as well as the overlap of absorption band of the semiconductor with the LSPR resonance band.

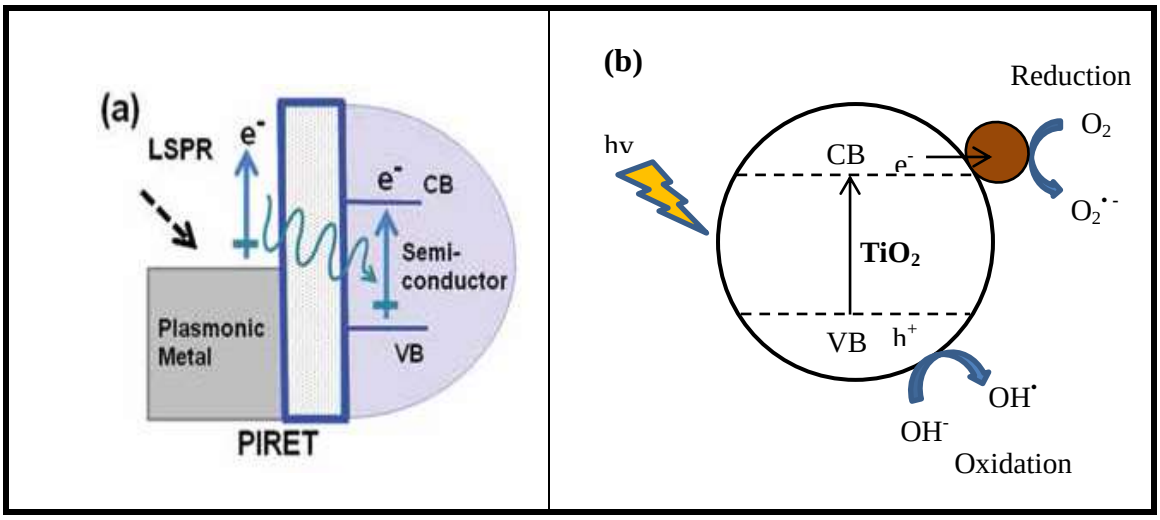

Figure 2.6: Schematic representation of surface plasmon enhanced photo-catalysis mechanism via (a) PIRET (Scott & Ninqiang., 2013) and (b) electron trapping by the metal nanoparticle.

When compared to DET, PIRET depends on spectral overlap and does not require physical contact between the plasmonic material and the semiconductor. It is important to note that both processes can coexist depending on the parameters of the material.

(iii) Electron capturing by metal nanoparticles

Previous studies on the use of plasmon elements have shown that the deposition of noble metals reduces the recombination of the photo-generated electron–hole pairs (Liu *et al.*, 2014). The contact between semiconductor photo-catalyst and the noble metal nanoparticles creates a Schottky junction which enhances the separation of charge carriers and suppresses their recombination. When Au/TiO_2 is irradiated with UV light, electrons in the conduction band of TiO_2 migrate to gold nanoparticles which act as an electron reservoir (Alvaro *et al*,

2010) as shown in Figure 2.6b. The enhancement can also be explained in terms of energy differences. For instance, in silver decorated photo-catalyst (Ag-TiO_2), the Fermi level of Ag is lower than the energy level of the bottom of the TiO_2 conduction band hence the electrons will transfer from TiO_2 to the deposited silver nanoparticles. Yu *et al.*, (2013) suggested that after the electron transfer from silver nanoparticles (AgNPs) to the conduction band of TiO_2, the resulting positively charged Ag^+ can oxidize organic molecules.

(iv) Light absorption enhancement

The semiconductor's light absorption is enhanced by the metal nanoparticles through increasing the optical path length and concentrating the incident field. The generation of the intense electric fields by plasmon elements results in an increase in the probability of interaction between light and TiO_2 semiconductor in close vicinity to the metallic nanoparticles. The heating effect produced at the surface and immediate vicinity of the metal nanoparticles heats up the environment around the nanoparticle which is believed to increase mass transfer of the molecules and enhancing the rate of reaction (Zhang *et al*., 2013). This phenomenon depends on particle size, light intensity and heat conductivity of the surrounding medium (Adleman *et al*., 2009). The surface plasmon also polarizes the molecules of the substance to be degraded resulting in the enhancement of its adsorption onto the metal and photo-catalyst surface (Zhang *et al*., 2013).

(v) Metal nanoparticles participation

When a noble metal absorbs photons, it experiences electronic transitions which can be divided into intraband and interband electronic transitions (Hopkins., 2010). Since UV light exceeds the minimum energy that is required for interband transitions in metals, it should be able to initiate electron excitation from filled valence band to unfilled conduction band. It is

therefore expected that the generated electron-hole pairs in these metals participate in redox reactions giving high photo-catalytic activities as shown in Figure 2.7.

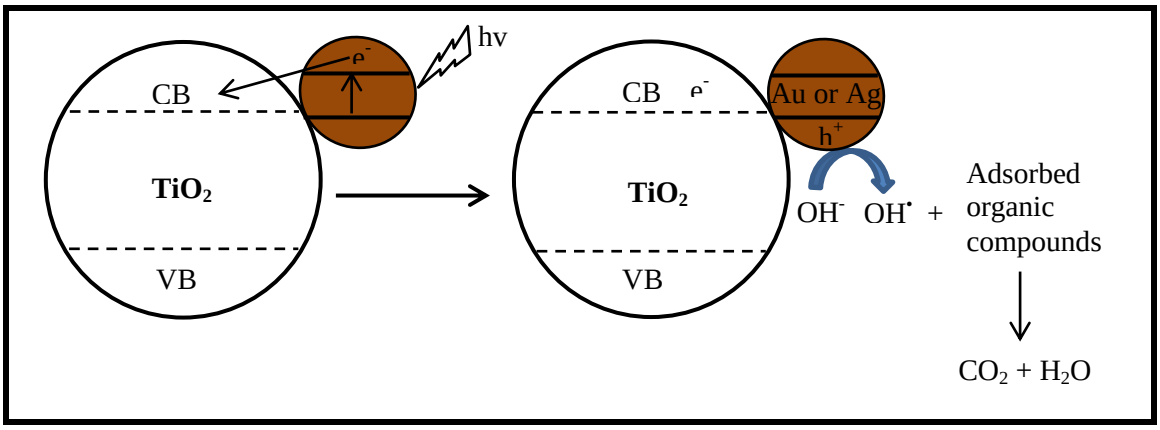

Figure 2. 7: Schematic representation of plasmon metal participation in photo-catalysis.

2.3.4.2 Surface Plasmon Resonance

Plasmons are defined as the collective oscillations of free electrons with respect to fixed positive ions in a conducting solid material and it is an important property of metals. The resonant interaction between the surface charge oscillation and the electromagnetic field of the light gives rise to absorption and scattering of light (Kefeng *et al.*, 2006). When light is below the plasma frequency, it is reflected because the electrons in the metal screen the electric field of the light and when the light is above the plasma frequency it is transmitted because the electrons cannot respond fast enough to screen it. Surface plasmons are oscillations that are confined to the surfaces of conducting materials and interact strongly with light whereas localized surface plasmon resonance (LSPR) is a result of the collective oscillation of conduction electrons within the metallic nanoparticle and metallic nanostructures when it interacts with light as illustrated in Figure 2.8.

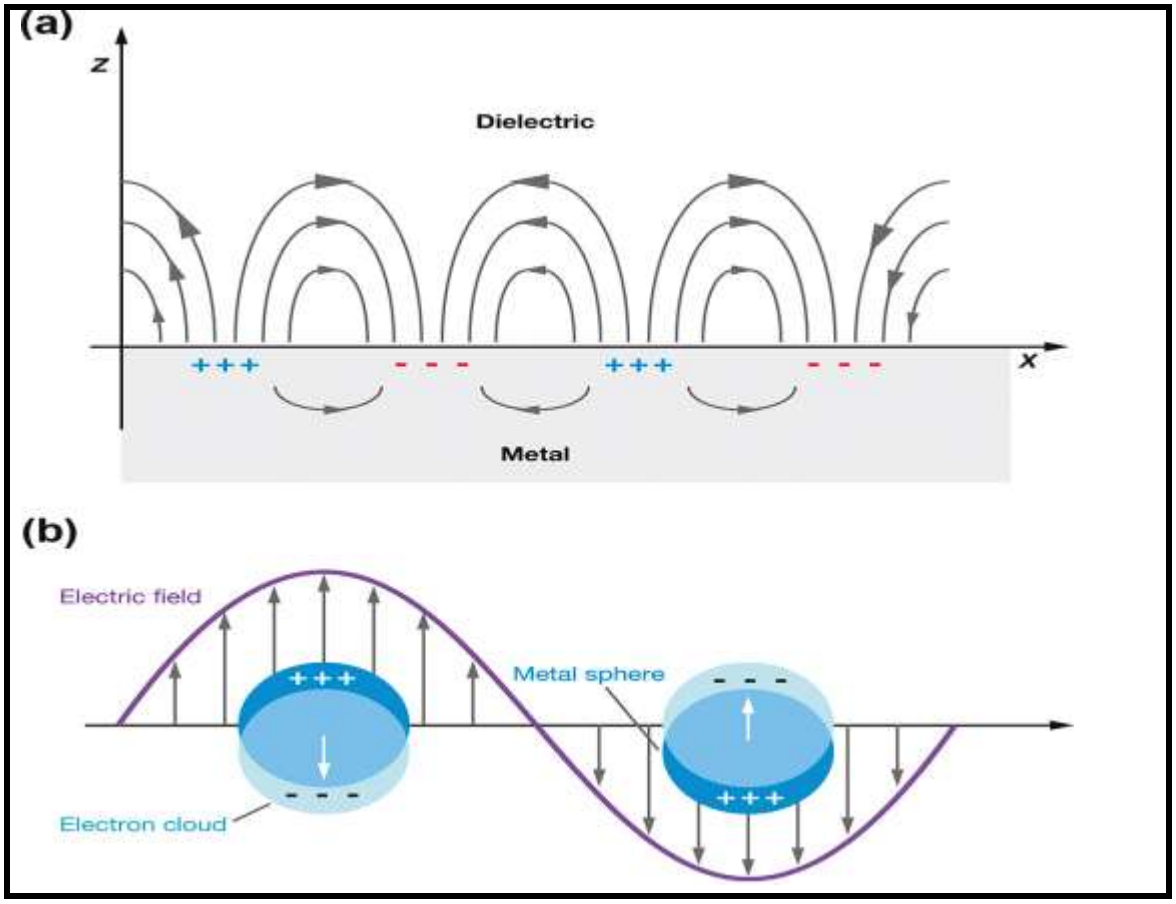

Figure 2. 8: Schematic illustrations of electron charge displacement in (a) Surface plasmon resonance (SPR) and (b) localized surface plasmon resonance (LSPR), (Jones *et al*., 2011).

2.3.4.3 Fundamentals of plasmonics

Spherical metal nanoparticles are the simplest and most fundamental structures to study the basis of plasmon phenomena. The understanding of how light interacts with plasmonic metal nanoparticles is necessary for applications. The interaction of light with matter especially the condition where the material size is less than or equal to incident light wavelength has been an interest for most scientists for a long time. In 1908, Gustav Mie established a versatile and relatively simple analytical solution to equations on the scattering of light on spherical particles. It is based on the assumption that the electromagnetic field interacts with the particle and results in an induced charge separation on the surface of the particle. For a metal nanoparticle to support localized surface plasmon resonance, it should have the following

properties: (i) its dimensions should be less than the incident radiation wavelength, (ii) the imaginary dielectric constant (ε_i) should be positive and small, and (iii) should have a negative real (ε_r) (Willets & Van Duyne., 2007). This can be illustrated by Mie theory for calculating the extinction cross section (C_{ext}) of a metal nanosphere in equation 2.10 (Huang & El-Sayed., 2010).

$$C_{ext} = \frac{24\pi^2 R^3 {\varepsilon_m}^{3/2}}{\lambda}\left[\frac{\varepsilon_i}{(\varepsilon_r + 2\varepsilon_m)^2 + {\varepsilon_i}^2}\right] \ldots\ldots\ldots\ldots\ldots\ldots\ldots 2.10$$

where λ is the wavelength of incident light, R is the radius of the sphere, ε_r is the real part and ε_m is the dielectric constant of the surrounding medium which is related to the refractive index of the medium by $\varepsilon_m = {n_m}^2$. For the particle to be in resonance, the denominator of the expression in brackets should approach zero, allowing C_{ext} to become exceedingly large. Hence, the optical absorption (C_{abs}) and scattering (C_{sca}) by the particle becomes extremely strong. This occurs when ε_r is approximately equal to $-2\varepsilon_m$ so that the denominator of the expression is small and imaginary. Equation 2.10 determines the shape of the absorption band of the particles while the bandwidth and peak height are approximated by ε_i.

The theoretical plasmon frequency of a small spherical nanoparticle is given by the following equation 2.11.

$$\omega = \frac{\omega_p \sqrt{\varepsilon_0}}{\sqrt{3\varepsilon_m}} \ldots\ldots\ldots\ldots\ldots\ldots\ldots\ldots\ldots 2.11$$

where ω_p is the plasmon frequency. Hence the resonant peak of a spherical nanoparticle should vary with the medium that surrounds it.

2.3.4.4 Origin of surface plasmon resonance in noble metal nanoparticles

In a metal, the free electrons (d electrons) are free to travel through the material. When light is in resonance with the surface plasmon oscillation, it causes the free electrons/conduction band electrons in the metal to oscillate. This resonance condition is established when the frequency of the light matches the natural frequency of the valence electrons oscillating against the restoring force. As the wave front of the light passes, the electron density in the particle is polarized to one surface and oscillates in resonance with the frequency of light causing a standing oscillation. This plasmonic oscillation occurs at a specific resonance wavelength that is dependent on the particle's properties and the dielectric constant of the host medium. Change in shape and size of the nanoparticle also changes the surface geometry resulting in a shift in the electric field density on the surface and this causes a change in the oscillation frequency of the electrons (Euistus *et al.*, 2006). The oscillation frequency for gold and silver is usually in the visible region giving rise to the strong surface plasmon resonance absorption. Metal surfaces as a support for plasmonic structures bear the advantage of direct electrical contact (Marcus *et al.*, 2008).

2.3.4.5 Factors affecting optical properties of metal nanoparticles

The electronic, optical and catalytic properties of metal nanoparticles are greatly influenced by factors that affect the electron charge density on the surface of the nanoparticle such as their size, shape, crystal structure, size distribution as well as the environment which surrounds them. The frequency of resonance i.e. the wavelengths at which resonance occurs can be changed by varying the size of the nanoparticles, shape, material and dielectric of the environment surrounding the particle (Kolwas *et al.*, 2009; Mock *et al.*, 2002; Kafeng *et al.*, 2006). All these aspects affect the polarizability or how easily the electrons move through

and away from the crystal lattice. Among the factors that affect the optical properties of the metal nanoparticles, the most important are;

(i) Shape effects

The plasmon resonance is heavily impacted by variation in particle shape. Mock *et al.*, 2002 found that a simple heat treatment of the silver nanoparticles can modify the shape of the nanoparticles resulting in a change in its optical plasmon resonant properties. When spherical metal nanoparticles are transformed into other shapes such as nanorods and triangular prisms, the surface plasmon resonance is affected strongly, typically red-shifting and splitting dipole modes (Hao & Schatz., 2004). The change in the plasmon resonance energies with a change in shape is due to the modification of the coupling strength between the electron cloud and the ionic core of the particle. Highly symmetric spherical particles exhibit a single scattering peak whereas anisotropic shapes such as rods, triangular prisms, and cubes exhibit multiple scattering peaks in the visible wavelengths due to highly localized charge polarizations at the corners and edges (Mie, 1908) as illustrated in Figure 2.9.

The other reasons for the multiple peaks are that, the non-symmetric particles can interact with light differently based on orientation and that there is a difference in the size of allowed surface modes in different directions. For instance, gold nanorods have been shown to have two plasmon resonances, one due to the transverse oscillation of the electrons around 520 nm and the other due to the longitudinal plasmon resonance at longer wavelengths (El-Syaed, 2001). Hao *et al.*, 2004, found that the plasmon resonance peak of gold is red-shifted from 500–530 nm for spheres to 690 nm for the branched Au particles. Mock *et al.*, (2002), prepared triangular silver nanoparticles which became more roundish with heat treatments at 200 °C causing the plasmon spectral peak to shift to lower wavelength.

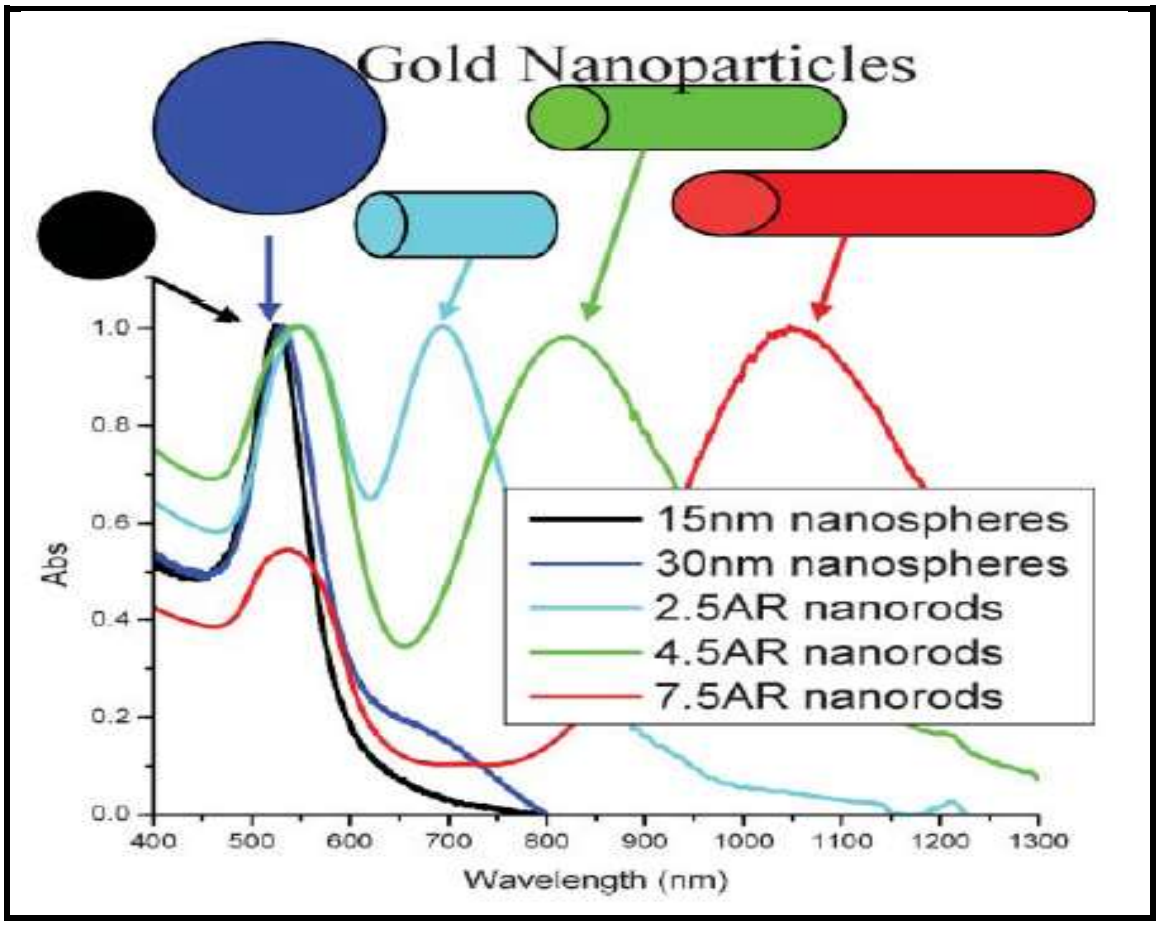

Figure 2.9: Schematic illustrations of effects of change in metal nanoparticle shape on the LSPR spectra (Eustis & El-Sayed., 2006).

(ii) Size Effects

Mie theory plays an important role in describing the optical properties of metal nanoparticles and one of its important uses is in describing the size dependence of LSPR. The theory easily describes the broadening and red shifts of the dipole plasmon resonance with increase in particle size (Hao & Schatz., 2004). When particle size is increased, the ratio of scattered light to absorbed light increases (Lee *et al.*, 2005), and the corresponding spectra are red shifted (Mock *et al.*, 2002). Classical electrodynamics theory predicts a blue shift for the SPR as the size of the nanoparticle decreases. Both red and blue shifts of the SPR frequency have

been reported as the size of the nanoparticles decreases (Kreibig & Vollmer., 1995; Kreibig & Genzel., 1985). For instance, the plasmon resonance of silver can be shifted from the UV range into the visible range by reducing the size of the nanoparticles (Hou *et al.*, 2012). The plasmon resonance of gold can also be shifted from the visible range into the infrared wavelength range by reducing the nanoparticle size. Classically, the resonance wavelength shifts to higher wavelength as the particle size increases because the Coulombic coupling of the regions of the negative and positive surface charge is relaxed as the particles' diameter increases. When the size of the nanoparticles is reduced, there is size confinement of the conduction electrons which influences considerably the electronic and optical properties.

(iii) Distance between metal nanoparticles

The resonant wavelength of two coupled particles in close proximity is red-shifted significantly from that of the individual particles and the shift decays almost exponentially with an increase in particle spacing (Su *et al.*, 2003) due to reduction in the overall resonance energy of the particle pair. Well separated metallic nanoparticles and nanostructures whose dimensions are smaller than the wavelengths of the exciting light are characterized by a broad, intense absorption band in the visible region (Hutter & Fendler, 2004). There will be no interaction of the localized surface plasmon resonances if the gap is not within 2.5 times the size of the particle (Su *et al.*, 2003: Funston *et al.*, 2009).

2.3.5 Properties of plasmon metals used in this study

The chosen noble metals used in this study; copper (Cu), silver (Ag) and gold (Au) all belong to Group 11 of the periodic table and their d-orbitals are completely filled.

2.3.5.1 Gold nanoparticles

At 560 nm gold nanoparticles exhibit an absorption band in the visible region that is responsible for the different colours in gold colloids. Balamurugan & Maruyama (2005) reported that gold nanoparticles strongly absorb both visible light and ultraviolet light due to the interband transition. Zhu *et al*, (2009) reported that the gold photo-catalysts showed a higher catalytic performance in the degradation of dye sulforhodamine-B (SRB) under UV irradiation when compared to degradation under blue light of wavelength between 400 and 500 nm. They also observed that the gold nanoparticles were able to oxidize phenol under UV light which they could not oxidize under visible light. At shorter wavelengths, interband absorption in noble metals may be due to the transition of an electron from the occupied d-level to the conduction band empty states. When gold nanoparticles are supported on TiO_2, the resulting material is purple–brown in colour due to the characteristic surface plasmon band of gold. Haruta, (1997) showed that the catalytic activity of gold comes from the nanometric size and disappears completely when the size of the gold particles are larger than 20 nm. But in photo-catalysis under visible-light irradiation, larger gold nanoparticles with high polydispersity in size and shape are desirable to enhance the photo-catalytic activity of TiO_2.

2.3.5.2 Silver nanoparticles

Silver nanoparticles display intense colours due to the plasmon resonance absorption and are extraordinarily efficient at absorbing and scattering light. A unique property of spherical silver nanoparticles is that the SPR peak wavelength can be tuned from 400 nm (violet light) to 530 nm (green light) by changing the particle size and the local refractive index near the particle surface. Jensen *et al.*, (1999), reported that Ag nanospheres of diameter 20 and 100 nm have surface plasmon peaks at about 370 and 600 nm, respectively. The nanoparticles are

good antibacterial agents. Guzman *et al.*, (2009) investigated the antimicrobial activity of silver on *Staphylococcus aureus S. aureus, Escherichia coli* and *Pseudomonas aeruginosa* and the results showed high inhibition of growth and multiplication of the tested bacteria.

2.3.5.2 Copper nanoparticles

Copper is the most widely used metal in electronics due to its high conductivity and low cost. It is prone to surface oxidation forming mainly Cu_2O and a little bit of CuO. Chan *et al.*, (2007) prepared copper nano-spheres of diameter 390 nm and they exhibited a very broad LSPR and they attributed this broadening of the LSPR peak to the presence of copper oxide shell surrounding the copper metal core to form a core-shell nanoparticle. Yeshchenk, (2013) studied 17-59 nm Cu particles embedded in a silica matrix between 293 and 460 K and they found that the surface plasmon resonance energy and width depended on temperature. An increase in temperature led to a red shift and broadening of the surface plasmon resonance. Copper also allows plasmon excitation in the visible region. When compared to Ag and Au, it is chemically more active and relatively cheap since it is more abundant. A summary of these properties are shown in Table 2.1.

Table 2. 1: Properties of gold, copper and silver

Property	Au	Cu	Ag
Work function (eV)	4.7	4.7	3.7
Fermi energy (eV)	5.5	7.0	5.5
Electrical resistivity (μΩ-cm)	2.44	1.7241	1.62
Temperature coefficient/°C	0.0034	0.00393	0.0038
Thermal conductivity (cal/cm-s-K)	0.7003	0.923	0.974
Coefficient of expansion/°C	14.43×10^{-6}	16.42×10^{-6}	18.6×10^{-6}
Specific heat capacity (cal/g-K)	0.0316	0.0918	0.0558
Melting point (°C)	1063	1083	961
Boiling point (°C)	2530	2325	1955
Hardness on Mohr scale	2.5	3.0	2.7

2.5 Applications of TiO_2

There are several applications of TiO_2 which can be grouped into two areas; environmental remediation and solar fuels applications. The most important applications include;

(i) Self-cleaning of building materials (Banerjee *et al*., 2015; Blossey., 2003)

(ii) Anti-fogging mirror (Hashimoto *et al*., 2005).

(iii) Solar water splitting to produce hydrogen (Fan *et al*., 2013; Li *et al*., 2007).

(iv) Photovoltaics (Zhang *et al*., 2012).

(v) Water purification and degradation of organic compounds (Zhou *et al*., 2012; Shah *et al*., 2015; Ochiai et al., 2010).

(vi) Sensors (oxygen gas sensors), (Zheng *et al*., 2000).

(vii) Pigments in paints and coatings (Berdahl., 1995).

(viii) Air purification (Masahiro *et al*., 1999).

(ix) Photo-reduction of CO_2 to hydrocarbon fuels (Hou *et al*., 2011).

(x) Anti-bacterial and anti-fungal (Yadav *et al*., 2014).

2.5.1 Organic pollutant removal

Research on photo-catalysis using semiconductors has been mainly on the removal of organic contaminants from water as these compounds could be completely mineralised into harmless products. Photo-degradation of different classes of organic pollutants such as polychlorinated bisphenols, organochlorine compounds, organophosphorus compounds, and phenolic compounds has been recently reviewed (Rammohan & Nadagouda, 2013). The attractive feature of photo-catalysis is the ability to degrade a wide variety of organic compounds that are difficult to remove with other water treatment methods. Two different models namely slurry reactors and immobilized TiO_2 photo-catalyst reactors have been used to degrade organic contaminants. Slurry reactors which use suspended powders have relatively high surface area for mass transfer due to the high specific surface area of the suspended powdered TiO_2 photo-catalyst. Organic compounds that have been removed from water using TiO_2 photo-catalyst include herbicides (Konstantinou *et al*., 2001), nitrophenols (Chen & Ray., 1998; Androzzi *et al*., 200), formic acid (Dijkstra *et al*., 2001), phenol and its derivatives (Choquette-Labbe *et al*., 2014) and dyes (Tayade *et al*., 2007). Minabe and coworkers completely decomposed glycerol trioleate and poly (ethylene glycol) (MW 500 000) on the TiO_2 surface under weak UV illumination (1 mW cm^{-2}) with the evolution of CO_2 as the only detectable gas-phase product (Minabe *et al*., 2000).

Due to the problem of separating photo-catalyst from treated water when TiO_2 is used as a powder, researchers have immobilized TiO_2 on different supports despite the reduction in photo-catalytic activity as a result of reduced surface area. Tennakone and coworkers

deposited TiO_2 on polythene films for the degradation of phenol under UV light (Tennakone *et al*., 1995). The disadvantage of using polythene films was the photo-degradation of the support too. Balasubramanian *et al*., (2004) prepared thin films of TiO_2 on flat stainless steel substrates and on glass beads for the photo-degradation of 4-chlorobenzoic acid.

2.5.2 Photo-catalytic disinfection

Antibacterial agents are very important in industries such as water disinfection, textile and food packaging industry. The use of TiO_2 nanoparticles as disinfectants is gaining interest since the use of organic chemicals for disinfection such as chlorination results in the formation of by products such as trihalomethanes (THM) which increase the risk of certain cancers (Dvorak & Skipton, 2008). The small size and high surface to volume ratio of the nanoparticles allows them to closely interact with cell membranes of microbes. The physicochemical properties of the nanoparticles such as shape, size and surface modifications affect their antibacterial properties (Huh & Kwon., 2011).

In Japan TiO_2 based antibacterial applications such as fibers, tiles and sprays have been commercialized. Several floors and hospital walls, especially operating rooms where sterile conditions are crucial, in Japan have been covered with antibacterial tiles (Fujishima & Zhang, 2006). Several studies have shown that the photo-catalytic process using TiO_2 in water is effective to kill a wide range of microorganisms such as bacteria, viruses, algae, fungi and cancer cells (Verdier *et al*., 2014; Jacoby *et al*., 1998; Sunda *et al.*, 1998). Kikuchi *et al.,* 1997 conducted antimicrobial test of TiO_2 coated on glass under weak UV illumination using *E. coli* suspension, containing 3×10^4 cells and they were all killed after one hour. The photo-catalyst produces highly reactive oxygen species and hydroxyl radicals which are responsible for killing microbial pathogens (McCullagh *et al*., 2007). Due to the use of both

light and photo-catalysts, the process is known as solar photo-catalytic disinfection. Verdier *et al*., (2014) studied the antimicrobial activity of TiO_2 using *Escherichia coli* CIP 53126 and they found that the photo-catalyst was active both in the dark and under light. This contradicts the work of Verbruggen *et al*, 2014 who reported that TiO_2 is valid as an antimicrobial agent only under UV light irradiation. Verdier and coworkers (2014) concluded that, the prolonged contact in the dark led to significant antibacterial activities due to bactericidal effect and growth inhibiting effect indicating toxicity of TiO_2. Most TiO_2 antimicrobial tests were done in aqueous solution as slurry.

Due to problems associated with the use of powdered TiO_2 such as separating the photo-catalyst from the treated or disinfected water, some researchers have developed reactors containing an immobilized photo-catalyst such as thin film fixed bed reactor, parabolic trough reactor and double skin sheet reactor (Khan *et al*., 2012). In these reactors there is no need for separation of the photo-catalyst from the disinfected water.

The use composites of TiO_2 and plasmon metal nanoparticles have been found to enhance the antimicrobial activity of TiO_2. Yu and coworkers prepared Ag-TiO_2 nanocomposite deposited on silicon wafers and they found that the composite displayed excellent antibacterial activity and better antibacterial effect than pure TiO_2 against gram-negative bacteria (*Escherichia coli* ATCC 29425), (Yu *et al*., 2011). The deposited plasmon elements can also act as antimicrobial agents when they leach into the solution or when they are in direct contact with the microorganisms, but levels of leaching need to be lower than WHO limits.

2.5.2.1 Silver as an antimicrobial agent

For a long time silver has been known to have a disinfecting effect and has been used in different applications ranging from traditional medicines to culinary items, (Savithramma *et al*., 2011). At low concentrations, it has been reported that silver nanoparticles are non-toxic to humans but very effective against bacteria, virus and other eukaryotic microorganisms (Jeong *et al.*, 2005). The antimicrobial activity of silver containing materials allow them to be used in various household products such as elimination of microorganisms on textile fabrics (Yuranova *et al*., 2003., Jeong *et al*, 2005), medical devices (Samuel & Guggenbichler, 2004), antibacterial spray and household water filters (Marambio-Jones & Hoek 2010). Silver nanoparticles have been shown to be effective against bacteria such as *staphylococcus aurus* (Shameli *et al*., 2012; Shahverdi *et al*., 2007), *Escherichia coli* (Kim *et al*., 2007; Pal *et al*., 2007) and *Bacillus subtilis* (Zhang *et al*, 2008). When silver is combined with TiO_2 to form a composite of nanoparticles it can be used in baby bottles and blood clotting agents to produce antimicrobial activity (Yeo & Kang 2008).

2.5.2.2 Gold as an antimicrobial agent

Gold has antimicrobial properties and its use in a reasonable amount does not affect human beings (Fricker, 1996). Some studies done by Lima *et al.*, (2013) on the antimicrobial activity of gold on *Escherichia coli* and *Salmonella typhi* which are both found in water and resistant to silver based antimicrobials showed that gold is capable of eliminating the bacteria. When compared to silver which have nonspecific biological toxicity, Au-NP have the advantage of being easily surface modified, photostable and relatively nontoxic (Panyala *et al*., 2008). This means that Au-NPs are the best candidate where undesirable properties such as cellular toxicity and instability are not needed.

2.5.2.3 Copper as an antimicrobial agent

Copper nanoparticles are potential antimicrobial agents, but they have been found to be toxic to eukaryotic cells for instance it has potential to damage dorsal root ganglion neuron (Prabhu *et al*., 2010). It is one of the multifunctional inorganic nanoparticles that have good antimicrobial properties, although excess copper in the human body can lead to the generation of radicals such as $OH^{\bullet}$ which are damaging (Montes *et al*., 2014). The major challenge on the use of Cu-NP as antimicrobial agents is the rapid oxidation to Cu_2O in air or aqueous media.

2.5.2.4 Mechanism of antibacterial activity

The mechanism of how TiO_2 or plasmon metal nanoparticles kill or inhibit bacterial cell growth and reproduction bacteria is not fully understood. It is complicated and debatable and researchers have come up with various theories. The nanoparticles are believed to disturb the bacteria cell growth and survival by attaching to the cells by electrostatic interaction (Thill *et al*., 2006; Prabhu & Poulose, 2012).

When exposed to light of appropriate wavelength, the TiO_2 generates reactive oxygen species such as $O_2^{\bullet-}$, H_2O_2 and $HO^{\bullet}$ which cause several oxidative damages on the microorganism such as mitochondria damage, protein denaturation, cell membrane and enzyme disruption, DNA damage and interrupted transmembrane electron transport. In some studies using *Escherichia coli,* the hydroxyl radicals were the major cause of the antibacterial effect (Sunada *et al*., 2003) and direct oxidation by h^+ from the valence band of TO_2 was reported by Nadtochenko *et al.,* 2008. When the cytoplasmic membrane is attacked and damaged, it loses its integrity involved in cellular respiration resulting in cell death (Verdier *et al*, 2014).

The mechanism of plasmon metal nanoparticles differs slightly from that of pure TiO_2 in that they are capable of producing ions easily in solution unlike TiO_2. Kim *et al.*, (2011) suggested that silver nanoparticles (Ag-NP) form free radicals when in contact with bacteria which damage the cell membrane leading to cell death. Feng *et al.*, (2008) proposed that the Ag-NP release ions that inactivate important enzymes by interacting with their thiol groups. The uptake of the ions by the cells inhibits cell functions and damages it. They also suggested that there is production of reactive oxygen species to attack the cells which they suspect are produced through the inhibition of respiratory enzymes by ions.

2.6 Photo-catalyst Supports

The use of supports originates from the need to use photo-catalysts in a continuous process where the use of powdered TiO_2 is technologically impractical. Also when applied in a slurry system, the small particles bring issues involving mass transport and excessive pressure drops. The fine particles have a tendency to agglomerate due to high surface area and surface energy resulting in a decrease in the reusable lifespan of the particulate photo-catalyst. Other difficulties include separation and reuse of powdered form TiO_2 which hinders its industrial application, and poses a risk to ecosystems and human health as a result of the release of nanoparticles into the environment. The post-separation of the photo-catalyst is a major problem when it comes to the practicability on an industrial scale; hence the fabrication of nanoparticles onto a solid support seems to be an effective approach to overcoming this problem.

Various materials have been investigated and found to be potential supports for TiO_2 for the photo-degradation of pollutants in water. The support can be opaque (metals, activated

carbon) or transparent (quartz, glass, fused silica) (Shan *et al.*, 2010). An ideal photo-catalyst support should have the following properties (Ding *et al*., 2006).

- No loss of the catalyst reactivity by the attachment process.
- Have a strong adsorption affinity towards the pollutants.
- Strong adherence between catalyst and support.
- Offer a high specific surface area.
- Transparent to UV/visible light illumination.
- Ease to separate from water for recycling purposes.
- Chemically inert.

The TiO_2 supports that have been used so far include silica (Zainudin *et al*., 2008), zeolites (Najafabadi & Taghipour., 2014; Zhu *et al*., 2000), glass plates and glass micro-fibres (Sarantopoulos *et al*., 2009), glass beads (Hanel *et al*., 2010), stainless steel (Fernhndez *et al*., 1995; Balasubramanian *et al*., 2004), clay (Hadjltaiefa *et al*., 2016), diatomite (Sun *et al*., 2015), polymeric membranes (Mukherjee *et al*., 2014; Singh *et al*., 2015). Hanaor & Sorrell, (2014), studied the effect of using quartz sand, rutile sand and zircon sand as TiO_2 support for water decontamination and the highest photo-catalytic activity was achieved by TiO_2 immobilized on quartz due to its higher light transmittance.

Since several supports are available for use, substrate selection is important since its surface chemistry and chemical composition plays an important role in determining the quality of the final product. The selectivity towards supporting nanoparticles is provided by the surface chemistry of the support. The chemical interaction between nanoparticles and support plays a critical role in the formation of monolayers hence the surfaces need to be modified to provide

chemisorption of the target atoms or particles. Nanoparticles that are physically bound to the surface with no chemical bonds are able to move on the surface because of lack of proper bonding resulting in aggregation which is not reversible.

The use of polymers as supports for TiO_2 has disadvantages and these include (i) loss of the support due to photo-degradation by the photo-catalyst and in such cases poly (dimethylsiloxane) can be used to protect the polymer support but this results in a decrease in the photo-catalytic activity of TiO_2, (ii) some polymer supports cannot withstand the high temperatures when thermal treatment is required for the photo-catalyst. The use of less durable fibers results in the wearing off of the photo-catalyst resulting in loss of photo-catalytic activity with time. The use of membranes has also been recently targeted due to the fact that the photo-catalytic reaction can take place on the surface of the membrane with water continuously discharged without loss of photo-catalyst particles. However in most studies, the polymer membranes may encounter deterioration, low photo-catalytic activity and loss of the deposited photo-catalyst (Chong *et al*., 2010).

Natural clays such as montmorillonite, zeolites and bentonite have been used as TiO_2 supports due to their high adsorption capacity and cost effectiveness. Their superior adsorption capacity is desirable for increasing the surface contact during photo-catalysis. There are a few drawbacks on the use of clay such as (i) swelling which is undesirable in reactors where hydrodynamics may be affected and (ii) the presence of surface bound impurities which affect the efficiency of the TiO_2 photo-catalyst (Chong *et al*., 2009). Zeolites are good supports for TiO_2 due to their high surface area, good thermal stability and high adsorption towards organic compounds but there is a problem of low light penetration, scattering and diffraction of UV light in the solution which results in the reduction of the

efficiency of the photo-degradation process (Corma & Garcia, 2004), as zeolites are also particulates.

Having considered all the discussed facts, quartz seems to be a good support due to its advantages which include transparency to light which is desirable in a technical application such as the dielectric barrier discharge (DBD) where the TiO_2 thin films should be placed in such a way that there is optimal irradiation of the immobilized catalyst. Even after deposition of thin films of photo-catalyst, quartz allows penetration of light which results in improved photo-catalysis. Several researchers used glass as a support for TiO_2. Fernandez *et al*., (1995) did a comparative study on the effect of supports (quartz, steel and glass) on the photo-catalytic activity of TiO_2 and they found that the TiO_2 immobilized on quartz had the highest photo-catalytic activity. In this study quartz was chosen as a support for the photo-catalyst because of its durability for instance in alkaline solution, easy to separate, transparent to light, relatively inert chemically, and can be designed in way that optimal irradiation of the immobilized photo-catalyst is achieved and operated continuously. The deposition of TiO_2 is widely done using the impregnation method which is straight forward but the resulting films are not homogenous and can be easily detached from the substrates whereas methods such as chemical vapor deposition and sol-gel give relatively homogenous coatings (Paez & Matousek., 2004) hence in this study the sol-gel and deposition methods were employed.

2.6.1 Quartz support

Quartz has a high resistance to water, salt solutions and acids and can only be attacked by hydrofluoric acid and phosphoric acid. One of the most attractive properties of quartz is the very low thermal coefficient of expansion which is about 5.0×10^{-7}/ °C. It is a good electrical insulator because of the large band gap in the electronic structure of the silicon-

oxygen bond. It is a dielectric material with a dielectric constant of about 4 which is lower than that of other glasses. The low dielectric constant is a result of the lack of highly charged mobile ions and the stiffness of the silicon-oxygen network which imparts a very low polarizability to the structure. An important property of a dielectric is its capability of supporting an electrostatic field with minimal dissipation of energy in the form of heat (Calla *et al*., 2008).

In addition to the above advantages, the study aims also to produce supported photo-catalyst with potential applications in the DBD system. Quartz is the commonly used dielectric in DBD systems because of its properties discussed above. It allows light to pass through hence it makes it possible to utilize the UV light produced in the DBD system so that it is not wasted. The increase in the utilization of electrical plasma technology for the removal organics has motivated the research in finding ways to utilize the UV light that is produced in the system. The electrical plasma technology leads to the formation of oxidizing species and excited species. The excited species are generated from the collision of electrons with neutral molecules and these excited species emit UV light due to relaxation to lower energy states.

For a photo-catalyst to be active it has to be illuminated and in suspended systems it is a challenge to illuminate all the photo-catalyst nanoparticles because some nanoparticles are shielded from light by other nanoparticles those closer to the source of light. But when the nanoparticles are immobilized, it is possible to get a configuration whereby all photo-catalyst nanoparticles are irradiated for instance a thin layer on a tube around a tube light (Dijkstra *et al*., 2001). Hence in this study, quartz immobilized TiO_2 photo-catalyst was used instead of the powdered photo-catalyst.

2.6.2 Adhesion Promoters

Quartz has a surface which is difficult for nanoparticles to stick with good adhesion hence the use of adhesion promoters is of paramount importance if the nanoparticles are to adhere well for use in water treatment. 3-Mercaptopropyl trimethoxysilane (MPTMS) an organofunctional alkoxysilane with bifunctional moieties that have specific affinity for gold or silver (Park *et al.,* 1999) is a good example of an adhesion promoter. One end of MPTMS consists of the SH group (mercapto) and the other end an alkoxy silane. The affinity of Au to the SH group of MPTMS allows the fabrication of films or nanostructures. Besides the thiol group, gold has also a strong affinity for amines (Bharathi *et al*., 1999) hence surface functionalization can be done using either thiol or amine groups. From previous studies, it was proven that uniform and well-defined films of gold or silver can be formed on surface modified quartz (Park *et al*., 1999). To control the final topological film properties, interparticle distance and surface coverage, the rate of formation of the films is very important.

The mechanism of adhesion of the silane depends upon the silanol reactivity for the adhesion to mineral surfaces (Plueddemann., 1983). The silane moieties covalently bind to the oxide surface of glass through siloxane bonds, while the thiol groups engage in strong binding to the gold or silver coating (Goss *et al.,* 1991). The alkoxy functionality (methoxy end groups) is converted to active groups (silanols) on hydrolysis.

The structure and morphology of the layers of MPTMS formed on the substrate depend on the MPTMS concentration. The behaviour of MPTMS on gold and their organizational structure were found to be influenced by the following forces: (i) interactions between the alkyl chains having dispersion character, (ii) interactions between the end groups of thiols

and (iii) interactions between the thiol head groups and gold lattice, meaning that the final topography is a result of the balance between these three forces (Poirier., 1997).

2.7 Characterization Techniques

This section of the thesis gives a brief description of the characterization techniques that were employed in this study.

2.7.1 Atomic Force Microscopy

The atomic force microscope (AFM) also known as scanning force microscopy (SFM) belongs to the branch of scanning probe microscopy (SPM) designed to measure the local properties such as the thickness of a film sample. It scans the surface and gives topographical images. SFM can probe and image samples in both aqueous and dry environments (Moreno-Herrero *et al*, 2004). It relies on the interaction between a sharp tip and the surface of the sample. The AFM instrument has a very fine tip mounted at the end of a small deflecting spring called a cantilever which is brought into contact with the sample and then moved across the sample surface in numerous line scans. The vertical deflection of the tip caused by short range repulsive interaction forces with the sample are measured by the detector with high accuracy and recorded during scanning. The normal tip to surface distance in the probe microscope is about 0.1 – 10 nm. A signal is then sent to a computer which then generates the sample surface map.

AFM can be operated in different modes to analyze the surface properties of the specimen and the most commonly used modes in AFM are contact, non-contact, and tapping modes. Its advantage over TEM and SEM is that it measures three dimensional images allowing the height and volume to be calculated.

2.7.2 Transmission electron microscopy

This technique is used to identify and characterize the microstructure of materials with high resolution owing to the small de Broglie wavelength of electrons. The technique gives size, shape and arrangement of the particle's agglomeration. It uses high energy electron beams that are transmitted through a thin sample to get an image of the materials with atomic scale resolution. Electromagnetic lenses focus the electrons and the image is recorded on a camera. For good analysis the TEM sample to be analyzed should have a thickness of about 100 nm or less at a particular area of interest (Mukhopadhyay., 2003).

2.7.3 Scanning electron microscopy

This analytical tool gives detailed morphological images, porosity, surface topography, material homogeneity and a quick identification of elements present. A high resolution SEM gives sample details down to 25 Angstroms and when coupled with energy dispersive spectroscopy (EDS), it gives the composition of the specimen. This instrument operates at a high vacuum. Basically a beam of electrons is generated by a source usually a tungsten filament or a field emission gun which is then accelerated through a high voltage resulting in the production of a thin beam of electrons which scans the sample surface. The interaction of the electrons with atoms in the sample produces various signals that are detected. The most common detection mode is by the secondary electrons that are emitted by excited electrons.

The samples to be analyzed are mounted on a specimen stub rigidly. It is important that the samples to be analyzed should be electrically conductive to prevent charging and should be electrically grounded to avoid charge accumulation at the surface.

2.7.4 Inductively Coupled Plasma/Optical Emission Spectrometry

Inductively Coupled Plasma (ICP) is one of the most powerful and common techniques for the determination of trace elements in samples. All kinds of gas or dissolved samples can be analysed, varying from concentrated salt solutions to diluted samples. Solid samples cannot be analysed in their solid state but require extraction or acid digestion so that the analytes are present in solution. In some cases a laser can used to directly convert the solid samples into an aerosol. The primary goal of ICP is to make the elements in solution emit light of characteristic wavelength which can be measured. When compared to other elemental analytical techniques, ICP offers the following advantages; (i) excellent stability and reproducibility, (ii) the ability to provide simultaneous determinations of up to 70 elements, (iii) little chemical interference between elements, (iv) high sensitivity (on the ppm and ppb level), (v) excellent detection limits for most elements (0.1 –100 ng mL^{-1}), (vi) low background emission and low susceptibility to matrix interferences, (vii) high stability leading to excellent accuracy and precision and (viii) cost-effective analyses.

The sample solution to be analyzed is converted into an aerosol using a nebulizer and then introduced into the central channel of ICP plasma by argon flow of about 0.5–1.5 L/min. The aerosol is quickly desolvated (removal of solvent), vaporized into gaseous state molecules and then atomized due to the high temperatures of roughly 10 000 K at the core of the ICP. Finally the atoms will be excited and ionized into their constituent atoms or ions followed by the emission of radiation of characteristic wavelength depending on the elements present. A portion of photons from ICP is collected and converted to an electrical signal by a photo-detector which is then amplified and processed by the computer. The wavelength of the photons is used to identify the elements. The total number of the photons is directly proportional to the concentration of the element in the original solution. In this study ICP was

used to determine the extent of leaching of plasmon elements during the photo-degradation process.

2.7.5 Carbon hydrogen nitrogen sulphur elemental analysis

The carbon hydrogen nitrogen sulphur (CHNS) elemental analyzer is an instrument that is used for determination of carbon, hydrogen, nitrogen and sulphur in organic, inorganic and polymeric materials. It is extensively used to analyze a wide variety of sample types including pharmaceuticals, chemicals, oil-related products, catalyst, food, polymers, chemicals and environmental. The sample to be analyzed is weighed in milligrams in a tin capsule which is dropped into a quartz tube at 1020 °C and combusted in a highly oxidizing, pure oxygen environment which guarantees almost complete combustion even of thermally resistant substances and conversion of oxides of nitrogen to elemental nitrogen gas. Some catalysts are normally added to the combustion section to aid complete combustion and absorbents to remove contaminants. Accurate weighing of samples is highly recommended for organic elemental analysis since results are presented on a weight percentage basis.

The resulting gaseous components of the combustion mixture are swept out of the combustion chamber by inert helium carrier gas and then passed over heated high purity copper to remove any oxygen not consumed in the initial combustion and convert any oxides of nitrogen into nitrogen gas. Finally the gases are passed over absorbents to leave only carbon dioxide, water, nitrogen and sulphur dioxide which are then detected by a thermal conductivity detector. It is only oxygen which is analyzed separately, in that case, the sample undergoes immediate pyrolysis in a helium stream which ensures that all the organic oxygen is converted into carbon monoxide and separated on a GC column packed with molecular sieves.

2.7.6 UV-Vis Spectroscopy

The UV-Vis instrument consists of three components: the source, the dispersive system and the detector. The photomultiplier tube consisting of photo-emissive cathode, dynodes an anode is the commonly used detector in the UV-Vis spectrophotometer. There are two types of light sources that are commonly used and these are: incandescent lamp which gives the visible portion of light, and the medium pressure deuterium lamp which gives UV light portion. The instrument operates by passing a beam of light through a sample and the detector measures the intensity of the light that reaches it. Radiation of different wavelengths is absorbed by different molecules resulting in an absorption spectrum which shows absorption bands corresponding to structural groups in the molecule.

When this technique is used in the analysis of organic compounds, absorption of both UV and visible light is restricted to certain functional groups called chromophores. There is a direct proportionality between the absorption and concentration for a given set of instrumental conditions (Pavia *et al*., 2001). In this work the technique was employed in the determination of changes in the concentration of the model pollutants in photo-degradation experiments.

2.7.7 BET-Surface area analysis

This technique was developed in 1938 by S. Brunauer, P. H. Emmet and E. Teller hence it was named after them (BET), (Santamarina *et al*., 2002). It is the most common technique employed for the determination of the surface area of powders and porous materials. This technique is the first to be developed to measure the specific surface area of finely divided and porous solids. It is applied in the analysis of medical implants, filters, cements, projectile propellants, catalysts and pharmaceuticals.

The specific surface area which encompasses external area and pore area of the material is determined by physical adsorption of a gas usually nitrogen on the surface of the solid and by calculating the amount of adsorbate gas corresponding to a monomolecular layer on the surface. To do the calculations, the knowledge of the cross-sectional area of the gas molecule being used as a probe is required and in case of nitrogen, the cross-sectional area is taken as 16.2 $Å^2$/molecule. The analysis is usually done at the temperature of liquid nitrogen (77 K) and relative pressure (P/P_0) of 0.3 where P_0 is the saturation pressure (Lowell *et al*., 2004). Prior to the analysis, the sample to be analyzed is pre-treated at elevated temperature under a vacuum or flowing gas in order to remove any contaminants. The amount of gas molecules adsorbed or desorbed is generally determined by the pressure variations.

2.7.8 X-Ray Diffraction

X-ray diffraction (XRD) is a powerful technique and when used for characterization of crystalline materials, it gives some information on the average grain size, phases, structures, crystallinity and crystal defects. Other applications include identification of mineral phases, polymer crystallinity, residual stress and texture analysis. The major advantages of this technique are; (i) there is minimal or no sample preparation required, (i) it is nondestructive and (iii) ambient conditions are used for analysis (Nel *et al*., 2006).

XRD is based on the interaction of monochromatic beams of X-rays with a crystal lattice. When X-rays interact with a crystalline substance, they produce a diffraction pattern which is more like a fingerprint of the substance. The diffraction peaks are produced when there is constructive interference of these monochromatic X-rays that are scattered at specific angles from lattice planes in the sample. This happens when a sample has lattice planes with d-spacings that are appropriate to diffract X-rays at that theta value. Munekwa, (1998) reported

that the number of crystal lattices that contribute to X-ray diffraction for thin samples of less than 1000 nm become less due to a decrease in the X-ray diffraction intensity and a rise in background. To overcome this problem, the diffractometer is designed such that the incident X-rays are fixed at small 2θ values of 3 to 5 to lengthen the optical path the X-ray beam passes through the film. An ideal sample for analysis is one that is homogeneous and the crystallites are randomly distributed

2.7.9 Particle-induced X-ray emission spectroscopy

Particle-induced X-ray emission spectroscopy is a powerful technique for elemental analysis which relies on the spectrometry of characteristic X-rays emitted by target elements when irradiated with a beam of high energy ions. It has several advantages such as high sensitivity, non-destructive, rapid multi-element analysis in a solid or liquid form, no sample preparation required thereby reducing errors and the measurements are done at atmospheric pressure. For accurate analysis an ideal specimen should be used which should be flat and uniform in composition to within the micron level (IAEA, 2000).

There are two stages in the PIXE analysis and the first one is when the elements in the sample are identified from the characteristic X-ray peaks and the second one is when the quantity of a particular element is determined from the intensity of the X-ray emission spectrum. When the sample is exposed to a beam of ions, there are some atomic interactions that take place that give off X-ray radiation specific to an element. The high energy protons strike the target atoms resulting in the ejection of electrons from the innermost shell. A vacancy shell is created in the innermost shell which is then filled by an electron from an outer shell resulting in the emission of characteristic X-rays equal in energy to the energy difference between the

two shells. The X-ray spectrum is recorded by a semiconductor X-ray detector and the intensities are then converted to elemental concentrations.

2.7.10 Diffuse reflectance Spectroscopy

Diffuse reflectance spectroscopy is a very good analytical tool for powdered or crystalline materials in the mid-IR and near infrared spectral ranges. Depending on the type of instrument used, the samples to be analyzed are generally ground and uniformly mixed well with transparent salts such as barium sulphate whereas in some instruments the powders or thin films are analyzed as neat samples. One of the greatest advantages of this characterization technique is that it is ideally amenable to automation. An integrating sphere can be attached to the conventional UV-Vis instrument so as to analyze the solid samples. The analysis relies on the focused projection of a beam of light into the sample where it is reflected in all directions, scattered and transmitted through the sample. The diffusely scattered and back reflected light is then collected and directed to the detector. The schematic representation of the instrument is shown in Figure 2.10.

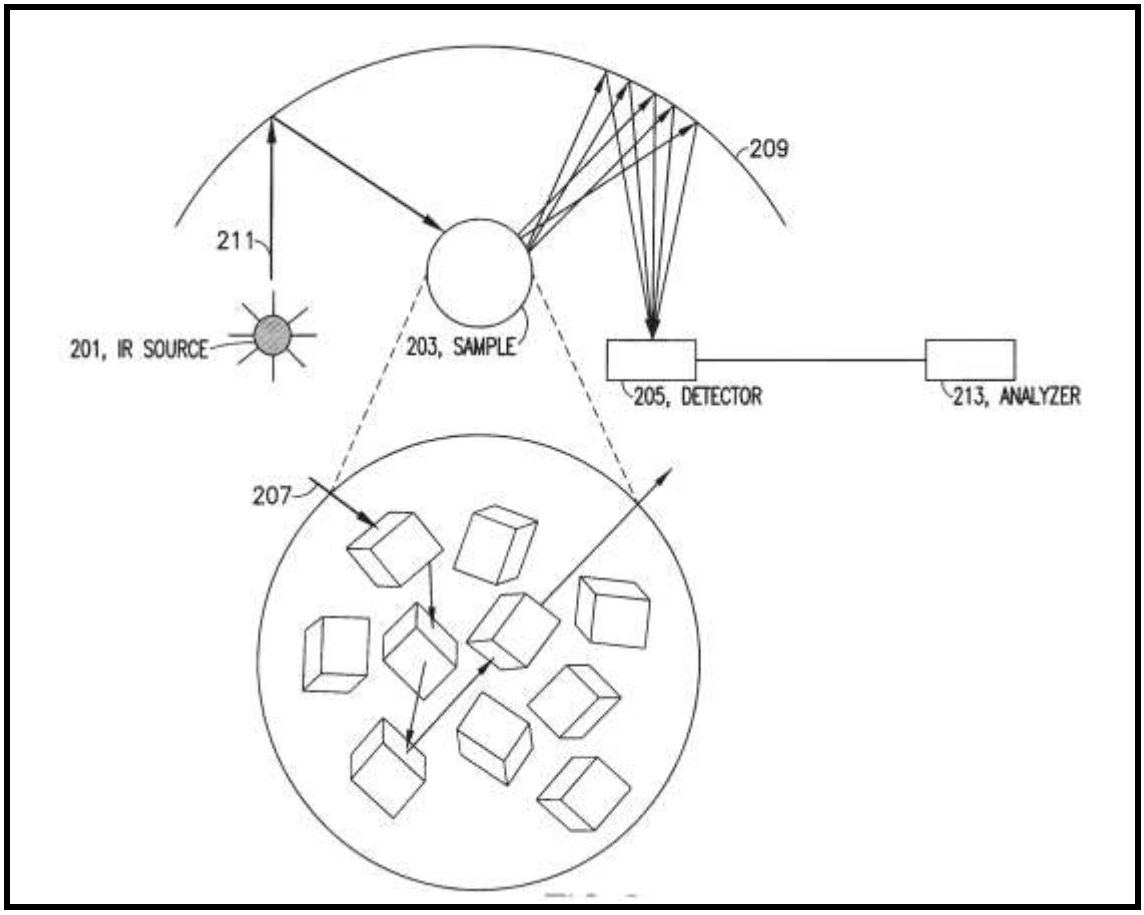

Figure 2.10: Schematic representation of a diffuse reflectance spectrometer (Herron *et al.*, 2013).

In the case of infinitely thick samples, thickness and the sample holder do not have influence on the reflectance hence the Kubelka-Munk conversion can be applied to the diffuse reflectance percentages using Equation 2.12 (Escobedo Morales *et al*., 2007).

$$\mathrm{F(R)} = \frac{(1-R)^2}{2R} = \frac{k}{s} \ldots\ldots\ldots\ldots\ldots\ldots\ldots\ldots\ldots\ldots 2.12$$

where: R is the absolute reflectance of the sampled layer

F(R) is the Kubelka-Munk.

k is the molar absorption coefficient.

s is the scattering

Tauc, Davis and Mott proposed an expression for the relationship between band gap (Eg) and the absorption coefficient and this relationship is shown in Equation 2.13, (Ghoneim *et al*., 2012)

$$(h\nu\alpha)^{1/n} = A(\text{hv - Eg})\text{……..2.13}$$

where α is the absorption coefficient

h is the Plank's constant

Eg is the band gap

A is the proportional constant

v is the frequency of vibration

n is the contant which denotes the nature of the sample preparation.

The value of n=1/2 is for direct allowed transition, 3/2 for direct forbidden transition, 2 for indirect allowed transition and 3 for indirect forbidden transition.

2.7.11 Fourier transform infrared spectroscopy

Fourier transform infrared spectroscopy (FTIR) is a non-destructive technique used to determine the structure, identify functional groups present in a given organic compound sample and also to analyze certain inorganic substances. To analyze a sample, a beam of infrared light is passed through the sample and the radiation absorption is measured as a function of frequency. The detectors for this instrument are designed to measure interferogram signals (Pavia *et al*., 2001). The resulting spectra give wavelengths at which the sample absorbs infrared red light allowing identification of functional groups and molecular structures. The fact that no two molecular structures give the same infrared

spectrum means that FTIR is a useful technique in identifying unknown materials, quality control and in quantitative determination of components in a sample mixture. Pure samples with few active infrared bonds normally give clear spectra whereas complex structures give complex spectra due to a lot of absorption bands. In this study this analytical technique was employed in the determination of the structural changes of methyl orange and bromocresol purple that occur during the photo-degradation.

2.7.12 Thermo-gravimetric Analysis

Thermo-gravimetric analysis (TGA) is one of the thermal analytical techniques which measures changes in weight of a material as a function of temperature or isothermally as a function of time under a controlled environment. The materials that can be analyzed using TGA include inorganic materials, glasses, metals, polymers and plastics, ceramics and composite materials. The advantages of this technique include the use of very small amounts of sample in the range 1 mg - 150 mg and it can reveal important information concerning the pathway followed by a reaction. The analysis relies upon a high degree of precision in three measurements and these are; weight, temperature and temperature change.

The applications of TGA include: (i) determination of thermal stability of a material, (ii) water and carbon content determination, (iii) measure evaporation rates (e. g. emissions of liquid mixtures), (iv) determination of Curie temperatures of magnetic transitions, (v) determination of the fraction of volatile components in a material and (vi) to determine the purity of a mineral, inorganic compound or organic material.

Samples to be analysed are placed in a specimen pan hanging from the balance. The changes in weight in the TGA analysis are monitored by a sensitive analytical balance and are due to

the breaking and formation of chemical bonds at elevated temperatures. There are photodiodes which serve as position sensors for the determination of any movement of the specimen pan such that any change in weight is sensed by the photodiodes. The chemistry of the gaseous products released can be known when the TGA is coupled with another characterization technique such as FTIR.

2.7.13 Liquid chromatography-Mass Spectrometry

Liquid chromatography-Mass Spectrometry (LC-MS) is used to identify, quantify and do mass analysis of a wide range of a complex mixture of organic compounds. It combines the separation abilities of liquid chromatography with mass analysis and detection power of mass spectrometry. It is a very powerful technique with high selectivity and sensitivity. The sample to be analyzed is injected into a liquid chromatography (LC) column where it is separated into various components which are then passed to the mass spectrometer (MS). The MS then ionizes the vaporized sample molecules resulting in the production of charged species which are then separated and identified based on their mass to charge ratio (m/z).

The ion sources include electrospray ionization source, atmospheric pressure photo-ionization and atmospheric pressure chemical ionization source. The mass analyzers which sort ions according to their mass to charge ratio by applying electromagnetic fields include quadruple analyzers, time-of-flight analyzers, ion trap analyzers and hybrid analyzers. The elemental composition, masses and structures are then determined by observing the fragmentation pattern.

As far as qualitative analysis is concerned, chromatography has the limitation of not being able to give an unequivocal identification of components of the mixture even if they are

separated completely. Its coupling with MS allows the identification of compounds with a high degree of confidence since the separated compounds introduced into the MS spectrometer with similar or identical retention characteristics have different mass spectra (Ardrey, 2003). In this study LC-MS was used to determine the photo-degradation products at certain stages of the photo-catalytic process.

2.7.14 Raman spectroscopy

Raman spectroscopy is a light scattering characterization technique that can be used to obtain information about the structure and properties of materials from their vibrational transitions. It has several advantages that include minimal or no sample preparation, nondestructive, very fast (1 min a scan), no preferred orientation, sensitive to nanoscale phases and has better sensitivity than XRD (Dorian & Sorrell, 2011). It is based on the inelastic scattering of monochromatic light after interaction with vibrating sample molecules. There are two types of Raman scattering, Stokes and anti-Stokes. Molecules that were initially in the ground vibrational state give rise to Stokes Raman scattering whereas those initially in the vibrational excited states give rise to anti-Stoke Raman scattering.

A Raman system consists of (i) laser source, (ii) sample illumination system and light collection optics, (iii) wavelength filter and (iv) detector. Laser sources for excitation are available in the visible, ultraviolet and near infrared spectral region. When Raman uses UV light, it means the technique will be more sensitive to the surface phase of the solid sample that absorbs UV light (Li *et al*., 2001). This allows investigation of phase transformation in the surface region of TiO_2 as it strongly absorbs UV light. If visible light is used for excitation, the Raman scattered light will also be in the visible region.

To get a Raman spectrum, the sample to be analyzed is irradiated with a laser beam and the scattered light is collected, sent through an interference filter and then to the detector. The Raman peaks in the spectrum can be associated with vibrational modes at molecular level. The intensities of the bands in the Raman spectrum depend on the nature of the vibration being studied, instrumentation and sampling factors. Intense Raman scattering normally occurs from vibrations that cause a change in the polarizability of the electron cloud around the molecule and usually symmetric vibrations bring about the biggest changes and scattering.

CHAPTER 3

Experimental: Materials and general procedures

3.0 Introduction

This chapter gives the experimental procedures, sample preparation and the operating conditions of the instruments employed for characterizing samples. The details of the reagents and materials used to achieve the aims of this study are also given.

3.1 Materials

All chemicals used in this study were analytical grade and were used as received without further purification. For all the preparations of solutions, deionized water was used. Polyvinylpyrrolidone (PVP) was purchased from Sigma Aldrich, silver nitrate ($AgNO_3$, 99.8%) from SAARCHEM SA, trisodium citrate ($Na_3C_6H_5O_7$, 99%) supplied by ACE , sodium borohydride ($NaBH_4$, 96%) purchased from Sigma Aldrich, methyl orange purchased from Merck, hydrogen peroxide purchased from SAARCHEM SA, sulphuric acid purchased from MET-U-ED, 3-mercaptopropyltrimethoxysilane (MPTMS) purchased from Alfa Aesar, hydrofluoric acid, bromocresol purple purchased from Associated Chemical Enterprises (Pty)(Ltd), bisphenol A purchased from glucose purchased from MET-U-ED, 2-propanol, trisodium citrate ($Na_3C_6H_5O_7$, 99%) purchased from ACE and hydrogen peroxide from Merck purchased from Sigma Alddrich. Tetrachloro auric acid ($HAuCl_4$) purchased from Labstuff, cetyltrimethylammonium bromide (CTAB, 98.5%) purchased from LABCHEM, ascorbic acid ($C_6H_8O_6$, 99.7%), sodium hydroxide (98%) and potassium hydroxide purchased from Merck.

3.2 Metal nanoparticle thin film deposition on quartz

The quartz support for the metal nanoparticle films was surface treated before deposition so as to enhance the adhesion of the nanoparticles.

3.2.1 Quartz surface preparation

The quartz glass slides were cleaned thoroughly with a detergent and rinsed with distilled water followed by washing with an acetone/ethanol mixture. The sizes of the quartz were 3.5 cm by 2.5 cm. The glass slides were then etched with a 10 % hydrofluoric acid solution followed by cleaning and sonication for 10 minutes. After rinsing with distilled water, the quartz slides were immersed in a piranha solution which was made up of H_2O_2 and H_2SO_4 in a 1:3 ratio v/v for 30 minutes. This was followed by immersion in a solution of 3-mercaptopropyltrimethoxysilane (MPTMS) which had been made up by mixing 20 mL of MPTMS, 20 mL of water and 60 mL of 2-propanol for 24 hours. The quartz were then rinsed by dipping in 2-propanol briefly to remove excess materials, blown by a jet of nitrogen gas and cured at 105 °C for 7 minutes.

3.2.2 Preparation of Cu, Au and Ag film

3.2.2.1 Thermal Evaporation

For the deposition of gold thin film on quartz, the gold source material was loaded onto a tungsten sample holder and placed in the center of a vacuum dome. The desired vacuum in the chamber was created using a vacuum pump. The current was then increased slowly until the gold source material started to melt and evaporate. The evaporated material got deposited on the quartz glass that had been placed above the chamber as shown in Figure 3.1. The QPod.exe software was used for film thickness determination. When the desired thickness was achieved, the swing arm shield was closed to prevent more material from depositing onto

the quartz substrates followed by switching off the vacuum pump and allowing air to get into the chamber to release the vacuum. The same procedure was repeated for the deposition of silver and copper films but using silver and copper as the source material respectively.

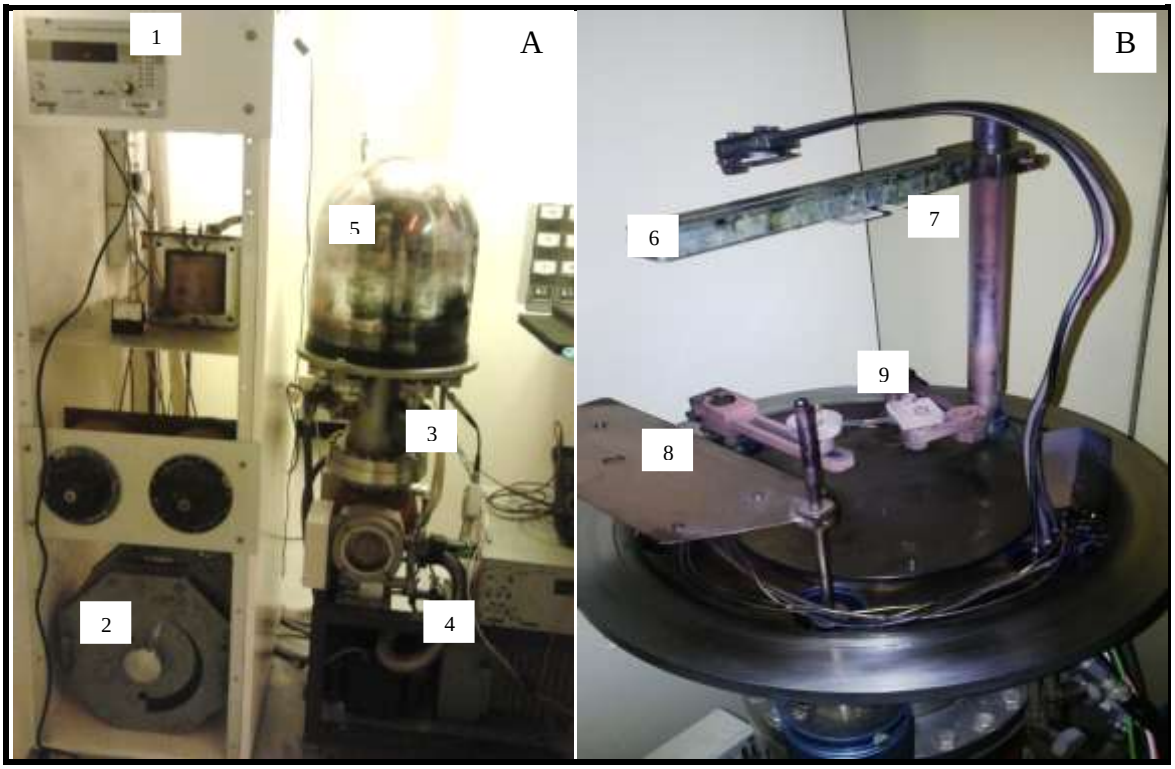

Figure 3.1: A photograph of (A) the complete thermal evaporation unit used for coating quartz with gold, silver and copper thin films. {1- Pirani cold cathode gauge; 2- Current control knob; 3- Opening and closing knob; 4 – Vacuum pump; 5- dome} and (B) the opened thermal evaporation unit. {6 - Substrate holder; 7 – quartz substrate; 8 – Swing arm shield; 9 - tungsten sample holder.

For the deposition of two layers or three layers of different plasmon elements, the quartz support previously coated with one plasmon element was put back in the thermal evaporation unit and coated with a different plasmon element using the procedure detailed earlier. The bimetallic layers were made up of different combinations of plasmon elements and these were Au/Ag, Au/Cu, Ag/Cu and for the three layer system Au/Ag/Cu.

Table 3.1 shows the parameters used for the deposition of the Au, Ag or Cu thin films on MPTMS treated quartz. The frequency was the same for all the depositions made. The vacuum pressure (3.0×10^{-3} Pa) was the same for copper and silver and for gold it was 1.9×10^{-3} Pa. Generally the conditions were similar, the only difference was the time taken to achieve the required film thickness of the plasmon metal. The film thickness was determined by QPod.exe software on the machine.

Table 3.1: Parameters used for metal film deposition using thermal evaporation technique.

Parameter	**Copper**	**Gold**	**Silver**
Vacuum Pressure (Pascal)	3.0×10^{-3}	1.9×10^{-3}	3.2×10^{-3}
Current (Amps)	95	100	100
Average rate of deposition	*0.025 nm/s*	*0.016 nm/s*	*0.015 nm/s*
Frequency (Hz)	591365.25	591365.25	591365.25

3.3 Preparation of titanium dioxide

Two methods were used for the preparation of titanium dioxide in this study, sputter coating technique and sol-gel method. The sol-gel method was used for the preparation of doped TiO_2 photo-catalysts.

3.3.1 Sputter coating of TiO_2 films

The titanium source material and the quartz supports to be coated were placed in the chamber of the instrument shown in Figure 3.2. After creating a desired vacuum which took about 40 minutes, the oxygen gas was introduced in the chamber to supply oxygen to react with titanium to form the desired product TiO_2. The high voltage (460-465 volts) used in the

process caused the acceleration of the gas atoms towards the titanium source material and the resulting bombardment of the titanium source material broke the bonds between atoms. The deposition rate of the film was approximately 1 nm per minute and to get a 100 nm TiO_2 film the deposition was done for 1 hour 40 minutes. The parameters used for depositing the thin film of TiO_2 were: current 0.28 amps, power 129 watts, voltage 460-465 volts and a pressure of 60 microns Hg.

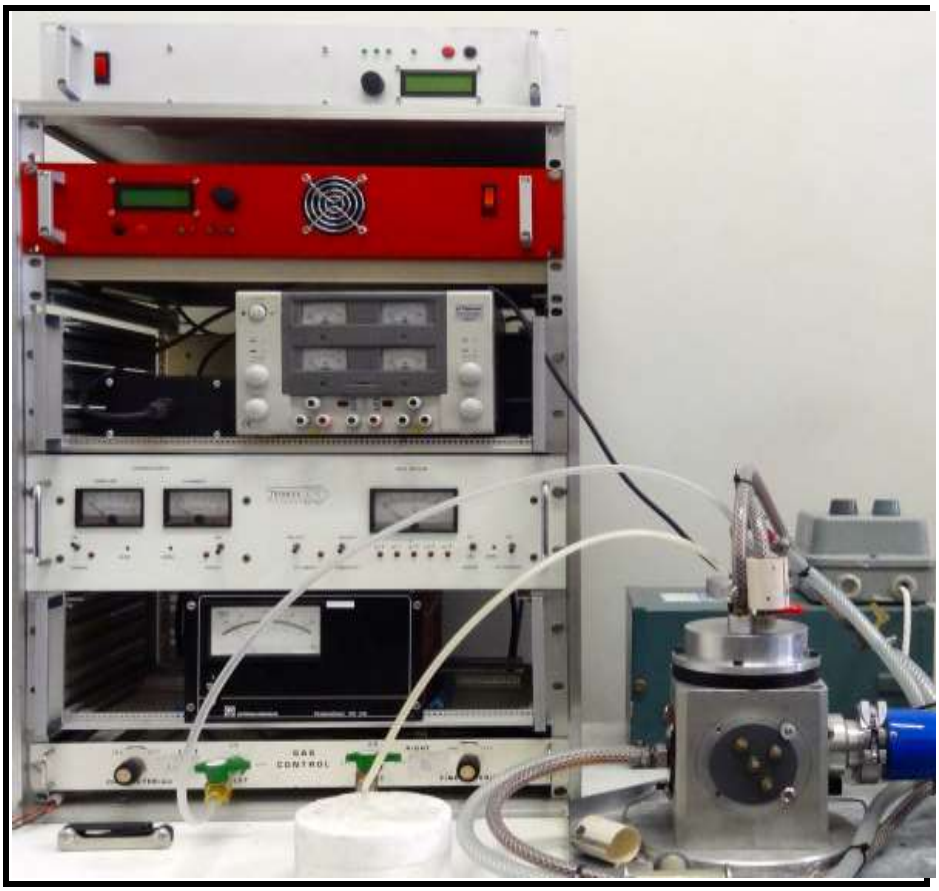

Figure 3.2: Sputtering unit for coating quartz with TiO_2 nanofilms.

Table 3.2 shows sample codes for (i) plasmon metal films deposited on quartz coated with TiO_2 photo-catalyst (ii) TiO_2 films deposited on quartz supports previously coated with plasmon metal film.

Table 3.2: Sample description and codes

Sample description	Sample Code
TiO_2 film with no metal film	T1
2 nm of Ag deposited on TiO_2 film	2AgT
2 nm of Au deposited on TiO_2 film	2AuT
2 nm of Cu deposited on TiO_2 film	2CuT
5 nm of Ag deposited on TiO_2 film	5AgT
5 nm of Au deposited on TiO_2 film	5AuT
5 nm of Cu deposited on TiO_2 film	5CuT
TiO_2 deposited on 5 nm Cu film	T5Cu
TiO_2 deposited on 10 nm Cu film	T10Cu
TiO_2 deposited on 20 nm Cu film	T20Cu
TiO_2 deposited on 25 nm Cu film	T25Cu
TiO_2 deposited on 5 nm Au film	T5Au
TiO_2 deposited on 10 nm Au film	T10Au
TiO_2 deposited on 20 nm Au film	T20Au
TiO_2 deposited on 25 nm Au film	T25Au
TiO_2 deposited on 5 nm Ag film	T5Ag
TiO_2 deposited on 10 nm Ag film	T10Ag
TiO_2 deposited on 20 nm Ag film	T20Ag
TiO_2 deposited on 25 nm Ag film	T25Ag

3.3.2 Sol-gel synthesis of doped TiO_2 nanoparticles

Doped titanium dioxide nanoparticles were synthesized using a sol-gel method with titanium tetrachloride as the precursor. Although there are several methods that can be used to synthesize TiO_2, the sol-gel method was chosen because it is very simple and allows easy control of particle

size, shape and distribution. This wet chemical technique proceeds via a base or an acid catalysed hydrolysis step of a titanium precursor. Typical precursors for TiO_2 are metal chlorides and metal alkoxides which undergo hydrolysis (Equation 3.1) and polycondensation (Equations 3.2 & 3.3) forming three dimensional polymeric skeletons with Ti-O-Ti extended chain network resulting in a system that contains both liquid and solid phases. The development of Ti-O-Ti chains is favoured with low hydrolysis rates, low water contents and excess titanium alkoxide in the reaction mixture (Malekshahi Byranvanda *et al*., 2013).

$$\text{Ti-OR} + H_2O \rightarrow \text{Ti-OH} + \text{ROH} \quad (3.1)$$

$$\text{Ti-OH} + \text{Ti-OR} \rightarrow \text{Ti-O-Ti} + \text{ROH} \quad (3.2)$$

$$\text{Ti-OH} + \text{Ti-OH} \rightarrow \text{Ti-O-Ti} + H_2O \quad (3.3)$$

The separation of the solid and thermal treatment of the amorphous powder is necessary to prevent further polycondensation. With thermal treatment, structural stability is improved and phase transformation from anatase to the more thermodynamically stable rutile occurs.

3.3.2.1 Synthesis of Ag/C co-doped TiO_2

Titanium tetrachloride (6.0 mL) was added drop wisely to a 100 mL of distilled water in a flask immersed in an ice bath with vigorous stirring. An appropriate amount of glucose (0.018 g) was added to get a final concentration of 0.001 M of glucose in the solution. This procedure was repeated to get six different sets. Silver chloride solution (0.01 M) was added to each of the six sets so as to get 0.2, 0.5, 0.7 and 1.0 mol % of Ag in the solution. This was then heated for 30 minutes at 95 °C and allowed to cool to room temperature. The pH was adjusted to 8.0 using potassium hydroxide and heated for another 30 minutes. The precipitate was separated from the solution by centrifugation, washed with deionised water to remove excess chloride ions, dried at

90 °C and then finally calcined at 500 °C for 2 hours to give Ag/C co-doped TiO_2. The graphical representation of the methodology is shown in Figure 3.3.

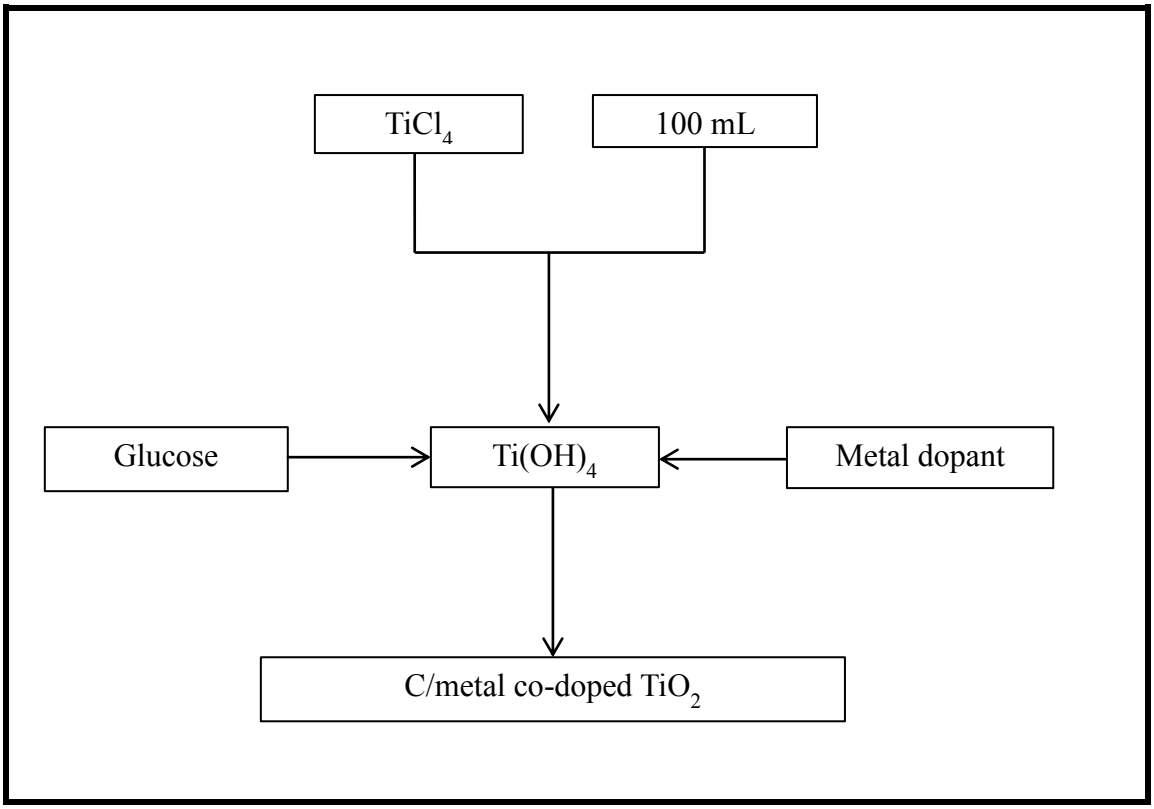

Figure 3.3: Schematic of the preparation of carbon/metal co-doped TiO_2.

3.3.2.2 Synthesis of Au/C co-doped TiO_2 nanoparticles

The procedure for the synthesis of Au/C co-doped TiO_2 was exactly the same as that for the preparation of Ag/C co-doped TiO_2 (Figure 3.3) but with the addition of gold as a dopant instead of silver. Tetrachloroauric acid solution (2 mM) was used as the source of gold. The dopant loadings of 0.2, 0.5, 0.7 and 1.0 mol % Au were used.

3.3.2.3 Synthesis of Au doped TiO_2 nanoparticles

The procedure for the synthesis of Au doped TiO_2 nanoparticles was the same as the method used to prepare Au/C co-doped TiO_2 photo-catalysts but with addition of gold as the only dopant.

3.3.2.4 Synthesis of Ag doped TiO_2 nanoparticles

The procedure for the synthesis of Ag doped TiO_2 nanoparticles was the same as the method used to prepare Ag/C co-doped TiO_2 photo-catalysts but with addition of silver as the only dopant.

3.3.2.5 Synthesis of undoped TiO_2 nanoparticles

The procedure for the preparation of undoped TiO_2 nanoparticles was the same as the procedure followed in the preparation of doped TiO_2 photo-catalysts but with no dopants added.

3.4 Deposition of the doped photo-catalysts

The prepared co-doped TiO_2 photo-catalysts were deposited on quartz supports using a modified version of the methodology used by Markelonis et al., (2015). The method has the advantages of being fast and simple compared to other currently known nanoparticle deposition techniques. The thickness of the films was controlled by the amount of the colloidal nanoparticle solution used in the deposition. A desired amount of TiO_2 (0.02 g) photo-catalyst to be deposited was mixed with absolute ethanol (15 mL) and then sonicated for five minutes to make sure the TiO_2 nanoparticles were well dispersed. The etched and MPTMS treated quartz substrate to be coated was placed in the centrifuge vial with the other side covered with sellotape so that only one side was coated. The sonicated TiO_2

nanoparticles were then poured into the centrifuge vials and centrifuged at 3500 rpm until a significant desired amount was deposited. The desired amount was determined by weighing the quartz support before and after deposition. After centrifugation, the supernatant was pipetted out and the quartz substrate with the deposited TiO_2 nanoparticles was then removed and allowed to dry in the air.

3.5 Preparation of spherical copper nanoparticles

About (1.0 g) of cupric acetate was dissolved in boiling water. In a separate beaker 2 mL of formaldehyde (34.5 %) were added to 50 mL of absolute ethanol followed by 1 mL of EDTA (0.1 M) and 1 mL of hydrazine with magnetic stirring. This mixture was then added drop wise to the boiling cupric acetate solution and heated for a further 15 minutes at 90 °C. The solution was left to cool and the resulting nanoparticles were separated by centrifugation.

3.6 Preparation of silver dendrites

About two drops of hydrogen peroxide were added to 50 mL of 0.2 mM silver nitrate solution in a conical flask with magnetic stirring. About 1 mL of 8.86 mM polyvinylpyrrolidone was then added drop wise to the solution followed by addition of 6 mL of 0.25 mM trisodium citrate. The mixture was stirred for thirty minutes before exposure to UV-light of wavelength 366 nm for 12 hours. The solution was then aged for 7 days undisturbed at room temperature and then separated from solution by centrifugation.

3.7 Preparation of silver nanorods

About 0.04 g of silver nitrate was dissolved in 100 mL of deionized water followed by addition of 10 mL of 0.03 M trisodium citrate with magnetic stirring. 5 mL of 0.16 M polyvinylpyrrolidone solution was then added with vigorous stirring followed by 0.2 mL of

hydrogen peroxide. The pH was adjusted to 9 by adding a few drops of sodium hydroxide solution (25 % w/v). After 10 minutes of vigorous stirring, 0.5 mL of 0.1 M sodium boron hydride was added drop wise. The reaction medium was then exposed to UV light of wavelength 365 nm for 30 minutes. The solution was then left for 24 hours stirring at room temperature. The color of the solution was yellowish brown.

3.8 Preparation of spherical silver nanoparticles

About 0.01 g of silver nitrate were dissolved in 33.3 mL of deionized water followed by addition of 0.007 mmol of trisodium citrate solution and 0.20 mmol of polyvinylpyrrolidone solution with vigorous stirring. About 0.2 mL of hydrogen peroxide was added to the reaction solution. After 10 minutes of stirring, 1.7 mL of 0.078 M sodium borohydride were added drop wise. The solution was then heated at 65 °C for 30 minutes and then left to cool to room temperature. Separation of the nanoparticles was achieved by centrifugation.

3.9 Preparation of spherical gold nanoparticles

About 3.0 mL of 2.5 mM tetrachloroauric acid solution were added to 100 mL of deionized water in 250 mL conical flask. This was followed by addition of 100 mL of 2.5 mM of trisodium citrate with magnetic stirring. The resulting solution was heated at 75 °C for 1 hour 30 minutes and left to cool to room temperature while stirring. The citrate acted as both the reducing agent and a capping agent. Aliquots were taken after every 30 minutes and analyzed by UV-Vis spectroscopy. The nanoparticles were separated from solution by centrifugation.

3.10 Preparation of TiO_2/plasmon metal composites

To prepare TiO_2/gold nanoparticle composites containing 0.1 wt %, 0.5 wt % and 1.0 wt % Au, about 2 g of TiO_2 were mixed with 2 mg, 10 mg and 20 mg of gold nanoparticles

respectively. The same procedure was followed to prepare TiO_2/Ag nanocomposites which had 0.1 wt %, 0.5 wt % and 1.0 wt % Ag. To prepare TiO_2/plasmon metal nanocomposites containing two or three plasmon elements, equal masses of the plasmon metal nanoparticles were mixed and about 2 mg of the mixture was then mixed with 2 g of TiO_2 to prepare TiO_2/plasmon metal with 0.1 wt % plasmon metal nanoparticles. The same procedure was followed to prepare nanocomposites containing 0.5 and 1.0 wt % plasmon metal nanoparticles. About 0.02 g of TiO_2/plasmon metal nanocomposites was then deposited on quartz supports using the method given in Section 3.4. The sample description and codes for the prepared composites are shown in Table 3.3.

Table 3.3: Sample description and codes for nanocomposites

Sample description	**Sample Code**
Spherical gold nanoparticles	AuSNP
Spherical silver nanoparticles	AgSNP
Silver dendrites	AgDR
Silver nanorods	AgNR
TiO_2/Au (1.0 wt % Au) nanocomposite	TAu1
TiO_2/Au (0.5 wt % Au) nanocomposite	TAu2
TiO_2/Au (0.1 wt % Au) nanocomposite	TAu3
TiO_2/Ag (1.0 wt % Ag) nanocomposite	TAg1
TiO_2/Ag (0.5 wt % Ag) nanocomposite	TAg2
TiO_2/Ag (0.1 wt % Ag) nanocomposite	TAg3
TiO_2/Cu (1.0 wt % Cu) nanocomposite	TCu3
TiO_2/Cu (0.5 wt % Cu) nanocomposite	TCu3
TiO_2/Cu (0.1 wt % Cu) nanocomposite	TCu3
TiO_2/Ag (0.1 wt % AgDR) nanocomposite	TAgDR

TiO_2/AgNR (0.5 % AgNR) nanocomposite	TAgNR
TiO_2/Au/Ag nanocomposite	TAuAg
TiO_2/Au/Cu nanocomposite	TAuCu
TiO_2/Cu/Ag nanocomposite	TAgCu
TiO_2/Au/Ag/Cu nanocomposite	TAAC
Ag/C co-doped TiO_2 (05 % Ag)/Au/Ag/Cu composite	dTAAC

3.11 Photo-degradation experiments

The photo-catalytic activity evaluations of the photo-catalysts were performed using methyl orange, bromocresol purple and/or bisphenol A under UV light with some chosen photo-catalysts under visible light irradiation. All photo-degradation experiments using methyl orange were conducted at a temperature of 25 °C and at pH 7 except where the effect of pH was being investigated. In case of bromocresol purple, pH 11 was used during its photo-degradation so that the disappearance of the intense purple color could be determined. Where pH adjustments were necessary, sodium hydroxide solution and hydrochloric acid were used.

The 2.5 cm x 3.5 cm photo-catalyst coated quartz was immersed in 100 mL of 10 ppm solution to be degraded leaving room at the bottom of the reactor by using a perforated plastic stand for the magnetic stirrer to rotate without scratching the photo-catalyst film. The quartz was placed in such a way that the entire photo-catalyst was uniformly irradiated with incident light. The sources of light used were (i) Osram 9 W UV lamp which gives light of wavelength of 365 nm (Figure 3.4) and (ii) an Oriel Newport solar simulator fitted with a 500 W xenon lamp (Figure 3.5). The solar simulator was Model 91150V was supplied by Oriel Instruments, USA and was set to give a power output of 1 000 W/m^2 using a spectral filter.

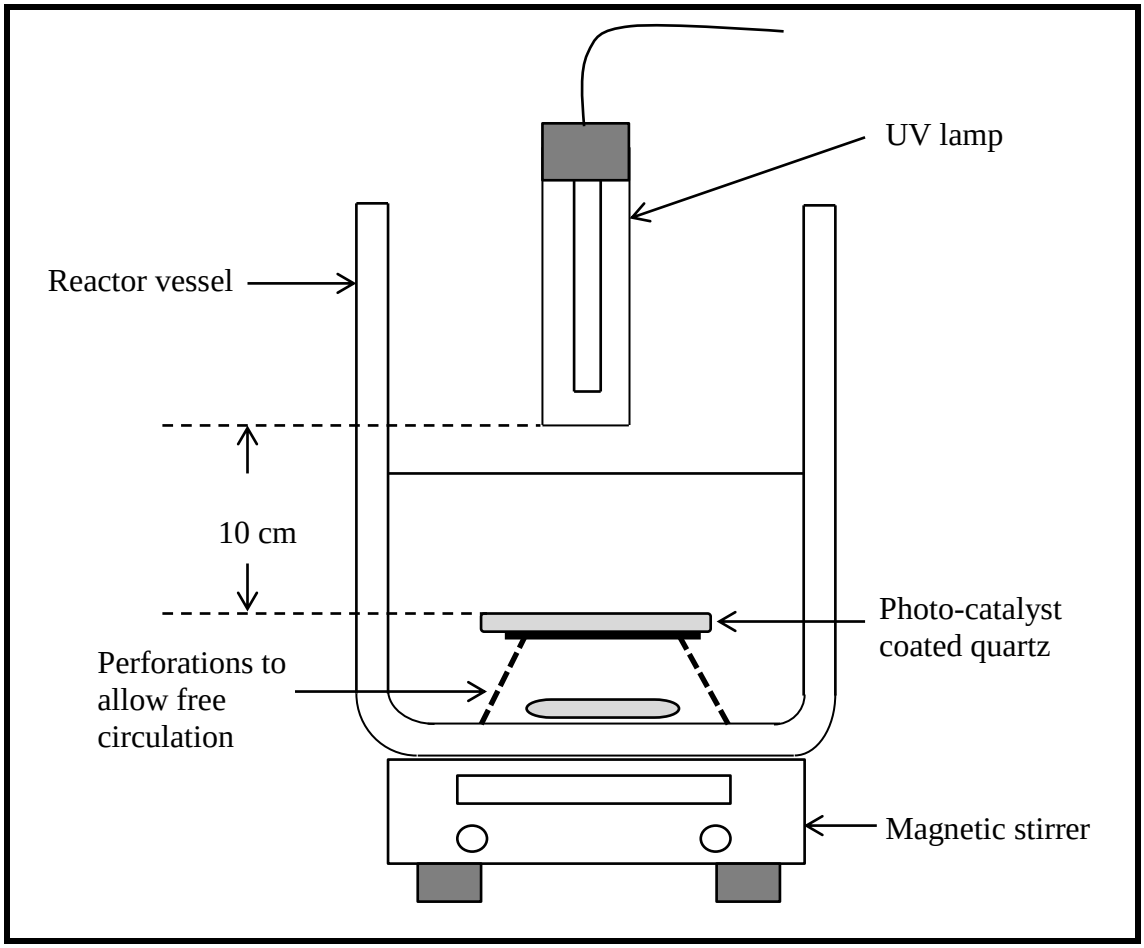

Figure 3.4: Schematic diagram of experimental setup using a UV lamp.

The UV lamp was fixed in the middle of the system at 10 cm above the surface of the solution. For adsorption and desorption equilibrium to be reached, the photo-catalyst was left in the solution for 30 minutes in the dark before irradiation. Aliquots of methyl orange solution were taken after every 30 minutes using a disposable plastic syringe and analyzed by a UV- a Perkin Elmer Lambda 35 UV-Vis spectrophotometer. All the experiments were conducted in a dark room to exclude natural light from interfering, thus solely illuminated by the specified light source.

The experimental set-up for photo-degradation experiments under visible light is shown in Figure 3.5

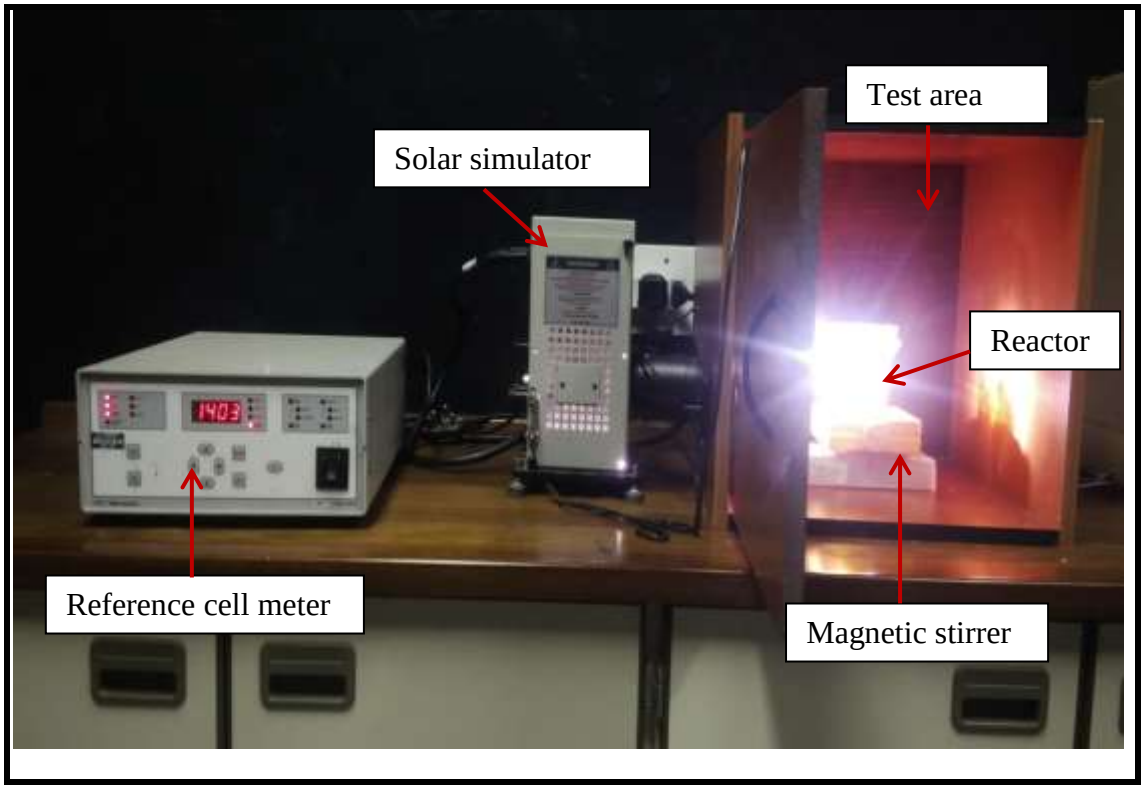

Figure 3.5: Photograph of the solar simulator and set–up used for visible light photo-degradation of methyl orange.

3.11.1 Determination of the effect of other organics on MeO photo-degradation

Methyl orange, bromocresol purple and bisphenol A were mixed in different ratios such as 1: 1: 1, but in such a way that the final concentration of the target compound was the same for all experiments. The photo-catalyst coated quartz was immersed in a 100 mL mixture of methyl orange and bromocresol purple and/or bisphenol A and irradiated with UV light fixed at a distance of 10 cm from the photo-catalyst (Figure 3.4). In the study of the effect of bromocresol purple, equal volumes (50 mL) of the same concentration (20 ppm) of methyl orange and bromocresol purple were mixed. Aliquots were taken after every 30 minutes using a disposable syringe and analysed by UV-Vis spectrometry.

3.11.2 Determination of the effect of salts on methyl orange photo-degradation

The salts that are normally used in the dye industry were chosen since their chances of being found in water are high. The combined effects all the three salts, sodium chloride, sodium sulphate and sodium nitrate were studied by adding the salts in methyl orange solution to be degraded. Appropriate amounts of the salts were added such that final concentration of each salt in 100 mL of the photo-degradation solution was 8.0×10^{-5} M.

3.11.3 Durability tests

To find out how durable the photo-catalysts were, 2AuT, 2AgT, 2CuT, T5Cu, T10Cu, T20Cu, T5Au, T10Au, T20Au, T5Ag, T10Ag and T20Ag photo-catalysts were tested for the extent of leaching after 300 minutes of photo-degradation of methyl orange under UV light at 25 °C and pH 7. TiO_2 photo-catalyst deposited on all the three plasmon metals (TiO_2/Au/Ag/Cu) was tested for both the extent of leaching and loss of photo-catalytic efficiency when used in photo-degradation experiments four times/four cycles. Aliquots were taken at the end of each cycle and analysed by ICP to find out if there are any elements that had leached out of the photo-catalyst film. The change in photo-degradation efficiency of the photo-catalyst was determined so as to know how long the photo-catalysts could be used before they can be regenerated.

3.11.4 Determination of the photo-degradation intermediates

LC-MS and FTIR were used to determine the reaction pathway followed by methyl orange and bromocresol purple during the photo-degradation process. To determine the nature of the intermediates formed, aliquots were taken from the reaction vessel after every 20 minutes and filtered using a nylon syringe filter of pore size 1.22 μm. The initial solution and the filtered

aliquots were then analyzed by LC-MS and FTIR techniques. To run the FTIR, a drop of the solution was mixed with KBr and pressed into a pellet which was then analysed.

3.12 Characterization of Materials

Several characterization techniques were used in this study to characterize the prepared samples. After characterization, a lot of information about the samples such as composition, particle size, surface morphology, elemental composition, functional groups and absorption edge was gathered depending on the characterization technique employed. This section of the thesis gives a brief description of the protocols for the characterization techniques that were employed in this study.

3.12.1 High resolution transmission electron microscopy

This technique was used to identify and characterize the microstructure of materials size, shape and arrangement of the particle's agglomeration. The high resolution transmission electron microscopy (HRTEM) images were collected on a Gatan Ultrascan 2000 CCD camera using a FEI Tecnai F20 field emission gun HRTEM operated at 200 kV in bright field mode. The samples were prepared by putting a drop of the colloidal solution on the TEM grids and the solvent was allowed to evaporate at room temperature.

3.12.2 High resolution scanning electron microscopy

This analytical technique was used to get detailed images and a quick identification of elements present, porosity, surface topography and material homogeneity. The samples to be analyzed were coated with gold to make them electrically conductive to prevent charging and then mounted on a specimen stub rigidly. The analysis was performed on a JEOL JSM-

6390LV Scanning Electron Microscope fitted with a secondary electron detector and energy dispersive spectroscope for elemental analysis.

3.12.3 Inductively Coupled Plasma/Optical Emission Spectrometry

Inductively Coupled Plasma (ICP) was used for the determination of the extent of leaching of plasmon elements during the photo-degradation process. It was done using a Spectro Arcos ICP-OES instrument equipped with a Side on Plasma Interface which was initialized for 20 minutes before analysis. Samples and controls were put in vials in a sequence and were sampled automatically using an auto sampler. Sample inlet was done using a four channel peristaltic pump which provides a segmented flow of the liquid samples. A 10 % solution of nitric acid was used for washing between sample analysis i. e before the next sample could be analyzed. Before the analysis, the ICP OES measurement conditions were optimized and the following conditions were used: Plasma power (w) 1400, pump speed (rpm) 30, coolant flow 14.00 L/min, auxiliary flow 2.10 L/min and nebulizer flow 0.80 L/min.

3.12.4 CHNS Elemental Analysis

The CHNS elemental analyzer was used for determination of carbon in the plasmon metal/carbon codoped TiO_2 photo-catalysts. The instrument used was a Thermo Scientific CHNS-O-Analyzer; Flash 2000. The solid sample to be analyzed was put into a reactor tube at 950 °C and combusted in a highly strong oxidizing pure oxygen environment. The carrier gas flow was 140 mL/minute and the reference flow was 100 mL/minute.

3.12.5 UV-Vis Spectroscopy

In this work the UV-Vis technique was employed in the determination of changes in the concentration of the model pollutants in photo-degradation experiments. The UV-Vis

spectrum of the methyl orange was obtained on a Perkin Elmer Lambda 35 UV–Vis spectrometer.

3.12.6 BET-Surface area analysis

BET-Surface area analysis was used to measure the specific surface area of the prepared powdered doped titanium dioxide photo-catalysts before immobilization on the quartz substrates. The instrument used was a micrometrics ASAP 2020, Surface area and Porosity analyzer. The samples were degassed at 50 °C for 90 minutes and at 80 °C for 1440 minutes.

3.12.7 X-Ray Diffraction

X-ray diffraction was used to determine the crystallinity and the ratio of the anatase to rutile phases in the prepared TiO_2 photo-catalysts and to also determine the different phases in the copper, gold and silver films. The X-ray diffraction patterns of the samples were obtained from a Bruker D8 Advance instrument with a Cu-Kα1 (λ – 1.54060) X-ray Tube and a LynxEye detector.

3.12.8 Diffuse reflectance Spectroscopy

Diffuse reflectance spectroscopy was used to study the optical properties of the prepared TiO_2 photo-catalysts which were then used to determine the band gaps and absorption wavelength by using the Tauc, Davis and Mott expression to relate band gap (Eg) to the absorption coefficient (Equation 3.4). The analysis was done at room temperature using a diffuse reflectance attachment of a Cary 500 UV-Vis –NIR spectrophotometer. The spectra were acquired from 800 nm to 200 nm. Both the reflectance and absorbance of the samples were measured.

$$(h\nu\alpha)^{1/n} = A(\text{h}\nu - \text{Eg}) \quad 3.4$$

where α is the absorption coefficient

h is the Plank's constant

Eg is the band gap

A is the proportionality constant

v is the frequency of vibration

n is the contant which denotes the nature of the sample preparation.

In this study the value of n used for the calculations was 2 since the absorption of TiO_2 has an indirect transition. To find the band gaps of the different samples, plots of $[F(R)*hv]^n$ versus photon energy "Tauc plots" were done.

3.12.9 Fourier transform infrared spectroscopy

In this study FTIR analytical technique using a Perkin Elmer FT-IR model 2000 instrument was employed in the determination of the structural changes of methyl orange and bromocresol purple that occurred during photo-catalytic degradation. The samples to be analyzed were spread on the sodium chloride windows and then a beam of infrared light was passed through the sample and the resulting radiation absorption was measured as a function of frequency. The technique was also used to characterize undoped and doped TiO_2 photo-catalysts.

3.12.10 Thermo-gravimetric Analysis

Thermo-gravimetric analysis (TGA) was used to study the thermal properties and determine the water and carbon content of the prepared TiO_2 samples by measuring the changes in weight of a

sample as a function of temperature under a controlled environment. About 10 mg of sample to be analysed was placed in a specimen pan hanging from the balance and then heated at a rate of 10 °C per minute under a nitrogen environment from 25 °C to 900 °C. The changes in the sample weight during the TGA analysis were monitored by a sensitive analytical balance. The instrument used was Perkin Elmer TGA 400 thermo-gravimetric analyser.

3.12.11 Liquid chromatography-Mass Spectrometry (LC-MS)

Liquid chromatography-mass spectrometry was used to determine the photo-degradation intermediates and the photo-degradation pathway followed by methyl orange. The sample to be analyzed was injected into a liquid chromatography (LC) column where it was separated into various components and then passed to the mass spectrometer (MS).

The instrumentation and chromatographic conditions used were as follows; the LC-MS instrument used was a 5600 AB SCIEX Triple TOF hybrid mass spectrometer (Applied Bio systems Sciex, USA) equipped with a high performance Agilent 1260 infinity liquid chromatography system and operated in the positive turbo ion spray (ESI) mode. The LC chromatography was fitted with a 4.6 x 50 mm reverse phase column Proshell 120; EC-C18 with diameter 7 µm. The mobile phase used was composed of two solvents; (Solvent A- water with 0.1 % formic acid; Solvent B- acetonitrile with 0.1 % formic acid). Bound compounds were eluted at a given gradient. The elution gradient was as follows: the mobile phase started with 5 % of acetonitrile, which was increased linearly to 95 % in 10 minutes and kept constant for 1 minute and finally returned to the initial conditions in 0.5 minutes and kept constant for 5 minutes giving a total run time of 17 minutes. The column was equilibrated for 5 minutes and the flow rate was 0.5 mL min^{-1}. Time of Flight MS parameters were as follows; the declustering potential (DP) was 60 V and collision energy (CE) was 35

V with collision energy spread (CES) of ±35 V. The product ion parameters were as follows; IonSpray voltage floating parameter (ISVF) 5500, Ion Source Gas 1 (GS1) parameter was 50 psi and Ion Source Gas 2(GS2) parameter was 50 psi. An Agilent 1260 high performance auto sampler, with a 100 µL syringe was used with an injection volume of 200 µL while the samples were drawn and injected at a speed of 200 µL/min. The Agilent column oven was set at 40 °C for both right and left temperatures with a temperature tolerance of ±2 °C.

3.12.12 Raman spectroscopy

Raman spectroscopy was used to obtain information about the structure and properties of materials from their vibrational transitions. The Raman spectra were obtained from a Raman microscope (Perkin Elmer RamanMicro 200) which was equipped with a device cooled at -50 °C. The 785 nm line of an argon laser was used as the excitation source. The instrument software was used for data acquisition, processing and analysis.

Chapter 4

Preparation of TiO_2/plasmon metal films for enhanced photo-catalytic activity towards organic contaminants

4.0 Introduction

The main focus of this chapter was to reduce the recombination rates of electron-hole pairs in TiO_2 photo-catalyst through the use of noble metal thin films. The chapter was also aimed at finding the effect of plasmon metal films on the photo-catalytic activity of TiO_2 photo-catalyst films when they are deposited layer by layer, hence it involves the preparation and evaluation of the photo-catalytic activity of the plasmon decorated TiO_2 photo-catalyst thin films immobilized on quartz glass. A systematic study of the effect of metal nanoparticle (MNP) film thickness, order of deposition of the films, use of bimetallic layers and the use of different plasmon elements (Au, Ag & Cu) is presented. Possible mechanisms of enhancement of TiO_2 photo-catalytic activity resulting from using different thicknesses of different elements are presented and their understanding might open new avenues for the application of the plasmon decorated TiO_2 photo-catalysts. The effect of bromocresol purple, bisphenol A and salts on methyl orange photo-degradation was also investigated and reported.

4.1 Experimental details

4.1.1 Deposition of TiO_2 on quartz

The sputter coating technique was used to coat the 8.75 cm^2 (3.5 × 2.5 cm) quartz supports. A detailed experimental methodology for the preparation of the TiO_2 films was reported in Section 3.3.1

4.1.2 Deposition of metal NP films by thermal evaporation

The detailed procedure and parameters used in the thermal evaporation technique are reported in Section 3.2.2.1. Samples 2Ag/T, 2Au/T, 2Cu/T, 5Ag/T, 5Au/T and 5Cu/T are those where the metal films were deposited on top of quartz coated with TiO_2 photo-catalyst and samples T5Ag, T5Au, T5Cu, T10Ag, T10Au, T10Cu, T20Ag, T20Au, T20Cu, T25Ag, T25Au and T25Cu are those where TiO_2 was deposited on top of the plasmon metal films as indicated in Table 3.3 in Section 3.3.1. Bimetallic systems and three layer systems consisting of all the metals under study (Ag, Au and Cu) were deposited layer by layer as also reported in Section 3.2.2.1.

4.2 Results and Discussion

The prepared films were characterized by HRTEM, HRSEM, PIXE, XRD and AFM. The rate of deposition was also measured.

4.2.1 Rate of metal deposition

The rate of deposition was difficult to control as it kept fluctuating with time and to see the changes a plot of rate of deposition against time was done and the resulting plots are shown in Figure 4.1. When depositing thicker films such as 25 nm, the fluctuations in the deposition rates observed were greater.

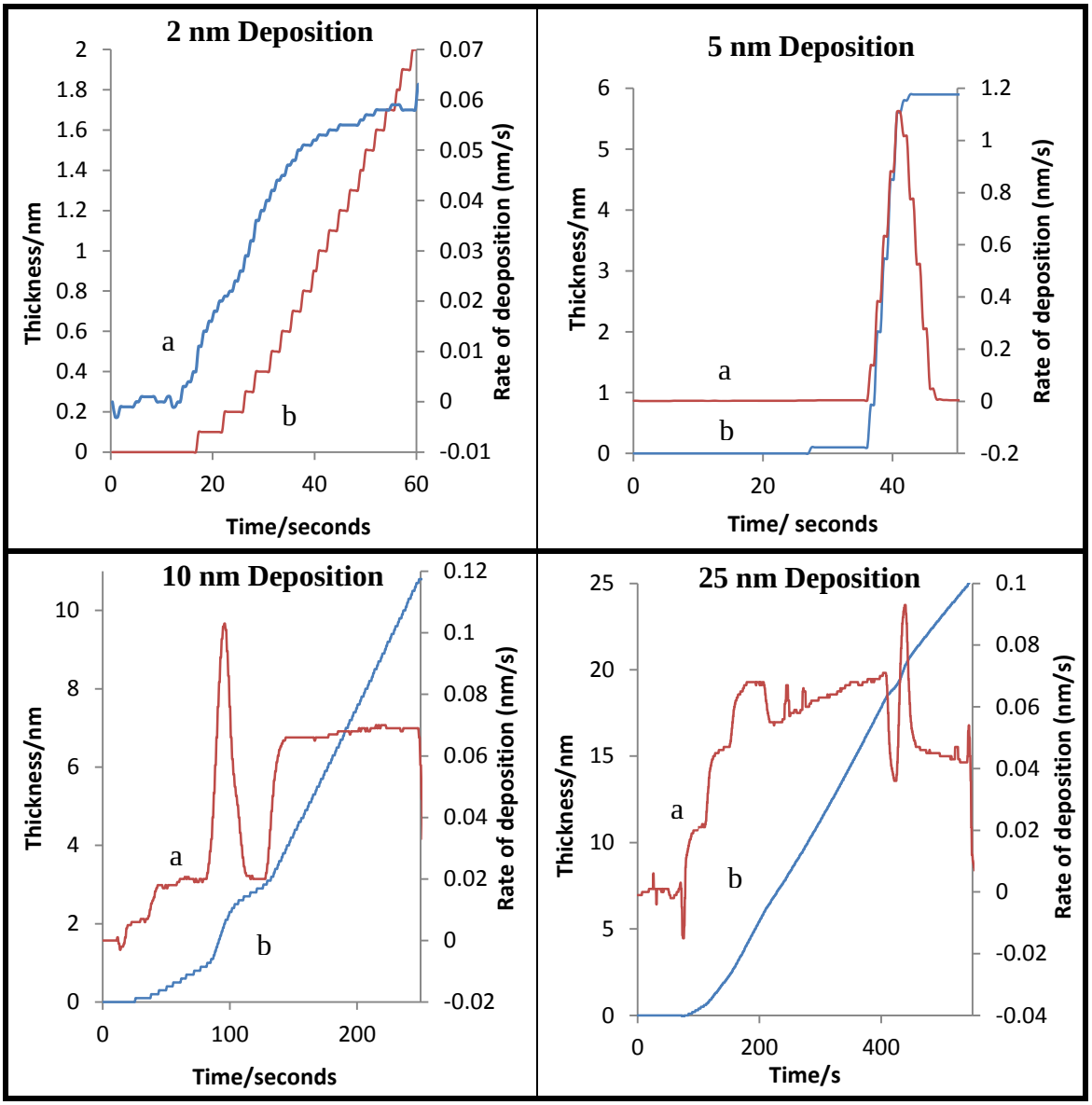

Figure 4.1: Graphs of (a) rate of deposition and (b) film thickness used for the deposition of 2 nm, 5 nm, 10 nm and 25 nm metal films of Ag.

4.2.2 HRTEM analysis of films

The HRSEM analysis was performed to study the surface morphology of the films using a Gatan Ultrascan 2000 CCD camera fitted with a FEI Tecnai F20 field emission gun HRTEM operated at 200 kV in bright field mode. The HRSEM images of MPTMS treated quartz glass and plasmon metal films (Ag, Ag, Au, Ag/Au and TiO_2) are shown in Figure 4.2.

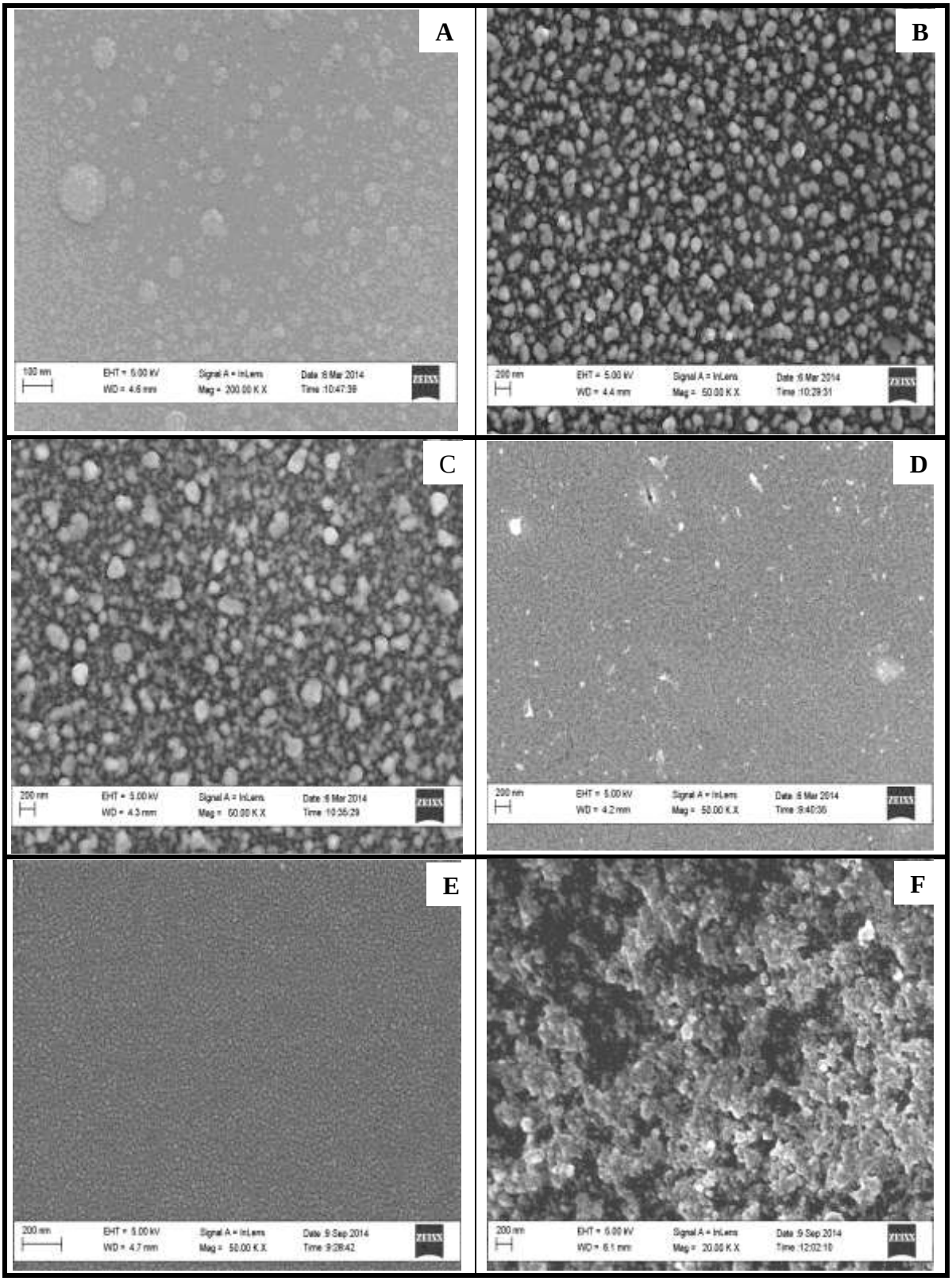

Figure 4.2: HRSEM images of (A) MPTMS treated, (B) 10 nm Ag film, (C) 10 nm Au film, (D) 10 nm Cu film, (E) Ag and Au film before TiO_2 deposition and (F) TiO_2 film on quartz.

The surface of the MPTMS treated quartz (Figure 4.2 A) was relatively uniform showing that the MPTMS film was slightly granular with grains in the sub 100 nm range. The process of the formation of the MPTMS layer on the quartz glass can be illustrated as follows as proposed by Park *et al*, 1999.

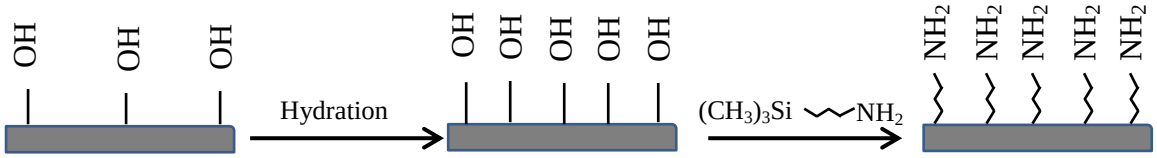

The images show that metal nanoparticles before depostion of TiO_2 photo-catalyst (Figure 4.2 B-E) were also relatively uniformly deposited on the silanized quartz. For all the metal films (Ag, Cu and Au), a 10 nm film was analysed for comparison. There were significant differences in the morphology between the Au film, Cu film and Ag film but an insignificant difference between Au and Ag films (Figure 4.2 B & C respectively). The monomettallic Ag and Au films had smaller NPs at the bottom than on top showing that as the thermal evaporation process continued, the size of the NPs increased with an increase in film thickness due to coalescence resulting in a wide particle size distribution (polydispersed nanoparticles). The copper film did not show any variation of particle size with thickness and had a unform particle size resulting in a smooth surface. The bimettallic Au and Ag codeposited film showed no size variation and the surface was smooth (Figure 4.2 E). TiO_2 film deposited on quartz was highly agglomerated (Figure 4.2 F).

4.2.3 PIXE analysis

Particle induced X-ray was performed to determine the elements in the quartz and the metal thin films. Figure 4.3 shows the PIXE results of the films of selected samples.

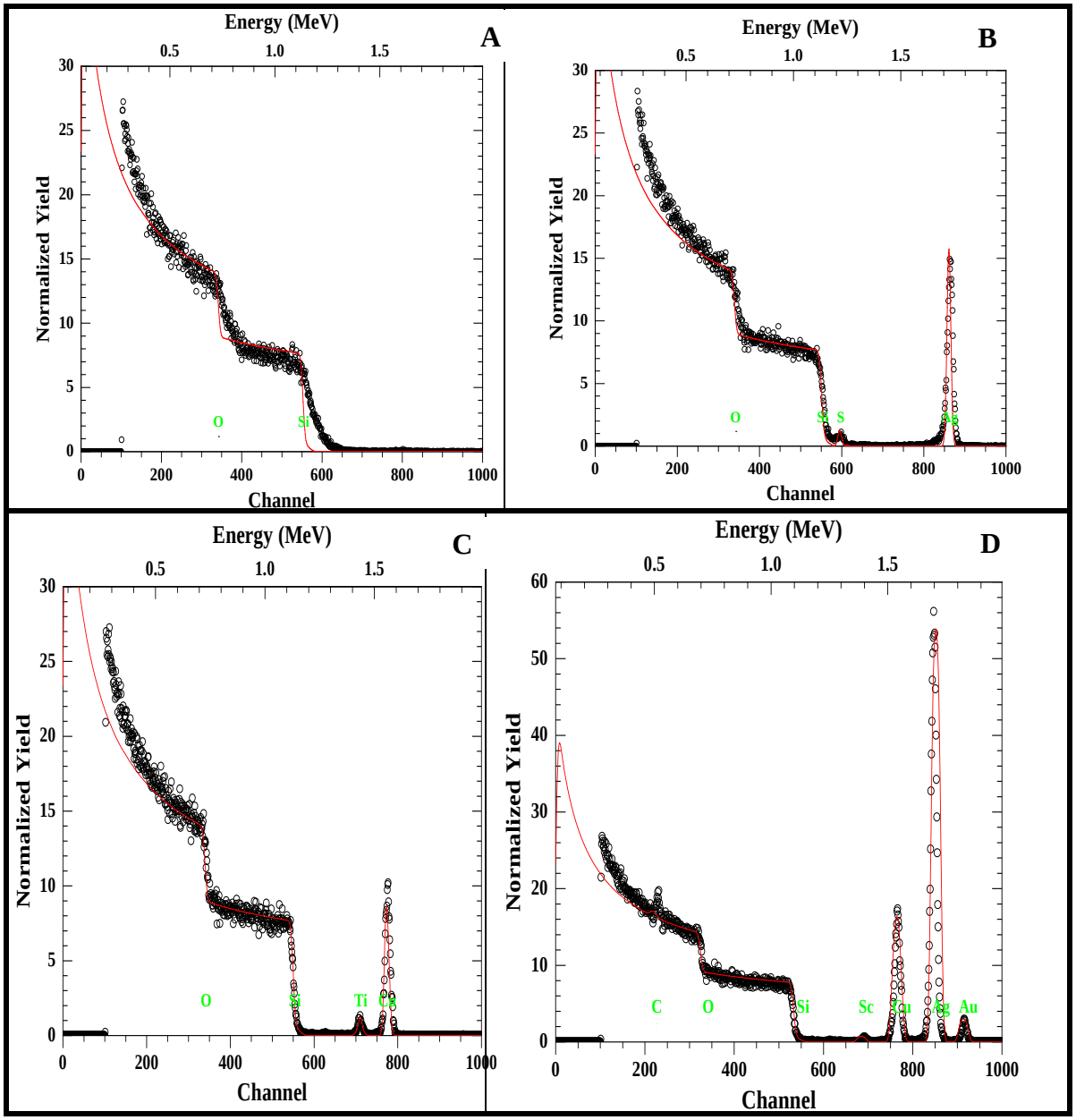

Figure 4.3: PIXE of (A) uncoated quartz, (B) Ag (10 nm) coated, (C) Cu (10 nm) coated and (D) Ag, Cu and Au coated quartz.

Quartz in its pure form consists of only silicon and oxygen and PIXE analysis of the quartz support showed that only those two elements were present in a ratio of 1:2. This shows that the quartz samples used in this study were pure and had been cleaned thoroughly as no other elements were found. The expected metal elements were found in their respective films but in some films such as Ag film, very small traces of sulphur (< 1 %) were also found. In the

copper films some traces of titanium (< 2 %) were found and the detected carbon and oxygen were ascribed to the MPTMS coating.

4.2.4 XRD Analysis

Figure 4.4 shows the XRD patterns of pure quartz, TiO_2 film, Ag film on quartz support, Au film on quartz support and Cu film on quartz support that were obtained using a Bruker D8 Advance instrument with a Cu-Kα1 (λ – 1.54060) X-ray Tube and a LynxEye detector. The XRD analysis was done on pure plasmon metal films of 25 nm and pure TiO_2 (100 nm) so as to see the peaks due to plasmon metals before the deposition of TiO_2 and peaks due to TiO_2 film before deposition of plasmon metal films respectively. A thickness of 25 nm for plasmon metals was chosen for XRD analysis so as to get clearer peaks.

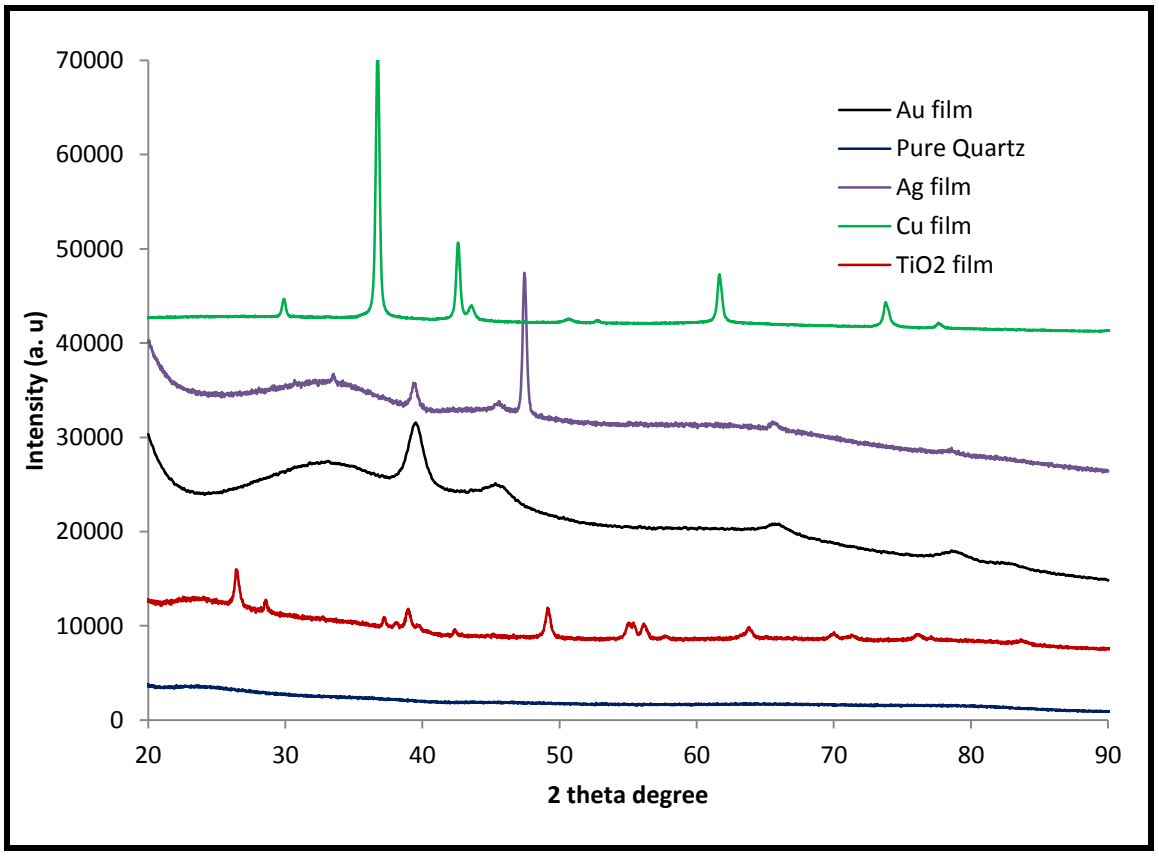

Figure 4.4: XRD patterns of 25 nm films of gold, copper, silver, quartz and 100 nm of TiO_2.

In the XRD pattern of TiO_2, the peaks at 2θ=27.53° and 55.21° indicated the presence of the TiO_2 in the rutile phase while peaks at 2θ=26.31°, 37.89°, 48.87°, and 64.33° indicated the presence of the anatase phase. In the XRD pattern of 25 nm Ag film, the peaks at 2θ = 39.15°, 44.60°, 64.58° and 77.72° were assigned to diffraction from the (111), (200), (220) and (311) lattice planes of pure face centered silver crystals respectively (Liao *et al*., 2011., Liu & Wang., 2013). In the spectra of 25 nm Au film, there were four diffraction peaks corresponding to the diffraction planes (111), (200), (220) and (311) due to the gold metal with face centered cubic structure. These peaks appeared at 2θ values of 38.5°, 44.7°, 64.8°, 77.8° respectively indicating that the nanostructured films were made of crystalline gold (Verma *et al*., 2011). No peaks were observed in the XRD pattern of MPTMS treated quartz substrate.

In the XRD pattern of 25 nm Cu film, the Bragg's reflections for copper nanoparticles were observed in the XRD pattern at 2θ values of 43.16°, 50.13° and 73.58° which correspond to (111), (200) and (220) planes of face centered cubic (*fcc*) structure of copper (Salavati-Niasari M & Davar., 2009). It can be seen that some traces of copper oxide were in the copper film as evidenced by its XRD peaks at 2 theta values of 36.58° and 61.52°.

The XRD patterns of Au films of different thicknesses deposited on quartz are shown in Figure 4.5. The QPod.exe software on the instrument used for deposition was used for film thickness determination.

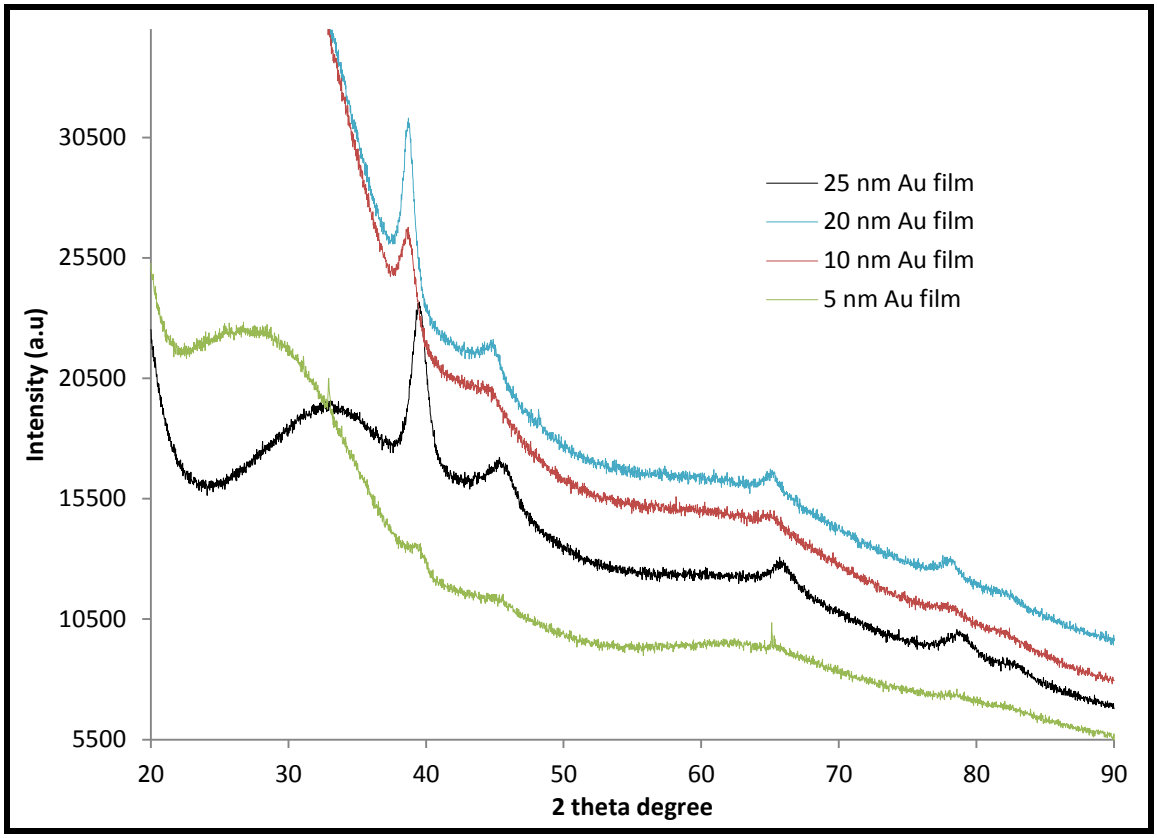

Figure 4.5: XRD patterns of Au films of different thicknesses deposited on quartz.

The characteristic peaks corresponding to (111), (200), (220), (311) of Au are located at 2θ = 38.4°, 44.7°, 64.5°, and 77.8°, respectively. It was observed that the XRD peaks of the 25 nm Au film all shifted by 2θ values of 1.0° and the peaks were more intense than thinner Au films due to 25 nm film thickness implying that the XRD peaks became more intense with increase in film thickness.

4.2.5 AFM Analysis of the metal NP films

The AFM images showing the topographical information of 10 nm Au, 10 nm Cu and 10 nm Ag films prepared by the thermal evaporation technique are shown in Figure 4.6 and these images were obtained under the similar imaging conditions.

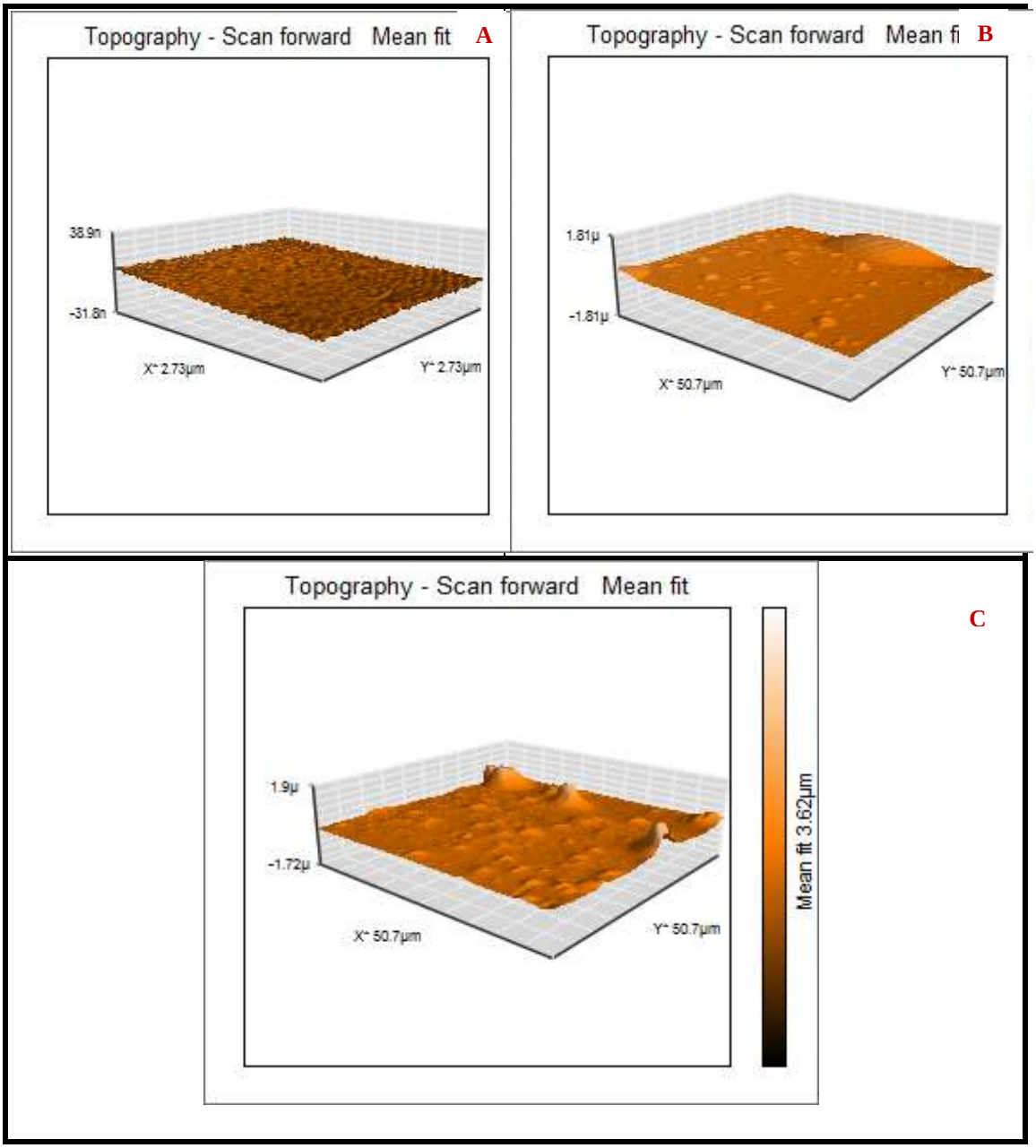

Figure 4.6: AFM topography of quartz coated with (A) 10 nm Au film, (B) 10 nm Ag film and (C) 10 nm Cu film.

Although the rate of deposition was changing (Figure 4.1), the resulting Au and Ag films were fairly uniform. The pronounced surface roughness on other sections of the Cu films was thought to be caused mainly by the inhomogeneous distribution of MPTMS adhesion promoter as seen in the HRSEM image (Figure 4.2A). In the AFM image of Ag, a pronounced hump could be observed due to the underlying MPTMS droplet. The other

reasons for the observed humps could be the etching process and coalescence of nanoparticles during deposition resulting in various nanoparticle sizes forming the film. This surface roughness is advantageous for the deposition of TiO_2 photo-catalyst as it aids good adhesion.

4.3 Photo-catalytic activity evaluation

This section presents the photo-degradation results of methyl orange under UV light using different plasmon decorated photo-catalysts. It is subdivided into subsections, each discussing a parameter that was varied. The change in concentration of the dye over time was obtained on a Perkin Elmer Lambda 35 UV–Vis spectrometer and was plotted against irradiation time for all the photo-catalysts.

The chosen model organic contaminants used in this study were two dyes, methyl orange and bromocresol purple and one endocrine disruptor compound, bisphenol A but the main focus was on methyl orange. Methyl orange was chosen as the major model pollutant of focus because it resembles azo dyes, which account for 60-70 % of all the dye groups that are used in the textile industry since they give out bright and high intensity colours compared to the other classes of dyes (Ghaly *et al*., 2014). The photo-catalytic activity efficiencies of the photo-catalysts were determined for each of the model pollutants and then as a mixture under UV and some under visible light. In each experiment a volume of 100 mL of 10 ppm MeO solution was used at 25 °C and pH 7 using a 9 W Osram UV lamp as the source of light (Figure 3.4, Section 3.11 in Chapter 3). The chemical structures of the model pollutants and their UV-Vis spectra measured using a 10 ppm solution on a Perkin Elmer Lambda 35 UV–Vis spectrometer are shown in Table 4.1. The maximum absorption of methyl orange (MeO)

was at 468 nm, bromocresol purple (BCP) at 586 nm and bisphenol A at 276 nm and the absorbance at these wavelengths were used for the determination of changes in concentration.

Table 4.1: Organic compounds used in photo-degradation experiments and their absorption spectrum.

Methyl Orange	Bromocresol purple	Bisphenol A
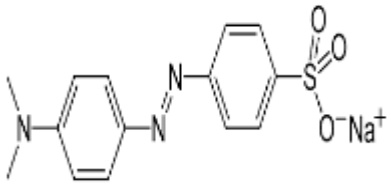	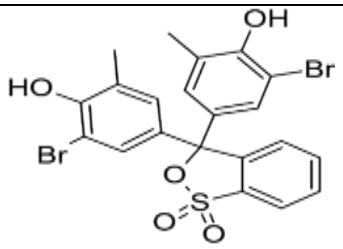	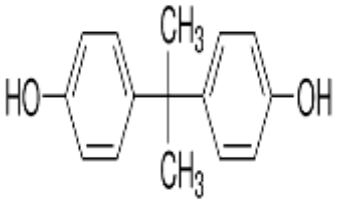
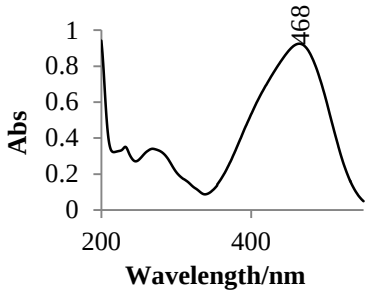	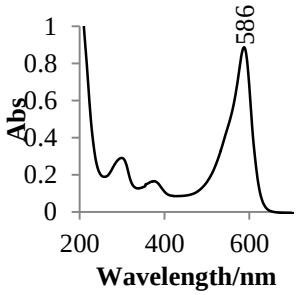	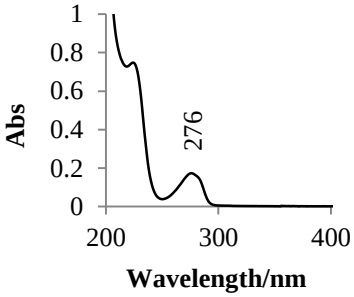

A detailed procedure for the photocatalytic activity evaluation was reported is Section 3.10.

4.3.1 Effect of film thickness

In this section, the effect of metal thickness (preparation method was reported in Section 3.2.2.1) was investigated in two settings (i) when the plasmon metal films were deposited on top of TiO_2 films supported on quartz and (ii) when the plasmon metal films were deposited underneath the TiO_2 photo-catalyst film support on quartz. The effect of loading of each metal (Au, Ag and Cu) film on the photo-catalytic activity was evaluated and compared to the pure TiO_2 photo-catalyst film. The control was the undecorated TiO_2 on MPTMS treated

quartz, the fixed parameter was the thickness of TiO_2 which was 100 nm and the variable was the thickness of the metal used to coat the TiO_2 photo-catalyst.

4.3.1.1 Effect of film thickness when metal films are deposited on top of TiO_2

Two different thicknesses of 2 nm and 5 nm were chosen from the range of samples to study the effect of metal films that were deposited on top of a 100 nm TiO_2 film on quartz treated with MPTMS. All TiO_2 photo-catalysts that were coated with plasmon metal films showed higher photo-catalytic activity than T1 (bare TiO_2) photo-catalyst as shown in Figure 4.7.

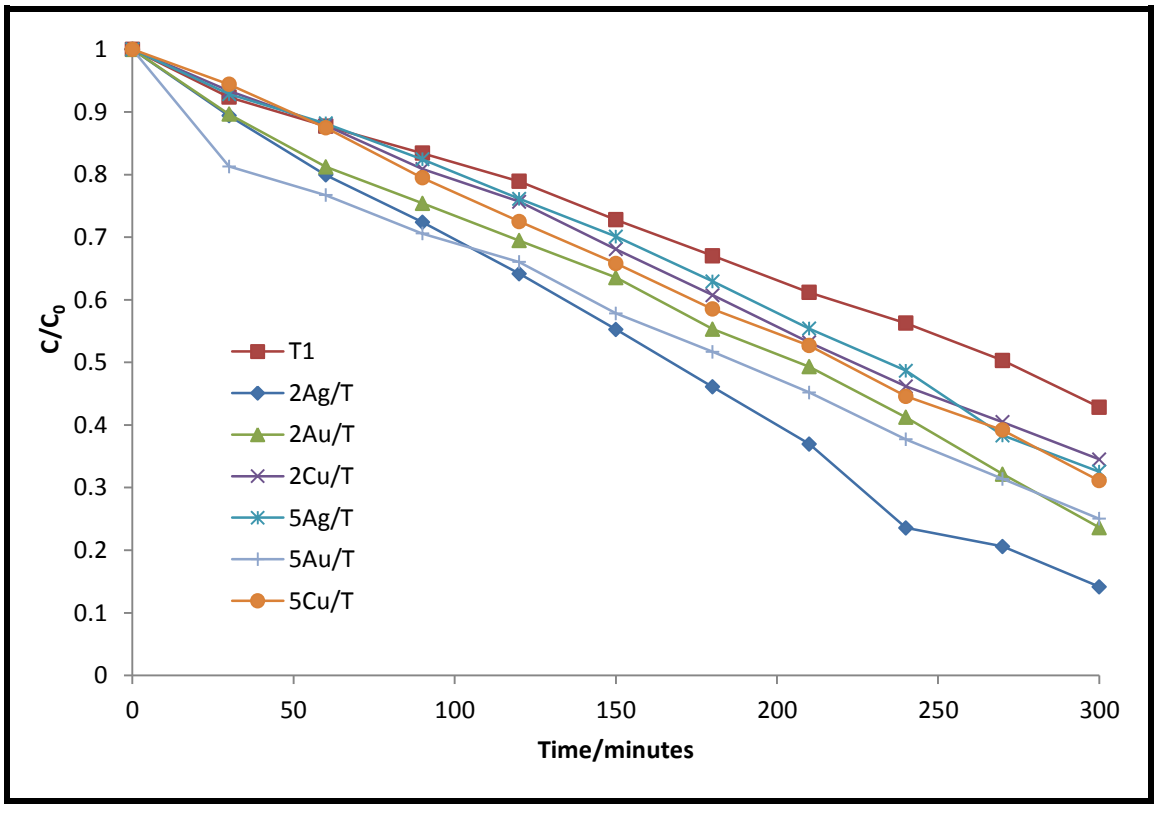

Figure 4.7: Photo-degradation profiles of 100 mL of 10 ppm methyl orange solution under UV light at 25 °C and pH 7 showing the effect of different metal thicknesses deposited on TiO_2 photo-catalyst on quartz.

There was a decrease in the photo-catalytic degradation activity of TiO_2 when the thickness of the Ag film was increased from 2 nm which showed an 85.85 % photo-degradation after 300 minutes to 5 nm which showed a 67.45 % photo-degradation for the same period of time. The reason for this 18.4 % decrease could be that, as the thickness of the Ag metal film increases, the amount of light reaching the TiO_2 photo-catalyst at the bottom is reduced resulting in reduced photo-catalytic activity. The less the metal on top the less UV light is blocked from reaching the TiO_2 surface to activate it. The decrease could also be due to the fact that the water was prevented from being oxidized or reduced at TiO_2 surface due to the thicker intervening Ag layer.

The same trend was also observed for the Au films. An increase in film thickness from 2 nm to 5 nm caused only a 1.41 % decrease in photo-catalytic activity which was not significant when compared to Ag. Although there were more AuNP on the 5 nm Au film compared to the 2 nm Au film to block light from reaching the TiO_2 photo-catalyst, the slightly bigger AuNP for the 5 nm adsorb more oxygen molecules to form reactive oxygen species as suggested by Shao *et al*., (2014), which offsets the effect of reduced light reaching TiO_2 hence there was a small difference in photo-catalytic activity when compared with the TiO_2 photo-catalyst with 2 nm Au film.

When copper was used, it showed a different trend from the Ag and Au films. There was an increase in photo-degradation from 65.50 % with a 2 nm film to 68.90 % with a 5 nm Cu film. The possible reason for this increase is that, Cu nanoparticles can easily be oxidised when exposed to air forming either CuO, Cu_2O or both since the oxides of copper are thermodynamically more stable than pure copper. These oxides are also photo-catalysts which can also participate in the photo-degradation of methyl orange.

The photo-degradation results of all the TiO_2 photo-catalysts decorated with plasmon elements of different thicknesses are summarized in Table 4.2.

Table 4.2: Photo-degradation results after 300 minutes of methyl orange (100 mL, 10 ppm) using quartz coated with 100 nm TiO_2 film decorated on top with plasmon metal films under UV light at 25 °C and pH 7.

Plasmon metal thickness on top of 100 nm TiO_2	**% Degradation of MeO under UV light**		
	Ag	**Au**	**Cu**
0 nm (control)	57.16	57.16	57.16
2 nm	85.85	76.39	65.50
5 nm	67.45	74.98	68.90

For a 2 nm metal film, Ag showed the highest activity followed by Au and lastly Cu. The reason for this trend could be that, silver has a surface that favours oxygen adsorption (Liu *et al*., 2004) hence promoting the formation of superoxide radicals which help to degrade contaminants since the reaction rate is controlled by charge transfer to O_2. For the 5 nm plasmon metal films, Au showed the highest activity and Ag showed the least among the three elements, showing that it is not just the metal type but also the layer thickness that has an effect on the activity and layer thickness had the most pronounced effect for Ag whereas for Au and Cu the effect was insignificant.

There are two possible reasons for the improved photo-catalytic activity of TiO_2 photo-catalysts decorated with metal thin films, (i) reduced electron hole recombination and (ii) the creation of the Schottky barrier. A simplified proposed mechanism for the activation, plasmon metal enhancement of TiO_2 photo-catalyst and degradation of adsorbed methyl orange is shown in Figure 4.8.

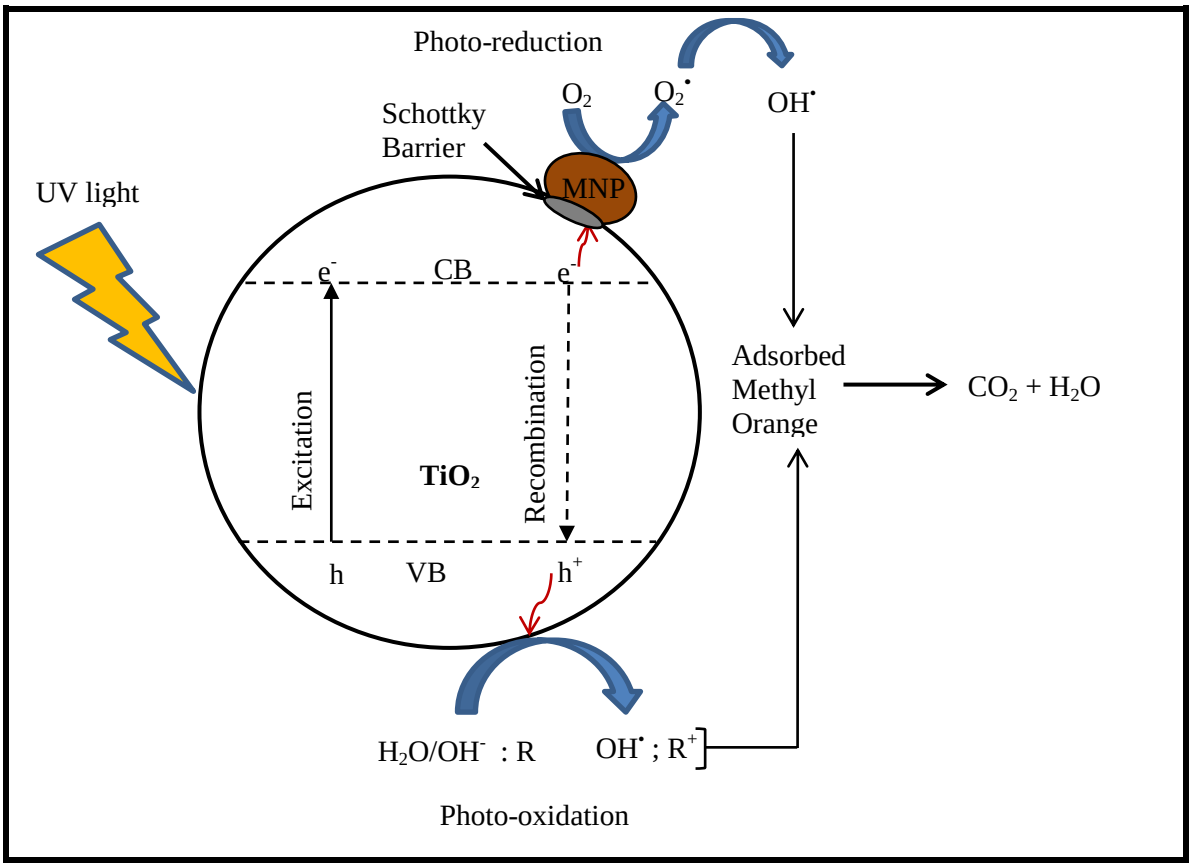

Figure 4.8: Schematic representation of the proposed mechanism of activation of TiO_2, electron trapping by metal nanoparticles (MNP) and photo-degradation of MeO under UV light.

When a metal is in contact with TiO_2, there is electron migration from TiO_2 with a low work function to the metallic nanoparticle with a high work function until their Fermi levels are aligned. The movement of electrons across the Schottky barrier leaves additional positive holes on TiO_2, which are capable of oxidizing more organic contaminants. The metal nanoparticles could also act as electron reservoirs thereby reducing electron-hole recombination.

4.3.1.2 Effect of metal film thickness when metal films are deposited underneath TiO_2

The effect of loading under this section was investigated using different metal film thicknesses of the same plasmon element deposited underneath the TiO_2 photo-catalyst film. The plasmon metal deposition procedure was reported in Section 3.2.2.1 and TiO_2 photo-catalyst deposition procedure in Section 3.3.1 in Chapter 3. The control was undecorated TiO_2 photo-catalyst, the fixed parameter was the thickness of TiO_2 film (100 nm) and the variable was the metal film thickness deposited below the TiO_2 photo-catalyst film. All the three elements (Au, Cu and Ag) were investigated separately.

(i) Effect of film thickness using silver

The procedures for the sample preparation of the silver films (5, 10, 20 and 25 nm) and 100 nm TiO_2 photo-catalysts were reported in Section 3.2.2.1 and Section 3.3.1 of Chapter 3 respectively. The sample descriptions and codes are shown in Table 3.2. Generally all the four photo-catalysts (T5Ag, T10Ag, T20Ag and T25Ag) showed higher photo-catalytic activity than pure TiO_2 photo-catalyst as shown in Figure 4.9 which implies that all Ag film thicknesses improved the photo-catalytic activity of TiO_2 photo-catalyst.

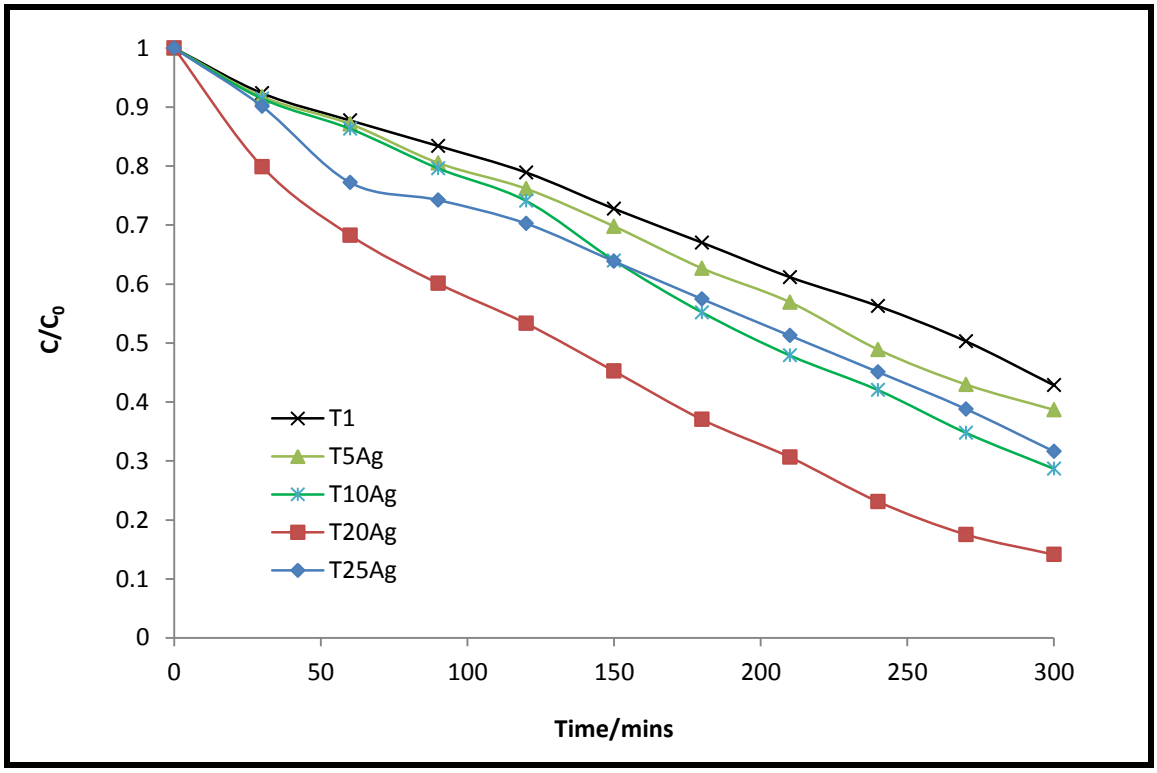

Figure 4.9: Photo-degradation profiles of methyl orange (10 ppm) using quartz coated TiO_2 photo-catalyst deposited on Ag films of different thicknesses (5, 10, 20 and 25 nm) under UV light at 25 °C and pH 7.

The reason for the observed increase in photo-catalytic activity is ascribed to the Schottky barriers formed between the TiO_2 and the Ag nanoparticles that may facilitate the transfer of electrons from TiO_2 nanoparticles with high Fermi level to silver nanoparticles which have a low Fermi level resulting in reduced electron-hole recombination rates.

There was a gradual increase in the photo-catalytic degradation of methyl orange as the film thicknesses were increased up to 20 nm. Further increase in film thickness to 25 nm caused a decrease in photo-catalytic by 16.89 % implying that 20 nm was the optimum loading for Ag. These results are summarized in Table 4.3 (page 145) and the general trend for these films is T20Ag > T10Ag > T25Ag > T5Ag > T1. The reason for this trend is that the thicker the Ag metal film, the better the displacement of the electrons to lower layers of the metal film. This

implies that there are more chances of the electrons to be far from the TiO_2 photo-catalyst layer where electron holes are confined hence the charge separation is better when compared with thin metal films. This is illustrated in the diagram shown in Figure 4.10.

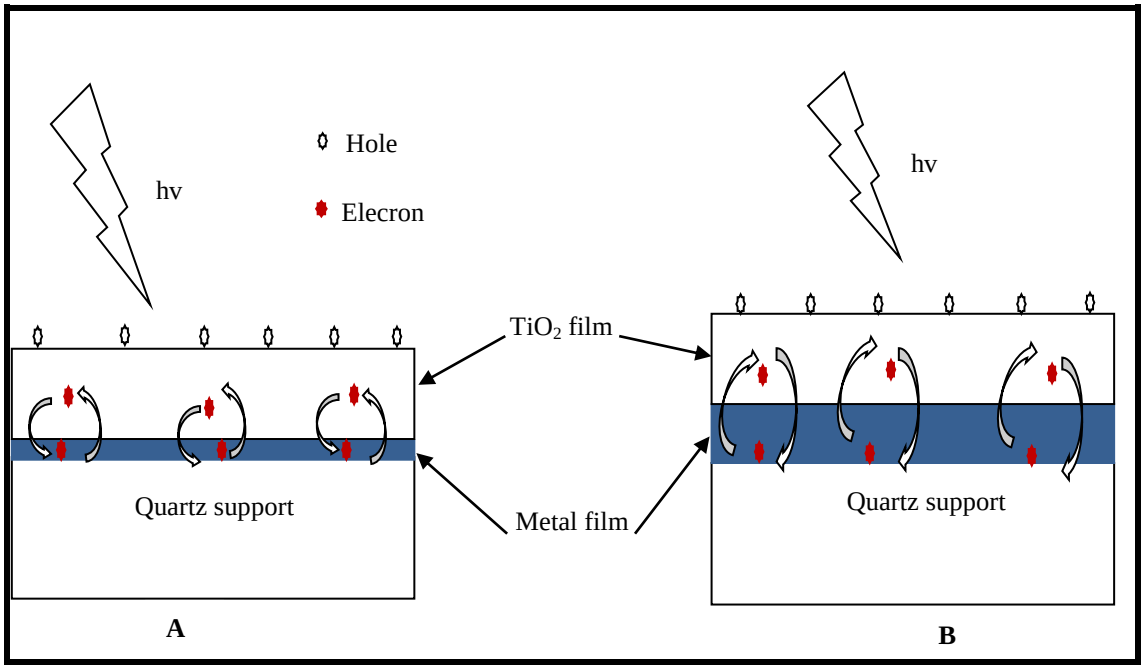

Figure 4.10: Schematic representation of the charge separation and distance of electrons from the holes for (A) a thin metal film and (B) thick metal film.

It can be seen in Figure 4.9 (B) where a thicker metal film is illustrated, the electrons have more room to travel far from the holes when compared to a case where a thin film was used. This leaves the surface of TiO_2 enriched with holes which can directly degrade methyl orange and oxidize water to produce hydroxyl radicals that degrade organics effectively.

(ii) Effect of film thickness using copper

The procedures for the sample preparation of the copper films (5, 10, 20 and 25 nm) and 100 nm TiO_2 photo-catalysts were reported in Section 3.2.2.1 and Section 3.3.1 of Chapter 3

respectively. The sample descriptions and codes (T5Cu, T10Cu, T20Cu and T25Cu) are shown in Table 3.2, Chapter 3.

Figure 4.11 shows the photo-degradation curves of methyl orange using 100 nm TiO_2 photo-catalyst film deposited on top of Cu films of different thicknesses on quartz support.

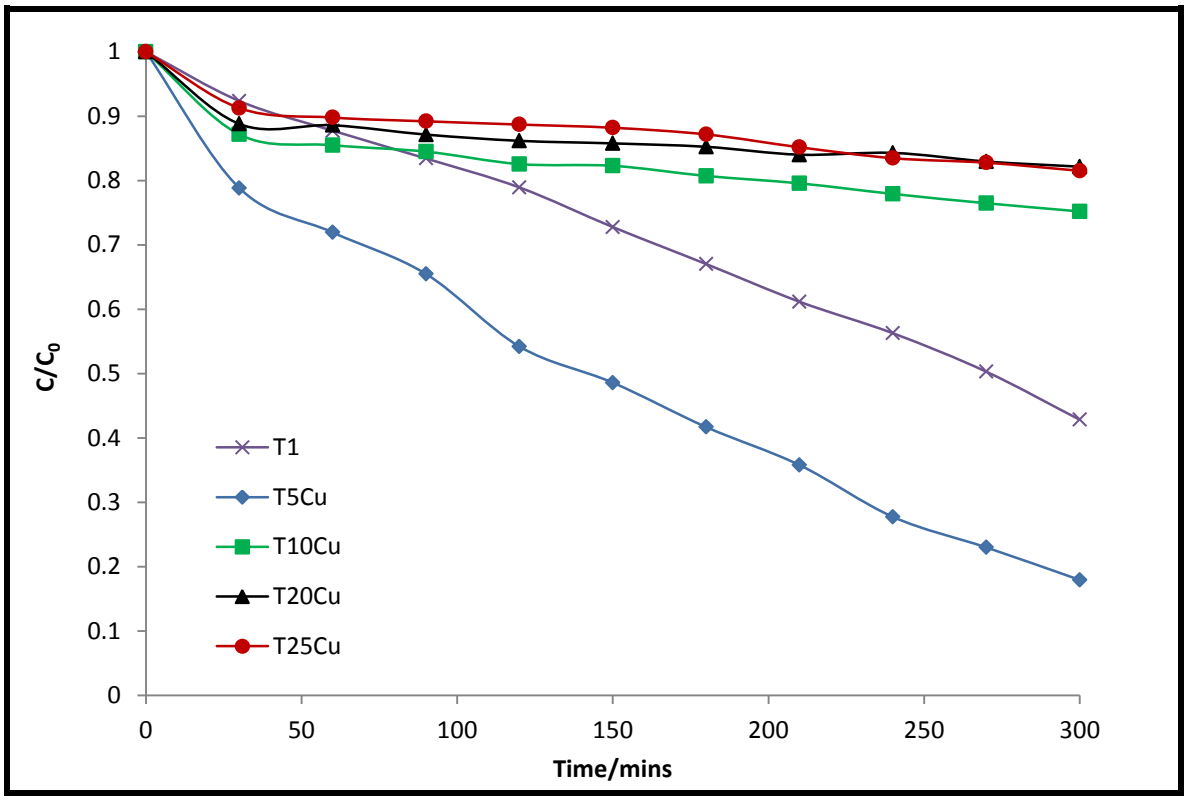

Figure 4.11: Photo-degradation curves of methyl orange using quartz coated TiO_2 photo-catalyst film deposited on top of Cu films of different thicknesses (5, 10, 20 and 25 nm) under UV light at 25 °C and pH 7.

The highest photo-catalytic activity was achieved with a 5 nm film which was the thinnest and further increase in film thickness above 5 nm had a detrimental effect on the photo-catalytic activity. The photo-catalytic activities of all the photo-catalysts with Cu film thicknesses above 5 nm were even below the photo-catalytic activity of T1 (bare TiO_2).

The better performance with a 5 nm when compared to pure TiO_2 is due to the fact that copper nanoparticles trap electrons from TiO_2 and the density of electrons increases in Cu NPs which also gives rise to a shift in plasmon. The reason for the observed trend T5Cu > T1 > T10Cu > T25Cu > T20Cu could be the presence of Cu^{2+} ions in solution due to minor leaching as detected by ICP (Table 4.8) which increased with increase in copper films thickness. These Cu^{2+} ions have been found to retard the photo-catalytic activity of TiO_2 due to, (i) the short circuiting reaction as shown in Equations (4.1) and (4.2), which cause electron-hole recombination and (ii) the deposition of Cu metal which causes reduction in light reaching TiO_2 (Dhananjeyan *et al*., 1997).

$$Cu^{2+} + e^- \longrightarrow Cu^+ + e^- \longrightarrow Cu \qquad (4.1)$$

$$Cu + h^+ \longrightarrow Cu^+ \xrightarrow{h+} Cu^{2+} \qquad (4.2)$$

There is controversy in literature on the effect of Cu^{2+} on the photo-degradation rate. Some mention an increase in photo-degradation rate until an optimum concentration (Brezova *et al*., 1995) while others mention a detrimental effect (Wei *et al*., 1992).

(iii) Effect of film thickness using gold

The procedures for the sample preparation of the gold films (5, 10, 20 and 25 nm) and 100 nm TiO_2 photo-catalysts were reported in Section 3.2.2.1 and Section 3.3.1 of Chapter 3 respectively. The sample descriptions and codes (T5Au, T10Au, T20Au and T25Au) are shown in Table 3.2, Chapter 3.

Figure 4.12 shows the photo-degradation curves of methyl orange using 100 nm TiO_2 photo-catalyst film deposited on top of Au films of different thicknesses on quartz support.

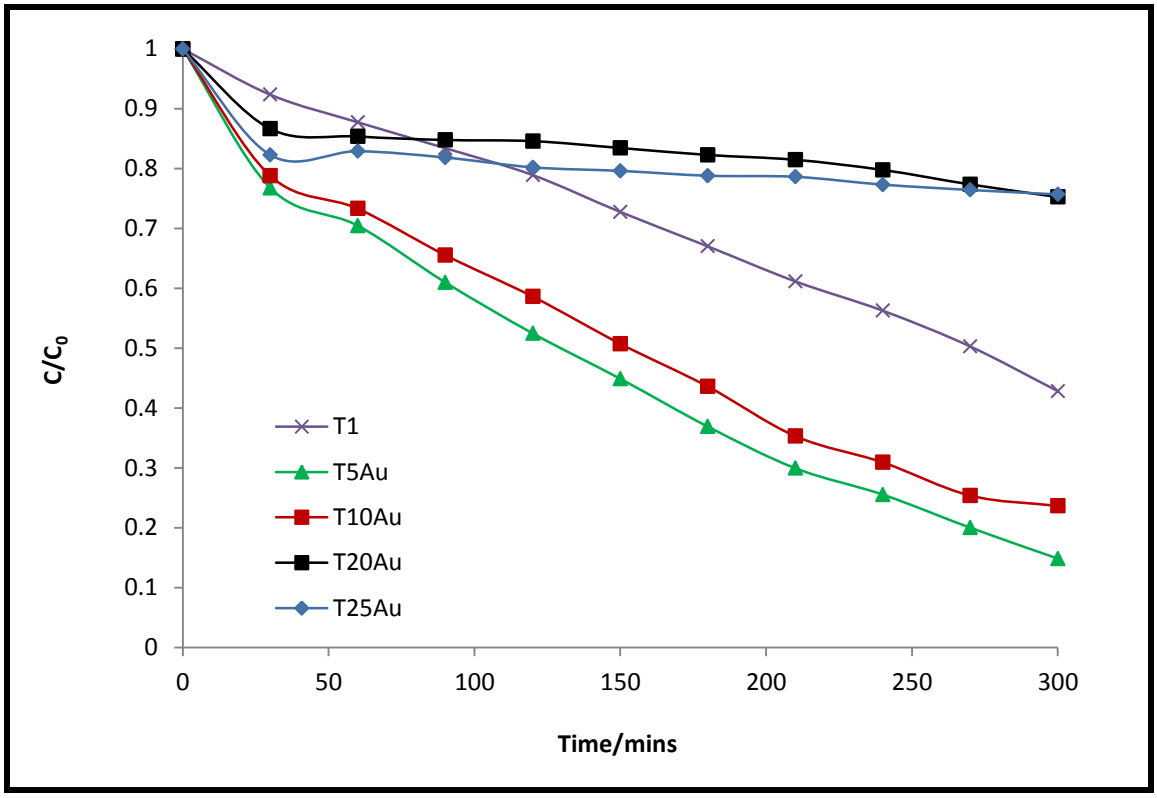

Figure 4.12: Photo-degradation curves of methyl orange using quartz coated TiO_2 photo-catalyst film deposited on top of Au films of different thicknesses (5, 10, 20 and 25 nm) under UV light at 25 °C and pH 7.

Gold films of 5 nm and 10 nm showed good enhancement of photo-catalytic activity of TiO_2 whereas the 20 nm and 25 nm films showed a deactivation of the TiO_2 photo-catalyst. The general trend followed was T5Au > T10Au > T1 > T20Au > T25Au that is, as the Au film thickness was increased beyond an optimum of 5 nm, there was a decrease in the photo-catalytic activity of TiO_2. The reasons for the improvement of photo-catalytic activity caused by the 5 nm and 10 nm Au films could be the same as those given previously for copper i. e the formation of Schotty barriers. The change in Au thickness from 10 nm to 20 nm showed significant decrease in photo-catalytic activity from 76.34 % after 300 minutes to 24.74 % respectively. Further increase in Au thickness from 20 nm to 25 nm did not show a significant change in photo-catalytic activity as the decrease was only 0.44 %. The reason for

the observed trend of decrease in photo-catalytic activity of TiO_2 with increase in metal films could be the reduced work function of the metal film. It has been reported that the work function of a metal film decreases with an increase in film thickness (Hornaner *et al*., 1989).

4.3.1.3 Comparison of the effect of Cu, Au and Ag on TiO_2 photo-activity

This section summarizes the results for the samples prepared as given in Section 3.2.2.1 and makes a comparative evaluation of the effect of using different plasmon metals on the photo-catalytic activity of TiO_2 towards methyl orange solution. The samples that were compared were T5Au, T10Au, T20Au, T25Au T5Ag, T10Ag, T20Ag, T25Ag T5Cu, T10Cu, T20Cu and T25Cu. The control was the pure TiO_2 photo-catalyst film on quartz, the fixed parameter was the metal thickness, and the variable was the type of the plasmon metal used.

The percentage photo-degradation of methyl orange using TiO_2 photo-catalyst on top of different plasmon metals layers are shown in Table 4.3. Results from the same plasmon metal thickness are compared in terms of the percentage increase relative to the TiO_2 photo-catalyst without a metal film.

Table 4.3: Percentage degradation of methyl orange using TiO_2 photo-catalyst on different metal films of different thicknesses.

Photo-catalyst	**% of Methyl orange photo-degraded after 300 minutes**			**% Increase relative to pure TiO_2 photo-catalyst**		
	Au	**Ag**	**Cu**	**Au**	**Ag**	**Cu**
TiO_2 on 0 nm	57.16	57.16	57.16	-	-	-
TiO_2 on 5 nm	85.13	61.33	82.04	+27.97	+4.17	+24.86
TiO_2 on 10 nm	76.34	71.32	24.80	+19.18	+14.16	-32.36
TiO_2 on 20 nm	24.74	85.27	17.84	-32.42	+28.11	-39.32
TiO_2 on 25 nm	24.30	68.38	18.48	-32.86	+11.22	-38.68

It can be seen from Table 4.3 that for a 5 nm metal film, the highest enhancement of 27.97 % was achieved by Au followed by copper (24.86 %) and lastly silver (4.17 %). For a 10 nm metal film, gold still showed the highest enhancement followed by silver. Copper showed no improvement but inactivation of the photo-catalyst occurred when compared to TiO_2 photo-catalyst with no metal film underneath. For 20 nm and 25 nm metal films, both gold and copper had a negative impact on the photo-catalytic activity while silver improved it by 11.22 %. The optimum loading for Au and Cu was 5 nm and for Ag it was 20 nm, which gave the best overall enhancement to the TiO_2 photo-catalysts deposited on metal films. Generally Cu gave the lowest enhancement to TiO_2 photo-catalyst probably because the Cu nanoparticles forming the film were not polydisperse (Figure 4.2 E) when compared to Ag and Au nanoparticles (Figure 4.2 B and Figure 4.2 C respectively).

4.3.2 Effect of order of metal deposition

This section presents an evaluation of the effect of order of deposition of metal films relative to TiO_2 to determine the best position (top or bottom) for the enhancement of photo-catalytic activity of TiO_2 towards organic contaminants for each plasmon metal (Au, Cu and Ag).

The effect of order of deposition was determined by depositing a thin film of noble metal on top of the quartz supported TiO_2 photo-catalyst and in the other case underneath the TiO_2 photo-catalyst as shown previously. The control was pure TiO_2, the variable was the position of the plasmon metal relative to TiO_2 photo-catalyst and the fixed parameters were the type of plasmon metal and film thickness. Each plasmon metal was evaluated separately. The choice of using very thin films of 2 nm and 5 nm on top of TiO_2 was based on the view of trying to minimize leaching of the noble metal nanoparticles (MNP) into the water as they would be in direct contact with water. When TiO_2 is deposited on metal nanoparticles, there

are two advantages that favour photo-catalysis and these are (i) reduced leaching of metal nanoparticles, and (ii) prevention of metal oxidation as TiO_2 acts as a protective layer for the MNP.

Table 4.4 shows the percentage photo-degradation of methyl orange using TiO_2 photo-catalyst when the plasmon metal was deposited either on top of the photo-catalyst or when the plasmon metal was deposited below the photo-catalyst.

Table 4.4: Percentage degradation of methyl orange under UV light using TiO_2/plasmon MNP films with different orders of deposition.

Plasmon element & thickness	**% Degradation of MeO under UV light**		**% Change when metal film was on top instead of underneath TiO_2**
	Metal film on top of TiO_2	**Metal film underneath TiO_2**	
2 nm Ag film	85.85	68.38	+17.47
5 nm Ag film	67.45	61.33	+6.12
2 nm Au film	76.39	82.07	-5.68
5 nm Au film	74.98	85.13	-10.15
2 nm Cu film	65.50	60.85	+4.65
5 nm Cu film	68.90	82.04	-13.14

The results presented in Table 4.4 are discussed in the following sections.

When a 2 nm or 5 nm film of a noble metal element Ag was deposited either on top or at the bottom of the TiO_2 photo-catalyst, there was better photo-catalytic activity in both cases when compared to pure TiO_2. A 2 nm Ag film deposited on top of TiO_2 photo-catalyst showed 85.85 % degradation of methyl orange after 300 minutes but when the 2 nm Ag film was deposited at the bottom of the TiO_2 photo-catalyst, there was a decrease in photo-

catalytic activity to 68.38 % which was still higher than TiO_2 film on its own. The same trend was also observed when the order of deposition was changed for the 5 nm Ag film but the change was insignificant (6.12 %) as shown in Table 4.4. The reasons for better performance of Ag in enhancing TiO_2 photo-catalytic activity when deposited on top for both films rather than when it is deposited below TiO_2 could be: (i) Ag absorbs in the UV region hence it created LSPR which boosted excitation of electrons in TiO_2 (Hedayati *et al*., 2014) and (ii) the oxidation of silver into silver oxide (silver slightly oxidizes to AgO, according to Dang *et al*., 2011). The resulting oxide can participate in the photo-degradation of methyl orange. The formation of the oxide is supported by the appearance of a minor peak at 2θ 33.4° which was assigned to the silver oxide (Ag_2O) in the XRD spectrum (Figure 4.4) implying that some part of the deposited Ag was oxidized but not to a great extent as can be observed from the intensity of the peak which was relatively lower.

There was better photo-catalytic activity when a gold film was deposited underneath the TiO_2 photo-catalyst for both the 2 nm and 5 nm Au films than when deposited on top of TiO_2. The reason for this could be that there was a reduction in surface area of TiO_2 when the gold metal film was on top and some active sites were covered by gold. This could have resulted in reduced contact between the pollutant and TiO_2 photo-catalyst surface during photo-degradation. When the metal was below the TiO_2 photo-catalyst, the Schottky barriers between the gold nanoparticles and the TiO_2 facilitated the movement of electrons from surface layer to the bottom layer leaving the holes on the surface resulting in reduced electron-hole recombination rates. This made the surface layer rich in positive holes which oxidize water to produce hydroxyl radicals which degrade the methyl orange effectively resulting in enhanced photo-catalytic activity.

The 2 nm Cu film increased TiO_2 photo-catalytic activity more when it was deposited on top of TiO_2 than when it was deposited below TiO_2 photo-catalyst. The reason for this could be that Cu can easily be oxidised when exposed to air forming its oxides which can participate in photo-degradation. The Cu_2O and CuO are p-type semiconductors with narrow band gaps of 1.2 eV and 2.2 eV respectively (Qu *et al*., 2012). The formation of the oxides is evidenced by the appearance of three peaks arising from the oxides in the XRD spectra (Figure 4.4). The results of the above findings on the effect of the order of deposition for all the three plasmon elements under study are summarized in Table 4.4.

4.3.3 Effect of using a bilayer or three noble metal films

Instead of using one noble metal film, two or three different noble metal films were deposited layer by layer. The combinations used were (i) Ag/Au, (ii) Au/Cu, (iii) Ag/Cu and (iv) Ag/Au/Cu. For the bimetallic layers, each metal was 5 nm thick to give a total of 10 nm film for both metals underneath the TiO_2 photo-catalyst. This was done so that the observed effect comes from different combinations and not the metal loading. The use of the bilayer/bimetallic metal films was compared to the monolayer of the same thickness. Table 4.5 shows the samples that were prepared where TiO_2 photo-catalyst films were deposited on two or three different plasmon metal films on quartz support as previously presented in Section 3.2.2.1 and Section 3.3.1. The metals that were in contact with TiO_2 as well as the metals that were in contact quartz support are shown in Table 4.5.

Table 4.5: Metal film positions in TiO_2 photo-catalysts deposited on top of bimetallic layers or three metal films on quartz support.

Sample	**Metal thickness underneath TiO_2 film on quartz**			**Metal in contact with quartz**	**Metal in contact with TiO_2**
	Au	Cu	Ag		
TiO_2 on Cu/Ag	-	5 nm	5 nm	Ag	Cu
TiO_2 on Au/Ag	5 nm	-	5 nm	Ag	Au
TiO_2 on Cu/Au	5 nm	5 nm	-	Au	Cu
TiO_2 on Au/Ag/Cu	~3.3 nm	~3.3 nm	~3.3 nm	Cu	Au

All combinations used to modify the TiO_2 photo-catalyst showed great improvement in the photo-degradation of methyl orange under UV light as shown in Figure 4.13. The highest enhancement of photo-catalytic activity of 29.10 % relative to bare TiO_2 was observed when all the three plasmon elements were used. The order of enhancement observed was Au/Ag/Cu > Au/Cu > Au/Ag > Ag/Cu.

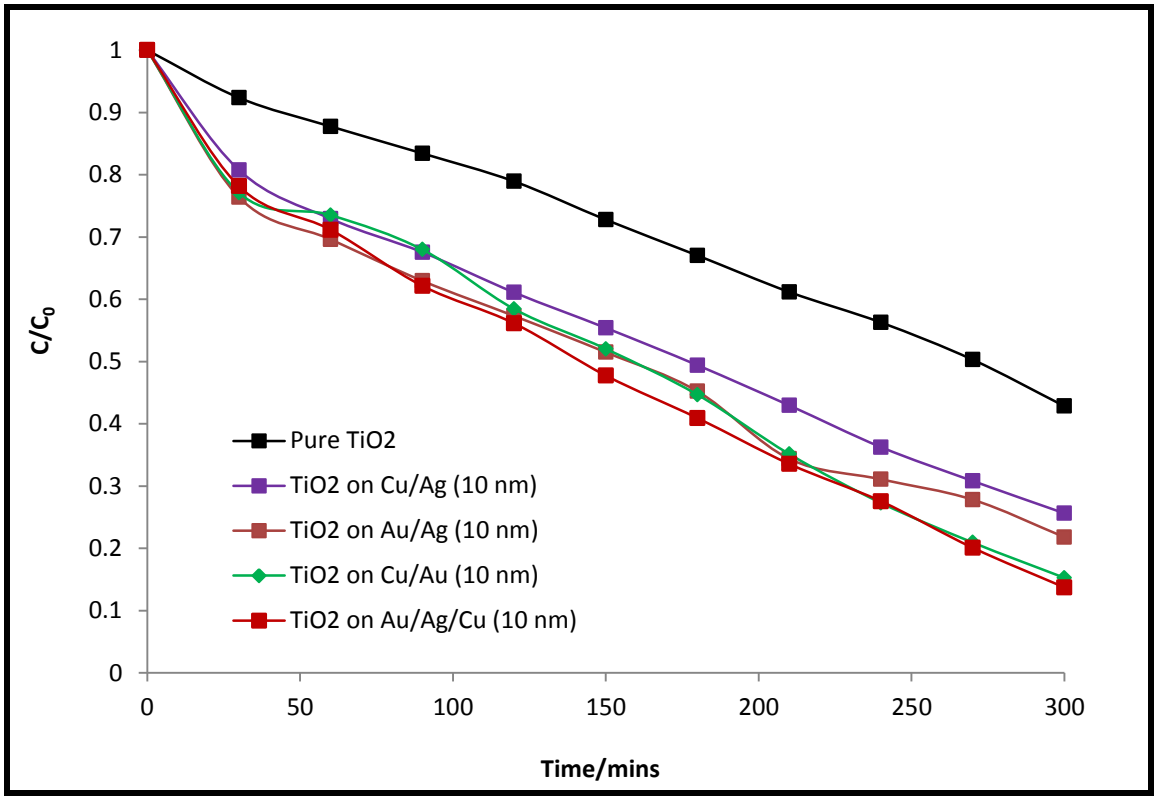

Figure 4.13: Photo-degradation curves of methyl orange using TiO_2 photo-catalyst deposited on top of a bilayer and three plasmon metal component system of 10 nm thick under UV light at 25 °C and pH 7.

When compared with TiO_2 photo-catalyst deposited on top of metal monolayers of the same thickness, all the bimetallic and the three component system showed an enhancement of TiO_2 photo-catalytic activity and the summary of the results are shown in Table 4.6. The general trend was; three component system > bilayer system > monolayer system. This shows that bimetal or three metals combined worked synergistically and performed better than the use of a single metal since the metals can augment one another. Also the high conductivity of these metals allows electrons to flow away from the region of contact with the photo-catalyst thereby reducing electron-hole recombination rate.

Table 4.6: Photo-degradation results and percent increase of TiO_2 photo-catalyst deposited on top of monolayer, bilayer and a three component system supported on quartz.

Photo-catalyst	% of Methyl orange photo-degraded after 300 minutes	% Increase relative to pure TiO_2 photo-catalyst
TiO_2 with no metal film	57.16	-
TiO_2 on Au (10 nm)	76.34	+19.18
TiO_2 on Ag (10 nm)	71.32	+14.16
TiO_2 on Cu (10 nm)	24.80	-32.36
TiO_2 on Cu/Ag (10 nm)	74.36	+17.20
TiO_2 on Au/Ag (10 nm)	78.19	+21.03
TiO_2 on Cu/Au (10 nm)	84.72	+27.56
TiO_2 on Au/ Ag/Cu (10 nm)	86.26	+29.10

When two metals whose work functions are different are brought into contact, charge transfer occurs whereby electrons flow from the metal with higher Fermi energy to that with lower Fermi energy. In this case the order of the work functions is $\varphi_{Au} > \varphi_{Cu} > \varphi_{Ag} > \varphi_{TiO_2}$, hence electrons were flowing to the metal from the semiconductor on contact. In a bilayer system, there are more than two contacts (TiO_2/metal, metal/metal and metal/quartz support) resulting in more than two Schottky barriers being formed which promote efficient electrons transfer from the photo-catalyst. This could have caused the observed enhanced photo-catalytic activity of TiO_2 by bilayer or trimetallic metal films.

4.4 Effect of organics and salts on photo-degradation of methyl orange

Real water systems that are found in the environment are quite complex meaning that they are not contaminated by only one pollutant but several organics and several dissolved salts. The water that comes from the dye industries contain several dyes and some dissolved salts such as sodium sulphate, sodium chloride and sodium nitrate which are added in the dyeing

process to help the dyes adhere to the cloth. It has been estimated that the mass of the salts used can make up to 20 % of the weight of the fiber (EPA, 1997). For instance between 0.6 to 0.8 kg of sodium chloride are added to 150 L of water when dyeing a kilogram of cotton cloth (Allegre *et al*., 2006). Formaldehyde is an example of one of the organic compounds that are used in the dyeing process to assist the dyeing of polyester fibers to yield greater colour value and brightness. These may strongly influence the efficiency and the rate of photo-degradation of methyl orange thus it is necessary to study the performance of the photo-catalysts when the water contains more than one organic contaminant and salts that are added in the dye bath so that their disturbances on the operation of TiO_2 based treatment process are minimized.

4.4.1 Effects of salts

The presence of inorganic ions in the water to be treated is expected. The combined effects of three salts; sodium chloride, sodium sulphate and sodium nitrate were studied. The final concentration of each salt in the photo-degradation solution was 8.0×10^{-5} M as previously reported in Section 3.11.2. T5Au was chosen as it showed high photo-catalytic activity towards pure methyl orange. The same procedure for photo-degradation of pure methyl orange as previously reported in Section 3.11 was used.

Figure 4.14 shows the photo-degradation curves of methyl orange using T5Au photo-catalyst in the presence of salts and formaldehyde under UV light at 25 °C and pH 7.

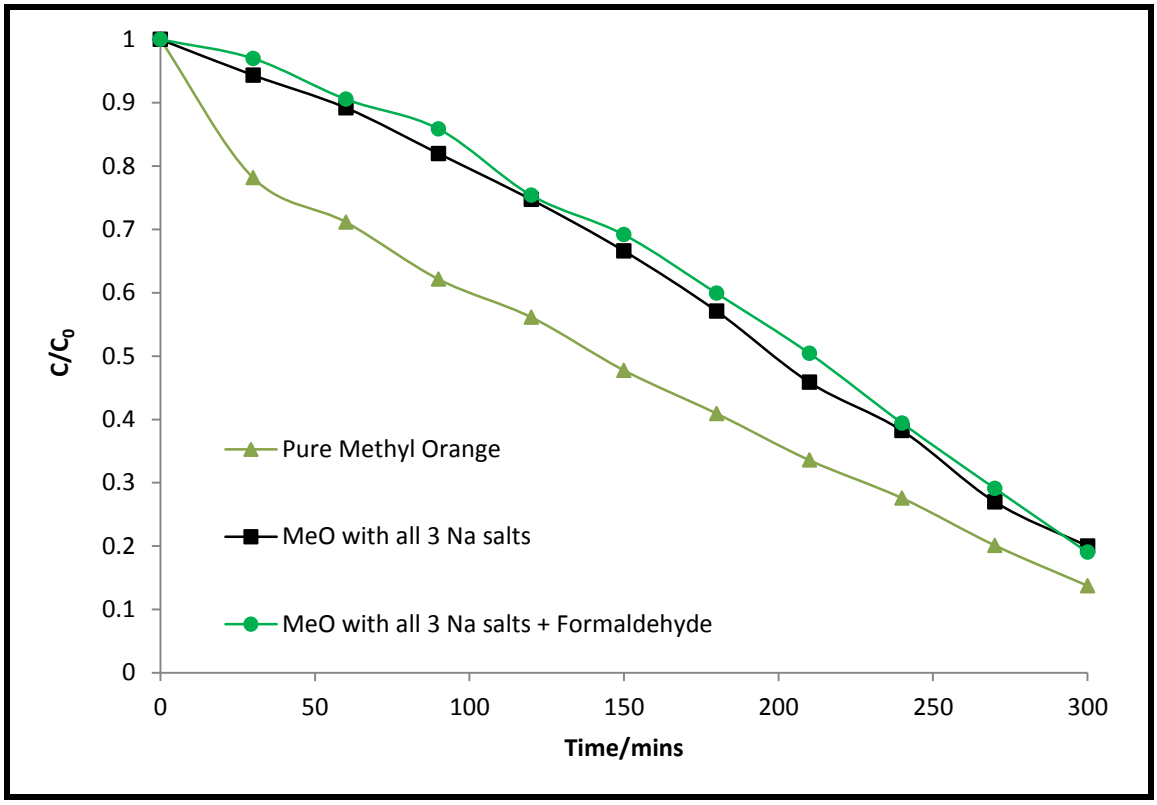

Figure 4.14: Photo-degradation curves of methyl orange using T5Au photo-catalyst in the presence of salts and formaldehyde under UV light at 25 °C and pH 7.

The addition of the salts was found to decrease the photo-catalytic activity of the photo-catalyst by 6.24 % from 86.26 % for pure methyl orange to 80.02 % for methyl orange with added salts. The decrease in photo-catalytic activity of T5Au photo-catalyst was probably due to two reasons: (i) the preferential adsorption of the Cl^- displacing the hydroxyl ions on the photo-catalyst surface (Chong *et al*., 2010) and (ii) radical scavenging effect of the Cl^- and SO_4^{2-} ions. The mechanism of the scavenging effect of the Cl^- ions is shown in equations 4.3 and 4.4 (Matthews & McEnvoy., 1992).

$$Cl^- + OH^{\cdot} \longrightarrow Cl^{\cdot} + OH^- \qquad 4.3$$

$$Cl^- + h^+ \longrightarrow Cl^{\cdot} \qquad 4.4$$

It can be observed from Figure 4.14 that the addition of formaldehyde slightly offset the decrease in photo-catalytic activity caused by salts in methyl orange photo-degradation. There was a slight increase of about 0.96 % from 80.02 % when only salts are added to 80.98 % when formaldehyde was added together with salts in the reactor system.

4.4.2 Effect of Bisphenol A on methyl orange photo-degradation

This section presents the evaluation of the effect of bisphenol A on methyl orange photo-degradation using T1 photo-catalyst film supported on quartz. Two different mixtures of the two organics were used (50 % v/v of each compound and 67 % methyl orange with 33 % bisphenol A) as previously reported in Section 3.11.1. The same procedure for the photo-degradation of pure methyl orange was used as previously reported in Section 3.11. The control experiment was the photo-degradation of 100 mL of 10 ppm pure methyl orange, the variable was the amount of bisphenol A added to methyl orange solution and the fixed parameters were the concentration of methyl orange, pH (7) and the type of photo-catalyst used. In the same experiment, the selectivity of the photo-catalyst for each contaminant over the other was also determined.

Figure 4.15 shows the effect of bisphenol A on the rate of photo-degradation of methyl orange and also the effect of methyl orange on the photo-degradation of bisphenol A using T1 photo-catalyst supported on quartz.

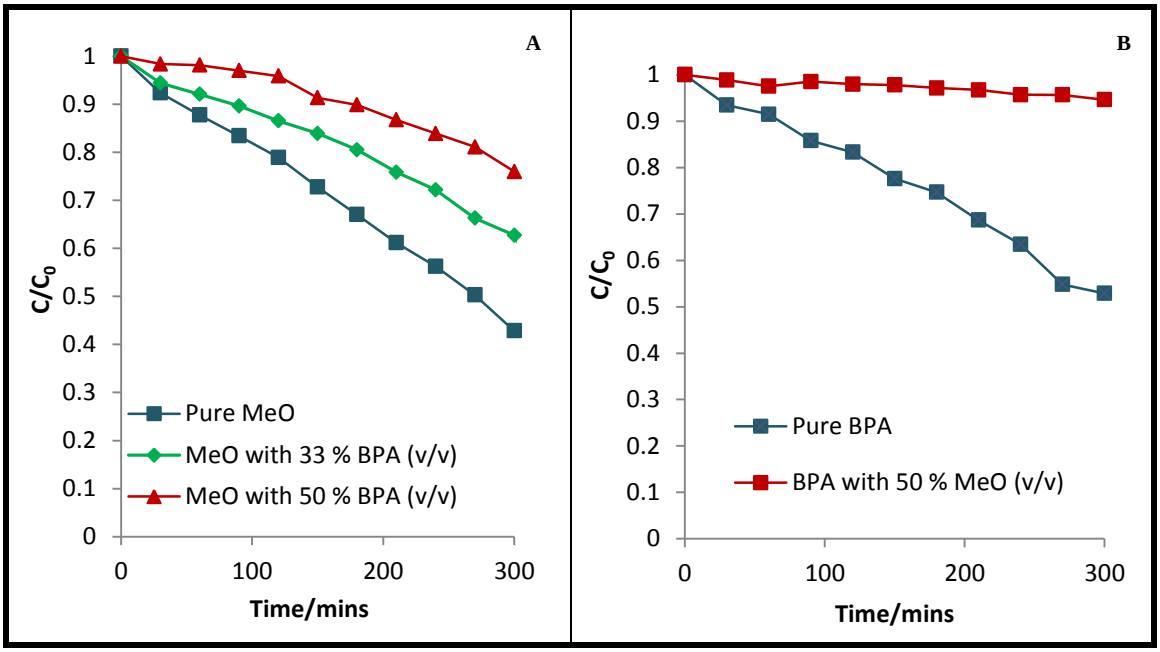

Figure 4.15: Photo-degradation of (A) MeO in the presence of BPA and (B) BPA in the presence of MeO using T1 photo-catalyst on quartz under UV light at 25 °C and pH 7.

After 300 minutes, 57.16 % of 100 mL of 10 ppm pure methyl orange (not mixed with BPA) had been photo-degraded and 47.10 % of pure BPA (100 mL, 10 ppm) was photo-degraded using the TiO_2 photo-catalyst film on quartz but when MeO and BPA were mixed, the photo-degradation rates of both contaminants decreased. When a 1:1 ratio v/v of methyl orange and BPA was used, 24 % of MeO was degraded while only 5.38 % of BPA was degraded showing a 33.16 % and 41.72 % decrease respectively. As the amount of bisphenol A added to MeO was increased from 33 % to 50 % v/v, the rate and amount of methyl orange photo-degraded also decreased from 37.27 % to 24.0 %. This shows that when there is more than one pollutant in water, the rate of photo-degradation of each pollutant is reduced and some are preferred more than the others and in this case the photo-catalyst was more selective on methyl orange than BPA. They were not degraded to the same extent even when the same concentrations and volumes were used. There are three possible reasons for such selectivity and these are: (i) MeO orange has a higher molar absorption coefficient than BPA hence its

rate of degradation will be higher, (ii) MeO could have been more adsorbed on the photo-catalyst than BPA. A contaminant needs to be in contact with the catalyst for it to be degraded hence if it is adsorbed more readily then, it blocks/reduces the adsorption sites for other species in this case BPA. Bhatkhnade *et al*., (2004), discovered that organic substrates with electron- withdrawing nature were found to strongly adhere and were more susceptible to direct oxidation than those with electron donating groups. MeO has more electron withdrawing groups than BPA, (iii) the azo bonds in the azo compounds are active and are easily degraded. Mozia *et al*., (2005) reported that azo bonds were the most active in azo-dye molecules hence would be susceptible to attack by positive holes and hydroxyl radicals.

4.4.3 Effect of bromocresol purple on methyl orange photo-degradation

This section presents the evaluation of the effect of bromocresol purple on methyl orange photo-degradation using TiO_2 photo-catalyst deposited on a trimetallic layer of Au, Cu and Ag on quartz. A 100 mL of a mixture of methyl orange (20 ppm) and bromocresol purple (20 ppm) was used in the study as previously reported in Section 3.11.1. The control experiment was the photo-degradation of pure unmixed methyl orange and the fixed parameters were the type of the photo-catalyst used, pH (7) and volume of the solutions used in the experiments.

The photo-degradation curves of (i) pure/unmixed methyl orange, (ii) pure/unmixed bromocresol purple and (iii) a mixture of methyl orange and bromocresol purple (BCP) using TiO_2 photo-catalyst deposited on a trimetallic layer of Au, Ag and Cu on quartz support under UV light at 25 °C and pH 7 are shown in Figure 4.16.

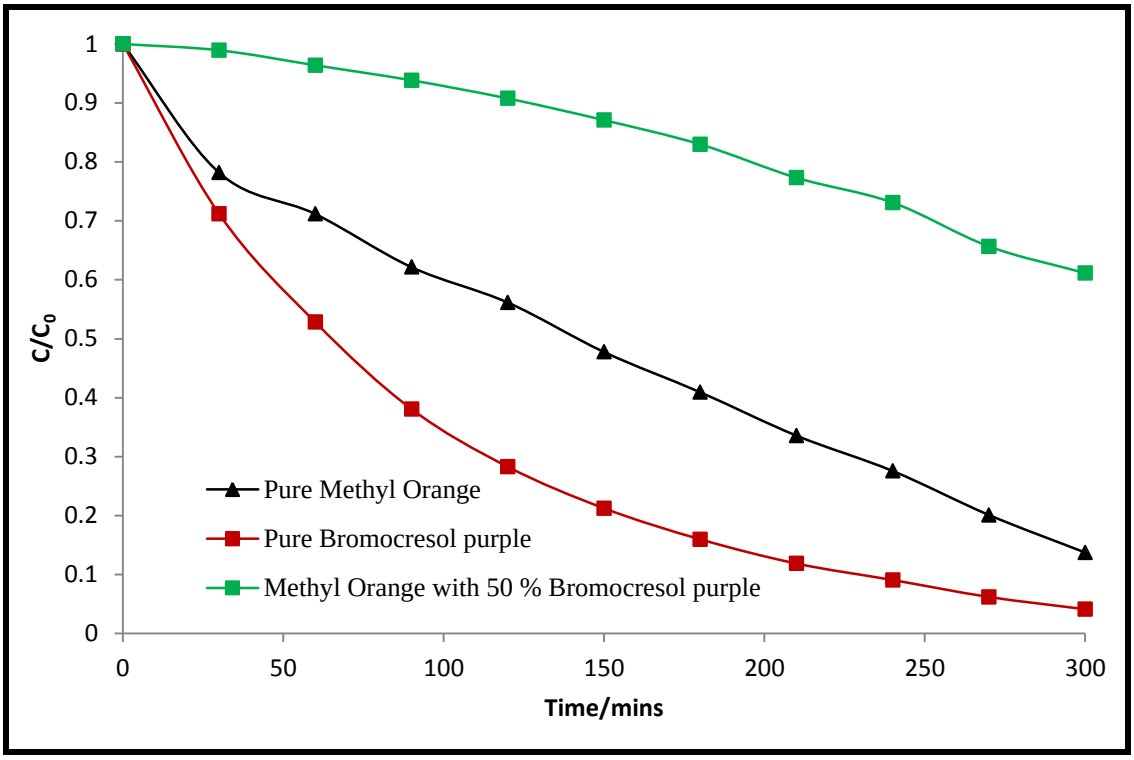

Figure 4.16: Photo-degradation curves of methyl orange, bromocresol purple and a mixture of the two dyes using TiO_2 photo-catalyst deposited on top of trimetallic layer (Au, Ag and Cu) under UV light at 25 °C and pH 7.

After 300 minutes 38.62 % of MeO was degraded when mixed with BCP but when it was pure or unmixed with BCP, 86.26 % was degraded. This shows that bromocresol purple was preferred over MeO and selectively degraded by the TiO_2 photo-catalyst deposited on trimetallic layer. The reason for this selectivity could be the preferential adsorption of bromocresol purple on the TiO_2 surface since it has more electron withdrawing groups than methyl orange. The more the electron withdrawing groups on a compound, the more it adheres strongly to TiO_2 and gets oxidised **(**Bhatkhnade *et al*., 2004).

The selectivity of the photo-catalyst towards BCP is also shown in Figure A.1 in Appendix A. Since absorbance is directly proportional to concentration, the rate of BCP photo-

degradation was higher than that of MeO as shown by the rate of decrease in absorbance at their λ_{max} of 586 nm and 468 nm respectively.

The calculated rate constant of the photo-degradation of pure MeO after 300 minutes was 1.98 min^{-1}, which was reduced to 0.49 min^{-1} when photo-degradation occurred in the presence of BCP as shown Figure 4.17.

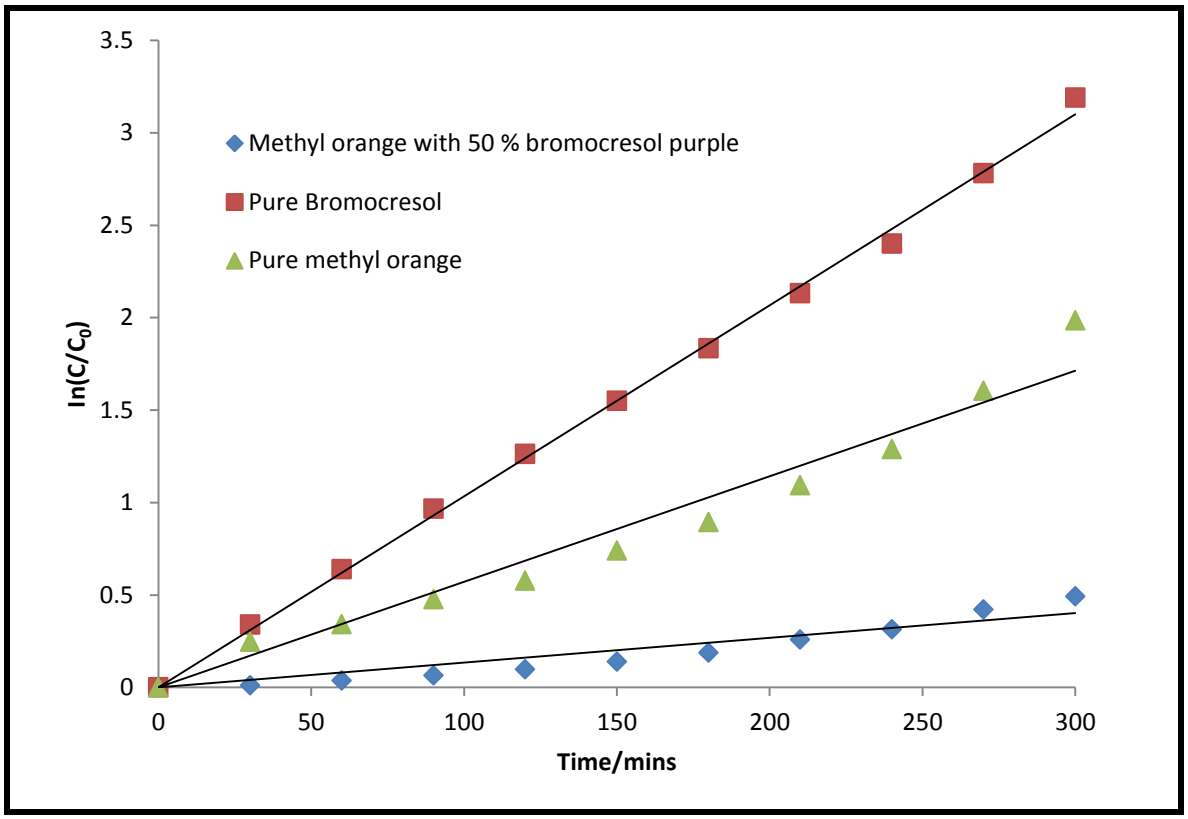

Figure 4.17: Kinetics of the photo-degradation of methyl orange, bromocresol purple and a mixture of the two dyes using TiO_2 photo-catalyst deposited on trimetallic layer (Au, Ag and Cu).

The rate constant of BCP photo-degradation when mixed with methyl orange was 2.38 min^{-1} which was quite higher than that of MeO meaning it was degraded faster than MeO. The presence of BCP had a significant negative impact on the photo-degradation of MeO. On the

other hand the presence of MeO had an insignificant effect on the photo-degradation of BCP (Figure 4.16) since the rate constant of BCP changed from 3.19 min^{-1} when pure (not mixed with MeO) to 2.38 min^{-1} (Δ = -0.81 min^{-1}) when mixed with MeO and the percentage degradation after 300 minutes changed from 95.88 % to 94.25 % (Δ = -1.63 %).

4.5 Effects of selected operational parameters on photo-catalysis

The photo-catalytic reaction rate and efficiency of a photo-catalytic system is dependent on several operational parameters and these include wavelength of light used, dissolved oxygen, pH, temperature, TiO_2 loading, contaminant concentration and light intensity used in the photo-catalytic process. These parameters govern the kinetics of the photo-degradation process. To study the effect of one parameter, the other operational parameters were kept constant. In this study only two operational parameters (contaminant concentration and pH) were selected and evaluated.

4.5.1 Effect of initial concentration

This section presents the evaluation of the effect of initial concentration of methyl orange using T1 photo-catalyst film on quartz. The detailed procedure was presented in Section 3.11 and the experimental setup in Figure 3.4. The variable was the concentration of the methyl orange solution and the fixed parameters were temperature, pH, light intensity, photo-catalyst loading and volume of the methyl orange solution.

Figure 4.18 shows the photo-degradation curves of methyl orange solutions of different concentrations (3.27, 5 and 10 ppm) using T1 photo-catalyst on quartz at 25 °C and pH 7 under UV light.

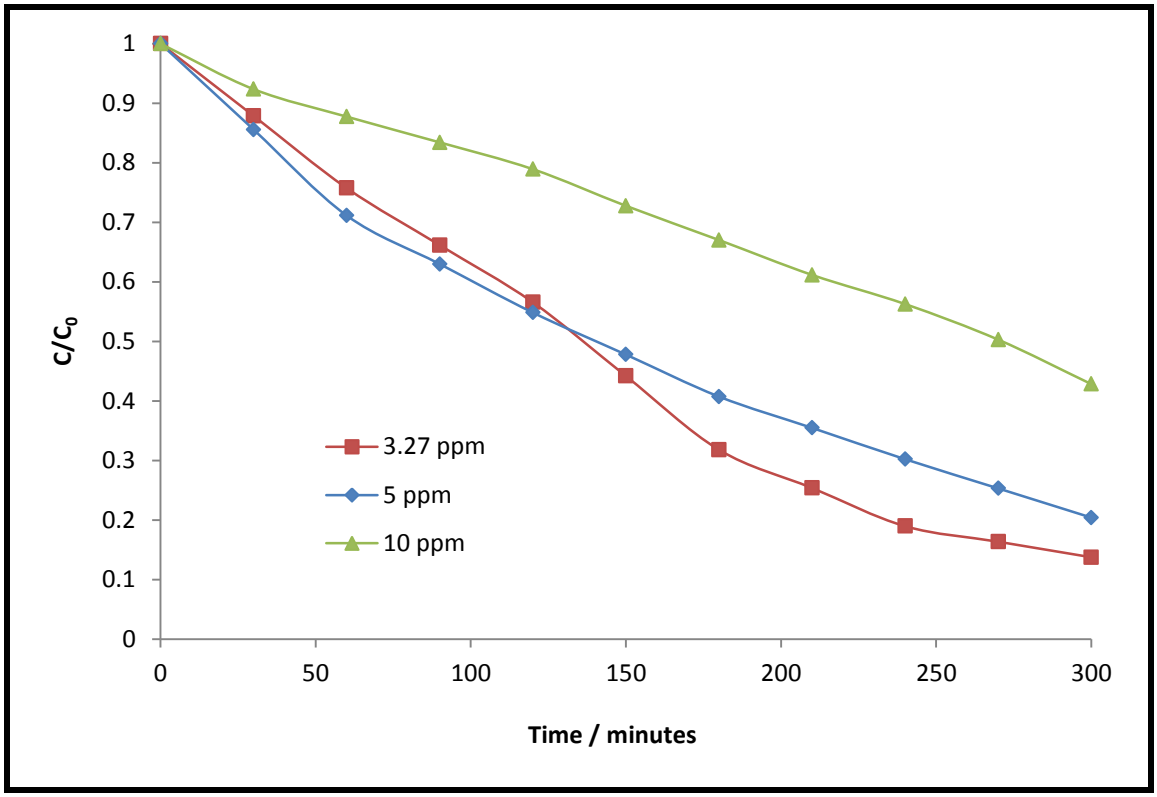

Figure 4.18: Photo-degradation curves of methyl orange solutions of different concentrations (3.27, 5 and 10 pmm) using T1 photo-catalyst on quartz under UV light at 25 °C and pH 7.

The initial concentration of methyl orange was found to affect the rate of photo-degradation. The rate constants for MeO photo-degradation were 0.848, 1.589 and 1.984 min^{-1} when using a 10 ppm, 5 ppm and 3.37 ppm MeO solution respectively. The higher the initial concentration of methyl orange the lower the photo-degradation rate and the kinetic rate constant which agrees with what was observed by other researchers (Lia *et al*., 2006).

The use of high initial concentrations of a contaminant lowers the photo-catalytic degradation due to the saturation of the TiO_2 surface which reduces the photonic efficiency and cause photo-catalyst deactivation (Saquib & Muneer, 2003). In the photo-catalytic reaction system of methyl orange, the dye also absorbs the illuminated light reducing its intensity and this affects the kinetic rate constant.

4.5.2 Effect of pH

The pH is one of the most important operational parameters since it affects surface charge of the TiO_2 photo-catalyst. Its effects on the photo-degradation of methyl orange were investigated under UV light irradiation using TiO_2 photo-catalyst deposited on a bimetallic layer of Au and Cu supported on quartz. The variable was the pH of the methyl orange solution (3.45, 8.5 and 11.5) adjusted using NaOH (aq) and HCl and the fixed parameters were temperature, concentration, photo-catalyst type and volume of MeO solution.

The photo-degradation profiles of methyl orange (10 ppm) using TiO_2/Cu/Au photo-catalyst deposited on quartz at pH values of 3.5, 8.5 and 11.5 at 25 °C are shown in Figure 4.19.

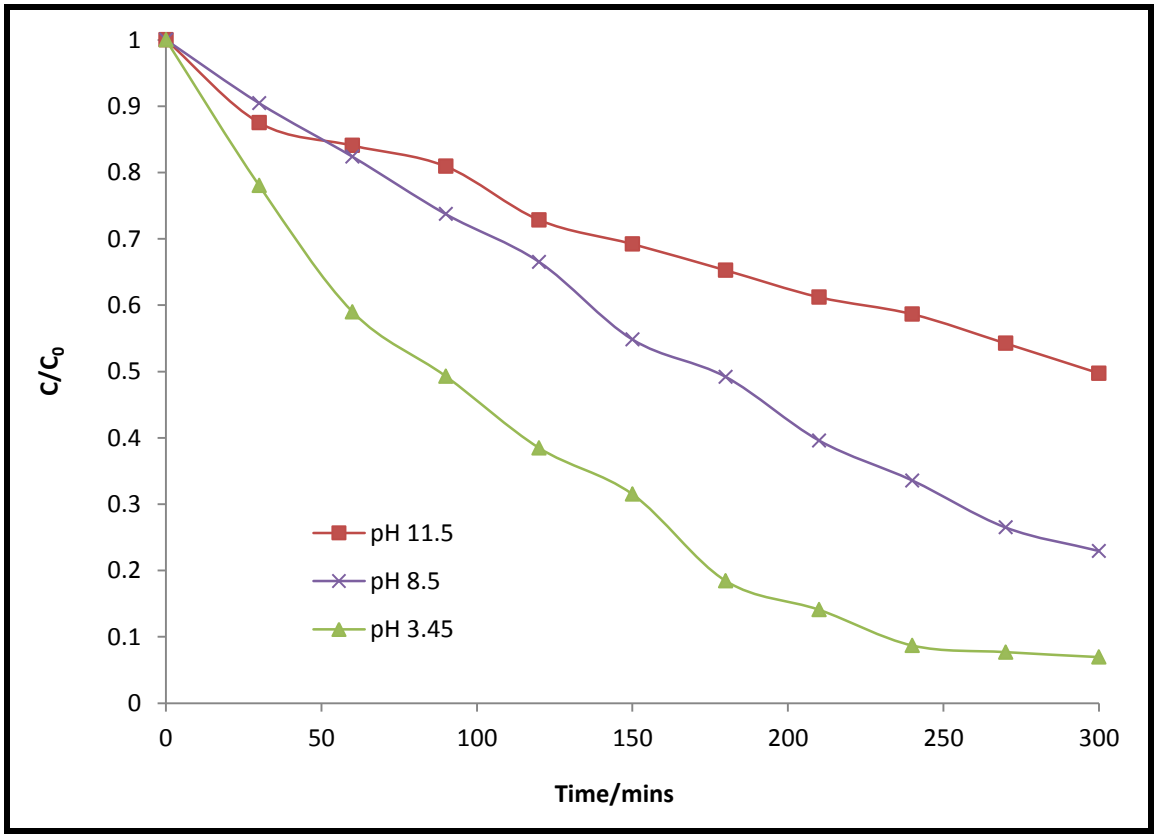

Figure 4.19: photo-degradation profiles of 10 ppm methyl orange solution using TiO_2/Cu/Au photo-catalyst deposited on quartz at pH values of 3.5, 8.5 and 11.5 at 25 °C under UV light.

The highest methyl orange photo-degradation of 93.06 % was achieved under acidic conditions at pH 3.45 and it decreased with further increase in pH. At pH above 10, the surface of the photo-catalyst is negative and at low pH it is positive due to $TiOH_2^+$ (Chong *et al*., 2010). This implies that the adsorption of the negatively charged methyl orange on TiO_2 surface is high under acidic conditions, which helps to explain the high efficiency of the photo-catalyst at low pH.

4.6 Photo-degradation under visible light

This section presents an evaluation of the photo-catalytic activity of 2AuT, 2AgT and 2CuT under visible light irradiation using methyl orange. The preparation method for the photo-catalysts was presented in Section 3.2.2.1 and Section 3.3.1 for the deposition of the metal films and TiO_2 photo-catalyst respectively. The sample codes and description are shown in Table 3.2. The detailed procedure of the photo-degradation process was presented in Section 3.11 and the experimental setup is shown in Figure 3.5. The variable was the type of plasmon metal deposited on top of TiO_2 photo-catalyst on quartz, the fixed parameters were methyl orange concentration, photo-catalyst loading, light source and intensity, temperature and pH. The control was TiO_2 photo-catalyst on quartz with no metal film deposited.

Figure 4.20 shows the photo-degradation curves of methyl orange using 2AuT, 2AgT and 2CuT photo-catalysts under visible light irradiation using methyl orange at 25 °C and pH 7.

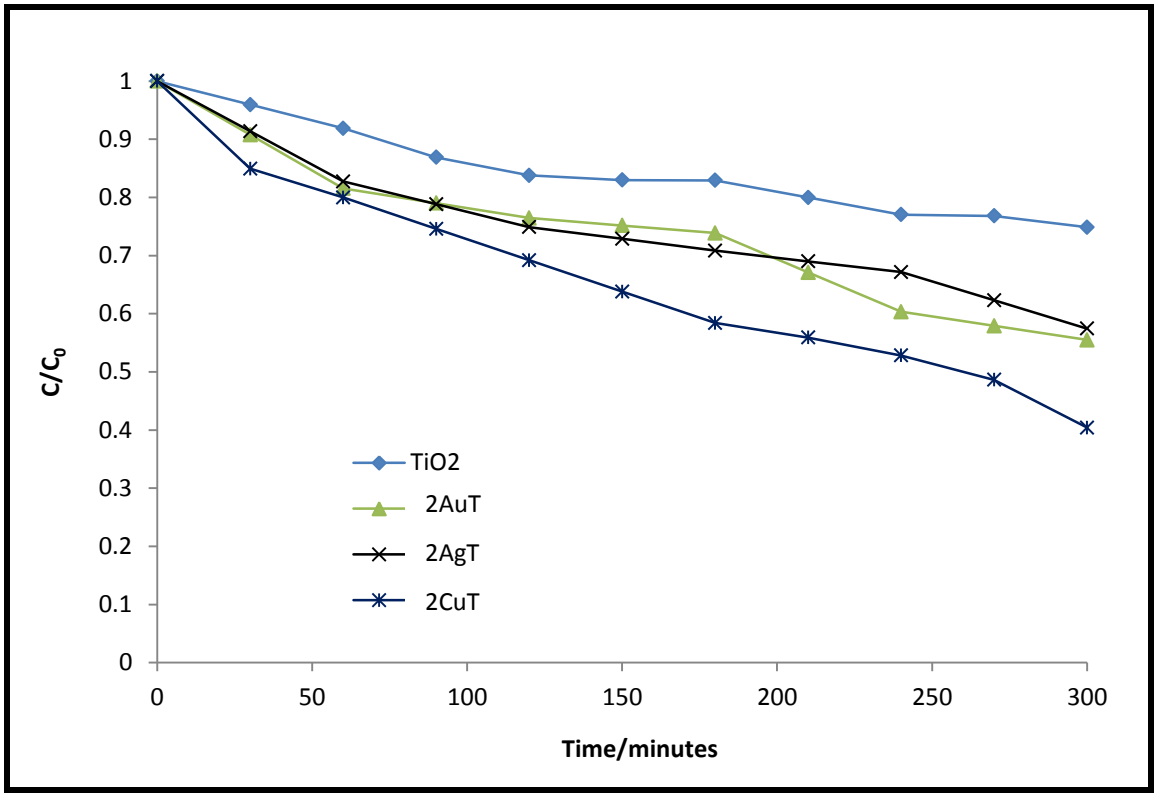

Figure 4.20: Photo-degradation curves of MeO (10 ppm) using TiO_2 photo-catalysts decorated on top with 2 nm film of different plasmon metals (Au, Ag and Cu) under visible light at 25 °C and pH 7.

All the plasmon decorated samples showed higher photo-catalytic activity than uncoated TiO_2 photo-catalyst. TiO_2 does not absorb much visible light implying that its photo-catalytic activity under visible light illumination is mainly initiated by the deposited plasmon metal nanoparticles. The highest photo-degradation was achieved by 2CuT which degraded 59.60 % of the methyl orange after 300 minutes while 2AuT and 2AgT degraded 44.52 % and 42.55 % respectively. The reasons for the observed trend 2CuT > 2AuT > 2AgT for methyl orange photo-degradation under visible light include,

(i) Cu and Au nanoparticles absorb visible light hence they can be easily activated under visible light irradiation. The activated plasmon metal will inject an electron

into the conduction band of TiO_2, which will then be scavenged by oxygen to form superoxide. This direct electron transfer results in the activation of TiO_2 even when the semiconductor does not absorb the light.

(ii) Since the metal film was deposited on the surface of TiO_2, it is exposed to air hence Cu being unstable relative to its oxides, will be oxidized to CuO and Cu_2O which both have small band gaps. These oxides can easily absorb visible light and could participate in the photo-degradation process and/or transfer electrons to TiO_2 to activate it (inter-particle electron transfer).

4.7 UV light versus visible light irradiation

This section presents a comparison of the results of photo-degradation of methyl orange (10 ppm) using 2AuT, 2CuT and 2AgT photo-catalysts under UV light at 25 °C and pH 7 and the photo-degradation results of methyl orange (10 ppm) using same type of photo-catalysts under visible light at 25 °C and pH 7. The detailed experimental procedure for the preparation of the photo-catalysts and photo-catalytic activity evaluation were presented in Section 3.2.2.1 and Section 3.11 respectively.

The efficiency of plasmon coated TiO_2 photo-catalysts (2AuT, 2CuT and 2AgT) relative to TiO_2 with no metal film (T1) under UV and visible light are shown in Table 4.7. The reason for using the selected photo-catalysts for tests under visible light also and compared with UV light photo-degradation results is that they were not the most active photo-catalyst under UV light.

Table 4.7: Photo-degradation results of methyl orange (10 ppm) using T1, 2AuT, 2CuT and 2AgT photo-catalysts under UV light and visible light at 25 °C and pH 7.

Photo-catalyst	% Degradation under UV light after 300 minutes	% Degradation under visible light after 300 minutes	% Increase relative to bare TiO_2 under UV	% Increase relative to bare TiO_2 under visible light
T1	57.16	25.12	-	-
2AuT	71.39	44.51	14.23	19.39
2CuT	65.50	59.59	8.34	**34.47**
2AgT	85.85	42.55	**28.69**	17.43

When the photo-degradation results after 300 minutes of the same photo-catalyst under UV light are compared to those under visible light, 2CuT showed the smallest decrease of 5.91 % from 65.50 % under UV light to 59.59 % under visible light followed by 2AuT (26.88 %) and lastly 2AgT (43.3 %). When both UV and visible light photodegradation results of plasmon decorated TiO_2 were compared to those of T1, Cu showed the highest improvement of 34.47 % increase under visible light and the least improvemnet of 8.34 % under UV light. 2AgT showed the highest improvement of 28.69 % under UV light and the least under visible light. The reason for better photocatalytic enhancement from both Au and Cu metal films under visible light than under UV light is that, both metals absorb in the visible region (Au λ=560 nm and can reach 700 nm or more depending on size and shape) and (Cu λ=570 nm) hence creating strong plasmonic electric fields which enhance light absorption and electron-hole generation. Ag absorbs close to UV hence it is expected that its activity is lower in sunlight than under visible light irradiation.

4.8 Durability tests

Durability tests were done by (i) determining the change in efficiency of the photo-catalyst with repeated use and (ii) measuring the concentration of the metal that leached into the solution using ICP-OES. Experiments were conducted using the same photo-catalyst for four cycles. The samples selected for durability tests were 2AuT, 2AgT, 2CuT, T5Cu, T10Cu, T20Cu, T5Au, T10Au, T20Au, T5Ag, T10Ag, T20Ag and TiO_2 on trimetallic layer. These photo-catalysts were selected so as to know if leaching was high when the plasmon metal is deposited on top of TiO_2 or underneath TiO_2 photo-catalyst. TiO_2 on trimetallic layer photo-catalyst was chosen for the determination of the change in efficiency with repeated use because it showed the highest photo-catalytic activity using methyl orange under UV light (Table 4.8) hence has potential to be used more than once. The experimental procedure of the photo-degradation process under UV light process is presented in Section 3.2.2.1.

The loss in photo-catalytic efficiency with repeated use and the loss of metal nanoparticles through leaching were evaluated using TiO_2 photo-catalyst on trimetallic layer and the results are shown in Table 4.8.

Table 4.8: Leached concentration of Au, Ag and Cu and photo-degradation results of BCP after 300 minutes using TiO_2 photo-catalyst on a 10 nm trimetallic film (Au/Ag/Cu).

Cycle	% Photo-degradation after 300 minutes	Leached concentration/ppm		
		Au	Ag	Cu
1st	95.88	0.0015	0.1531	0.0173
2nd	94.25	0.0049	1.5224	0.0223
3rd	90.76	0.0092	5.4640	0.0276
4th	80.98	0.0093	10.421	0.0460

The total amount of BCP photo-degraded decreased slightly from 95.88 % in the first cycle to 94.25 % in second cycle. The amount was further reduced to 90.76 % and 80.98 % in the third and fourth cycles respectively. The overall changes in the photo-catalytic activity were low thus the photo-catalyst was generally efficient for repeated use of the photo-catalyst since a significant amount of the contaminant (BCP) is still being photo-degraded even after repeated cycles. The efficiency of a photo-catalyst in a given process is a significant component for determining its economic viability and with these observed results, the process may be viable economically using this photo-catalyst.

The decrease in the photo-catalytic activity of the photo-catalyst could be due to loss of nanoparticles resulting from leaching and photo-catalyst deactivation. The TiO_2 can also be deactivated by the accumulation of surface species, intermediates, or by-products that have good adsorption ability upon the photo-catalyst surface (Larson & Falconer., 1997) and diminution of hydroxyl radicals. Reactivation can be achieved by regeneration of the $OH^{\bullet}$ radicals or by oxidation of the products on the surface of the photo-catalyst by heating at temperatures high enough to decompose the intermediates.

Leaching of the noble metals increased with an increase in the number of cycles (Table 4.8). The leaching of Ag was highest reaching a concentration of 10.42 ppm after the fourth cycle followed by Cu with 0.046 ppm and Au with the lowest at a concentration of 0.0093 ppm. The concentrations of copper leached are less than the recommended guide line value of 2 ppm (WHO, 2006). In South Africa, it is also the value that has been agreed between Department of Water Affairs and South African Bureau of Standards (SABS). In drinking water this value ranges from 0.005 ppm to 30 ppm as a result of corrosion of the interior of copper plumbing pipes.

Table 4.9 shows the concentrations of leached metals into the solution from 2AuT, 2AgT, 2CuT, T5Cu, T10Cu, T20Cu, T5Au, T10Au, T20Au, T5Ag, T10Ag, T20Ag photo-catalysts after 300 minutes of photo-degradation under UV light at 25 °C and pH 7.

Table 4.9: Concentration of metals that leached in solution after 300 minutes of photo-degradation process.

Metal film thickness	**Metal position relative to TiO_2 film**	**Leached amount/ppm**		
		Au	**Ag**	**Cu**
2 nm	Top	0.0045	1.8612	0.0154
5 nm	Underneath	0.0001	1.2518	0.0386
10 nm	Underneath	0.0006	1.1375	0.0471
20 nm	Underneath	0.0038	1.2260	0.0543

It is clear that when monometallic films plasmon metals were deposited on top of the photo-catalyst layer, the amount of the leached metals was higher than when the metal films were deposited underneath the TiO_2 photo-catalyst. This might be so because the metal films were in direct contact with the solution at the top layer hence making it easy for the metals to leach. For the same metal film deposition, it was observed that leaching increased with an increase in film thickness even though these films were under the TiO_2 photo-catalyst layer. The highest leaching was observed for Ag whether above or below the TiO_2 layer followed by Cu and Au was the least. The copper that leached was well below the recommended guide lines of 1.3 ppm (EPA; 2009). The toxicity of silver is well understood being an effective bactericide capable of damaging biological systems hence in the US, silver concentrations of only 0.05 – 5 ppm are allowed in municipal waters (Carp *et al*., 2004), hence Ag should be used with caution as a plasmonic metal in photo-catalysts.

Although the photo-catalytic efficiency was higher when thicker films of Ag were used, there is a disadvantage of increased leaching hence a compromise has to be reached between the rate of photo-degradation and human safety. Generally silver is not considered to be toxic to human health hence the U.S. EPA has not set a maximum contaminant level but has set a non-mandatory secondary maximum contaminant level of 0.1 ppm to serve as a guideline in water quality. From the above results it can be seen that silver has the disadvantage of poor stability and lower bio-compatibility hence the use of Au films will be preferred for higher chemical stability.

4.9 Summary

Plasmon metal films were successfully deposited upon and also underneath TiO_2 layers supported on quartz using the thermal evaporation technique. The layering of TiO_2 with plasmon metal films either above or below has proved to be a promising way of enhancing the photo-catalytic activity of the photo-catalyst. The photo-catalysts can be activated by either UV or visible light due the presence of the plasmon elements even when the TiO_2 does not absorb visible light. The mechanism of enhancement of photo-activity depends on the type of the light used for activation. Under UV irradiation, noble metal nanoparticles on TiO_2 nanoparticles enhance transfer of photo-generated electrons from the photo-catalyst thereby prolonging the lifetime of the charge carriers. Among the photo-catalysts with metal films deposited on top of TiO_2 film, the best metal was Ag with a thickness of 2 nm. The best overall position of the metal films for better photo-catalytic activity was underneath the TiO_2 photo-catalyst film. The photo-catalysts that did not work were T10Cu, T20Cu, T25Cu, T20Au, T25Au as they reduced the photo-catalytic activity of TiO_2. This is because leaching increased with an increase in film thickness and in case of copper the leached Cu^{2+} retards photo-catalytic activity due to short circuiting reactions (Equations 4.1 and 4.2).

The use of bimetallic layers proved to be better than the use of one type of metal because of their promoting effect attributed to improved charge separation and charge transfer from metal to TiO_2 conduction band or from TiO_2 to metal nanoparticles due to synergism. For the bimetallic layers, the best combination was that of copper and gold. The photo-catalyst that gave the highest photo-degradation of methyl orange was TiO_2 deposited on a trimetallic layer of Au, Ag and Cu. The addition of salts and contaminants were found to reduce the photo-degradation of the target compound. Plasmon decorated TiO_2 photo-catalysts still performed better than the pure TiO_2 even in the presence of other contaminants other than the target compound implying that they have potential application in the industry in any kind of environment.

Chapter 5

Doped TiO_2 for visible light dye photo-degradation

This chapter presents the characterization and application of the TiO_2 semiconductor co-doped with a nonmetal (carbon) and a plasmon metal (Au or Ag) on quartz support. The chapter's major goal is to evaluate the effects of gold and silver metal when they are used as dopants together with carbon instead of films on top or underneath TiO_2 as reported in Chapter 4. The effect of plasmon metal loading on the band gap and the resulting photo-catalytic activities are explored.

5.1 Introduction

TiO_2 photo-catalyst is the most promising semiconductor for photo-catalysis but has a wide band gap (Eg = 3.2 eV) which limits its applications. Several ways including doping have been tried to engineer the band gap of TiO_2 so that it can absorb visible light. It is known that doping TiO_2 with transition metals could shift its optical absorption into the visible region without prominent change in band gap (Xin *et al*., 2012). However Palanivelu *et al*., (2007) reported that transition metal doping suffers from thermal instability and low quantum efficiency of the photo-catalyst. In this section of the study TiO_2 was therefore co-doped with a plasmon transition metal and a nonmetal to improve its photo-catalytic activity. The effects of transition metal have been widely investigated but it is still difficult to make comparisons and draw conclusions since different preparation procedures and parameters have been used (Wang *et al*., 2014). Also detailed information on changes in crystal and electronic structures is still lacking as there are disputes related to the research. Hence in this Chapter it is aimed to show the preparation and effects of co-doping TiO_2 with Au/C or Ag/C and determine the optical properties and the photo-catalytic activity under visible light irradiation.

5.2 Experimental procedures

5.2.1 Preparation of Ag/C co-doped TiO_2

A modified sol-gel method by Mungondori *et al*., (2013) was used to prepare the Ag/C co-doped TiO_2 using glucose as the source of carbon and silver nitrate solution (0.01 M) as the source of silver. A detailed experimental procedure is provided in Section 3.3.2.1. The amount of carbon added in all samples was kept constant. Silver nitrate solution (0.01 M) was added to give Ag: Ti mol ratio of 0.2, 0.5, 0.7 and 1.0 mol %. The nanoparticles were separated from the solution by centrifugation and the resulting powder was dried in an oven at 90 °C and then finally calcined at 500 °C for 2 hours to give Ag/C co-doped TiO_2 before deposition on quartz

5.2.2 Preparation of Au/C co-doped TiO_2

The same procedure used for the preparation of Ag/C co-doped TiO_2 was followed for the preparation of Au/C co-doped TiO_2 as reported already in Section 3.3.2.2. Tetrachloroauric acid was used as the source of gold. $HAuCl_4$ (2 mM) was added to give Au: Ti mol ratio of 0.2, 0.5, 0.7 and 1.0 mol %.

5.2.3 Deposition of the photo-catalysts on quartz

The photo-catalysts were deposited on quartz using the method described in Section 3.4.

5.3 Characterization of materials

The materials were characterized using diffuse reflectance spectroscopy, X-ray diffraction, Fourier transform infrared spectroscopy, X-ray photoemission spectroscopy, thermogravimetric analysis, BET surface area, CHNS elemental analysis and Raman

spectroscopy which were discussed in detail in Chapter 2 and the operating conditions were given in Chapter 3.

5.4 Photo-catalytic activity evaluation

The photo-catalytic performances of the Ag/C co-doped TiO_2 and Au/C co-doped TiO_2 photo-catalysts were evaluated using methyl orange under visible light illumination. The experimental set up (Figure 3.5, Chapter 3) and details are as given in Section 3.11.

5.5 Results and Discussion

5.5.1 Optical properties

This section presents the characterization of Ag/C co-doped TiO_2 photo-catalyst with different contents of Ag, Au/C co-doped TiO_2 photo-catalyst with different contents of Au, undoped TiO_2, Au doped TiO_2 and Ag doped TiO_2 photo-catalyst using UV-Visible and diffuse reflectance spectroscopy. The UV-Vis absorption analysis was done to establish the region in which the prepared photo-catalysts absorb light.

The absorption spectra of Ag/C co-doped TiO_2 with different contents of Ag, C doped TiO_2, Ag doped TiO_2 and undoped TiO_2 photo-catalysts are shown Figure 5.1.

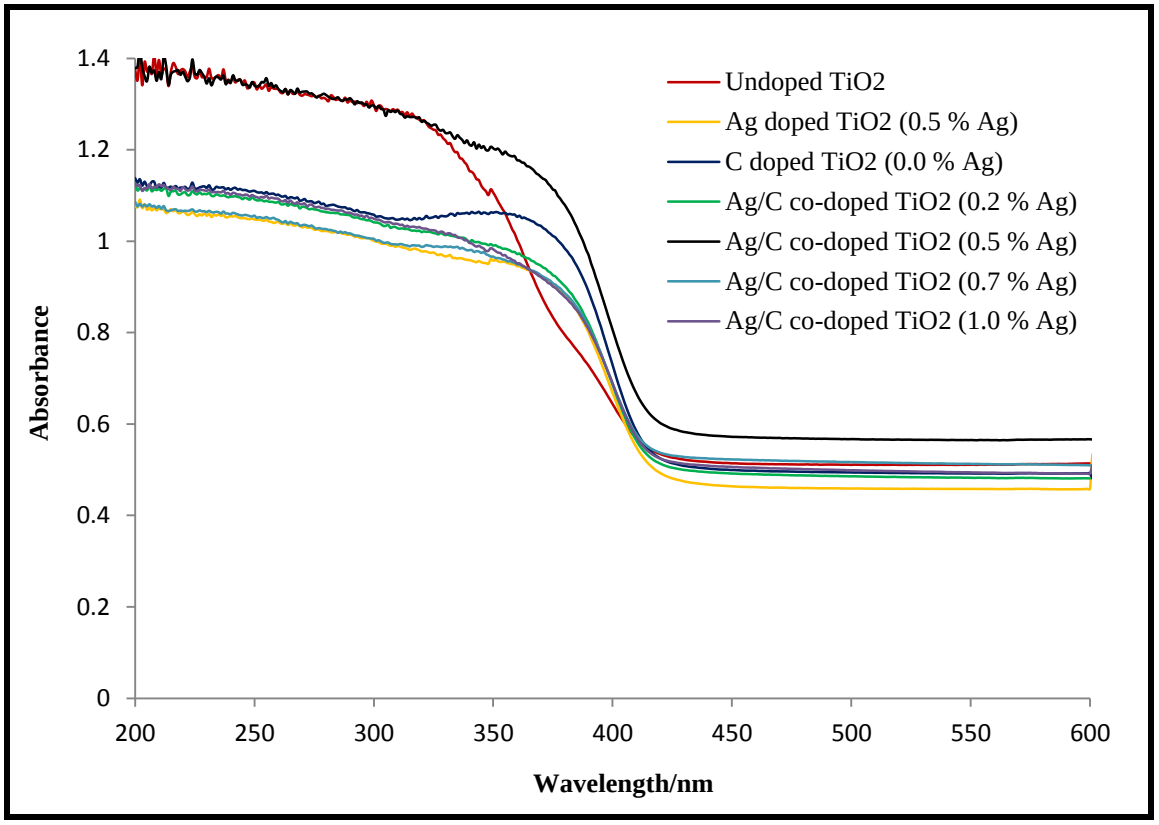

Figure 5.1: Absorption spectra of the undoped TiO_2, Ag doped TiO_2, C doped TiO_2 and Ag/C co-doped TiO_2 photo-catalysts with different Ag loadings.

All the co-doped TiO_2 and undoped TiO_2 photo-catalysts showed a broad absorption in the UV region below 400 nm attributed to the band gap absorption of TiO_2 as a result of electron excitation transition between O 2p states at the valence band and Ti 3d states at the conduction band (Rahulan *et al.*, 2011). The absorption edge of all the co-doped photo-catalysts red shifted and the highest shift was achieved by the photo-catalyst with 0.5 % Ag loading. With increase in loading from 0.5 % to 1.0 % Ag, the absorbance blue shifted implying that the optimum loading for Ag in this study was 0.5 %.

Gold and carbon co-doped TiO_2 photo-catalysts were also characterized by UV-Vis spectroscopy. The absorption spectra of Au/C co-doped TiO_2 photo-catalysts with different Au loadings are shown in Appendix B Figure B-1. It can be seen that below 400 nm, all the

Au/C co-doped TiO_2 photo-catalyst showed a broad absorption peak due to the charge transfer from the valence band to the conduction band of TiO_2.

The diffuse reflectance spectra (operating conditions presented in Section 3.12.8) of Ag/C co-doped TiO_2 with different contents of Ag, C doped TiO_2, Ag doped TiO_2 and undoped TiO_2 photo-catalysts are shown in Figure 5.2.

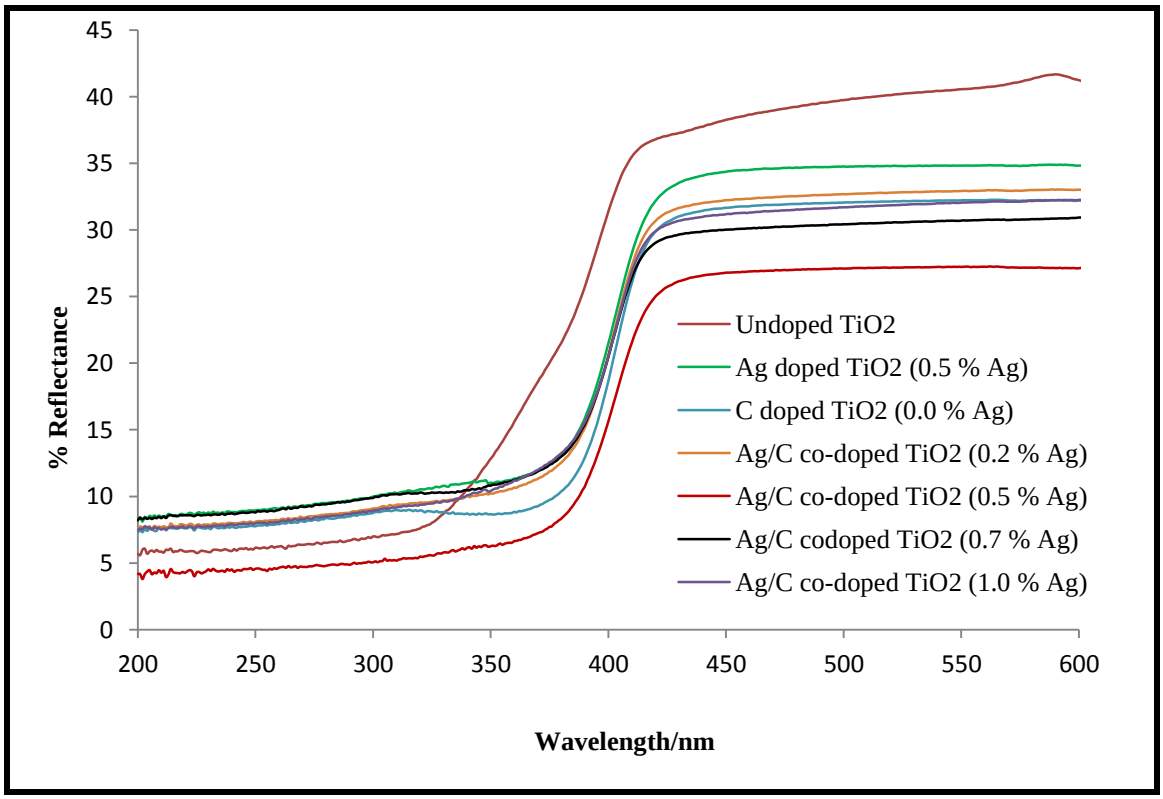

Figure 5.2: Diffuse reflectance spectra of undoped TiO_2, Ag doped TiO_2, C-doped TiO_2 and Ag/C co-doped TiO_2 photo-catalysts with different Ag loadings.

The diffuse reflectance spectra in Figure 5.2 show a very clear and significant shift of the absorption edges of the doped photo-catalysts to higher wavelengths when compared to the undoped TiO_2. The reason for the red shift allowing visible light absorption is the introduction of the impurity levels with Ag doping (Harikishore *et al.*, 2014), since the

electron transfer from one of the additional impurity energy levels within the band gap of the semiconductor requires lower photon energy than in undoped TiO_2 photo-catalyst. There were very small differences between the absorption edges of the photo-catalysts with 0.2 %, 0.7 % and 1.0 % Ag loading. A significant shift was observed for the photo-catalyst with Ag loading of 0.5 %. Of all the doped photo-catalysts, the one doped with carbon as the only dopant (0.0 % Ag) showed the least shift, which shows that co-doping is better than the use of one dopant in enhancing visible light absorption.

Gold and carbon co-doped TiO_2 photo-catalysts were also characterized by diffuse reflectance spectroscopy. The diffuse reflectance spectra of the Au/C co-doped TiO_2 photo-catalysts are shown in Figure 5.3.

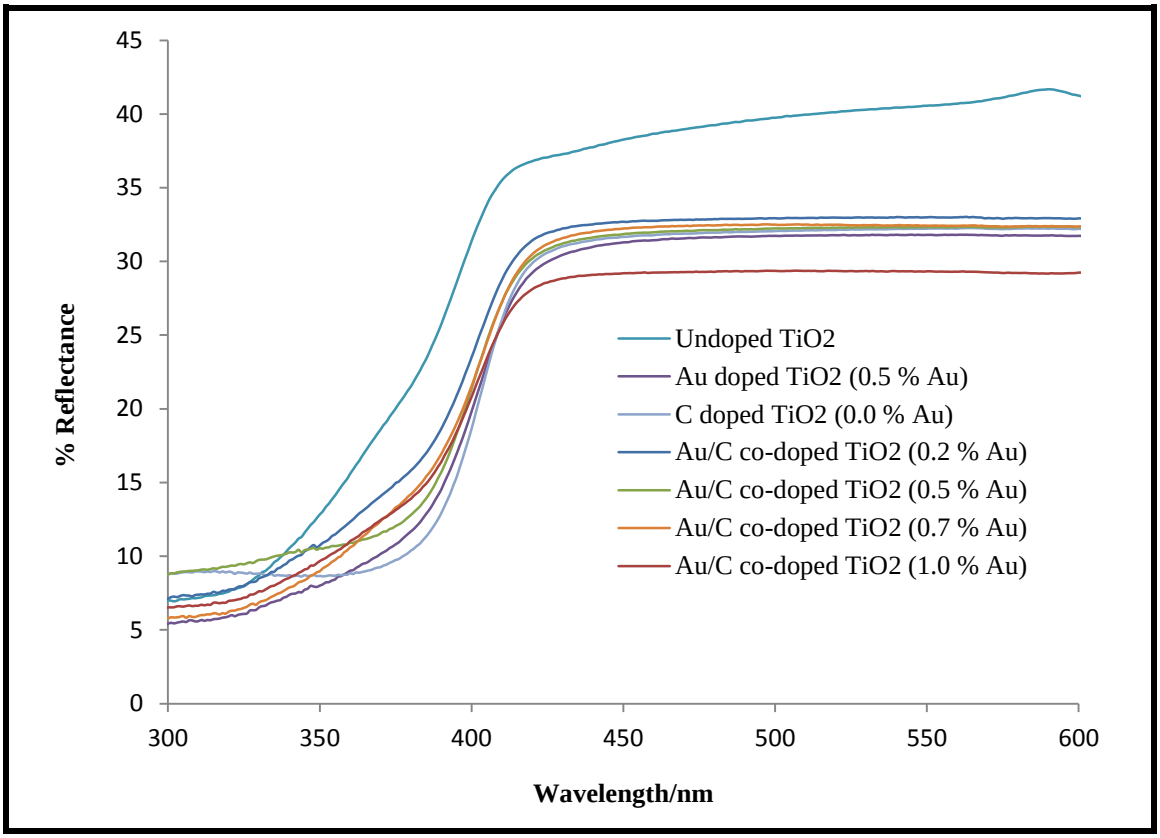

Figure 5.3: Diffuse reflectance spectra of the undoped TiO_2, C-doped TiO_2 and Au/C co-doped TiO_2 photo-catalysts with different Au loadings.

There was a shift of the absorption edges of all the doped photo-catalysts into the visible region when compared to undoped TiO_2. The reason for this red shift was probably the formation of new energy levels above the valence band of TiO_2 due to the incorporation of carbon and Au into TiO_2 (Jiang *et al*., 2013). Au/C co-doped TiO_2 (0.0 % Au) exhibited better red shift than all the Au/C co-doped TiO_2 photo-catalysts. As the Au loading was increased from 0.2 % to 0.5 %, the absorption edge significantly shifted to higher wavelength (low energy) and then it slightly shifted to low wavelength when the Au loading was further increased to 0.7 %. This explains the importance of optimum doping of transition metal otherwise the synergistic benefits of co-doping may not come into effect. In this study the optimum Au loading for co-doping TiO_2 with carbon and gold was found to be 1.0 % although there was a very small difference between the absorption edge compared to TiO_2 photo-catalysts with 0.5 and 0.7 % Au contents.

5.5.1.2 Tauc plots for band gap determination

The band gaps were determined by the use of Tauc plots which are plots of $[F(R)*hv]^{1/2}$ versus photon energy. In the calculations, the value of n was 2 for indirect allowed transitions since it fitted well when compared to n=1/2 for the direct allowed transitions. The extrapolation to the horizontal axis (energy axis) gave an estimate of the value of the band gap (E_g). Undoped TiO_2 gave the most well defined absorption edge that made it quite easy to make an extrapolation and determine the band gap more accurately. Generally, the band gaps of all the Ag/C co-doped TiO_2 photo-catalysts were lower than that of undoped TiO_2.

The Tauc plots of undoped TiO_2, Ag doped TiO_2 and Ag/C co-doped TiO_2 photo-catalysts with different contents of Ag are shown in Figure 5.4

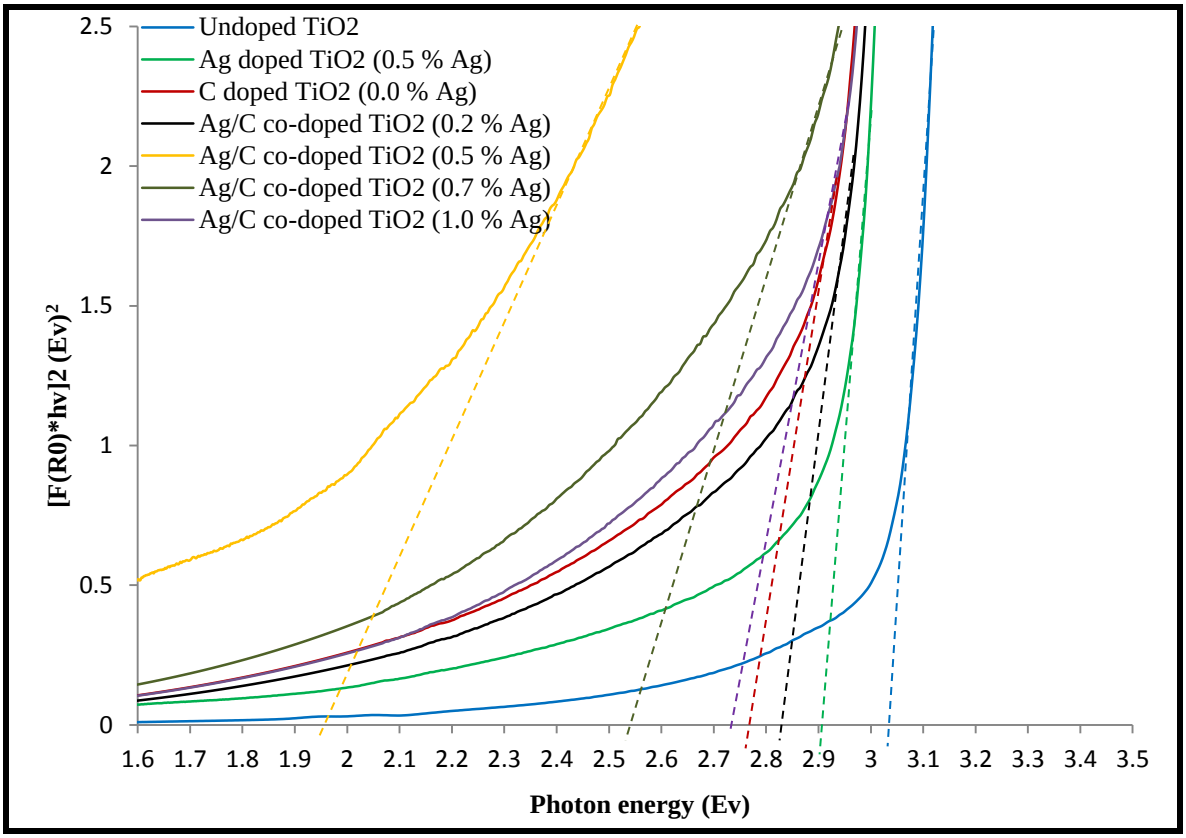

Figure 5.4: Tauc plots of undoped TiO_2, Ag doped TiO_2 and Ag/C co-doped TiO_2 with different contents of Ag.

There was a decrease in the band gap from 2.83 eV to 1.95 eV as the Ag loading was increased from 0.2 % to 0.5 % and a further increase in the metal loading caused band gap widening as shown in Figure 5.4. The possible reason for the increase in band gap with increase in Ag content above 0.5 % was the dominance of the d-d transitions over the sp-d transitions. In this study, the optimum loading of Ag to achieve the lowest band gap when co-doping TiO_2 with silver and carbon was found to be 0.5 %. It is important to note that there is formation of new occupied bands as a result of the hybridization of Ag 4d and Ti 3d states which can affect the properties of the semiconductor.

The Tauc plots of undoped TiO_2, Au doped TiO_2 and Au/C co-doped TiO_2 photo-catalysts with different contents of Au are shown in Figure 5.5

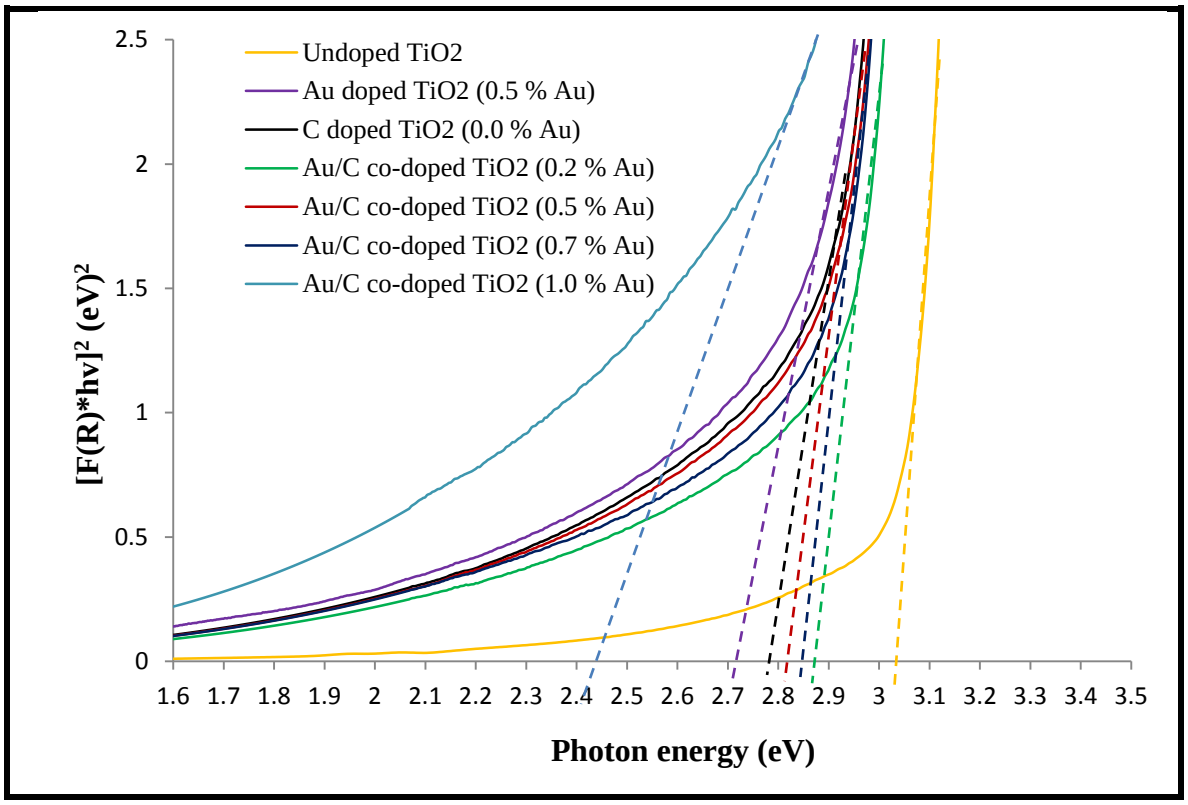

Figure 5.5: Tauc plots of undoped TiO_2, Au doped TiO_2 and Au/C co-doped TiO_2 with different contents of Au.

It can be seen from the Tauc plots that there was no regular trend for band gaps as the amount of Au was increased from 0.0 % to 1.0 %. The TiO_2 photo-catalyst doped with carbon only (0.0 % Au) had a lower band gap (2.77 eV) than TiO_2 photo-catalysts with 0.2 % (2.88 eV), 0.5 % (2.83 eV) and 0.7 % Au (2.85 eV) implying that, with these Au contents there was no synergy between carbon and Au in reducing band gap of TiO_2 unlike in the case with Ag. When gold was used as the only dopant, it also resulted in a lower band gap TiO_2 than the co-doped TiO_2 with 0.2 %, 0.5 % and 0.7 % Au. These findings suggest that the ratio between the elements used as dopants should be optimized if the synergy is to come into play. The differences in the band gap values were also very small in these three samples. The lowest band gap of 2.45 eV was achieved with Au content of 1.0 %.

The effect of dopant content on the band gap of TiO_2 photo-catalysts is summarized in Table 5.1.

Table 5.1: Band gaps of undoped TiO_2, Au/C co-doped TiO_2 and Ag/C co-doped TiO_2 with different contents of Au and Ag.

	Band gaps from Tauc plots	
Sample (M=Au or Ag)	**Au**	**Ag**
Undoped TiO_2	3.02	3.02
M doped TiO_2	2.75	2.90
C doped TiO_2 (0.0 % M)	2.77	2.77
C/M co-doped TiO_2 (0.2 % M)	2.88	2.83
C/M co-doped TiO_2 (0.5 % M)	2.83	**1.95**
C/M co-doped TiO_2 (0.7 % M)	2.85	2.53
C/M co-doped TiO_2 (1.0 % M)	2.45	2.72

When compared to gold, silver has better synergistic properties with carbon as this combination gave the highest visible light absorption enhancement using a dopant level of 0.5 % Ag resulting in a TiO_2 photo-catalyst with a band gap of 1.95 eV. The reason for the better performance of Ag in making TiO_2 visible light responsive could be its small size/atomic radius when compared to Au hence its incorporation into the TiO_2 crystal structure is more likely favored than Au.

5.5.2 Raman Analysis

Anatase and rutile phases of TiO_2 can be identified by Raman spectroscopy based on their spectra. On the basis of the factor group analysis, the anatase phase has six active modes at 144 cm^{-1} (E_g), 197 cm^{-1} (E_g), 399 cm^{-1} (B_{1g}), 513 cm^{-1} (A_{1g}), 519 cm^{-1} (B_{1g}) and 639 cm^{-1} (E_g) (Brojcin *et al*., 2005; Zhang *et al*., 2006). The Raman bands typical of the rutile phase appear

at 143 cm^{-1} (normally superimposed with anatase peak at 144 cm^{-1}), 235 cm^{-1}, 447 cm^{-1} and 612 cm^{-1} due to B_{1g}, two-phenon scattering (TPS), E_g, and A_{1g} modes respectively (Chaves *et al*., 1974).

5.5.2.1 Raman analysis of Ag/C co-doped TiO_2 photo-catalysts

The Raman spectra of undoped TiO_2, Ag doped TiO_2 and Ag/C co-doped TiO_2 photo-catalysts with different Ag contents are shown in Figure 5.6. Preparation of the doped samples is presented in Section 3.3.2.1 and Section 3.3.2.4.

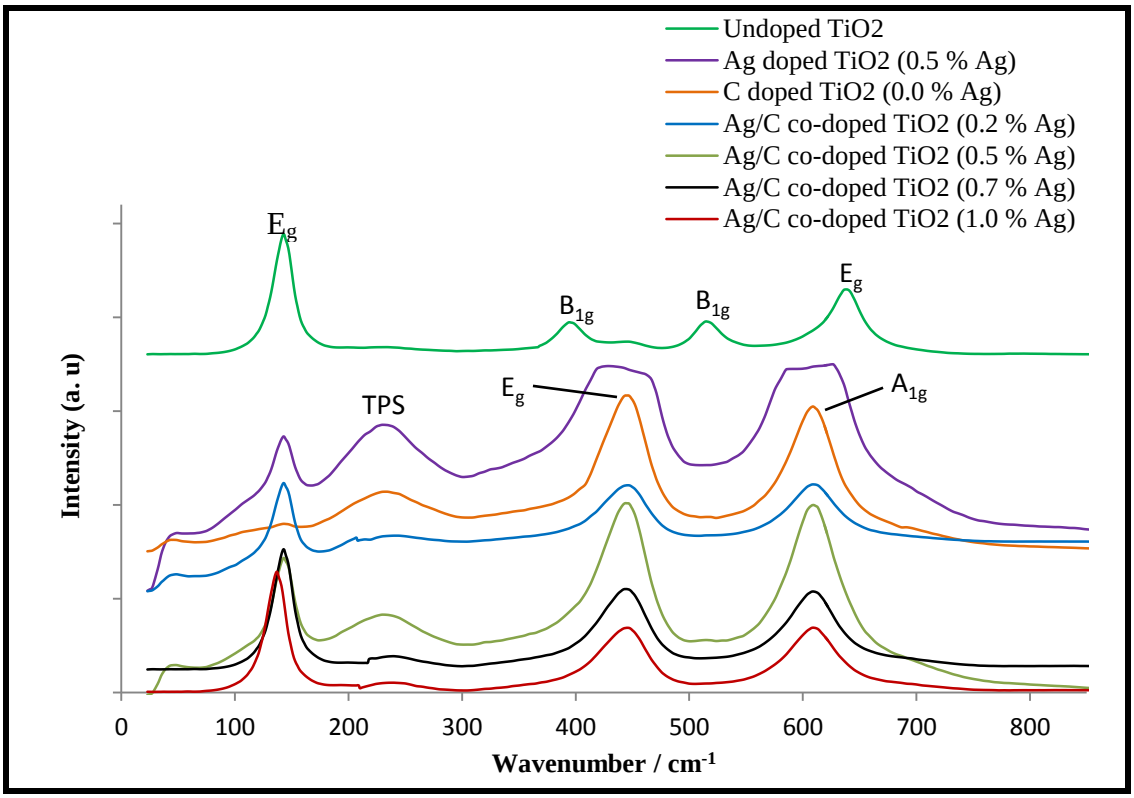

Figure 5.6: Raman spectra of undoped TiO_2, Ag doped TiO_2 and Ag/C co-doped TiO_2 with different contents of Ag dopant.

All the Ag doped TiO_2 photo-catalysts had major peaks from the rutile phase. The major peak common to all samples, due to the E_g mode, was found at 145 cm^{-1} in the spectra of the

undoped TiO_2 photo-catalyst and at 147 cm^{-1} in the spectra of all doped TiO_2 samples showed a slight shift of 2 cm^{-1}. This peak is very sensitive to the vibrational mode of the O-Ti-O bond (Lin *et al*., 2007). It is important to note that the strength of the Raman peak depends on the polizability of the O^{2-} around the Ti^{4+} hence the presence of oxygen vacancies affects Ti-O vibration resulting in Raman shifts and changes in peak width (Sahoo *et al*., 2009).

With carbon and silver co-doping, new peaks at 237 cm^{-1}, 451 cm^{-1} and 615 cm^{-1} (all major peaks) from the rutile phase of TiO_2 appeared due to two-phenon scattering, E_g and A_{1g} respectively. The two-phenon scattering peak was more intense in the spectra of TiO_2 doped with Ag only, carbon only and C/Ag-TiO_2 with 0.5 % Ag loading. Three peaks at 405 cm^{-1} (B_{1g}), 525 cm^{-1} (B_{1g}) and 645 cm^{-1} (Eg) which appeared in the spectra of C and Au co-doped TiO_2 did not appear at all in the spectra of C/Ag co-doped TiO_2. This means that different dopants result in different anatase to rutile ratios even when the dopant levels are the same (Table 5.3). No apparent changes in Raman shifts were observed when the Ag loading was increased from 0.2 % to 1.0 %. When compared to Au doping, Ag doping caused a significant reduction in intensity of the E_g peak assigned to anatase implying that Ag promoted anatase to rutile phase transformation more than Au.

5.5.2.2 Raman analysis of Au/C co-doped TiO_2 photo-catalysts

The Raman spectra of undoped TiO_2, Au doped TiO_2 and Au/C co-doped TiO_2 photo-catalysts with different Au contents are shown in Figure 5.7.

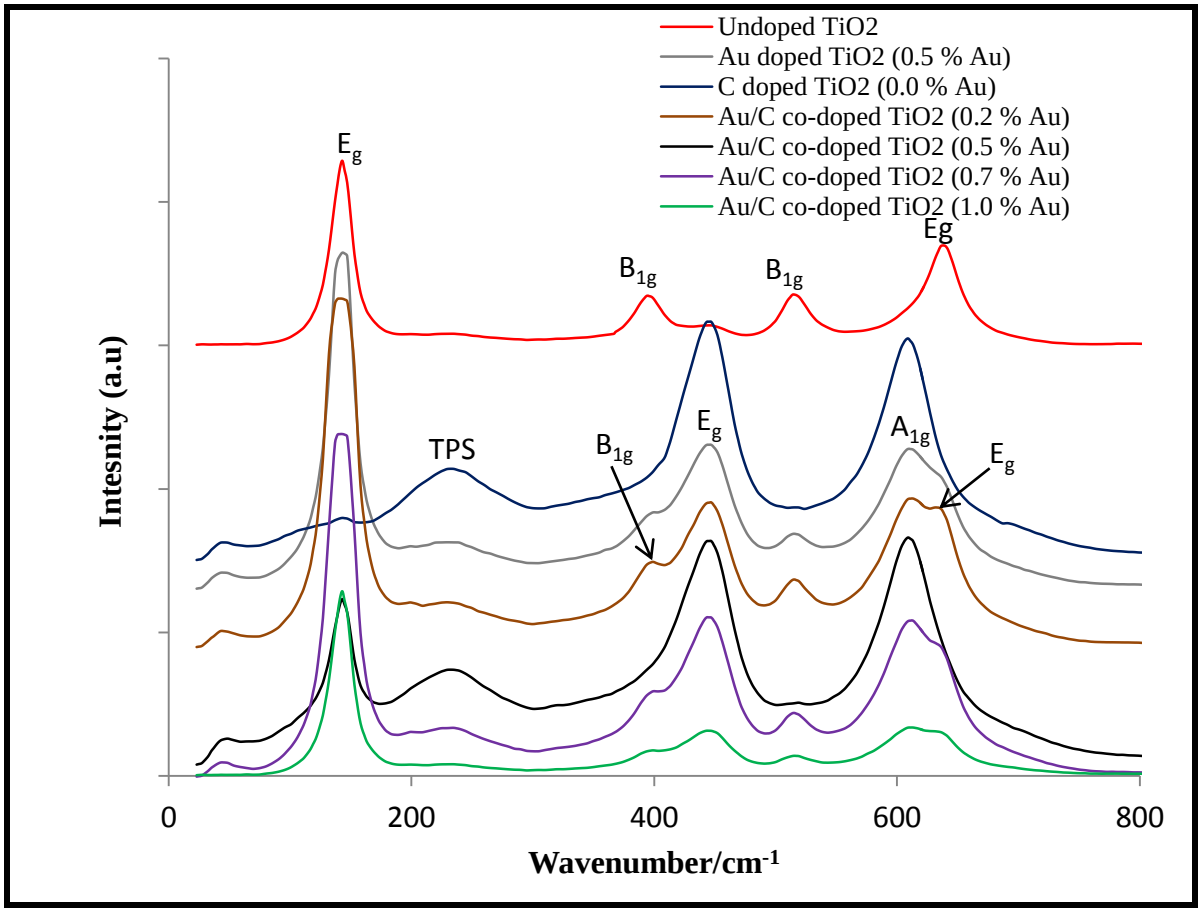

Figure 5.7: Raman spectra of undoped TiO_2, Au doped TiO_2 and Au/C co-doped TiO_2 with different loadings of Au dopant.

Well defined peaks were observed at 145 cm^{-1} (E_g), 244 cm^{-1} (two-phenon scattering), 404 cm^{-1} (B_{1g}), which was prominent in undoped TiO_2, 453 cm^{-1} (E_g), 525 cm^{-1} (B_{1g}), 617 cm^{-1} (A_{1g}) and 641 cm^{-1}(E_g). With an increase of gold content, no apparent change of Raman shifts were observed for most peaks except for the decrease in intensity and appearance of new Raman peaks. When the gold content was increased from 0.2 % to 0.5 %, there was a major decrease in the intensity of the peak at 144 cm^{-1}, disappearance of three peaks at 404 cm^{-1} (B_{1g}), 519 cm^{-1} (B_{1g}) 641 cm^{-1}(E_g) and an increase in intensity of peaks at 237 cm^{-1}, 451 cm^{-1} and 617 cm^{-1}. With a further increase in gold content up to 1.0 %, the peaks that had disappeared reappeared.

The strongest band for the anatase phase was at 145 cm^{-1} in the spectra of undoped TiO_2 and it slightly shifted to 147 cm^{-1} in the spectra of doped TiO_2 photo-catalysts. The presence of the 244 cm^{-1} peak due to the rutile phase was observed in all doped TiO_2 samples but not the undoped TiO_2 which showed that the introduction of impurities in the crystal structure of TiO_2 promotes anatase to rutile phase transformation. This was also supported by the reduction in intensities of the anatase peaks at 404 cm^{-1} and 644 cm^{-1} and a huge increase in the intensities of the rutile peaks at 453 cm^{-1} and 617 cm^{-1} in the spectra of doped TiO_2 photo-catalysts. The vibrational mode of the rutile phase at 143 cm^{-1} in all samples could not be detected probably due to the superimposition of the anatase peak at 144 cm^{-1}. Generally all peaks in the spectrum of undoped TiO_2 are due to the anatase phase. When only carbon was used as the dopant, the E_g peak at 144 cm^{-1} nearly disappeared and all its major peaks were due to the rutile phase.

5.5.3 XRD Analysis

This section presents the XRD analysis of undoped TiO_2, Ag doped TiO_2, Au doped TiO_2, C doped TiO_2, Ag/C co-doped TiO_2 and Au/C co-doped TiO_2 photo-catalysts. The operating conditions and model of the instrument used for analysis was presented in Section 3.12.7

5.5.3.1 XRD analysis of Ag/C co-doped TiO_2 photo-catalysts

The XRD patterns of undoped TiO_2 and Ag/C co-doped TiO_2 photo-catalyst are shown in Figure 5.8.

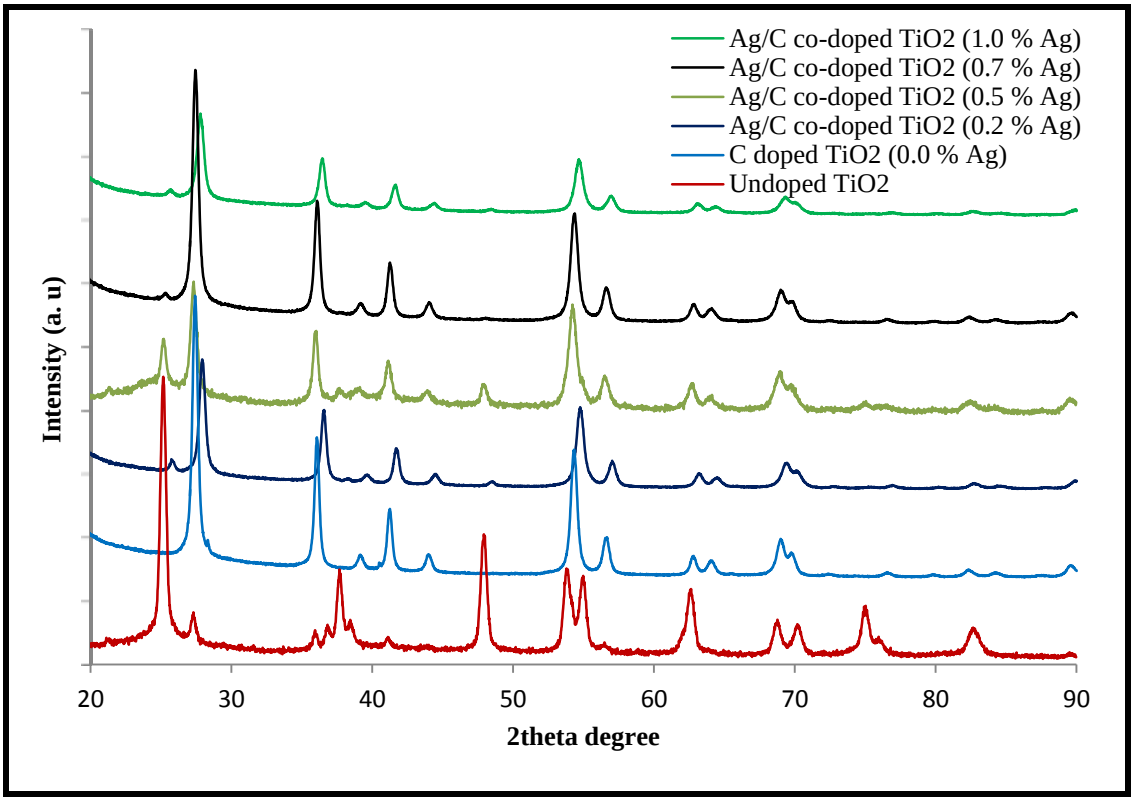

Figure 5.8: XRD patterns of undoped TiO_2 and Ag/C co-doped TiO_2 photo-catalysts with different contents of Ag.

In Figure 5.8 the peaks at 2θ 25.1°, 37.6°, 47.8°, 53.9°, 56.2 °,62.5°, 68.8°, 70.4°, 74.8° and 82.4° for all samples correspond to the diffraction of (101), (004), (200), (105), (211), (204), (116), (301), (215), and (224) crystal faces of the anatase phase of TiO_2 (An *et al*., 2012). The peaks at 27.6°, 36.1 °, 41.1°, 43.81°, 54.6° (only found in undoped TiO_2) and 68.8° were due to the (110), (101), (200), (210), (220) and (301) mirror planes of the rutile phase which support Raman data. The peak at 2 theta 63.7 ° which was only present in the doped photo-catalysts could be assigned to the (220) crystal planes of Ag (Barakat *et al*., 2011). All the XRD peaks for the photo-catalysts with Ag loading of 0.2 % and 1.0 % shifted slightly by approximately 2θ = +0.3°.

When the spectrum of undoped TiO_2 is compared with doped TiO_2 photo-catalysts, the relative intensities of some peaks and peak areas for example at $2\theta = 47.8°$ were altered due to lattice distortion and change in the degree of crystallinity caused by dopants. The ratio of XRD peaks was also changed due to transition from anatase to rutile resulting in larger rutile grain size (Dorian & Sorrell., 2011).

The XRD results were in agreement with Raman results which also showed that Ag and carbon co-doping of TiO_2 promoted anatase to rutile phase transformation. For instance, the intensity of the major peak at $2\theta = 25.1°$ due to anatase in the spectra of the undoped TiO_2 reduced significantly when the TiO_2 was co-doped with Ag and C (all samples) and it completely disappeared in the spectrum of TiO_2 doped with carbon only. The peaks at $2\theta = 27.3°$, 36.2 ° and 41.1 ° due to rutile phase which were very small in the spectra of undoped TiO_2 increased in intensity in the spectra of all doped TiO_2 photo-catalysts indicating phase transformation had been induced by doping with Ag and carbon. There was a new peak at 2θ value of 43.8° due to anatase which was non-existent in the spectra of undoped TiO_2 but present in all doped TiO_2 samples. The major phase in the C-doped TiO_2 (0.0 % Ag) was rutile as shown in its spectrum in Figure 5.8 with very intense peaks due to rutile when compared to other spectra. Two new peaks at $2\theta = 43.6°$ and 63.6° assigned to the rutile phase and Ag respectively appeared in the spectra of all doped samples but were not visible in the spectra of undoped TiO_2.

5.5.3.2 XRD analysis of Au/C co-doped TiO_2 photo-catalysts

The XRD patterns of undoped TiO_2 and Au/C co-doped TiO_2 photo-catalysts are shown in Figure 5.9.

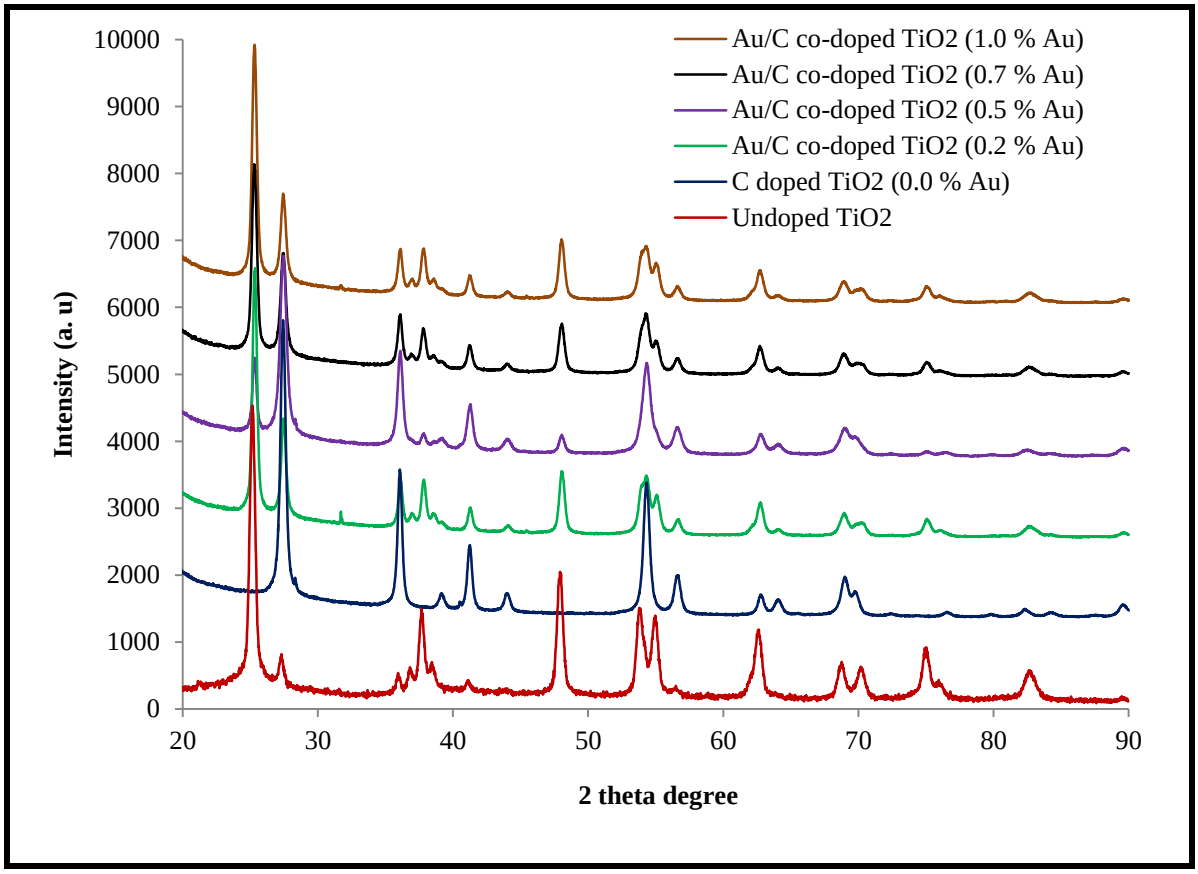

Figure 5.9: XRD patterns of undoped TiO_2 and Au/C co-doped TiO_2 photo-catalysts with different contents of Au.

Generally as Figure 5.9 shows, there was no general trend followed as the Au dopant content was increased. The peaks observed in the Au/C co-doped TiO_2 samples due to anatase and rutile phases were also found in the spectra of Ag/C co-doped TiO_2 but with differences in relative peak intensities. The major peak at $2\theta = 25.2°$ due to anatase which completely disappeared in the spectra of TiO_2 doped with carbon only {C doped TiO_2 (0.0 % Au)} is found in the spectra of all gold/carbon co-doped TiO_2 photo-catalysts and undoped TiO_2. A significant decrease in intensity of this peak ($2\theta = 25.2°$) was only found in the spectra of Au/C co-doped TiO_2 (0.5 % Au). This shows that doping with Au does not cause much anatase to rutile phase transformation when compared to the silver. This is further supported by the anatase diffraction peak at $2\theta = 37.5$ ° which appeared in the gold/carbon doped series

of samples but disappeared completely in the spectra of the Ag/C co-doped TiO_2. New diffraction peaks were observed at 43.5° and 63.72° in the spectra of the gold/carbon doped series of samples due to rutile and anatase respectively. The peak at $2\theta = 54.4°$ which is due to anatase phase appeared in the gold doped samples but was not present in the spectra of Ag/C co-doped samples and disappeared completely. As a comparison, Au/C co-doped TiO_2 showed more intense peaks due anatase than due to rutile whereas Ag/C co-doped TiO_2 showed intense peaks due to rutile than anatase phase. Therefore silver doping favoured anatase to rutile phase transformation but gold does not.

Table 5.2 shows detailed XRD results (accurate peak positions, d-spacing, relative intensities, peak heights and full width half maximum (FWHM)) for undoped TiO_2 photo-catalyst which is the reference for all the series of doped TiO_2 photo-catalysts. From the relative intensities, it could be seen that the major peak for undoped TiO_2 was at $2\theta = 25.13°$ due to the anatase phase.

Table 5.2: Detailed XRD values of undoped TiO_2 photo-catalyst.

Pos. [2 Theta °]	Height [cts]	FWHM[2 Theta °]	d-spacing [Å]	Rel. Int. [%]
18.1639	51.05	3.2118	4.88407	1.41
25.1581	3618.42	0.8029	3.53988	100.00
27.2099	385.28	0.8029	3.27743	10.65
37.7769	976.21	1.0706	2.38144	26.98
41.0751	123.24	0.8029	2.19752	3.41
47.9233	1781.63	0.5353	1.89827	49.24
53.8523	1267.29	0.5353	1.70244	35.02
55.0533	945.41	0.8029	1.66811	26.13
62.6063	1009.71	0.5353	1.48381	27.90
68.7461	505.43	0.5353	1.36551	13.97
70.2036	457.50	0.5353	1.34069	12.64
75.0119	717.44	0.5353	1.26623	19.83
82.6978	412.39	0.8029	1.16695	11.40

The crystallographic parameters of the sol-gel synthesised undoped TiO_2 obtained from the XRD instrument were as follows; crystal system: tetragonal, space group: P42/mm, space group number: 136 and the lattice constants a(Å), b(Å) and c(Å) were 4.5928, 4.5928 and 2.9605 respectively. The volume of the cell was 62.45 × (10^6 pm^3). From this information it shows that the prepared undoped TiO_2 had no brookite phase but only anatase and rutile.

To estimate the anatase percentage (A %), equation 5.1 was used for calculations (Lu *et al*., 2014).

$$A\ \% = \frac{100}{(1+1.265\frac{I_r}{I_a})} \qquad 5.1$$

Where: I_r is the peak intensity of rutile at 2 theta value of 27.4°.

I_a is the peak intensity of anatase at 2 theta value of 25.3°.

The amount of rutile that was transformed as a mass fraction (F_R) was calculated using equation 5.2 (Dang *et al*., 2010)

$$F_R = \frac{1}{(1+0.79\frac{I_A}{I_R})} \qquad 5.2$$

where: I_A is the integrated intensity of (101) anatase (2θ = 25.3°)

I_R is the integrated intensity of (110) rutile (2θ = 27.45°)

The calculated percentage of the anatase phase in the undoped TiO_2 photo-catalyst was found to be 88.13 % and the fraction of rutile using equation 5.2 was 0.1188 which is 11.88 %. The calculated anatase and rutile phases in all the sol-gel synthesized undoped and doped TiO_2 photo-catalysts are shown in Table 5.3.

Table 5.3: Calculated percentages of anatase and rutile phases.

Sample	**Percentage of Anatase**	**Percentage of Rutile**
Undoped TiO_2	88.13	11.88
C doped TiO_2 (0.0 % Au)	2.09	97.91
Au/C co-doped TiO_2 (0.2 % Au)	63.32	36.68
Au/C co-doped TiO_2 (0.5 % Au)	23.73	76.27
Au/C co-doped TiO_2 (0.7 % Au)	55.96	44.04
Au/C co-doped TiO_2 (1.0 % Au)	64.63	35.37
C doped TiO_2 (0.0 % Ag)	2.09	97.91
Ag/C co-doped TiO_2 (0.2 % Ag)	22.60	77.40
Ag/C co-doped TiO_2 (0.5 % Ag)	22.95	77.05
Ag/C co-doped TiO_2 (0.7 % Ag)	2.20	97.80
Ag/C co-doped TiO_2 (1.0 % Ag)	13.92	86.08

When carbon was the only dopant used, it was observed that the highest anatase to rutile phase transformation occurred and the sample had 2.09 % anatase and 97.91 % rutile followed by Ag/C co-doped TiO_2 (0.7 % Ag) photo-catalyst with 2.20 % anatase and 97.80 % rutile. There was no general trend followed on the extent of anatase to rutile phase transformation as the Au content was increased. In case of Ag doping, there was a general increase in the anatase to rutile phase transformation with an increase in the Ag content. When compared to Au, Ag favoured more anatase to rutile transformation and these results are in agreement with the observed Raman results.

5.5.4 Carbon content determination

This section presents the CHNS analysis of Au/C co-doped TiO_2 photo-catalysts. The procedure for the analysis was presented in Section 3.12.4. The CHNS analyser was used to determine the carbon content in all carbon and gold co-doped TiO_2 photo-catalysts to determine the amount of carbon in the resulting co-doped photo-catalysts. The percentage of carbon in Au/C co-doped TiO_2 photo-catalysts are shown in Table 5.4.

Table 5.4: Carbon content analysis of Au/C co-doped TiO_2 photo-catalysts with different Au contents.

Sample	**Percentage of Carbon**
C doped TiO_2 (0.0 % Au)	0.46
Au/C co-doped TiO_2 (0.2 % Au)	0.44
Au/C co-doped TiO_2 (0.5 % Au)	0.55
Au/C co-doped TiO_2 (0.7 % Au)	0.53
Au/C co-doped TiO_2 (1.0 % Au)	0.41

There was no general trend that was found for the amount of carbon in the doped TiO_2 photo-catalysts. The highest carbon content was found in the TiO_2 photo-catalyst doped with 0.5 % Au and the least in the sample that was doped with 1.0 % Au as shown in Table 5.4. There was also no general trend that was observed on the band gap shifts reported in Section 5.5.1.2 with the amount of carbon that was found in the Au/C co-doped TiO_2 photo-catalysts.

5.5.5 FTIR analysis of co-doped TiO_2 photo-catalysts

The FTIR analysis procedure was presented in Section 3.12.9. The FTIR spectra of the Ag/C-TiO_2 photo-catalysts in the region between 400 cm^{-1} and 4000 cm^{-1} are shown in Figure 5.10.

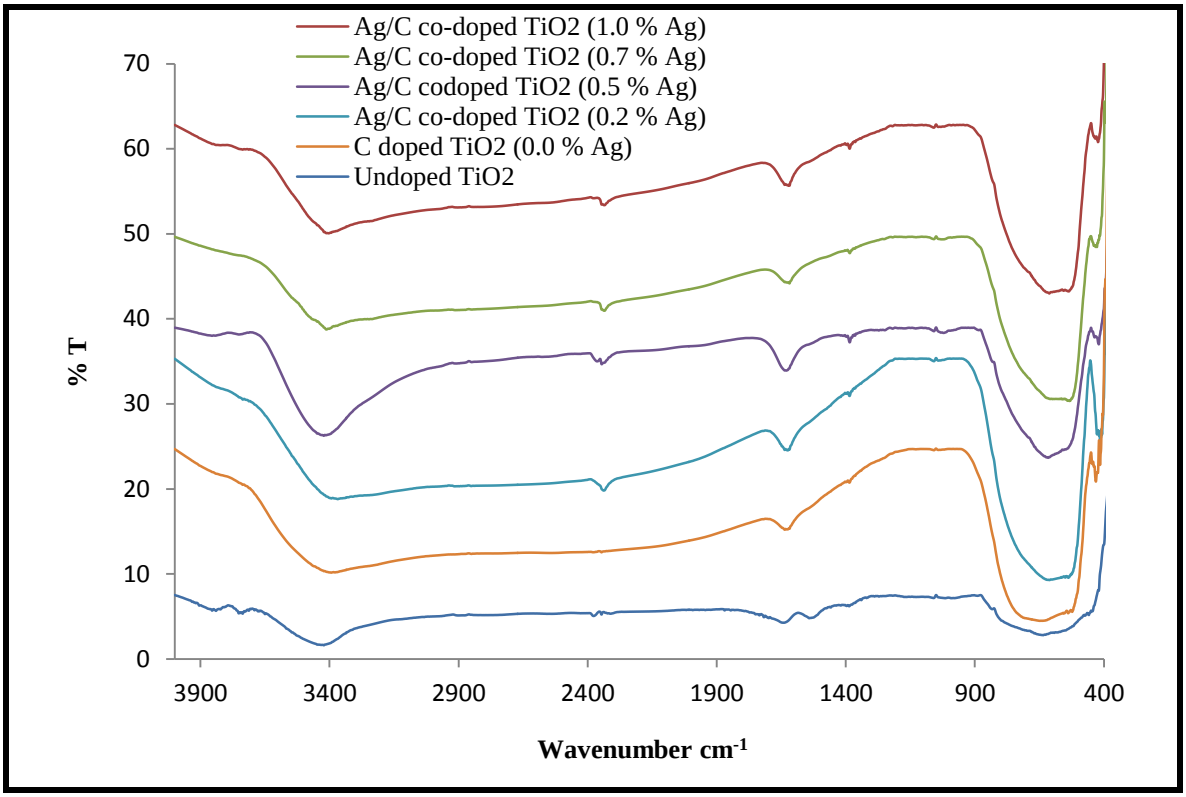

Figure 5.10: FTIR spectra of Ag/C co-doped TiO_2 photo-catalysts with different Ag contents.

The broad peaks around 3450 cm^{-1} and at 1655 cm^{-1} were assigned to the stretch vibration and characteristic bending frequency of O-H groups of adsorbed water respectively (Ding *et al*, 2000). These were more intense in the spectrum of the photo-catalyst with Ag loading of 0.5 %. The pronounced broad band in the range 400-900 cm^{-1} was assigned to the stretching vibration of the Ti-O bond and it was common in the spectra of all samples. The peak at 2358 cm^{-1} due to the presence of carbon species (Palanivelu *et al*., 2007) is common to all samples except TiO_2 that had 0.0 % Ag loading and undoped TiO_2. From this observation it can be assumed that the appearance of this peak was caused by the presence of Ag in the TiO_2 photo-catalysts. The undoped TiO_2 is the only photo-catalyst that has a peak at 1557 cm^{-1}.

The FTIR spectra of Au/C co-doped TiO_2 photo-catalysts are shown in Appendix B Figure B-2. The spectra are similar to those of the Ag/C co-doped TiO_2 photo-catalysts but with

relatively lower intensities of the peak around 2358 cm^{-1}. The spectrum of Au/C co-doped TiO_2 with Au loading of 1.0 % showed the most pronounced peaks around 3450 cm^{-1} and 1655 cm^{-1} assigned to the hydroxyl group of adsorbed water.

5.5.6 BET surface area analysis of doped TiO_2

The BET surface area analysis was used to determine the surface area, pore volume and pore size of the undoped and doped TiO_2 photo-catalysts and the detailed procedure for analysis was presented in Section 3.12.6. The BET surface area, pore volume and pore size of undoped TiO_2 and doped TiO_2 photo-catalysts are shown in Table 5.5.

Table 5.5: BET surface area, pore volume and pore size of undoped TiO_2 and doped TiO_2 photo-catalysts.

Sample	BET surface area (m^2/g)	Pore volume (cm^3/g)	Pore size (nm)
Pure TiO_2	68.97	0.28	16.48
Au doped TiO_2	50.25	0.26	24.37
Ag doped TiO_2	33.75	0.12	14.47
C-doped TiO_2 (0.0 % Ag)	83.14	0.23	15.35
Ag/C co-doped TiO_2 (0.2 % Ag)	11.14	0.10	36.47
Ag/C co-doped TiO_2 (0.5 % Ag)	15.07	0.13	33.54
Ag/C co-doped TiO_2 (0.7 % Ag)	32.00	0.28	35.31
Ag/C co-doped TiO_2 (1.0 % Ag)	28.66	0.13	18.50
Au/C co-doped TiO_2 (0.2 % Au)	47.04	0.26	22.23
Au/C co-doped TiO_2 (0.5 % Au)	47.53	0.26	24.12
Au/C co-doped TiO_2 (0.7 % Au)	47.77	0.26	25.28
Au/C co-doped TiO_2 (1.0 % Au)	23.20	0.16	27.32

The differences in the surface area and porosity of particles of the same material, which otherwise may have the same physical dimensions; can greatly influence its performance characteristics. The highest surface area was achieved when carbon was used as the dopant implying that carbon doping increases the surface area of TiO_2. When silver or gold were used as the only dopants there was a decrease in the surface from 68.97 m^2/g for undoped TiO_2 to 33.75 m^2/g and 50.25 m^2/g for silver and gold doped TiO_2 respectively. These results show that doping with either silver or gold reduces the surface area of TiO_2.

The surface area of the silver carbon co-doped TiO_2 photo-catalysts increased slightly with increase in the silver content and decreased with silver contents above 0.7 %. The no trend was also observed when the gold content was increased. It is believed that a photo-catalyst with high surface area is desirable since an enhanced surface area allow greater adsorption of pollutants resulting in enhancement of photo-catalytic activity. The results from this analysis showed that co-doping of TiO_2 with either silver and carbon or gold and carbon results in a decrease in the surface area of TiO_2 photo-catalyst.

5.5.7 Thermal properties co-doped TiO_2 photoatalysts

The thermograms of the prepared photo-catalysts were obtained by heating samples (10 mg) from 20 °C to 800 °C at a heating rate of 20 °C/min in a nitrogen environment. The samples were analysed in powder form after calcination as is detailed in Section 3.12.10. The thermograms showing the percentage weight loss of undoped TiO_2 and Au/C co-doped TiO_2 photo-catalysts with increasing temperature are shown in Figure 5.11.

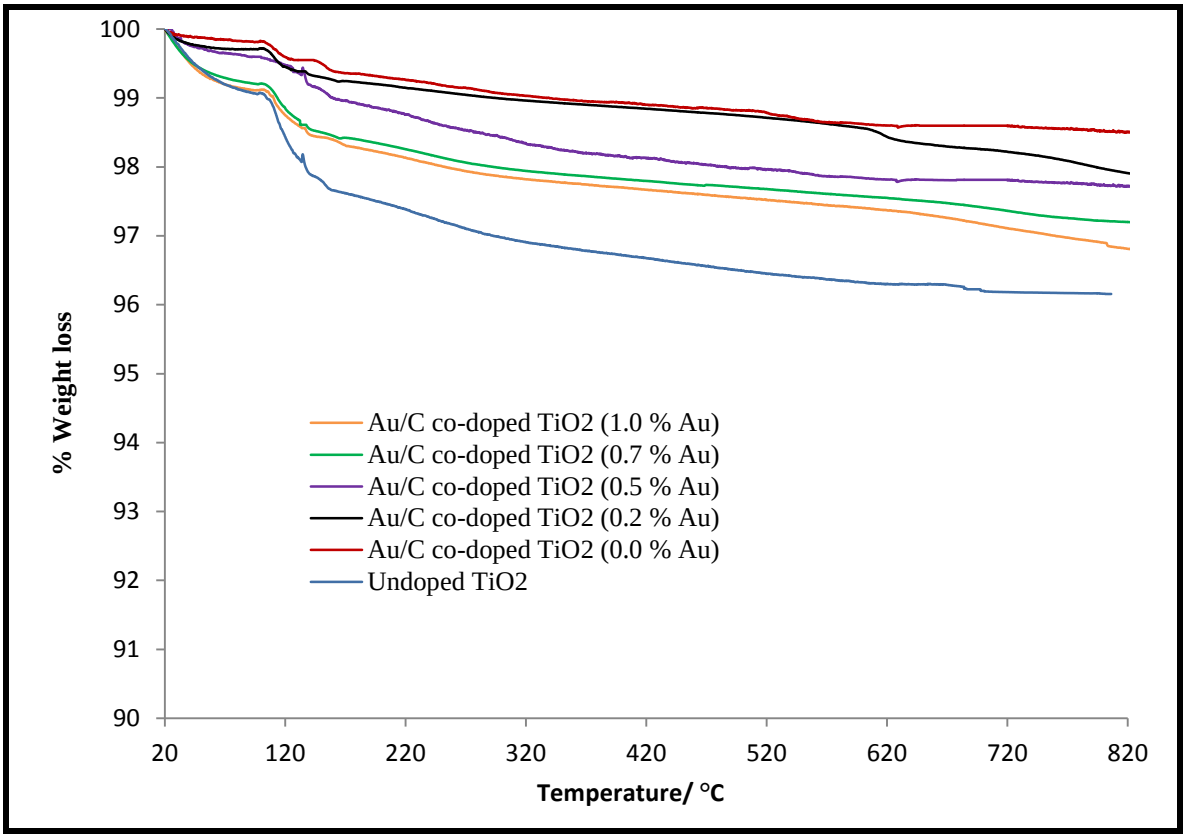

Figure 5.11: Thermograms of undoped TiO_2 and Au/C co-doped TiO_2 photo-catalysts in powder form.

All the Au/C co-doped TiO_2 and undoped TiO_2 photo-catalysts showed a mass loss at around 100 °C due to the loss of adsorbed water from the TiO_2 surface. There was a gradual increase in total weight loss until 800 °C with an increase in Au content. The TiO_2 with 0.0 % Au showed a total weight loss of 1.48 % whereas the TiO_2 with 1.0 % Au showed 3.35 % weight loss. Since the total mass lost was less than 3.35 %, it suggests that the photo-catalysts were thermally stable. It is likely that most carbonaceous material from glucose (C-dopant source) was combusted during the calcination process in air.

The thermograms of carbon and silver co-doped TiO_2 photo-catalysts are shown in Appendix B Figure B-3. The percentage weight loss of the photo-catalysts also increased with increase in Ag loading. When the total weight losses were compared between the Au/C co-doped TiO_2

and Ag/C co-doped TiO_2 photo-catalysts, generally the gold doped TiO_2 photo-catalysts lost more weight than the silver doped TiO_2 photo-catalysts for the same metal content as shown in Table 5.6.

Table 5.6: TGA percentage weight loss of C/metal co-doped TiO_2 photo-catalysts.

Photo-catalyst	**Percentage weight loss**	
	M = Au	**M = Ag**
Undoped TiO_2	3.83	3.83
C doped TiO_2 (0.0 % M)	1.46	1.46
C/M co-doped TiO_2 (0.2 % M)	1.99	1.73
C/M co-doped TiO_2 (0.5 % M)	2.25	1.76
C-M co-doped TiO_2 (0.7 % M)	2.78	2.18
C/M co-doped TiO_2 (1.0 % M)	3.08	2.36

The small change in weight of the undoped TiO_2, Au/C co-doped TiO_2 and Ag/C co-doped TiO_2 photo-catalysts was due to the fact that, the samples had already been subjected to calcination before the TGA analysis thus most volatiles would have evolved.

5.5.8 Photo-catalytic evaluations under visible light irradiation

This section presents the evaluation of the photo-catalytic activities of quartz supported undoped TiO_2, Ag/C co-doped TiO_2 and Au/C-co-doped TiO_2 photo-catalysts that were prepared according to the procedure specified in Section 3.3.2 using methyl orange solution under visible light irradiation at 25 °C and pH 7 as detailed in Section 3.11. The experimental set-up of the photo-degradation process is shown in Figure 3.5. The varied parameter was the metal dopant content in the TiO_2 photo-catalyst, the control was undoped TiO_2 photo-catalyst and the fixed parameters were the experimental conditions (initial methyl orange concentration and volume, light intensity, pH and temperature)

5.5.8.1 Photo-degradation of methyl orange using Ag/C co-doped TiO_2

Figure 5.12 shows the photo-degradation curves of methyl orange (100 mL, 10 ppm) using undoped TiO_2, Ag doped TiO_2 and Ag/C co-doped TiO_2 photo-catalysts with different contents of Ag under visible light irradiation at 25 °C and pH 7.

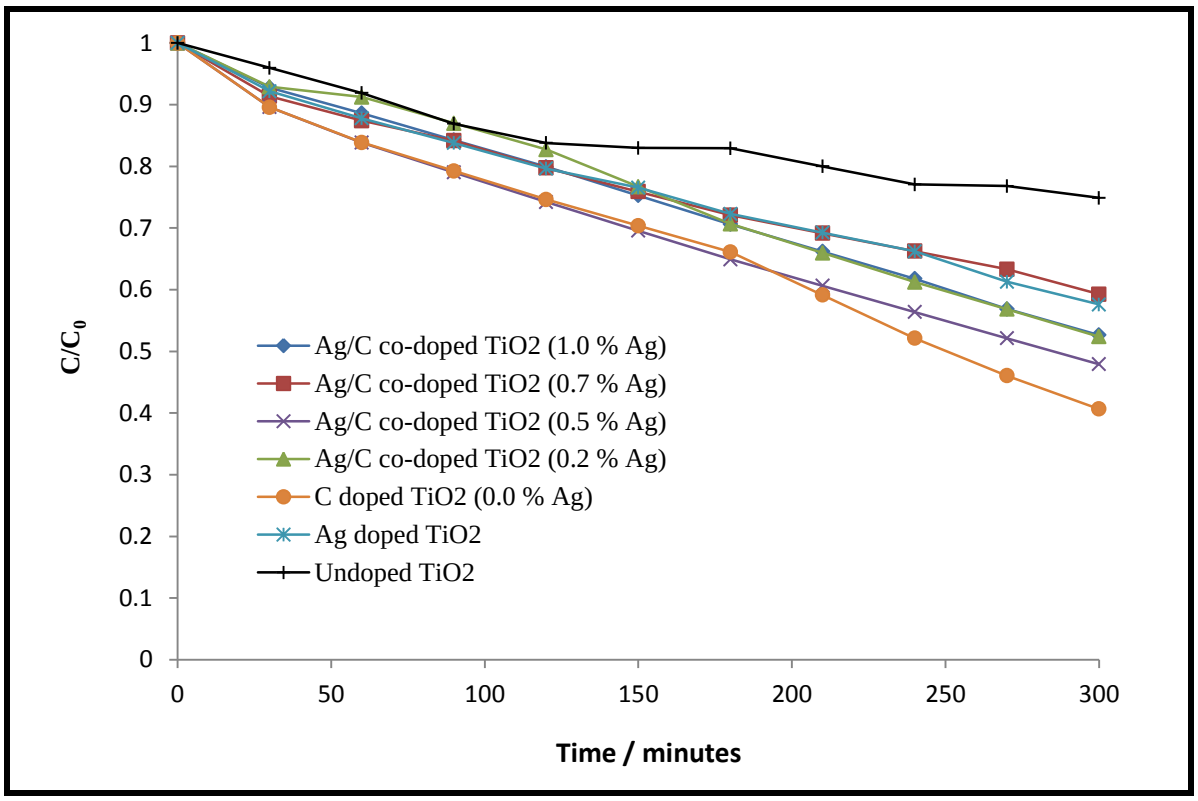

Figure 5.12: Photo-degradation curves of 10 ppm methyl orange solution using Ag/C co-doped TiO_2 photo-catalysts with different contents of Ag under visible light irradiation at 25 °C and pH 7.

The Ag/C co-doped photo-catalysts showed different photo-degradation rates which were higher than that of undoped TiO_2 photo-catalyst. The possible reasons for the differences in the photo-degradation activities include (i) the differences in the anatase to rutile ratios in the samples, (ii) surface area/particle size differences, (iii) different contents of residual carbon, (iv) different rates of recombination of charge carriers and (v) different band gap values.

The highest photo-degradation of 60 % under visible light for a period of 300 minutes was achieved by TiO_2 doped with carbon only (0.0 % Ag) probably because of the high surface area for adsorption of the contaminant. For the carbon and silver co-doped photo-catalysts, there was an increase in photo-degradation of methyl orange from 47.61 % to 52.07 % after 300 minutes when the Ag loading was increased from 0.2 % to 0.5 % and it decreased with further increase in Ag content to 0.7 % as shown in Figure 5.12.

The optimum loading of Ag in the Ag/C co-doped TiO_2 photo-catalysts for efficient photo-degradation of methyl orange was found to be 0.5 %. The reason for this high activity is ascribed to the lower band gap of 1.95 eV (Table 5.1) and thus improved visible light absorption. It is important to note that the material with a lower band gap will not always have higher photo-catalytic activity. For instance, the photo-catalytic activity of Ag/C co-doped TiO_2 (0.7 %) with a calculated band gap of 2.53 eV was lower than that of Ag/C co-doped TiO_2 (1.0 %) with a band gap of 2.72 eV which was unexpected on the basis of band gaps. This observation suggests that, band gap narrowing could improve the visible-light absorption but without necessarily improving visible-light photo-catalytic activity. In some cases the band gap reduction cannot give good photo-degradation efficiencies as expected due to other factors such as dopant level, or surface areas which come into play. The dopant level directly influences e^-/h^+ recombination rates and for optimal e^-/h^+ separation, the magnitude of the potential drop across the space-charge layer should be greater than 0.2 V (Gautron *et al*., 1981, Gupta & Tripathi.; 2011). As a result there is an optimum dopant loading that gives a space-charge region that allows for efficient separation of the charge carriers. Hence Ag/C co-doped TiO_2 (1.0 %) photo-catalyst could have lower recombination rates than Ag/C co-doped TiO_2 (0.7 %) which explains the observed results. These findings

show that the optimum dopant level to achieve low band gaps is different from the optimum loading to achieve low recombination rates.

Anatase has been reported to be more photo-catalytically active than the rutile phase but all the co-doped samples particularly the C doped TiO_2 photo-catalyst, which had lower anatase showed higher photo-catalytic activity than undoped TiO_2 which had more anatase than rutile. However, it has been found that a mixture of anatase and rutile with a ratio of 75: 25 is beneficial in reducing recombination of charge carriers resulting in a much higher photo-catalytic activity than either pure anatase or pure rutile TiO_2 photo-catalyst (Haizel 2013; Zhang *et al*., 2008). This could also partially explain why Ag/C co-doped TiO_2 (0.5 %) showed the highest photo-catalytic activity.

5.5.8.2 Photo-degradation of methyl orange using Au/C co-doped TiO_2

The photo-degradation curves of methyl orange (100 mL, 10 ppm) using undoped TiO_2 and Au/C co-doped TiO_2 photo-catalysts with different contents of Au under visible light irradiation at 25 °C and pH 7 are shown in Figure 5.13.

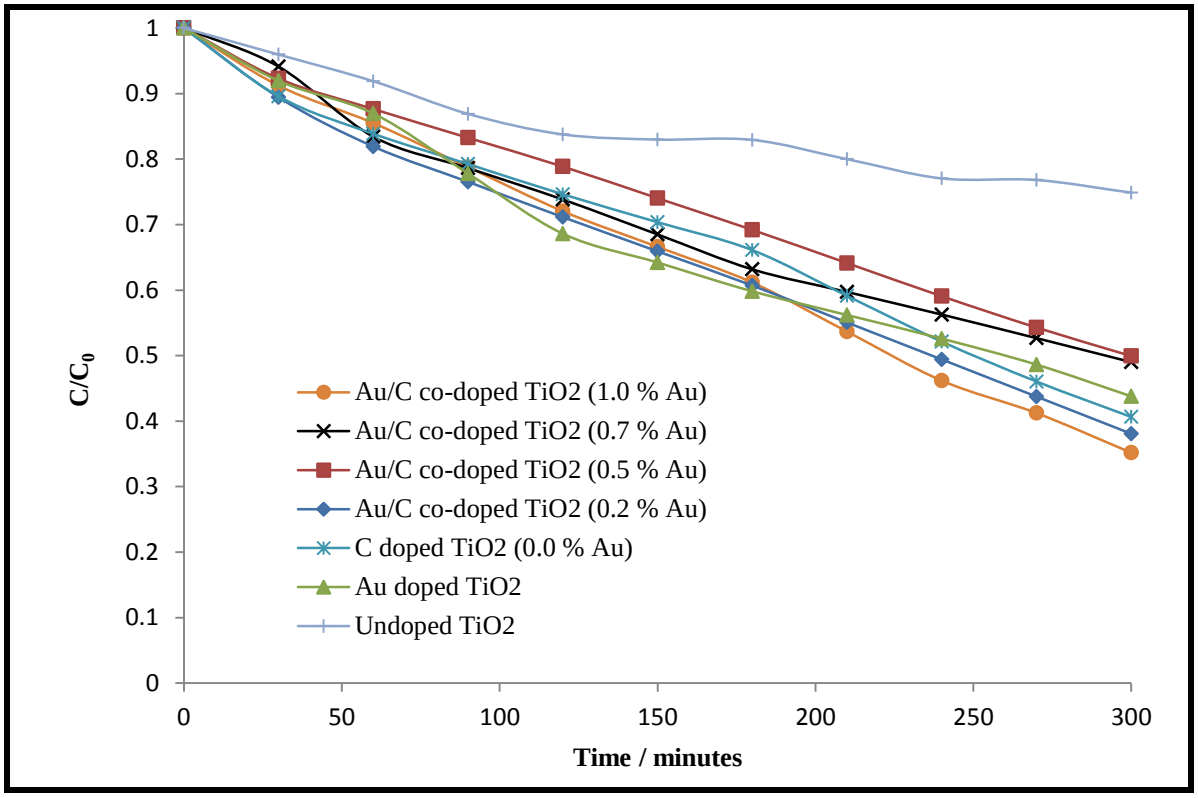

Figure 5.13: Photo-degradation curves of 10 ppm methyl orange solution using Au/C co-doped TiO_2 photo-catalysts with different contents of Au under visible light irradiation at 25 °C and pH 7.

The Ag/C co-doped TiO_2 photo-catalysts performed better than the undoped TiO_2 photo-catalyst but there was no correlation observed between photo-catalytic activity and the increasing Au content. The highest photo-catalytic activity was achieved by the photo-catalyst with the highest Au content and the smallest band gap hence the efficient visible light absorption gives a rationale for this observed result. The sample with a gold content of 0.7 % had the highest BET surface area among the gold doped TiO_2 photo-catalysts but its photo-catalytic activity was not the highest as could be expected. Hence higher surface does not necessarily mean high activity. The better performance of the doped TiO_2 could also be attributed to the trapping of photo-generated electron pairs thereby effectively separating the electron-hole pairs (Jiang *et al*., 2013). On the other hand, the incorporation of dopants can

introduce defect levels and break the crystal symmetry resulting in an increase in visible light absorption thus enhancing efficient photo-catalysis (Stoneham *et al*., 2007).

It has been reported that co-doping with different elements could achieve some synergistic effects between the incorporated elements resulting in better performance of the TiO_2 photo-catalyst than the single element doped TiO_2 (Jiang *et al*., 2013). In this study co-doping TiO_2 with carbon and gold (1.0 %) was found to improve photo-degradation of methyl orange more than using TiO_2 doped with carbon only although this was not the case with carbon co-doping with Ag, hence the metal type also plays a role in the photo-activity

5.5.8.3 Comparison of the effects of Au, Ag and C on TiO_2 photo-activity

This section presents a comparison of the effects of both Au and Ag when they are used with carbon to co-dope TiO_2 photo-catalyst. Table 5.6 shows the percent photo-degradation of methyl orange (100 mL, 10 ppm) after 300 minutes by C doped TiO_2, Au doped TiO_2, Ag doped TiO_2, Au/C co-doped TiO_2 and Ag/C co-doped photo-catalysts.

Table 5.7: Percent photo-degradation of MeO using Ag/C co-doped TiO_2 and Au/C co-doped TiO_2 photo-catalysts under visible light irradiation at 25 °C and pH 7.

Photo-catalyst	**% Degradation after 300 minutes**	
	M (Ag)	**M (Au)**
M doped TiO_2	42.40	56.21
C doped TiO_2 (0.0 %)	59.36	59.36
C/M co-doped TiO_2 (0.2 % M)	47.61	61.92
C/M co-doped TiO_2 (0.5 % M)	52.07	50.06
C/M co-doped TiO_2 (0.7 % M)	40.74	50.98
C/M co-doped TiO_2 (1.0 % M)	47.36	64.81

Table 5.7 shows that, Au generally improved that photo-catalytic activity of TiO_2 than silver hence metal type plays a role in TiO_2 photo-activity. There was no general trend followed in the photo-catalytic activities with an increase in metal loading. It is clear from the table that when carbon is used as the only dopant, it performs better than silver or gold doped TiO_2 whereas the Ag or Au carbon co-doped TiO_2 photo-catalysts were not as active, apart from Au/C co-doped TiO_2 photo-catalyst. This could be ascribed to the high surface area of the C doped TiO_2 photo-catalyst. Higher surface area promotes adsorption of the contaminants resulting in an increase in photo-degradation. The synergistic effects came into play in reducing the band gap, which was not the only parameter that affected photo-catalytic activity. The catalytic performance depended also on surface properties particularly the surface phases since the reactions took place on the surface of TiO_2. Hence the TiO_2 surface phase that was exposed to light plays an important role in the photo-degradation process (Linsebigler *et al*., 1995). This explains why some photo-catalysts with low band gap had lower photo-catalytic activities than some photo-catalysts with a slightly higher band gap. In case of carbon and gold co-doping, it was only the photo-catalysts that had Au content of 0.5 % and 0.7 % which showed a lower photo-catalytic activity than the single element doped TiO_2. This showed that there is an optimum dopant level that is required to have a synergy between the carbon and the Au.

5.5.9 Kinetics of methyl orange photo-degradation by co-doped TiO_2

The kinetics of methyl orange photo-degradation under visible light by co-doped TiO_2 photo-catalysts are given in graphical form by plotting the logarithm of the normalized methyl orange concentration against irradiation time. The reactions followed first-order kinetics regardless of the type of photo-catalyst used, as was evidenced by the linear relationships between irradiation time and the logarithm of the normalized concentration, shown in Figure

5.14 for Ag/C co-doped TiO_2 and Figure 5.15 for Au/C co-doped TiO_2 photo-catalysts. All the series of doped TiO_2 photo-catalysts showed higher photo-catalytic activity and rate constants than the undoped TiO_2 photo-catalyst.

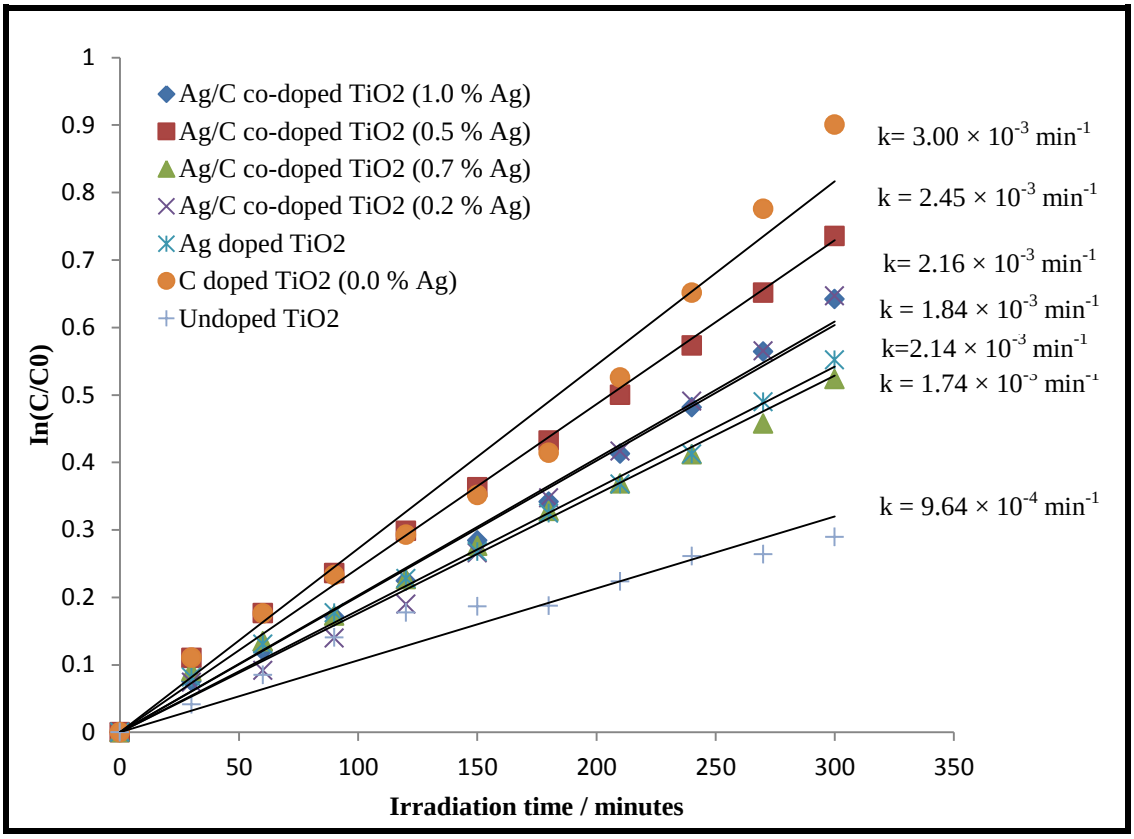

Figure 5.14: Kinetics of the photo-degradation of methyl orange using carbon and silver co-doped TiO_2.

Figure 5.14 shows that the C-doped TiO_2 had the highest rate when compared to Ag/C co-doped TiO_2 photo-catalysts. Among the Ag/C co-doped TiO_2 photo-catalysts, the highest rate of 2.45 $x10^{-3}$ min^{-1} was achieved by the photo-catalyst with a silver content of 0.5 % while the photo-catalyst with 0.7 % Ag content gave the lowest photo-degradation rate of 1.74 $x10^{-3}$ min^{-1}. The photo-degradation rate increased when the Ag loading was increased from 0.2 % to 0.5 % then decreased when the Ag loading was increased above 0.5 %. Co-doping of TiO_2 with Ag and C yielded better photo-degradation rates than co-doping with Ag only but

overall TiO_2 doped with only carbon performed better than the metal co-doped TiO_2 photo-catalysts.

Figure 5.15 shows the kinetics of the photo-degradation of 10 ppm methyl orange using undoped TiO_2, Au doped TiO_2 and Au/C co-doped TiO_2 photo-catalysts with different contents of Au.

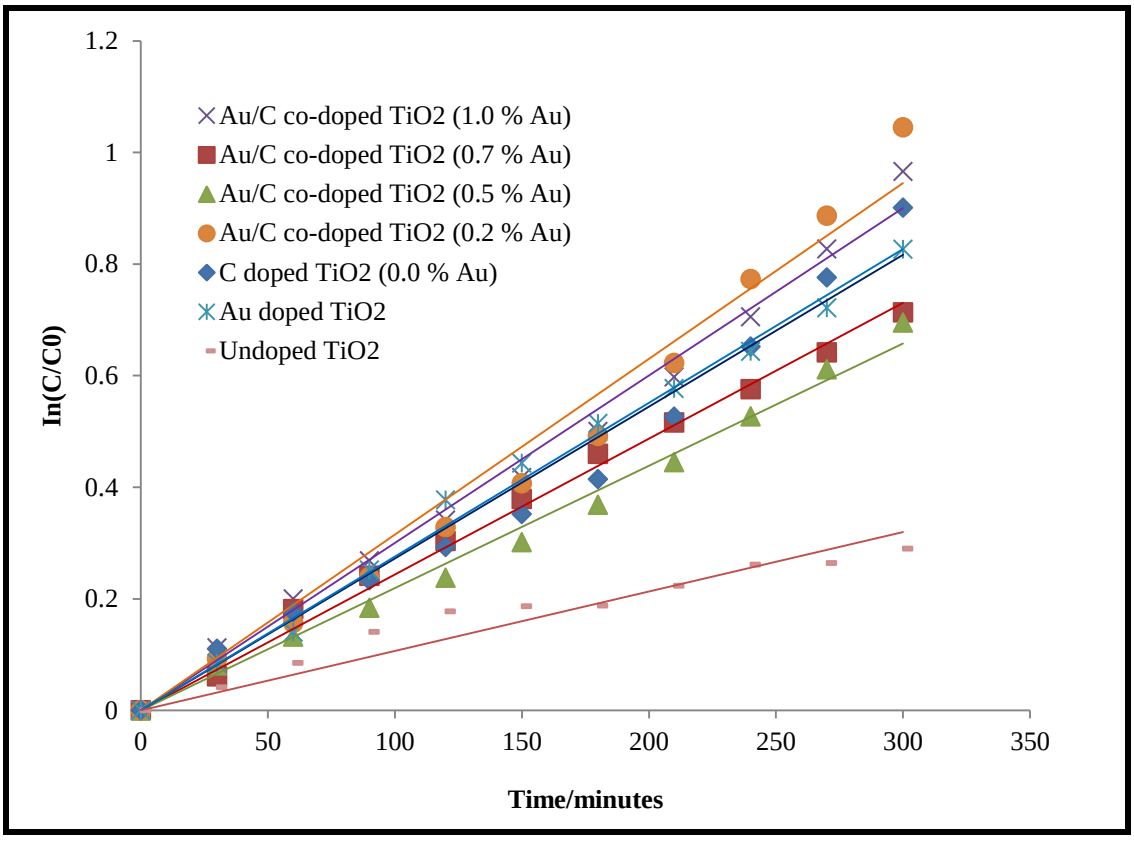

Figure 5.15: Kinetics of the photo-degradation of methyl orange using carbon and gold co-doped TiO_2.

Among the Au/C co-doped TiO_2 photo-catalysts, the sample with the highest Au loading gave the highest photo-degradation rate of 3.22×10^{-3} min^{-1} and the least photo-degradation rate of 2.32×10^{-3} min^{-1} from TiO_2 photo-catalyst with 0.5 % Au.

5.10 Summary

Au/C co-doped TiO_2 and Ag/C co-doped TiO_2 photo-catalysts were successfully prepared by a simple sol-gel technique and uniformly deposited on the quartz substrates. The agreement between the XRD and Raman analysis, which is surface sensitive suggests that the crystal phase in the surface region was the same as that in the bulk region. Raman spectroscopy made it possible to correlate the surface phase of TiO_2 to the photo-catalytic activity. No general correlation was observed between the band gap reduction and photo-catalytic activity with an increase in metal loading. The lowest band gap of 1.95 eV was achieved by co-doping with carbon and a Ag loading of 0.5 %. The optimal contents of Ag or Au for better photo-catalytic activities were 0.5 % and 1.0 % respectively but in general the Au/C co-doped TiO_2 photo-catalysts were more active than Ag/C co-doped TiO_2 photo-catalysts under the applied conditions. The higher photo-catalytic activities of the Au/C co-doped photo-catalysts could be explained by the high anatase than the rutile phase content. This is in agreement with literature that anatase is more active photo-catalytically than rutile but a mixture of the two in a ratio 4:1 anatase to rutile could be better than both pure anatase and pure rutile due to improved charge transfer and charge separation at the interfaces of the two polymorphs. The highest photo-catalytic activity for the degradation of 100 mL of 10 ppm methyl orange of 64.81 % after 300 minutes under visible light at 25 °C and pH 7 was achieved by using Au/C co-doped TiO_2 (1.0 % Au) photo-catalyst.

Chapter 6

Preparation of TiO_2/plasmon metal nanocomposite materials for the removal of dyes in water

6.0 Introduction

Attempts to improve the photo-catalytic activity of TiO_2 to efficiencies above 50 % by increasing its spectral response into the visible region through narrowing its band gap by doping have proven to be challenging. This is because of defect-induced charge trapping and recombination sites of photo-excited charge carriers, which compromise its photo-catalytic activity. This chapter reports on the evaluation of the photo-catalytic activity of nanocomposites of TiO_2 photo-catalyst and plasmon metal nanomaterials (Au, Ag and Cu). The chapter addresses the advantages of combining low band gap doped TiO_2 photo-catalyst and metal nanoparticles to reduce electron-hole recombination rates.

Plasmon metal nanostructures used to prepare the nanocomposites included spherical nanoparticles, nanorods and dendritic structures. In the case of spherical plasmon nanoparticles, copper, gold and silver nanoparticles of different contents (0.1, 0.5 and 1.0 % w/w) were mixed with undoped titanium dioxide as previously reported in Section 3.10. Nanocomposites of plasmon metals and Ag/C co-doped TiO_2 (0.5 % Ag), which had the lowest band gap (Table 5.1 in Chapter 5) were also prepared as previously detailed in Section 3.10. The effect of each nanomaterial on both boosting electron production under visible light due to localized surface plasmon resonance (LSPR) and/or acting as electron reservoirs under UV light and visible light was evaluated. The photo-catalytic activity evaluation experiments were carried out as reported in Section 3.11 so as to know the best metal compositions for the

enhancement of the photo-catalytic activity of TiO_2 photo-catalyst. The model pollutants used for the photo-catalytic activity evaluation were methyl orange and bromocresol purple using both visible light and UV light of wavelength 254 nm. A solar simulator was used as the source of light in experiments that were conducted using visible light.

6.1 Experimental procedures

The preparation of the following samples were reported in Chapter 3 under the sections given in brackets; doped TiO_2 nanoparticles (Section 3.3.2.5), spherical copper nanoparticles (Section 3.5), silver dendrites (Section 3.6), silver nanorods (Section 3.7), spherical silver nanoparticles (Section 3.8) and spherical gold nanoparticles (Section 3.9) .

6.1.2 Preparation of TiO_2/plasmon metal composite

The detailed procedure for the preparation of TiO_2/plasmon metal composites was reported in Section 3.10. To prepare TiO_2/gold nanoparticle composites containing 0.1 wt %, 0.5 wt % and 1.0 wt % Au, about 2 g of TiO_2 were mixed with 2 mg, 10 mg and 20 mg of gold nanoparticles respectively. The same procedure was followed to prepare TiO_2/Ag and TiO_2/Cu nanocomposites that had 0.1 wt %, 0.5 wt % and 1.0 wt % Ag or Cu.

6.1.3 Fabrication of TiO_2/plasmon metal composite films

A detailed method used for deposition of the nanoparticles on quartz as films was reported in Section 3.4. Prior to deposition of the films, the quartz supports were cleaned thoroughly, etched and then surface treated with MPTMS as previously discussed in detail in Section 3.2 of Chapter 3.

6.1.4 Determination of photo-degradation intermediates of methyl orange

The detailed experimental procedure for the sample preparation and operating conditions of the LC-MS instrument were reported in Chapter 3 Section 3.10.4 and Section 3.11.11 respectively. During the photo-degradation process of methyl orange at 25 °C and pH 7, aliquots were taken from the reaction vessel after every 20 minutes and filtered using a nylon syringe filter of pore size 1.22 μm and then analysed by LC-MS. The aliquots were also analysed by FTIR to establish the changes in the functional groups. The FTIR analysis was done by mixing a drop of the sample with KBr followed by pressing into a pellet which was then analysed.

6.2 Results and discussion

6.2.1 HRSEM and HRTEM Analysis

The HRSEM and HRTEM images of TiO_2 nanoparticles, silver dendrites (AgDR), silver nanorods (AgNR) and TiO_2/Au composite material are shown in Figure 6.1.

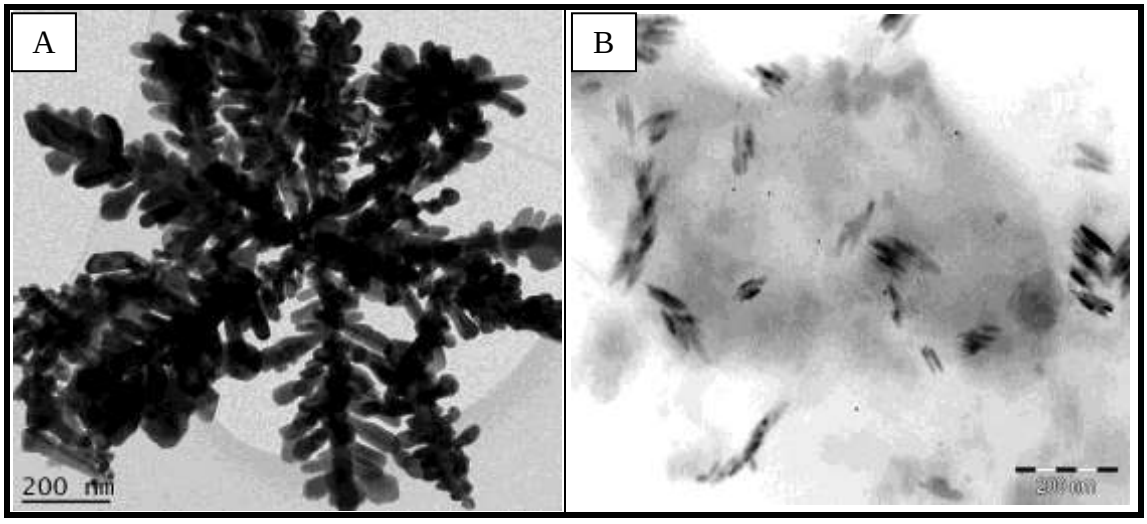

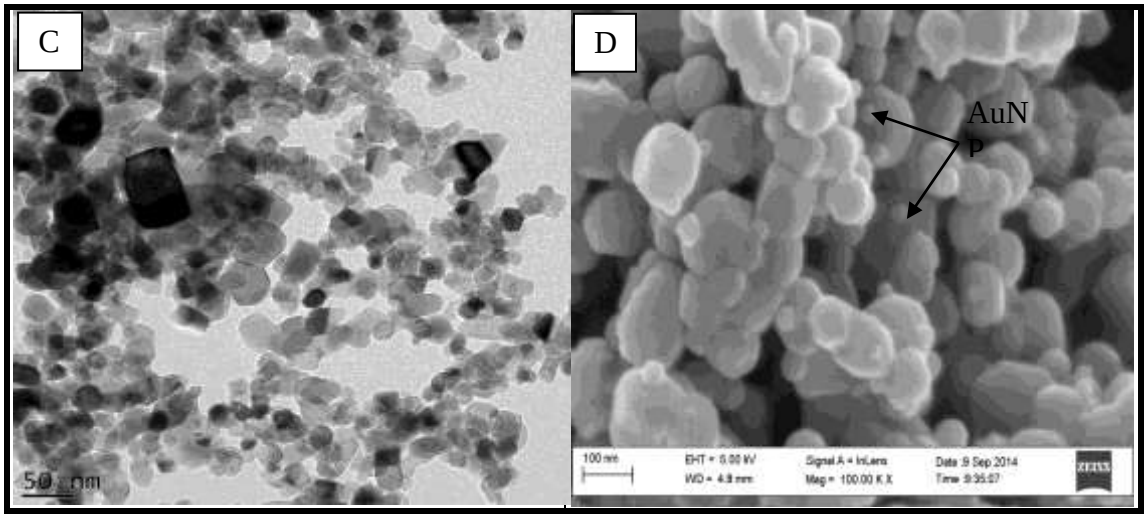

Figure 6.1: HRTEM images of (A) silver dendritic nanostructures, (B) Ag nanorods, (D) TiO_2 nanoparticles and (D) HRSEM of TAu1composites.

The prepared silver dendrites (Figure 6.1 A) had trunks that all grew from the center and spread outwards forming a star or flower like structure. As the branches grew from the trunks, they overlapped or joined other branches from other trunks forming a relatively dense network as shown in the HRTEM images in Figure 6.1 A. The individual dendrite was observed to be three dimensional with some branches that were connected to one main trunk in a regular pattern. The angles between the branches and the trunk were not the same, they varied approximately between 45 ° and 60 °. A closer look at the structures showed that some small branches also started to grow on some of the previously formed branches. The mechanism of growth of these dendrites in this way is not fully understood.

From the HRTEM image (Figure 6.1 B), it could be observed that the silver nanorods that were prepared by the reduction method were almost of the same size. Their lengths were between 51.22 nm and 82.83 nm and their width was approximately 15.86 nm. In TAu1 composite, HRSEM confirmed that the spherical plasmon metal nanoparticles were much

smaller than the TiO_2 nanoparticles and were on the surface of the semiconductor photo-catalyst (Figure 6.1 D).

6.2.2 Optical properties

This section presents the analysis of the selected samples (TAu1, TAu2, TAu3, TAg1, TAg2, TAg3, AgSNP, AgNR and AgDR) using UV-Vis spectroscopy to establish the region in which the samples absorb light. The sample codes and description were presented in Table 3.3 in Chapter 3.

6.2.2.1 UV-Vis spectroscopy analysis

The UV-Visible absorption spectra of colloidal spherical silver nanoparticles (AgSNP), silver nanorods and silver dendrites are shown in Figure 6.2.

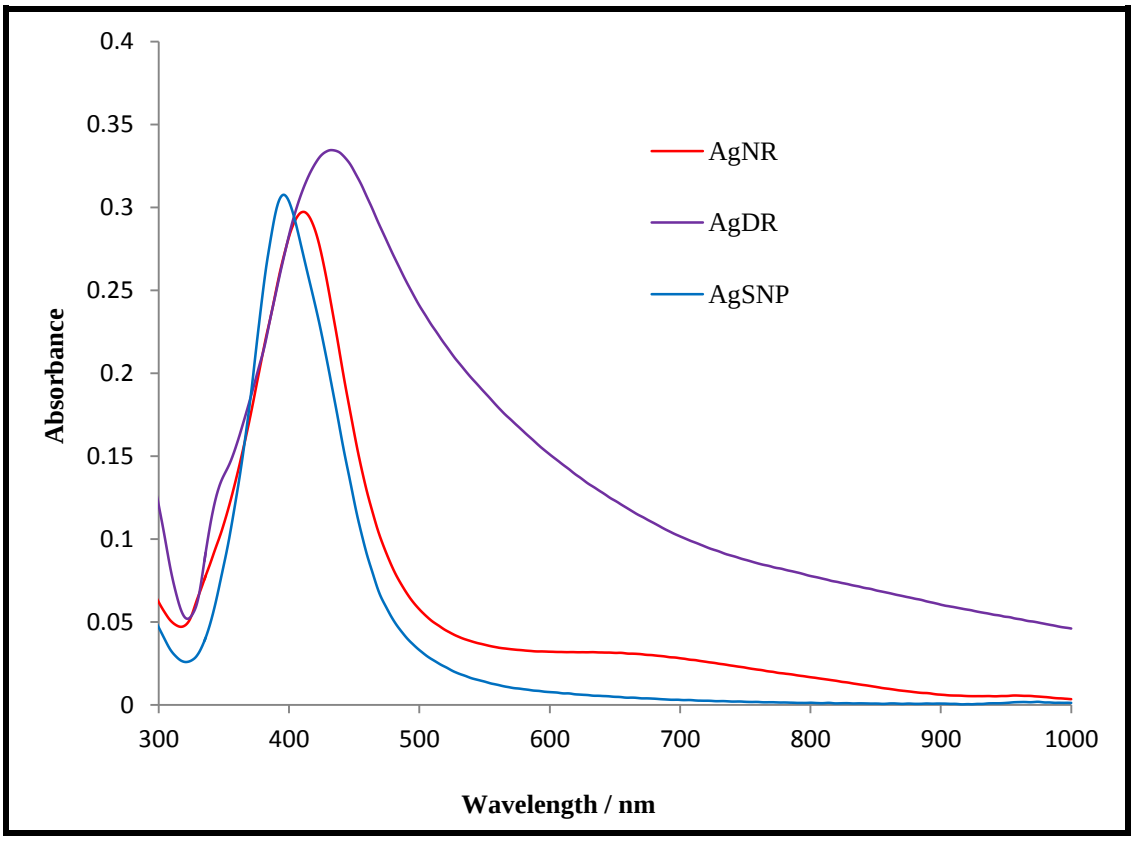

Figure 6.2: UV-Vis absorption spectra of colloidal AgNR, AgDR and AgSNP.

The spectra of the nanorods showed two peaks, a sharp one at 407 nm and a broad one around 690 nm due to transverse oscillation and longitudinal oscillations respectively. This agrees well with what is detailed in theoretical investigations as reported by Ojha *et al*., (2013). The spherical silver showed a sharp peak centered at 401 nm. The peak of the silver dendrites was broad and it shifted to higher wavelength (442 nm) when compared to spherical silver nanoparticles. This was due to the bigger size of the dendritic nanostructures.

The UV-Vis absorption spectra of the powdered nanocomposites were obtained as previously reported in Section 3.12.8 in Chapter 3. The absorption spectra of Ag/TiO_2 nanocomposites in powder form with different contents of Ag are shown in Figure 6.3.

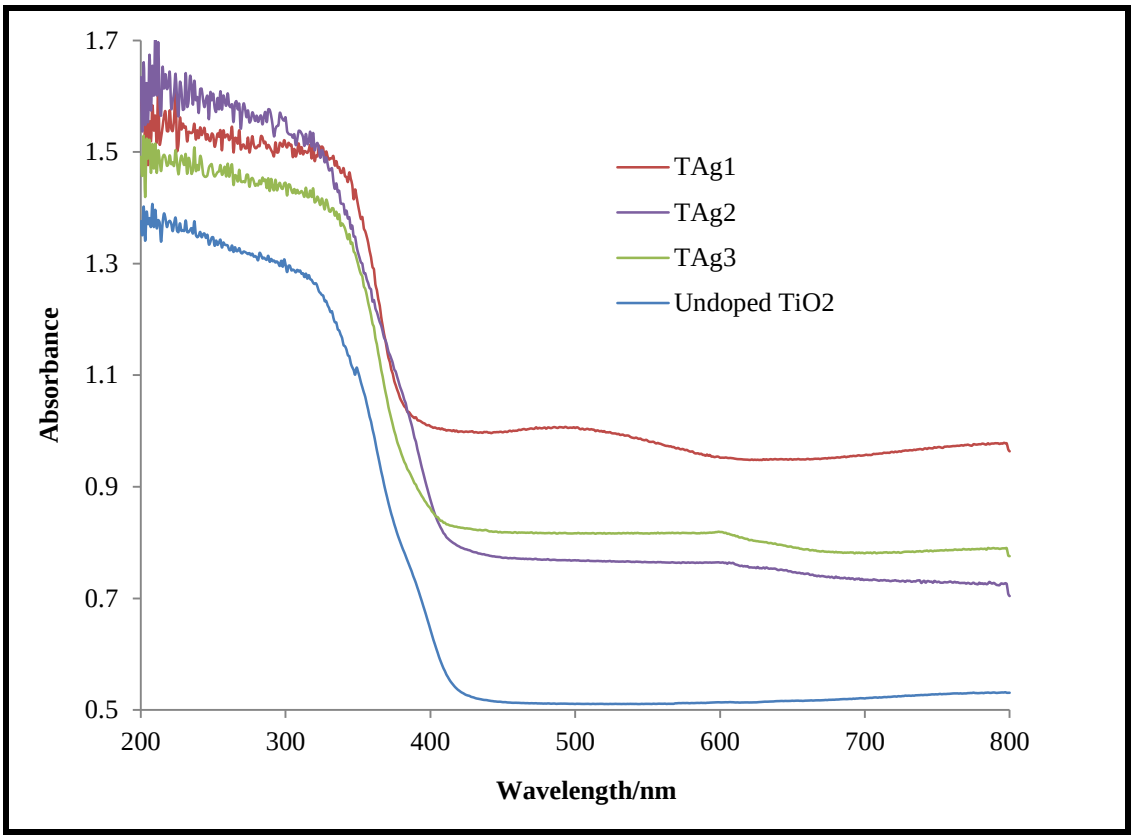

Figure 6.3: Absorption spectra of undoped TiO_2, TAg1, TAg2 and TAg3 composites.

A slight shift into the visible region was observed for the nanocomposites when compared to undoped TiO_2. There was no significant change in the absorption edge when the silver content was increased. The TiO2/Ag nanocomposite with 1.0 wt % Ag showed an additional broad peak around 500 nm.

The UV-Vis spectra of powdered TiO_2/gold nanocomposites with different contents of gold nanoparticles are shown in Figure 6.4.

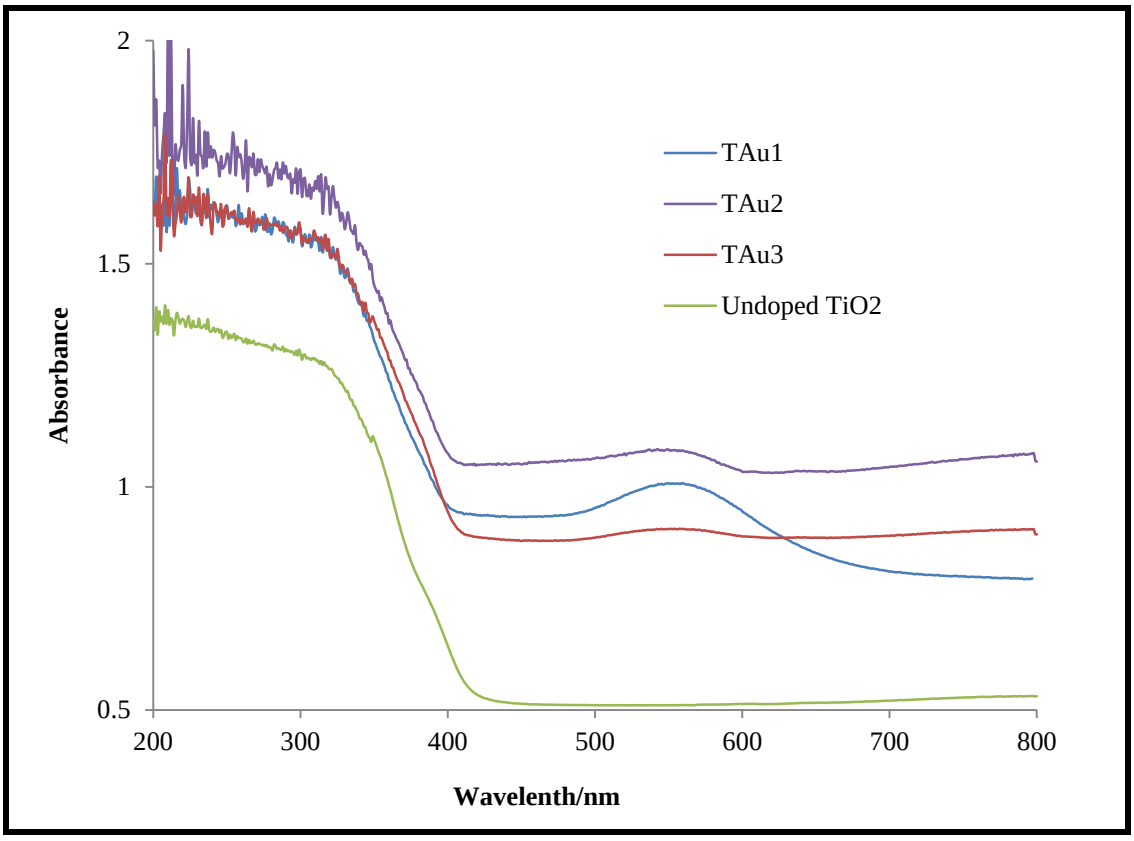

Figure 6.4: Absorption spectra of undoped TiO_2, TAu1, TAu2 and TAu3 composites.

There was also slight shift in the absorption of the composites towards the visible region when compared to undoped TiO_2 photo-catalyst. Two peaks were observed in the absorbance spectra of TiO_2/Au composites, one due to gold nanoparticles in the visible region centered at 560 nm and the other due to TiO_2 nanoparticles in the UV region. There was no shift in the

position of the plasmon peak with increase in gold content except an increase in peak intensity. Undoped TiO_2 photo-catalyst had only one peak in the UV region due to the excitation of electrons from the valence band into the conduction band.

6.2.2.2 Diffuse reflectance spectroscopy

The diffuse reflectance spectra of undoped TiO_2, TAu1, TAgNR and TAg1 composite material and their derivatives are shown in Figure 6.5.

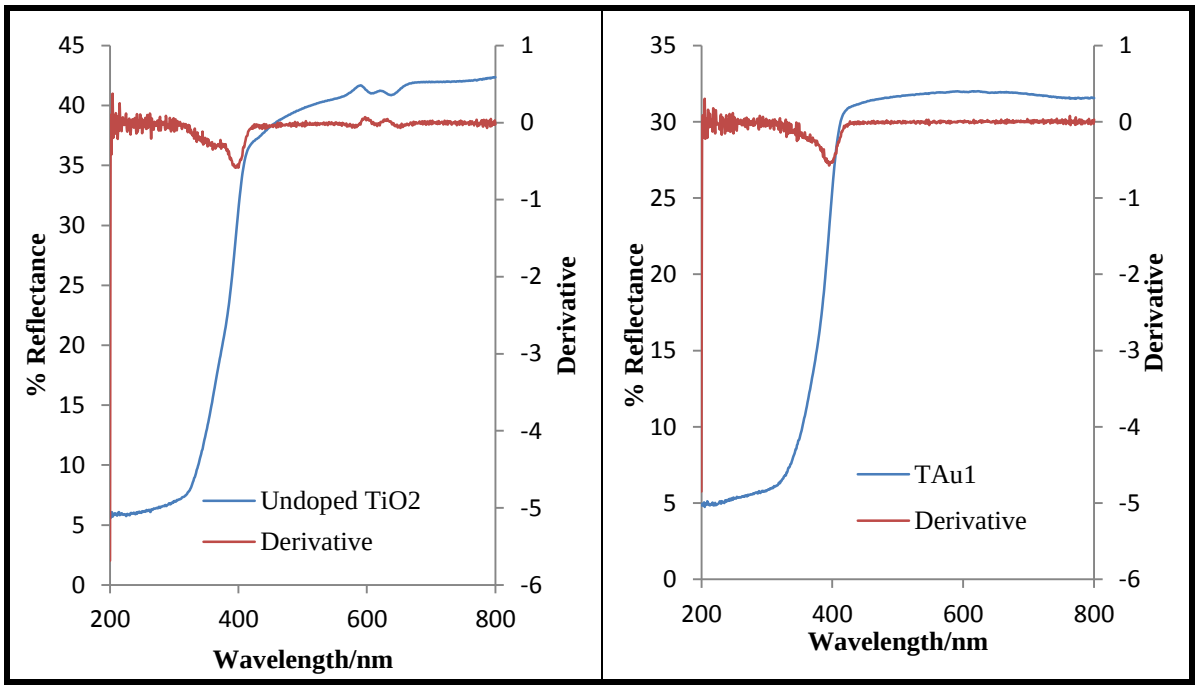

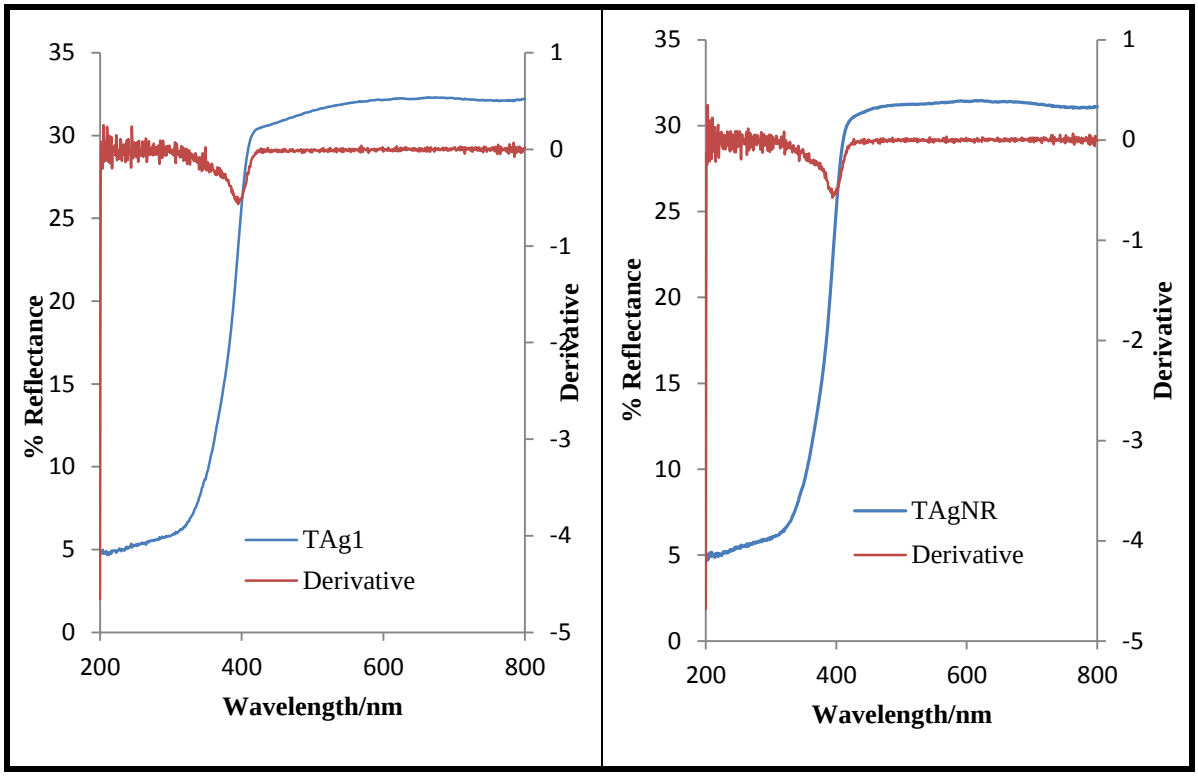

Figure 6.5: Diffuse reflectance spectroscopy spectra of TiO_2/plasmon metal nanocomposites and their derivatives.

There was a slight red shift when the TiO_2 was combined with plasmon metal nanomaterials to form TAu1, TAgNR and TAg1 nanocomposites. No shift in the absorption edge was observed when the plasmon metal was changed from Ag to Au. The reason for the observed results was that, the plasmon metals were not incorporated into the crystal system of the semiconductor photo-catalyst. Significant red shifts were observed when the impurities were incorporated in the crystal system of TiO_2 as can be observed in carbon, silver and gold co-doping in Chapter 5 (Table 5.1).

The derivatives (Figure 6.5) were used to find the absorption edges (λ_{edge}), which were then used to calculate the band gap using Equation 6.1.

$$Eg = \frac{1239}{\lambda edge} \quad \text{.....6.1}$$

The calculated band gaps of pure TiO_2 and the composites are shown in Table 6.1.

Table 6.1: Calculated band gaps of undoped TiO_2 and selected nanocomposites.

Photocatalyst	Optical absorption edge (nm)	Calculated band gap (eV)
Undoped TiO_2	403	3.07
TAg1	404	3.06
TAgNR	405	3.06
TAu1	404	3.06

From the calculated band gaps in Table 6.1, it can be clearly seen that there was an insignificant change in band gap when the TiO_2 was mixed with metal nanoparticles to form nanocomposites. This shows that the TiO_2 photo-catalyst show band gap reduction when the impurities are incorporated in its crystal system.

6.3 Photo-catalytic activity evaluation

This section presents the evaluation of the photo-catalytic activity of undoped TiO_2 photo-catalyst, a series of TiO_2/gold composites and a series of TiO_2/Ag composites using methyl orange as model pollutant at 25 °C and pH 7 under UV light. The detailed experimental procedure was reported in Section 3.11. The control of the experiments was the photo-degradation of methyl orange using undoped TiO_2 photo-catalyst, the variable was the type of the photo-catalyst used and the fixed parameters were the methyl orange volume and concentration, light intensity, temperature and pH of the methyl orange solution.

6.3.1 Photo-catalytic activity evaluation of TiO_2/spherical metal nanoparticle composites

Figure 6.6 shows the photo-degradation profiles of methyl orange using quartz supported undoped TiO_2, TAu1, TAu2 and TAu3 composite photo-catalysts. The photo-degradation profiles of methyl orange using TAg1, TAg2, TAg3, TCu1, TCu2 and TCu3 composite photo-catalysts were presented in Appendices B.

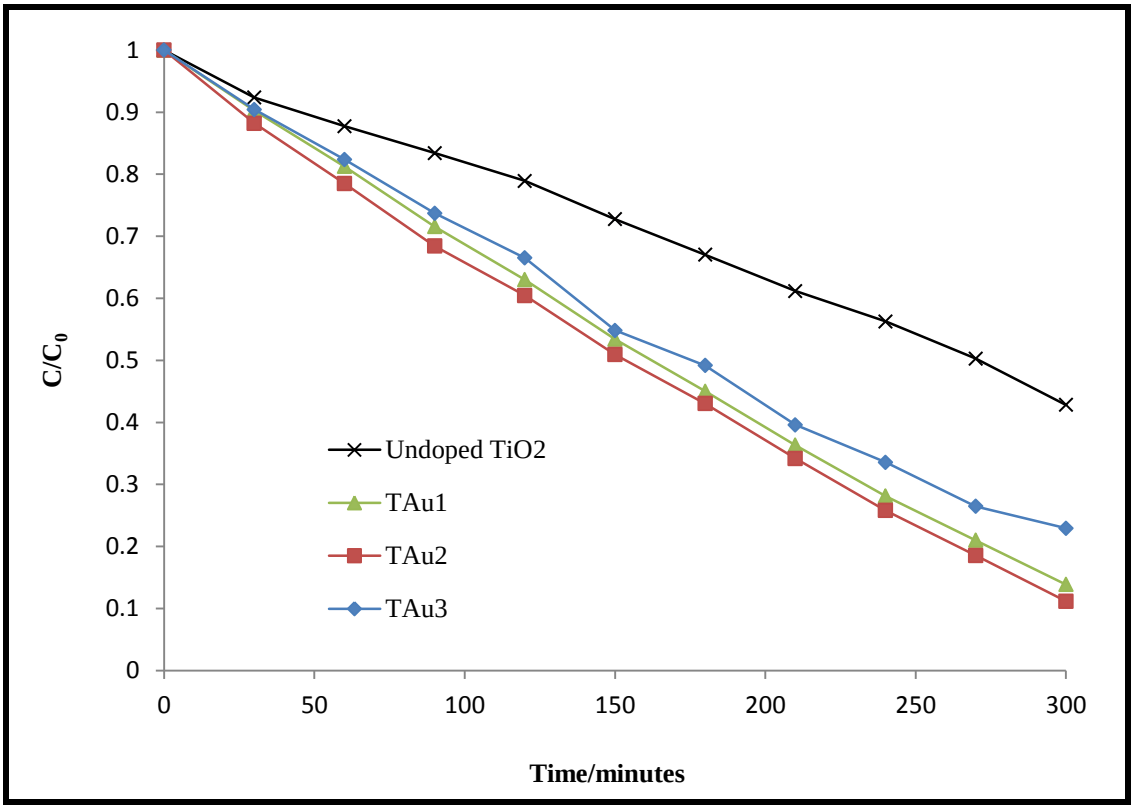

Figure 6.6: Photo-degradation curves of methyl orange using Au/TiO_2 composites on quartz support under UV light at 25 °C and pH 7.

All the composites under study in this section showed higher photo-catalytic activity than undoped TiO_2 photo-catalyst. It is important to note that this improvement in photo-catalytic activity was not due to band gap engineering as there was no significant change in band gap of the composite materials (Table 6.1). Generally the composites had a rough surface (Figure

C5 Appendix C), which could be beneficial to photo-catalysis as it has been found that rough surfaces help in the lateral scattering of incident light by NPs thus increasing the optical path of the light making it more easily absorbed (He & Que., 2013).

The highest photo-degradation of methyl orange after 300 minutes of 91.94 % was achieved by TiO_2/Au composite with a weight percent of 0.5. For both Au and Ag composites, there was an increase in the photo-degradation when the metal loading was increased from 0.1 % to 0.5 % and then it decreased with further increase in metal loading. The optimum loading for both Au and Ag on TiO_2 to act as electron reservoirs was found to be 0.5 %. The reasons for the decrease in photo-catalytic activity above optimum loading were (i) the decrease in the average distance between trap sites such that metal particles attract holes promoting electron–hole recombination (Carp *et al*., 2004), (ii) excessive coverage of the photo-catalyst reduces the amount of light reaching the photo-catalyst surface and this reduces the number of photo-generated electron-hole pairs, and (iii) reduced electron density due to attraction by several metal nanoparticles and the resulting complicated field configuration has a negative impact on charge separation (Pachat., 1993).

There was no significant change in the photo-catalytic activity of TiO_2 when the copper loading was increased (Figure C1, Appendix C). The reason for copper not to effect any significant change in TiO_2 photo-catalytic activity with increase in loading is not clear although it is believed that the deposition of plasmon metal nanoparticles on TiO_2 can be beneficial or detrimental on photo-catalytic activity depending on contaminant nature (Hu *et al*., 2003).

A summary of the methyl orange photo-degradation results for the series of Au, Cu and Ag/TiO_2 composite photo-catalysts under UV light at 25 °C and pH 7 are shown in Table 6.2.

Table 6.2: Photo-degradation results of methyl orange using a series of Au, Cu and Ag/TiO_2 composite photo-catalysts at 25 °C and pH 7 under UV light.

Noble metal loading (wt %)	**Photo-degradation after 300 minutes**		
	TiO_2/Au	TiO_2/Ag	TiO_2/Cu
0.0	57.16	57.16	57.16
0.1	80.98	77.06	85.94
0.5	91.94	88.83	84.69
1.0	90.30	86.12	86.02

From Table 6.2 it can be seen that Au proved to be the most efficient among the three elements to reduce electron-hole recombination as evidenced by the high performance of the series of composites of Au and TiO_2 photo-catalysts. The reason for this could be that, Au has the highest work function among the three metals and forms the highest Schottky barrier resulting in efficient charge separation.

6.3.2 Effect of using two or three different metals on the photo-activity of TiO_2/plasmon metal composites

Figure 6.7 shows the photo-degradation profiles of methyl orange (100 mL, 10 ppm) using composites of TiO_2 and at least two plasmon elements under UV light at 25 °C and pH 7. The combinations of the plasmon elements used to prepare the composites were Au/Ag, Ag/Cu, Au/Cu and Au/Ag/Cu and their codes were TAuAg, TAgCu, TAuCu and TAAC respectively (Table 3.3 in Chapter 3).

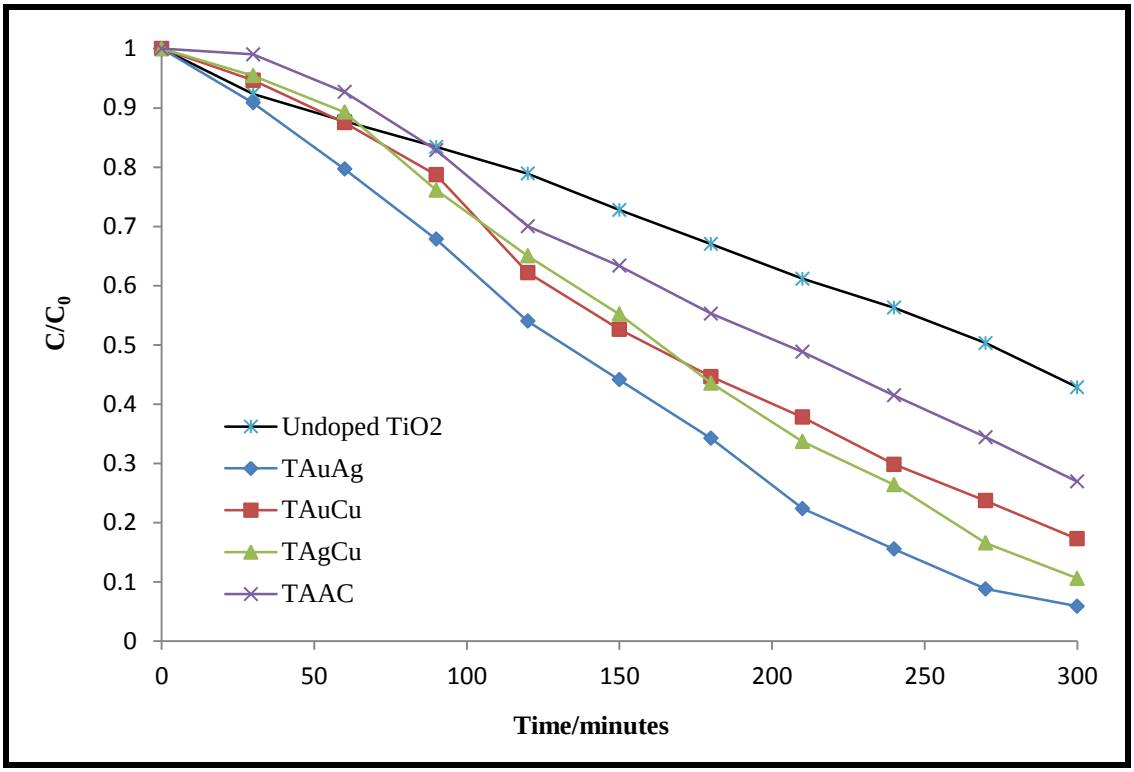

Figure 6.7: Photo-degradation curves of methyl orange using undoped TiO_2 and TiO_2/plasmon metal nanocomposites under UV light at 25 °C and pH 7.

When more than one plasmon metal was used to prepare composites, all the resulting TiO_2 photo-catalytic composite materials exhibited higher photo-catalytic activity than undoped TiO_2 as shown in Figure 6.7. The highest enhancement in photo-catalytic activity was achieved by TiO_2 with silver and gold nanoparticles (TAuAg), which degraded 94.11 % of methyl orange solution under UV light irradiation in 300 minutes followed by TiAgCu with 89.39 %, TAuCu, 86.74 % and lastly TAAC with 73.07 % as shown in Figure 6.7. There are two possible reasons for the improved photo-catalytic activity of the composites under UV light irradiation when compared to bare TiO_2, (i) reduced electron-hole recombination and (ii) the creation of the Schottky barrier. A simplified proposed mechanism for the activation of TiO_2 photo-catalyst and photo-degradation of adsorbed methyl orange is shown in Figure 6.11 in the next section.

When compared to photo-catalysts containing the same elements but deposited as films on top of each other (Table 4.6 in Chapter 4), TAuAg, TAgCu and TAuCu composites showed an improvement of 15.92, 15.03 and 2 % respectively whereas TAAC showed a decrease of 13.19 % as shown in Table 6.3.

Table 6.3: Percentage degradation results of TiO_2/ plasmon metal nanocomposites.

Composite photo-catalyst	**% Degradation under UV light after 5 hours**	**% Enhancement compared to metal films of same elements**	**% Enhancement relative to bare TiO_2**
Undoped TiO_2	57.16	-	-
TAuAg	94.11	15.92	36.95
TAgCu	89.39	15.03	32.23
TAuCu	86.74	2.00	29.58
TAAC	73.07	-13.19	15.91

The reason for the better TiO_2 photo-catalytic activity enhancement by plasmon elements when used as composites than when used as films deposited layer by layer was the increase in contact between the plasmon metal nanoparticles with TiO_2 nanoparticles and this improved the flow of electrons from the TiO_2 surface to the metal nanoparticles. Hence charge separation was more effective resulting in low electron-hole recombination rates thus favoring photo-catalysis.

6.3.3 Effect of plasmon metal shape on photo-activity of TiO_2 composites

This section gives a comparative study of the photo-degradation activities of nanocomposites of TiO_2 and silver nanomaterials of different structures which were: dendrites, nanorods and

spherical nanoparticles. The control was undoped TiO_2 photo-catalyst, the variable was the shape of the silver nanomaterials and the fixed parameters were the amount of TiO_2 used in making the composites, methyl orange concentration, pH and temperature.

The photo-degradation curves of methyl orange under UV light irradiation at 25 °C and pH 7 using TAgDR, TAgNR and TAg2 composite photo-catalysts, which contain the same contents of plasmon nanomaterials are shown in Figure 6.8.

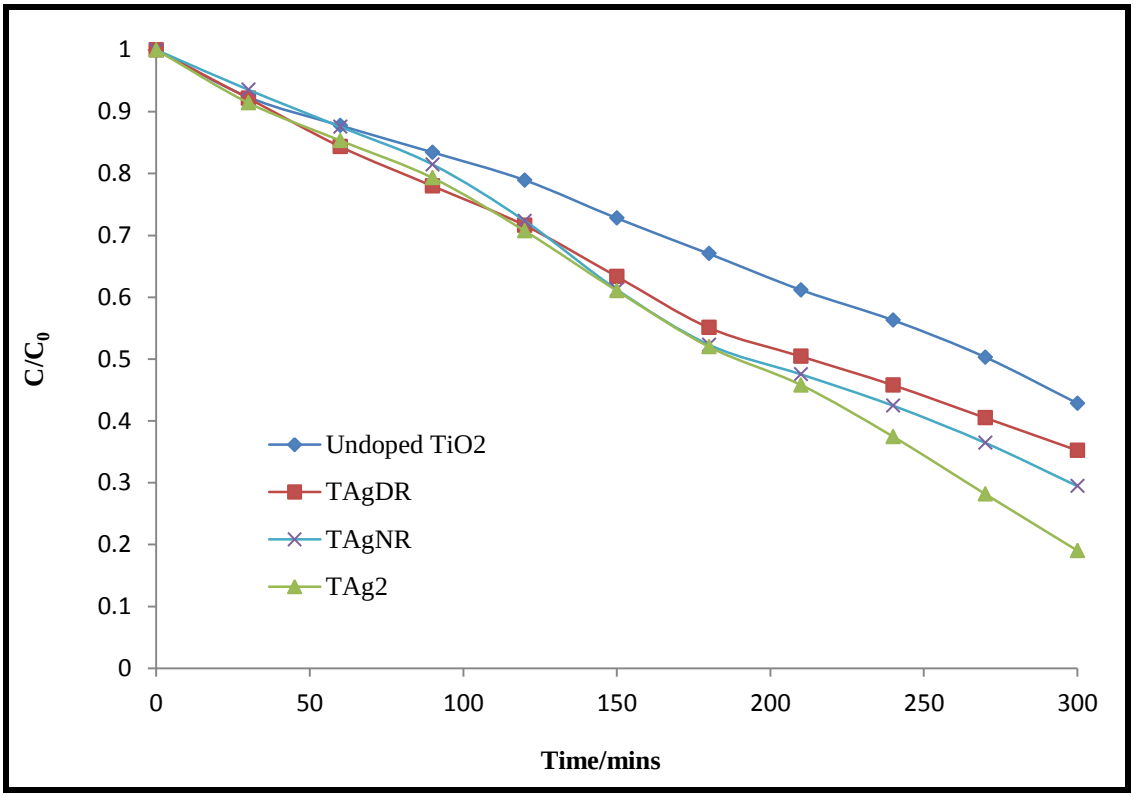

Figure 6.8: Photo-degradation curves of methyl orange using nanocomposites of TiO_2 and Ag nanostructures of different shapes at 25 °C and pH 7.

The TiO_2/Ag composite materials showed higher photo-catalytic activities than undoped TiO_2 photo-catalyst. The highest TiO_2 photo-catalyst enhancement was achieved by spherical silver nanoparticles where 80.98 % of methyl orange was degraded after 300 minutes

followed by silver nanorods with 70.55 % and lastly silver dendrites with 64.78 %. The reason for the observed trend of enhancement was probably the differences in size and shape of the silver nanostructures. The smaller the Ag nanostructures the greater the surface area that would be available for contact with TiO_2 and this promotes electron transfer resulting in low electron-hole recombination rates. The other reason for the observed trend could be the differences in the wavelengths at which the Ag nanostructures absorb light. The zero dimensional spherical nanoparticles absorb at lower wavelength when compared to one dimensional AgNR with maximum absorption at 405 nm (Figure 6.2) and dendritic nanostructures with maximum absorption at 444 nm (Figure 6.2). Since the experiments were conducted under UV light, AgSNP absorbed more light than both AgNR and AgDR resulting in more localized surface plasmon resonance (LSPR) which aided photo-catalysis.

6.4 Photo-degradation under visible light

This section presents an evaluation of the photo-catalytic activity of dTAAC photo-catalyst, undoped TiO_2 and TAAC under visible light at 25 °C and pH 7 using methyl orange (100 mL, 10 ppm) and bromocresol purple (100 mL, 10 ppm). Sample codes and description are presented in Table 3.3.

Figure 6.9 shows the photo-degradation curves of methyl orange and bromocresol purple under visible light using dTAAC, Ag/C co-doped TiO_2 (0.5 % Ag), undoped TiO_2 and TAAC photo-catalysts at 25 °C and pH 7.

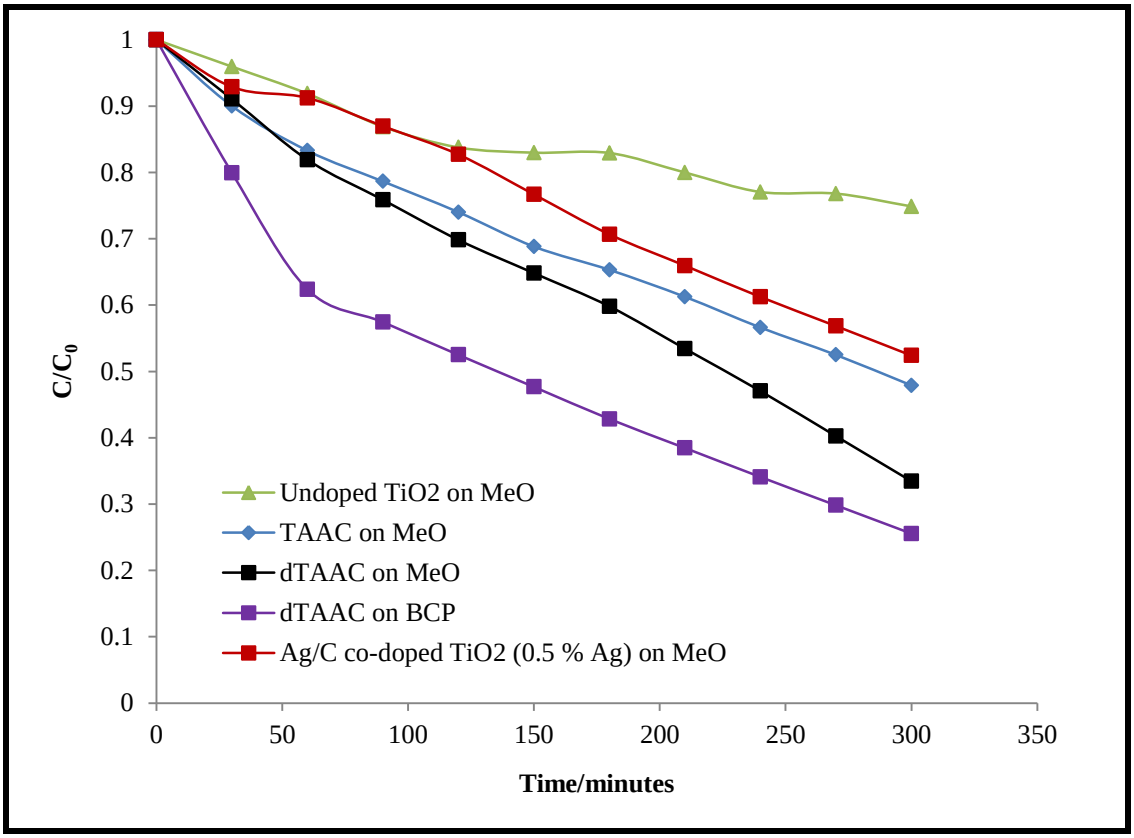

Figure 6.9: Photo-degradation curves of MeO and bromocresol purple by Ag/C co-doped TiO_2 (0.5 % Ag) photo-catalyst and its composites under visible light at 25 °C and pH 7.

Under visible light irradiation, a nanocomposites prepared from the three plasmon metal nanoparticles (Au, Cu & Ag) and Ag/C co-doped TiO_2 (0.5 % Ag) showed 66.46 % degradation of methyl orange after 300 minutes however, when the Ag/C co-doped TiO_2 (0.5 % Ag) and the three metal TiO_2 composite (TAAC) were used separately they showed 47.61 % and 52.11 % degradation respectively as shown in Figure 6.9. This showed that the use of the three plasmon metal nanoparticles (Au, Ag and Cu) together with Ag/C co-doped TiO_2 (0.5 % Ag) photo-catalyst improved photo-catalytic activity. The nanocomposites prepared from doped TiO_2 performed better than those prepared from undoped TiO_2 for the same metal nanoparticle type and loading.

When the Ag/C co-doped TiO_2 (0.5 % Ag) photo-catalyst was used to degrade bromocresol purple (BCP) under the same conditions, 74.45 % degradation was achieved after 300 minutes. This indicated that the azo dyes are more difficult to degrade when compared to other dyes hence the chemical nature of the pollutant plays an important role on the photo-degradation rate.

Figure 6.10 shows some plots of $\ln(C_0/C)$ against time for both bromocresol purple (100 mL, 10 ppm) and methyl orange (100 mL, 10 ppm). The kinetics were for photo-degradation experiments done using dTAAC photo-catalyst under visible light at 25 °C and pH 7.

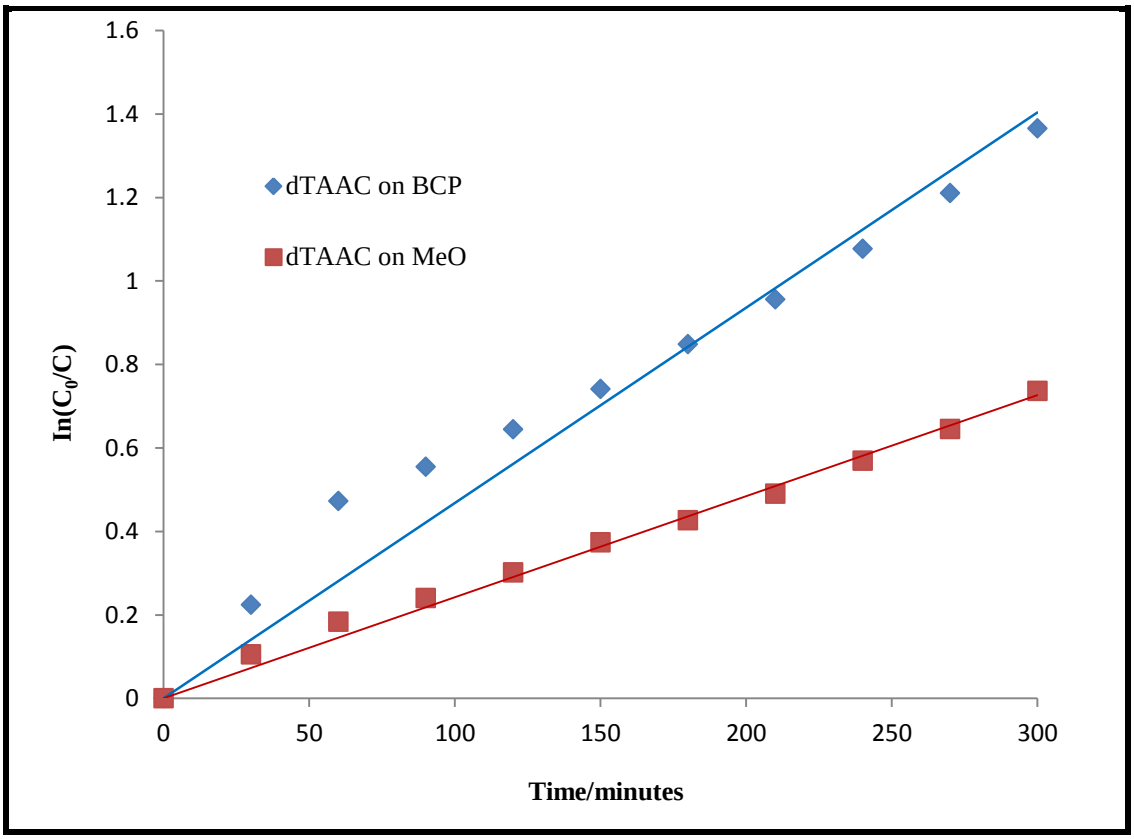

Figure 6.10: Bromocresol purple and methyl orange kinetics by dTAAC photo-catalyst under visible light at 25 °C and pH 7.

The linear relationships observed indicated first order reaction kinetics of the photo-degradation of both dyes under study. The rate constant for bromocresol purple was 4.55 x 10^{-3} min^{-1} which was almost twice that of methyl orange of 2.45 x 10^{-3} min^{-1}. The rates increased with time since the Langmuir-Hinshelwood model is surface area dependent as there will be less organic compound remaining with increased irradiation times. The difference in the rate constants of bromocresol purple and methyl orange was probably due to the differences in the degradation pathways that they followed. Contaminants that have a lot of photo-degradation intermediates will prolong the time needed for complete mineralization.

There are several reasons that could have led to the improved photo-catalytic activity of the doped TiO_2/metal nanocomposites under visible light irradiation when compared to undoped TiO_2 and these include:

(i) Reduced electron hole recombination due to the metal nanoparticles.

(ii) Creation of intense electric fields when metal nanoparticles are irradiated at their plasmon resonance frequency. Non-radiative transfer of energy from the LSPR of the metal to the transition dipole of the semiconductor occurs resulting in the excitation of electrons in the semiconductor. This extends the photo-catalytic activity of wide band gap TiO_2 semiconductor into the visible region of the solar radiation.

(iii) The heating effect produced at the surface and immediate vicinity of the metal nanoparticles heats up the environment around the nanoparticle and it is believed to increase mass transfer of the molecules and enhancing the rate of reaction (Zhang *et al*., 2013).

(iv) Reduced band gap as a result of doping.

(v) The surface roughness helped in the lateral scattering of incident light by nanoparticles resulting in an increase of the optical path of the light making it more easily absorbed (He & Que., 2013).

All the latter processes could have been occurring simultaneously resulting in high photo-degradation rates of methyl orange using the composite photo-catalysts tested in this study. A simplified proposed mechanism for the activation of TiO_2 photo-catalyst and degradation of adsorbed methyl orange is shown in Figure 6.11. Generation of the superoxide radical could be on both TiO_2 surface and metal nanoparticles thereby giving a high yield of $OH^{\bullet}$ radicals, which degrade the methyl orange.

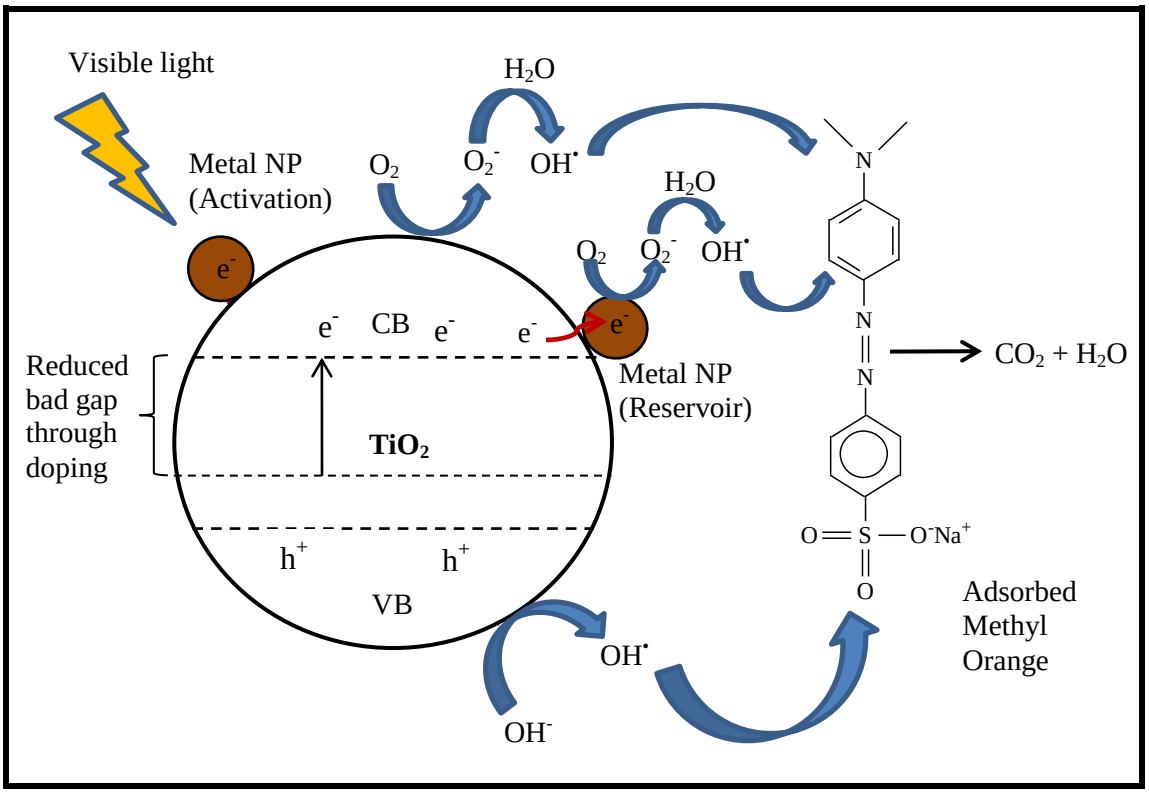

Figure 6.11: Schematic representation of the proposed activation mechanisms of TiO_2 by metal nanoparticles (MNP) and photo-degradation of methyl orange under visible light.

6.5 Determination of methyl orange photo-degradation products

The change in concentration shown by the photo-catalytic activity curves in this study and the disappearance of colour, which was observed during the photo-degradation process, did not imply that all the organic content was completely mineralised into harmless products. Hence the study of the photo-catalytic degradation pathway of organic compounds and the extent of the photo-degradation process was necessary so as to establish the nature of the products formed since in some cases; intermediates may be more toxic than the targeted starting pollutants. In such cases it will be important to mineralize the organics completely into harmless products. It is important to note that evolution of intermediates prolongs the time required for complete mineralization due to the competition between intermediates and original target pollutant over the photo-catalyst surface. The photo-degradation pathway followed by a pollutant is dependent on the reaction conditions and the structure of pollutant molecule. Knowing the photo-degradation pathway can help in gaining an understanding of how to improve the efficiency of the photo-catalyst.

6.5.1 Mass spectrometry determination of photo-degradation pathway

Methyl orange in solution is an anionic compound. When it is analyzed in the positive mode, it is protonated on the SO_3^- group to make it neutral and then gains another proton to give a detectable characteristic positive molecular adduct $[M + H]^+$. The molecular mass calculator of the instrument was used to determine the m/z of the parent molecule, which was 306.

The LC-MS elution spectra obtained for the photo-degradation of methyl orange at different photo-degradation times (0, 30, 60, 90 and 300 minutes) are shown in Figure 6.12.

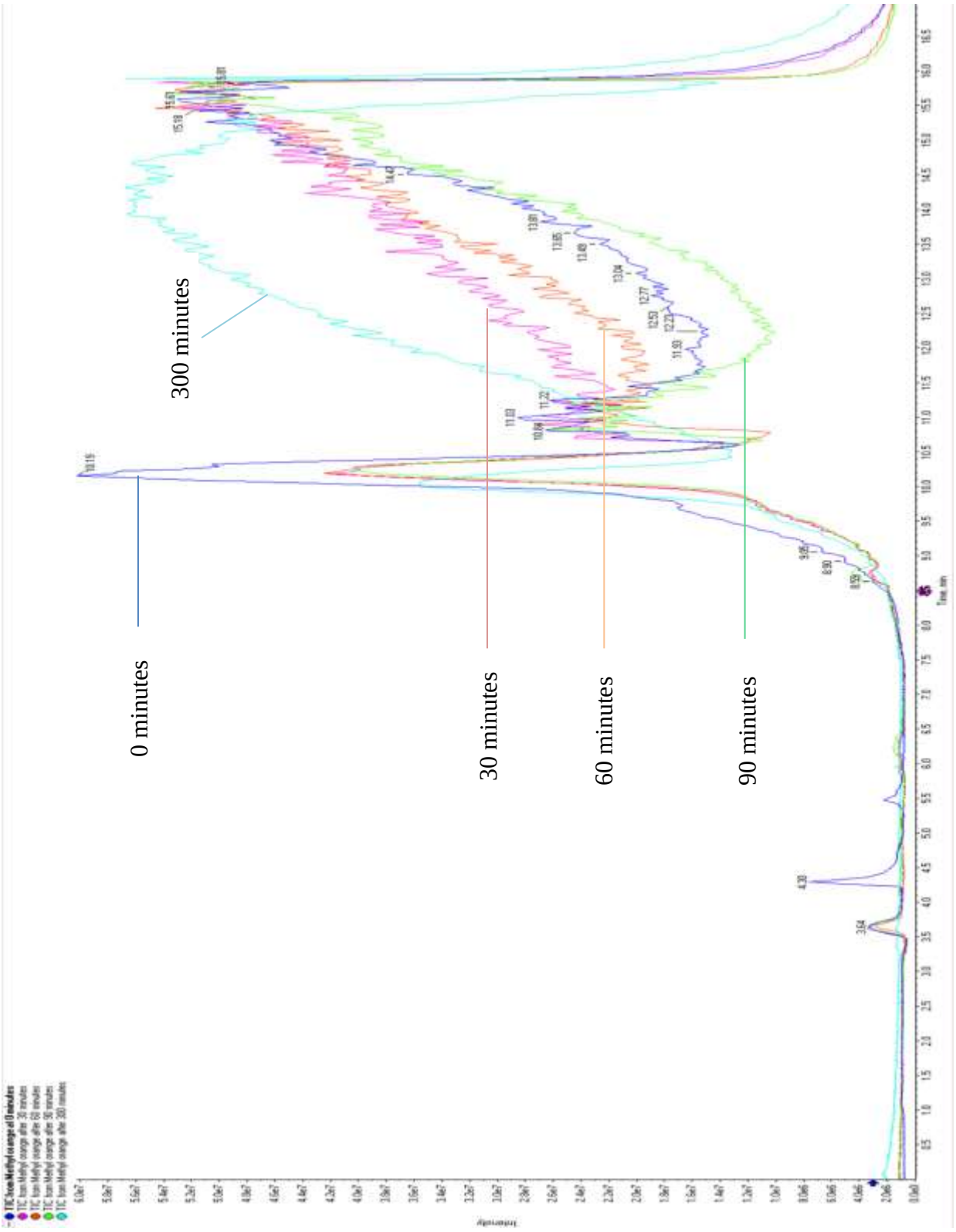

Figure 6.12: Elution time of methyl orange and photo-degradation intermediates of methyl orange at different photo-degradation times.

All the spectra had a peak at a retention time of 3.64 minutes except the spectrum of the sample at 300 minutes indicating that the compound eluting at this retention time had been completely degraded. The peaks at retention times of 4.30 and 5.50 minutes in the spectrum of methyl orange at 0 minutes which had intensities of 8.0×10^6 and 1.90×10^6 respectively completely disappeared in the spectra of methyl orange at 30 to 300 minutes. New peaks appeared at retention times of 6.25 and 8.65 minutes, which were prominent in the spectra of methyl orange after 90 minutes indicating the formation of new compounds (intermediates). The reduction in intensity of this peak with time and its complete disappearance after 300 minutes showed that, the newly formed compound was also completely degraded. The major peak common to all spectra at retention time of 10.19 minutes reduced in intensity with increase in photo-degradation time from 6.0×10^7 at zero minutes to 3.6×10^7 after 300 minutes.

The MS/MS spectra of the methyl orange at zero minutes and after 90 minutes are shown in Figure 6.13. The signal at m/z 306 was due to the positive ion of the parent molecule. The MS/MS analysis of this ion gave at least ten significant m/z values of 65.04, 81.03, 101.03, 120.08, 121.09, 133.08, 134.08, 185.01 and 291.07. A visualization of the results is shown in Figure 6.14 of the possible intermediates formed based on the bonds that were more susceptible to breakdown. In this study it was observed that homolytic bond breaking became competitive irrespective of the absence of stabilization of an odd electron. This was shown in the formation of the fragment with m/z of 291. The possible intermediates suggested in this study were not the only ones present in the photo-degradation solution as some possible structures could not be deduced from the given m/z values. To the best of our knowledge, this was the first LC/MS analysis of photo-degradation products of methyl orange in the positive mode. Most researchers analysed it in the negative mode as it easily loses the sodium ion in

solution and becomes negatively charged. A difference in the detected intermediates was observed when run in the positive mode instead of the commonly used negative mode.

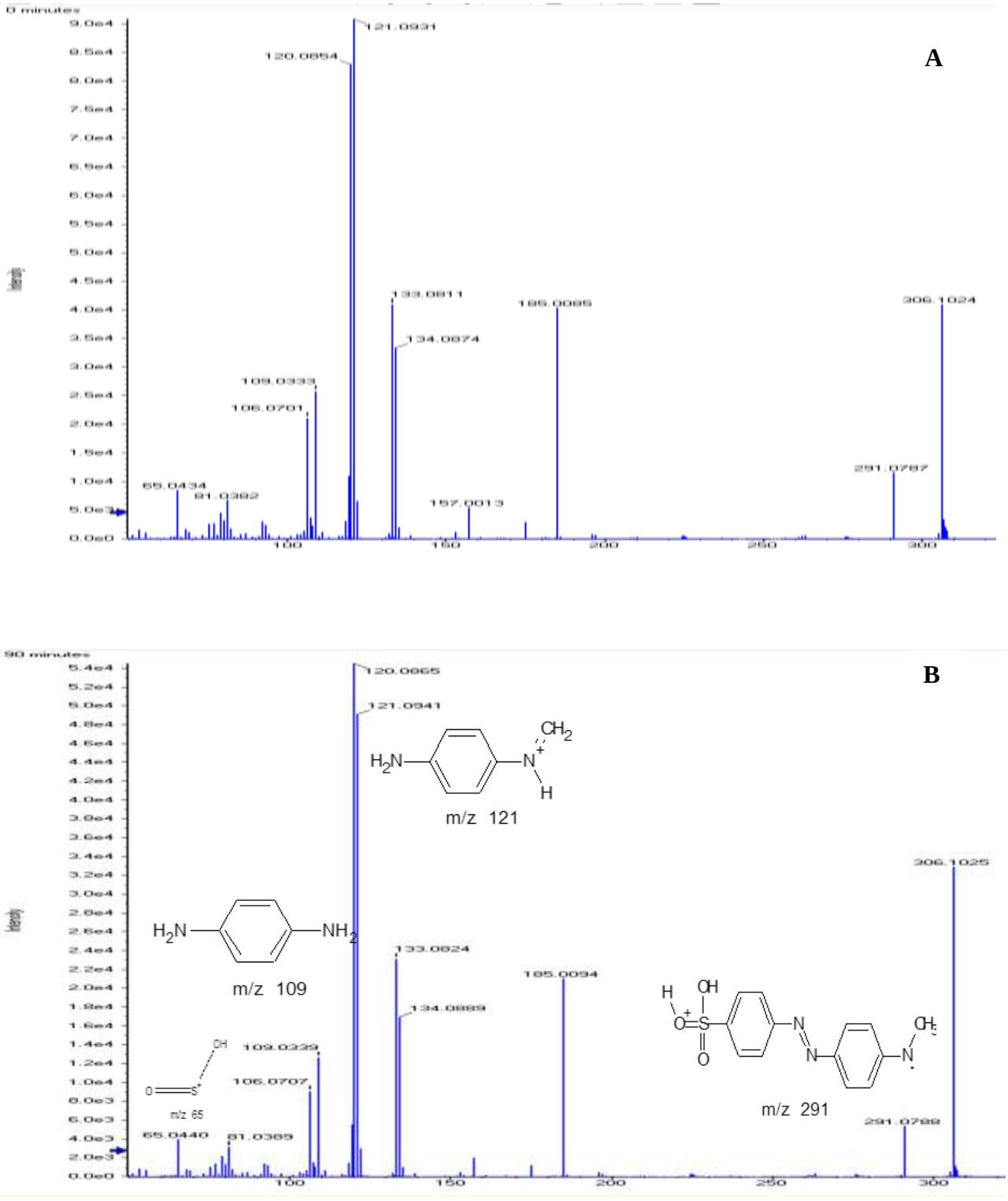

Figure 6.13: Positive-ion MS-MS of methyl orange at (A) zero minutes and (B) 90 minutes.

The proposed photo-degradation pathway and some of the intermediates of methyl orange based on the LC-MS results obtained are shown in Figure 6.14.

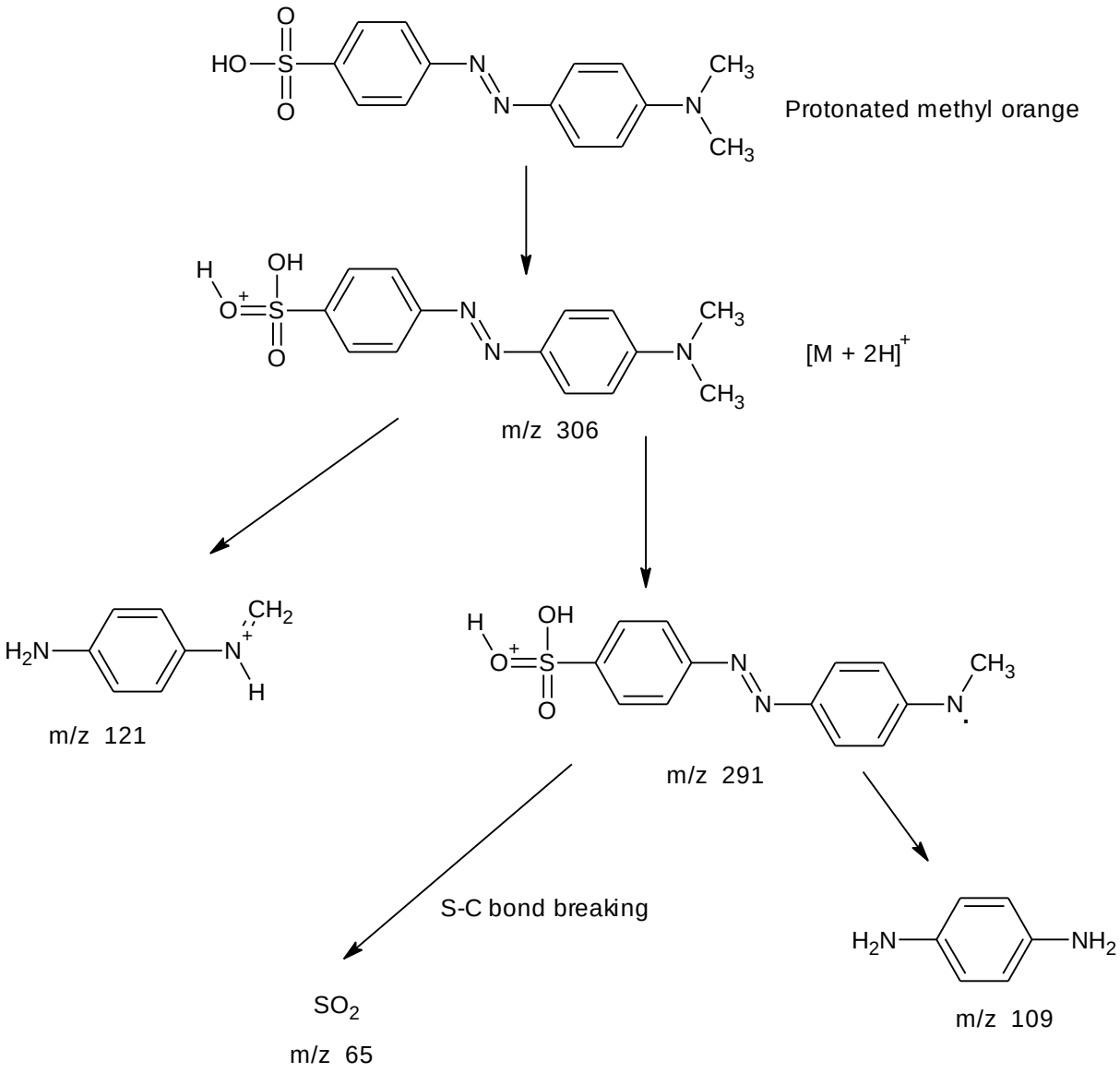

Figure 6.14: Proposed photo-degradation pathway and some of the intermediates of methyl orange based on the LC-MS results obtained.

6.5.2 FTIR analysis of degradation products

The photo-degradation of methyl orange was also studied using FTIR whereby the analysis was done on a 10 ppm methyl orange solution before degradation and after every hour for

300 minutes of photo-degradation. This analysis gave an idea on the way the methyl orange was photo-degraded in terms of which bonds were cleaved. This was observed in the decrease in the intensity of certain characteristic peaks of some functional groups as illustrated in Figure 6.15.

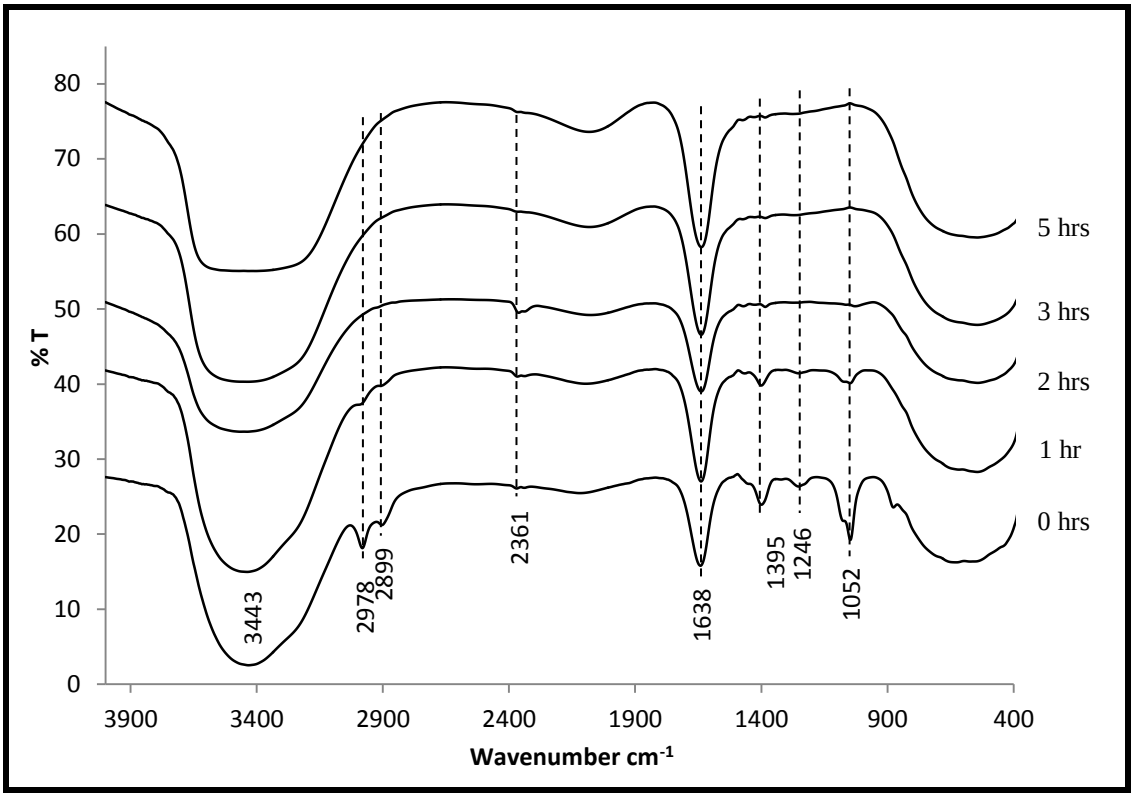

Figure 6.15: FTIR spectra of methyl orange at different stages of photo-degradation.

The characteristic peaks due to the C-H stretching of the methyl groups around wavenumber 2978 cm^{-1} and 2899 cm^{-1} found in the spectrum of the initial methyl orange were seen to have almost disappeared in the spectrum of the photo-degraded methyl orange extract after 5 hours. This could be due to the fragmentation and destruction of the methyl groups from the methyl orange. In the spectra of the extracts, the peaks at 1395 cm^{-1} (C-H stretching of methyl), 1246 cm^{-1} (=C-N stretching) and 1052 cm^{-1} (C-N stretch) significantly decreased compared to the spectrum of the initial methyl orange. This showed that the functional groups

that gave rise to those peaks had been degraded to some extent with the major degradation or cleavage taking place on the C-N bonds as evidenced by the major decrease in the C-N peak at 1052 cm^{-1}. The peak at 876 cm^{-1} (=C-H bending) completely disappeared after photo-degradation implying the complete destruction of the groups giving rise to that peak. The breakdown of the C–N bond was faster than that for C–C bonds as evidenced by the rate of decrease of the intensity of the corresponding FTIR peaks. Hence it can be concluded that the degradation of methyl orange occured via an electrophilic attack by the $OH^{\bullet}$ radicals leading to an abstraction of a hydrogen atom and resulting in the cleavage of the C-N bond. A similar mechanism was suggested by Klare and co-workers, (2000) for the degradation of alkanolamines.

6.6 FTIR analysis of photo-degradation products of bromocresol purple

The FTIR spectra of bromocresol purple at different times of photo-degradation are shown in Figure 6.16. Generally, major changes in the spectra were observed after five hours of photo-degradation. There was no significant change of the peak around 2890 cm^{-1}, which was assigned to C-H bond stretching of the methyl groups in the first 3 hours of the photo-degradation process. The significant decrease in the C-H peak intensity was observed after 5 hours. The peak at 1660 cm^{-1} due to the C=C aromatic bending increased in intensity after 5 hours of photo-degradation was probably due to the formation of photo-degradation products carrying C=C bonds. The peak at 1325 cm^{-1} due to the stretching frequency of S=O completely disappeared in the spectra of the sample taken after five hours. There was a gradual decrease in the peak intensity of the peak at 1441 cm^{-1} owing to the gradual degradation of the group giving that peak.

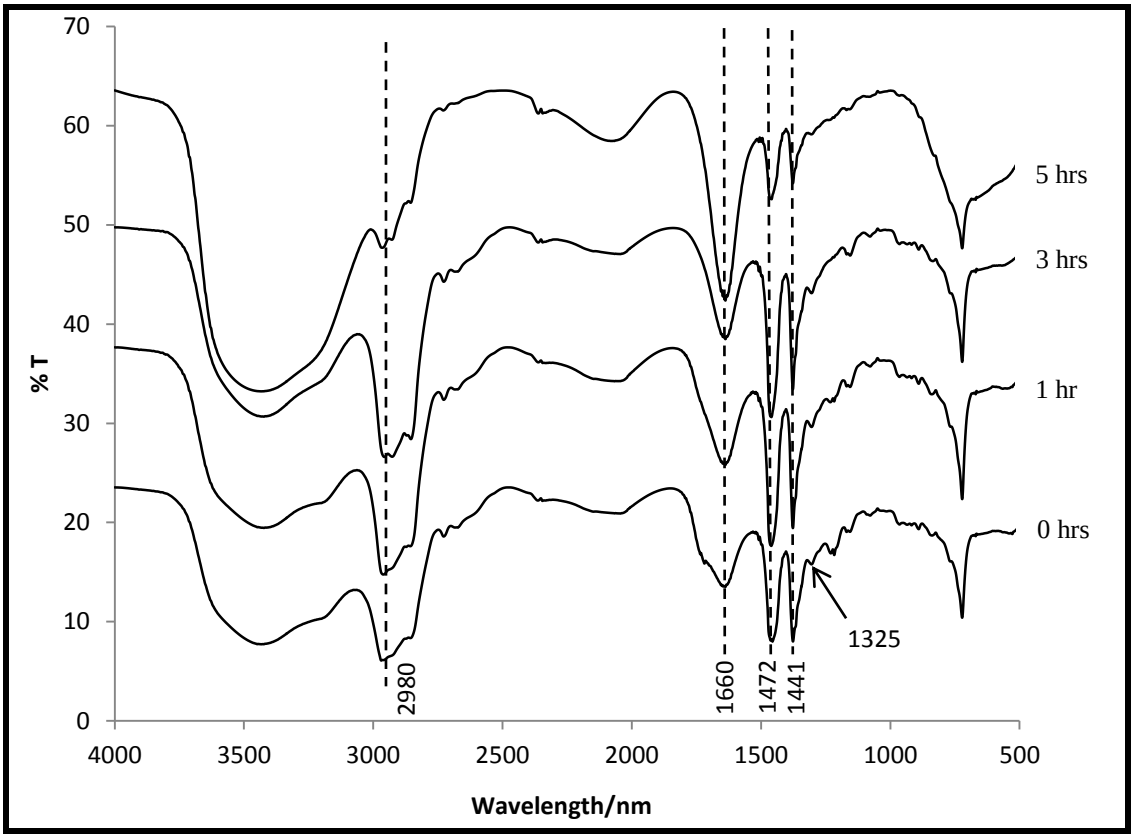

Figure 6.16: FTIR spectra of bromocresol purple at different stages of photo-degradation.

6.8 Summary

The use of nanocomposites prepared from doped TiO_2 and plasmon metal nanostructures dramatically improved the photo-catalytic removal of methyl orange and bromocresol purple from water. The study clearly indicated that the combination of (i) the effect of LSPR of plasmon metal nanostructures, (ii) the reduced electron-hole recombination by plasmon metal nanoparticles and (iii) the narrowed TiO_2 band gap is a potential way for the enhancement of photo-degradation of organic contaminants in water. Hence the increasing number of electron-hole pairs and the separation of electron-hole pairs at the surface of TiO_2 are the key factors to improve the photo-catalytic abilities of TiO_2. Based on the FTIR and LC/MS facts, it was possible to draw some conclusions on the bonds that were broken and come up with some of the chemical structures of the possible intermediates and the possible photo-

degradation pathway of methyl orange. LC/MS proved that the observed loss of colour with time does not imply complete mineralisation as peaks were observed in the colourless sample. It can be concluded that the attack of the electron donor groups results in azo compounds being weakly coloured as the absorption corresponds to the low intensity n-$\pi^\star$ star transition of the azo group.

Chapter 7

Antimicrobial studies

This chapter is about the application and determination of the extent to which selected plasmon decorated TiO_2 photo-catalysts and carbon/plasmon metal co-doped TiO_2 destroy bacteria in water. The antimicrobial studies were carried out in water using *Escherichia coli* ATCC 3695 as a model microorganism. The study focused on evaluating the effectiveness of plasmon decorated TiO_2, silver/carbon co-doped TiO_2 and gold/carbon co-doped TiO_2 photo-catalysts immobilized as films on quartz substrates.

7.0 Introduction

Water treatment does not involve only removal of organic contaminants and heavy metals but can also include the destruction of bacteria and other pathogens to make the water safe for human consumption. The presence of pathogens in both drinking and wastewater raises concerns of water borne diseases; hence the killing or removal of pathogenic organisms in water is important. The current disinfection techniques include use of chemicals, filtration and photochemical damage. Chlorination, which is the most widely used technique prevents infectious diseases but it is not effective for the removal of spores, cysts and some viruses (Zszewsyk *et al*., 2000). The use of chemicals also leaves undesirable chemical residues and generates toxic by-products that may pose a health risk to humans hence the use of photo-catalysts such as TiO_2 for disinfection could be desirable. The photo-catalysts produce hydroxyl radicals and other highly reactive oxygen species that are capable of destroying microbial pathogens.

TiO_2 slurries have been used in solar disinfection and showed effectiveness for treating drinking and waste water (Pablos *et al*., 2011; Blanco-Galvez *et al.*, 2007), however the use of slurries creates problems of separating the photo-catalyst hence the use of immobilized photo-catalyst for disinfection is desirable. Most studies concentrated more on application of immobilized TiO_2 photo-catalyst for photo-degradation of organic contaminants but the present section of this study reports on the use of plasmon metal decorated TiO_2 and doped TiO_2 photo-catalysts immobilized on quartz substrates in the disinfection of water contaminated with *E. coli* ATCC 3695 as a model pathogen under both natural sunlight and weak UV light. The importance of silver, copper and gold in medical applications and the antibacterial activity of TiO_2 have motivated combining the photo-catalyst with these plasmon metal nanoparticles to improve the antibacterial activity of the nanomaterials. With this kind of photo-catalyst, it is possible to simultaneously degrade organic compounds and kill pathogenic microorganisms.

7.1 Experimental

7.1.2 Preparation of a McFarland turbidity standard

A McFarland 0.5 turbidity standard was prepared by mixing 19.95 mL of a 1 % solution (v/v) of H_2SO_4 with 0.05 mL of a 1 % solution (w/v) of $BaCl_2$ (McFarland., 1907). To assure uniformity of the suspension of latex particles, the solution was shaken several times. This standard was used to estimate the concentration of bacteria in a liquid suspension

7.1.3 Preparation of Luria broth agar (LBA)

The LBA was prepared using a method reported by Gerhardt (1994) and Sambrok & Russell (2001). About 5 g of sodium chloride, 5 g tryptone powder, 2.5 g yeast extract and 7.5 g agar bacteriological were dissolved in 500 ml of distilled water. This solution was then autoclaved

at 120 °C for 20 minutes. The agar was then poured onto disposable petri dishes and was left to cool and solidify. The plates were then stored in a refrigerator at 4 °C.

7.1.4 Culturing of the bacteria

The *E. coli* ATCC 3695 were streaked onto freshly prepared nutrient agar using a sterile inoculating loop and incubated at 37 °C for 24 hours to get active growing bacteria colonies. The cultured bacteria were then inoculated into 10 ml of saline water after the incubation period and the turbidity was adjusted to get a 0.5 McFarlad standard containing roughly 1.5×10^8 CFU/ml. The standardized solution with the bacteria was then used in all the antimicrobial studies.

7.1.5 Antimicrobial experiments

The experiments were performed under both UV and visible light irradiation with shaking. Only the doped samples were evaluated under sunlight irradiation. A series of photo-catalytic TiO_2 coated quartz substrates were used in the experiments and uncoated quartz substrates were used as blank reference samples. The coated quartz were placed in petri dishes and then autoclaved for 15 minutes at 120 °C before use. About 25 mL of autoclaved water was added to each petri dish containing the photo-catalysts. *E. coli* ATCC 3695 (0.1 mL) was then added to each petri dish to contaminate the water with bacteria and stirred for homogeneity. A shallow reservoir of cool water was used to stabilize the temperature throughout the experiment. Before exposure to light, the petri dishes were covered to prevent contamination and loss of water due to evaporation. Seven experiments were carried out in duplicate using the selected photo-catalysts, Ag/C-TiO_2 (0.5% Ag), Au/C-TiO_2 (0.5% Au), TiO_2/Au (5 nm), TiO_2/Au (10 nm), TiO_2/Ag (5nm), TiO_2/Ag (10 nm), TiO_2/Cu (5 nm) and TiO_2/Cu (10 nm). After 30 minutes, 60 minutes and 90 minutes, a volume of 0.1 mL was taken from each petri

dish and spread on the freshly prepared nutrient agar. The plates were then incubated at 37 °C for 24 hours and the number of active *Escherichia coli* cells was determined by colony count. The schematic of the experimental set-up done under sunlight is shown in Figure 7.1.

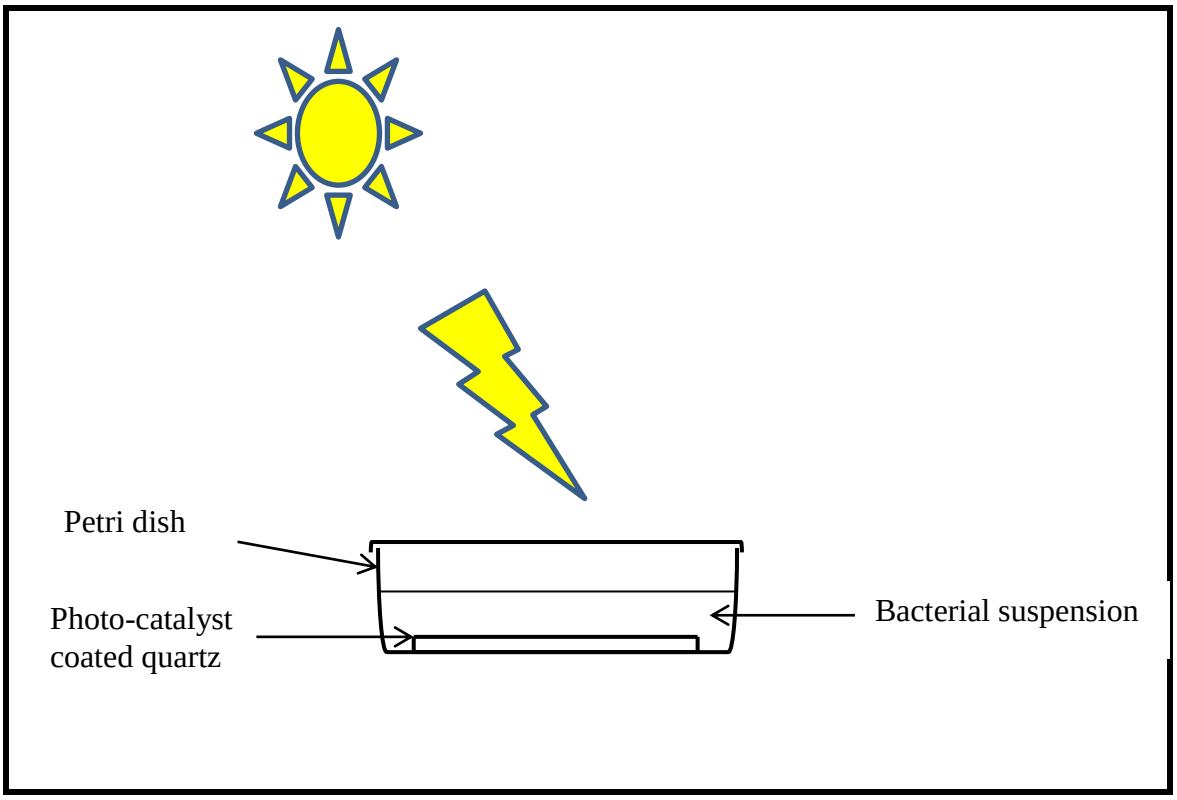

Figure 7.1: Antimicrobial activity experimental set up under sunlight.

7.2 Results and discussion

This section presents the inactivation results obtained from the evaluation of *E. coli* ATCC 3695 using pure TiO_2, 0.5 % Au/C co-doped TiO_2, 0.5 % Ag/C co-doped TiO_2, TiO_2/Ag (5 nm), TiO_2/Ag (10 nm), TiO_2/Au (5 nm), TiO_2/Au (10 nm), TiO_2/Cu (5 nm) and TiO_2/Cu (10 nm).

7.2.1 Inactivation of *E. coli* ATCC 3695 using TiO_2 deposited on plasmon metal films

The section gives an evaluation of the effect of;

(i) Using different plasmon metals (Au, Ag and Cu) on the antibacterial action of TiO_2 photo-catalyst against *E. coli* ATCC 8739 under weak UV light illumination. The positive control was pure TiO_2, negative control was the quartz substrate with no photo-catalysts deposited and the fixed parameter was the thickness of the plasmon metal used together with TiO_2 photo-catalyst.

(ii) Plasmon metal loading on the antibacterial properties of TiO_2 photo-catalyst against *E. coli* ATCC 8739. The effect of loading of all the three metals (Au, Ag and Cu) under study was evaluated. The control was the quartz support with no photo-catalyst, the fixed parameter in each case was the type of the plasmon metal used and the variable parameter was the amount of plasmon metal used with TiO_2 photo-catalyst

The profiles of the inactivation of *E. coli* ATCC 3695 using TiO_2/Au (5 nm), TiO_2/Au (10 nm), TiO_2/Cu (5 nm), TiO_2/Cu (10 nm), TiO_2/Ag (5 nm) and TiO_2/Ag (10 nm) are shown in Figure 7.2.

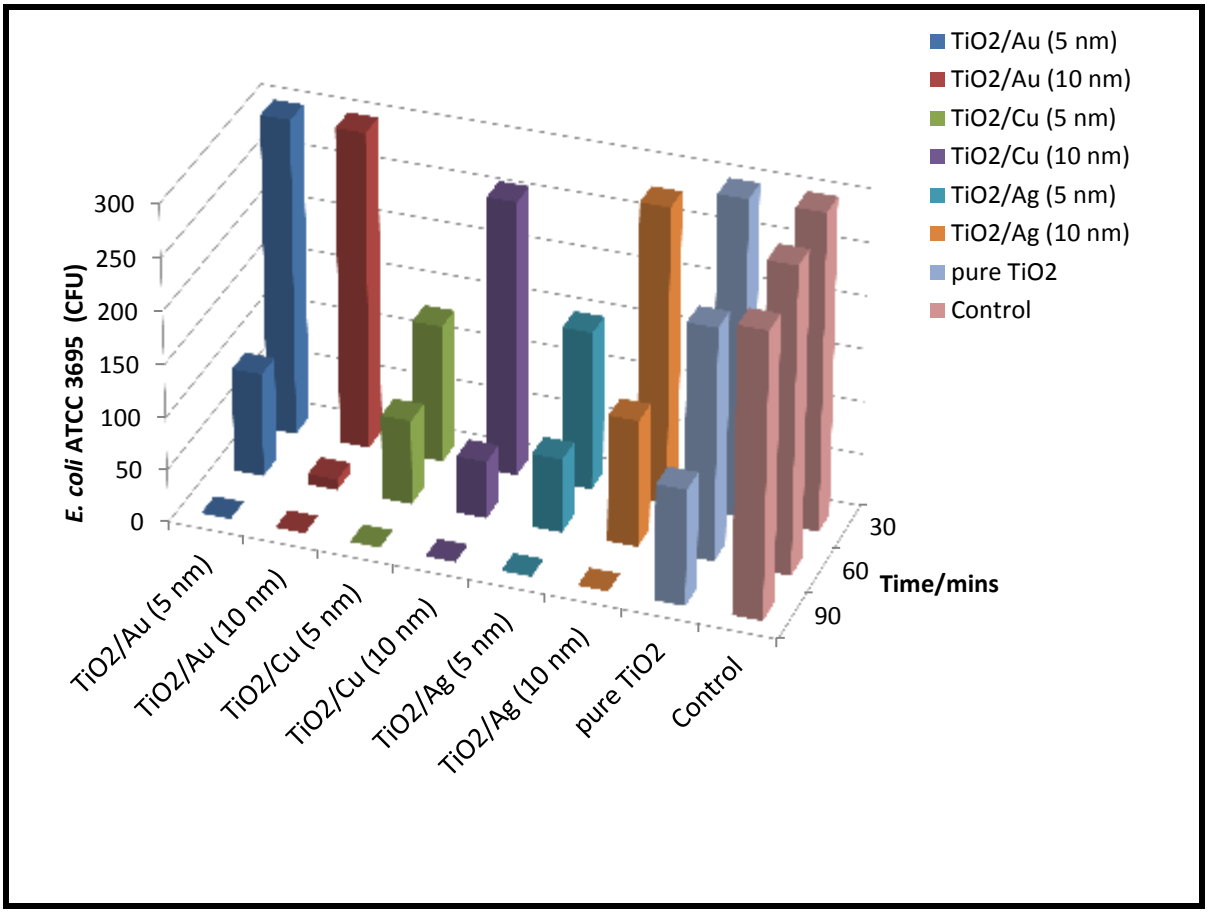

Figure 7.2: Inactivation of *E. coli* in water by immobilized photo-catalysts.

There was an insignificant decrease in the number of *E. coli* ATCC 3695 colony forming units (CFU) that was observed after 90 minutes for the control experiment, which was found to be only 30 CFU. This value was used to adjust the inactivation of other photo-catalysts to account for the effect of UV light only. All the photo-catalysts including pure TiO_2 showed a decrease in the number of colony units with time under weak UV illumination. Pure TiO_2 photo-catalyst showed the least and steady decline in the number of *E. coli* ATCC 3695 colony forming units. When the TiO_2 photo-catalyst was deposited on plasmon metal films, the rate of decrease in the number of *E. coli* ATCC 3695 colony forming units increased and a significant inactivation was observed after 60 minutes of exposure. The highest rate of inactivation of about 9.67 CFU/min between 30 minutes and 60 minutes was observed from TiO_2/Au (10 nm).

The higher antibacterial properties of the plasmon metal decorated TiO_2 photo-catalysts when compared to pure TiO_2 was due to the increase in the lifetime of charge carriers. Their extended lifetime means that; (i) there are more holes to kill bacteria. Direct oxidation by h^+ from the valence band of TO_2 was reported by Nadtochenko *et al*, 2008, (ii) the generation of reactive oxygen species such as $O_2^{\bullet -}$, H_2O_2 and $HO^{\bullet}$ which cause several oxidative damages on the microorganism is promoted. Sunada and coworkers, 2003 found out that the hydroxyl radicals were the major cause of the antibacterial effect. Although all photo-catalysts stopped bacterial growth after 90 minutes, there was a difference in the rate at which the inactivation occurred.

Increasing the thickness of the gold increased the inactivation of *E. coli* ATCC 3695 in water. After 60 minutes of exposure, there was reduction of *E. coli* ATCC 3695 colonies by 96 % using TiO_2/Au (10 nm) photo-catalyst as opposed to 67.33 % using TiO_2/Au (5 nm) photo-catalyst for the same period of exposure. When the thickness of silver was increased from 5 nm to 10 nm, there was a decrease of 10 % after 60 minutes on the inactivation of *E. coli* ATCC 3695. Copper films followed the same trend as that observed on Ag films of the same thickness only in the first 30 minutes of exposure. As the time of exposure was increased to 60 minutes, 82 % inactivation of *E. coli* ATCC 3695 was achieved by TiO_2/Cu (10 nm) whereas TiO_2/Cu (5 nm) inactivated 73.33 % of the bacteria. These results show that plasmon metal film thickness is important in determining the extent to which TiO_2 photo-catalyst destroys bacteria.

The findings of this study showed that Au, Ag and Cu films enhance antibacterial action of TiO_2 on *E. coli* ATCC 3695. The only difference was the rate at which the *E. coli* ATCC

3695 was inactivated. The highest rate of inactivation was achieved by TiO_2/Au (10 nm) photo-catalyst and the least was TiO_2/Ag (10 nm) photo-catalyst.

7.2.2 Inactivation of *E. coli* ATCC 3695 using Ag/C co-doped TiO_2 and Au/C co-doped TiO_2 photo-catalysts under sunlight

This section presents the evaluation of the inactivation of *E. coli* ATCC 3695 using doped TiO_2 photo-catalysts under sunlight. The control was the quartz with no photo-catalyst but also exposed to the sun, the fixed parameter was the amount of the plasmon metal dopant in TiO_2 photo-catalyst and the variable was the type of the plasmon metal used as the dopant. The profiles of the inactivation of *E. coli* ATCC 3695 using Ag/C co-doped TiO_2 (0.5 % Ag), Au/C co-doped TiO_2 (0.5 % Au) and undoped TiO_2 photo-catalysts are shown in Figure 7.3.

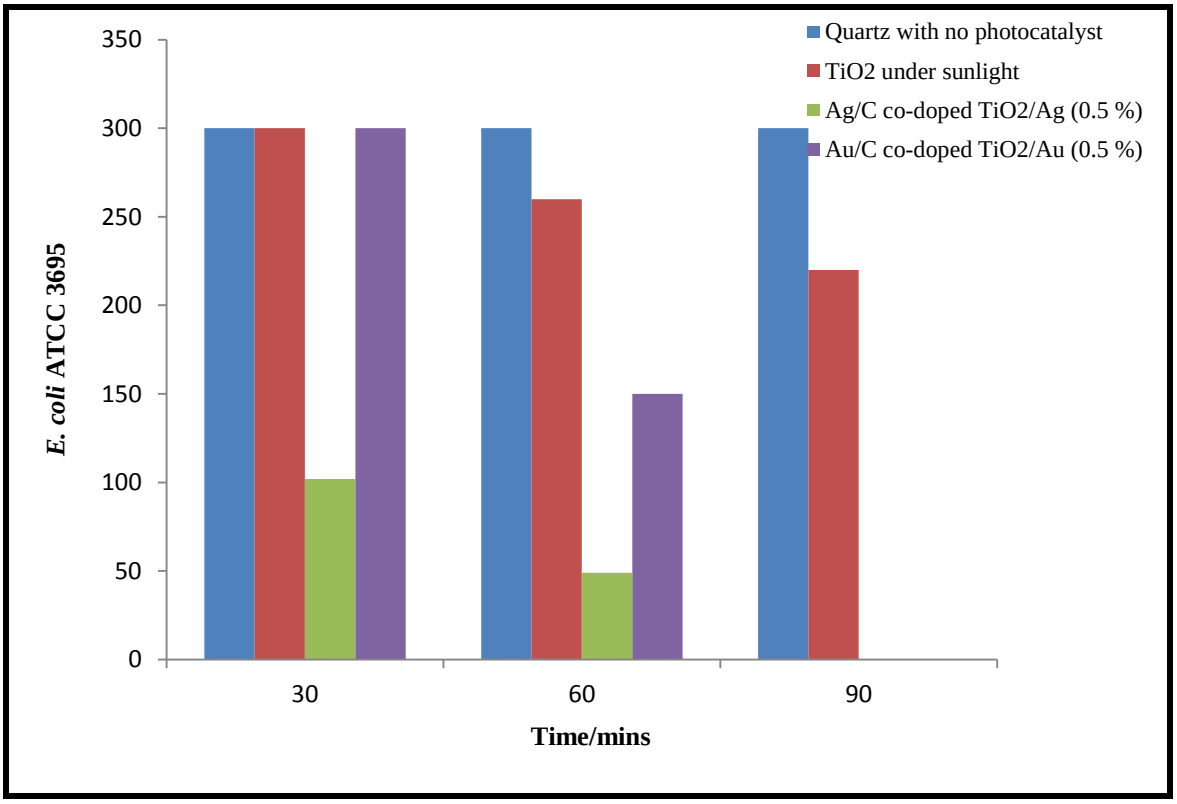

Figure 7.3: Inactivation of *E. coli* ATCC 3695 in water by immobilized photo-catalysts.

There was no inactivation under sunlight from the control implying that the inactivation that was observed in other experiments was actually due to the photo-catalysts. The inactivation due to undoped TiO_2 under weak UV light was 63.33 % and under sunlight 26.67 % after 60 minutes of exposure implying that TiO_2 is more active under UV than sunlight because of its wide ban gap. When the doped TiO_2 photo-catalysts were used, there was an improvement in inactivation of *E. coli* ATCC 3695 from 26.67 % for undoped TiO_2 to 50 % inactivation by Au/C co-doped TiO_2 (0.5 % Au) and 83.67 % by Ag/C co-doped TiO_2 (0.5 % Ag) after 60 minutes of exposure to sunlight. The reason for the highest inactivation due to Ag/C co-doped TiO_2 (0.5 % Ag) is the low band gap of 1.95 eV meaning it was capable of absorbing visible light to generate e^--h^+ pairs and reactive oxygen species responsible for inactivating the growth of bacteria in water.

The images of *E. coli* ATCC 3695 growing on nutrient agar petri dishes after exposure to, (A) TiO_2/Au (5nm), (B) TiO_2/Au (10 nm), (C) TiO_2/Cu (10 nm), (E) TiO_2/Cu (5 nm), (F) 0.5 % Au carbon co-doped TiO_2 and (G) 0.5 % Ag carbon co-doped TiO_2 are shown in Figure 7.4.

Figure 7.4: Images of colonies of E. coli ATCC 3695 treated with (A) TiO_2/Au (5nm), (B) TiO_2/Au (10 nm), (C) TiO_2/Cu (10 nm), (E) TiO_2/Cu (5 nm), (F) 0.5 % Au carbon co-doped TiO_2 and (G) 0.5 % Ag carbon co-doped TiO_2.

The images agree well with the information that has been provided in the inactivation profiles discussed earlier. All the images show a decrease in the number of colonies with increase in time of exposure and no colonies were observed after 90 minutes except for the controls. The

results showed that the inactivation of *E. coli* ATCC 3695 by TiO_2 photo-catalyst is greatly improved by plasmon elements when used as dopants or when deposited layer by layer. These results are similar to some work that has been reported by Stoyanova *et al*, 2013 where they found out that Fe-doped TiO_2 exhibited very high antibacterial action. They achieved 95.7 % removal efficiency in the first 5 minutes and complete killing of bacteria in 10 minutes. They also found out that the doped photo-catalyst could kill bacteria both under UVA and visible light illumination.

7.3 Summary

This study showed that the reduction in band gap of TiO_2 making it visible light responsive improves its antibacterial action against *E. coli* ATCC 3695. The highest antibacterial action was observed from Ag/C co-doped TiO_2 (0.5 %) photo-catalyst under sunlight. When deposited layer by layer, all the plasmon metals (Au, Ag & Cu) were found to enhance the antibacterial action of TiO_2. There was an increase in the antibacterial action of TiO_2 when the plasmon metal content was increased from 5 nm to 10 nm for Au and Cu but a decrease in case of Ag. When all the three metals were compared, the highest enhancement of TiO_2 antibacterial action was achieved by Au for the same metal content and the best antibacterial inactivation under weak UV light was achieved by TiO_2 photo-catalyst deposited on 10 nm of gold film.

Chapter 8

Conclusions and Recommendations

8.1 Conclusions

Plasmon metal decorated TiO_2 films and nanocomposites were successfully prepared and tested for their photo-catalytic and antimicrobial activities. The deposition of a thin layer of plasmon metal nanoparticles on top of TiO_2 enhanced the photo-catalytic activity of the photo-catalyst under both UV and visible light irradiation. Thinner films showed better enhancement than thicker films and the highest enhancement was achieved by using a 2 nm of Ag since Ag was found to favour oxygen adsorption promoting formation of superoxide radicals. All the different elements Au, Ag and Cu proved that they are capable of enhancing photo-activity by acting as electron reservoirs. When the order of deposition was changed, TiO_2 now being deposited on top of the plasmon metal films, all the Ag films of different thicknesses improved the photo-catalytic activity of TiO_2 whereas in case of Au and Cu, only the thinner films improved and the thicker films >10 nm deactivated the photo-catalyst. These findings suggest that, better photo-catalytic enhancement is achieved with optimum loading of the plasmon elements otherwise they will be detrimental to the photo-catalyst. Au films were found to enhance photo-activity better when they were deposited at the bottom of TiO_2 than on top as there is no reduction in the amount of light reaching the TiO_2 surface when compared with a photo-catalyst with Au film on top. Ag films performed better in enhancing photo-activity when they were deposited on top of TiO_2. Under visible light irradiation, the order of enhancement using a 2 nm metal film on TiO_2 was TiO_2/Cu > TiO_2/Au > TiO_2/Ag which was opposite under UV light. These findings point out that the correct order of deposition should be employed for a particular type of light used for

irradiation so as to achieve the best photo-catalytic activity enhancement of the TiO_2 photo-catalyst.

One of the significant findings of this study was that, the use of bimetal or three layers of different plasman elements are better than the use of a monometallic layer in achieving good photo-catalytic activities. The creation of more than one Schottky barriers was effective in separating the charges thereby reducing electron hole recombination rates as evidenced by the highest enhancement from 57.16 % for pure TiO_2 to 86.26 % by the three layer system. This also showed that metals combined synergistically are promising in producing photo-catalysts with higher photo-efficiencies.

The presence of salts and other contaminants other than the target pollutant have been found to reduce the photo-degradation of the target contaminant due to preferential adsorption of other contaminants. In such cases, the plasmon decorated TiO_2 photo-catalysts still performed better than the pure TiO_2 meaning they have potential application in any kind of environment. When methyl orange was mixed with bromocresol purple, it was found that bromocresol purple was degraded more than methyl orange for the same period of time showing that the photo-catalysts are selective to the contaminants that they degrade and this depends on the charges on both the TiO_2 surface and the organic pollutant. The photo-activity of methyl orange was also found to increase with a decrease in the pH of the solution which was attributed to the positive charge acquired by the photo-catalyst surface at low pH which made it easy for methyl orange adsorption with a negative charge arising from the ionized sulphonic groups.

The photo-catalysts tested for durability showed that they are durable and can be used for at least four times without appreciable loss of photo-catalytic activities. For instance TiO_2 on a three layer system (TiO_2/Au/Ag/Cu) showed 95.88 % degradation of bromocresol purple after five hours and after the fourth application 80.98 % which was still good. Leaching from this photo-catalyst increased with increase in the number of cycles and was minimal for Au and Cu with values of 0.0093 ppm and 0.0460 ppm respectively on the fourth application but for Ag it was 10.42 ppm. Leaching was also found to depend on the position of the plasmon element relative to the photo-catalyst.

The study also showed that carbon and a plasmon element (Ag or Au) can be simultaneously introduced into the crystal system of TiO_2 photo-catalyst forming a non-metal and metal co-doped photo-catalyst. The incorporation of impurities into the crystal structure proved to be a promising way of enhancing the photo-catalytic activity of the photo-catalyst. Doping increased the surface area of the photo-catalyst, promoted anatase to rutile phase transformation and allowed utilization of visible light due to reduced band gap. No general trend was observed on the band gap reduction and plasmon metal content but the optimal loading of Ag and Au for better photo-catalytic activities was 0.5 % and 1.0 % respectively.

The combination of the doped photo-catalyst and plasmon metal nanoparticles to form nanocomposites improved photo efficiencies dramatically as both the doped photo-catalyst and plasmon metal nanoparticles absorbed visible light. Nanocomposites produced from TiO_2 and different structures of plasmon elements such as dendrites and nanowires showed good photo-efficiencies. The results of this study also showed that polydispersity of the nanoparticles was beneficial for photo-catalytic activity enhancement under sunlight since

wide size and shape distribution have the ability to absorb light in a wide range of wavelength.

The selected photo-catalysts showed very good antimicrobial activity against *Escherichia coli* ATCC 3695 in water.

8.2 Recommendations

The results from this study provide several perspicacities for future research and these are discussed in the following paragraphs.

Further work needs to be done to study the effect of other operational parameters such light intensity, photo-catalyst loading, type of contaminant, temperature and radiation source. Although there are some works done on the effect of these operational parameters, it is difficult to compare the results due to the differences in the type of TiO_2 photo-catalyst and reactor set-up used. To make a general trend on the effects of these parameters, there is need to do further work using one type of photo-catalyst in the same reactor set-up.

The study showed that the photo-catalysts are indiscriminant and can degrade any organic contaminant but some target pollutants took long to degrade hence these photo-catalysts can be coupled with another water treatment technology to give synergistic effects that can reduce economic cost and the time required to produce clean water. Since photo-catalytic efficiency of the photo-catalysts did not decrease significantly with repeated use, further studies where the photo-catalysts are applied in continuous systems need to be done. Pilot plant investigations on the use of the photo-catalyst to produce large volumes of clean water

could be done to assess application in the industry since it would give kinetic parameters needed for scale-up.

The effect of different supports need to be explored as some supports help improve the photo-degradation of the organic contaminants.

Leaching was found to be a disadvantage on some photo-catalysts and there is need for improvement of the adhesion of the photo-catalyst to minimize loss of the photo-catalyst when used for more than one cycle.

Further studies could be done using water sampled from actual polluted streams that contain several other contaminants besides the target compound. This would also help understand the effect of other pollutants of different nature on the degradation pathway followed by the target pollutant.

The safety and long-term effects of nanoparticles that might have leached in water are not fully understood and their environmental impacts need to be explored. Investigation of the inactivation of different types of pathogens such as protozoa and viruses also needs to be done so as to know which pathogens are effectively removed from water by TiO_2 photo-catalysts.

References

Adleman, J. R.; Boyd, D. A.; Goodwin, D. G.; Psaltis, D. Heterogenous Catalysis Mediated by Plasmon Heating, *Nano Letters*, **2009**, 9, 4417-4423.

Ahmed, S.; Rasul, M. G.; Martens, W. N.; Brown, R.; Hashib, M. A. Heterogeneous Photocatalytic Degradation of Phenols in Wastewater: A Review on Current Status and Developments. *Desalination*, **2010,** 261, 3–18.

Akpan, U. G & Hameed, B. H. Parameters affecting the photocatalytic degradation of dyes using TiO_2-based photo-catalysts: A review. *Journal of Hazardous Materials*, **2009**, 170, 520–529.

Alinsafi, A.; Evenou F.; Abdulkarim, E. M.; Pons, M. N.; Zahraa, O.; Benhammou, A.; Yaacoubi, A.; Nejmeddine, A. Treatment of textile industry wastewater by supported photocatalysis. *Dyes and Pigments*, **2007**, 74, 439- 445.

Allegre, C.; Moulin, P.; Maisseu, M.; Charbit, F. Treatment and reuse of reactive dyeing effluents. *Journal of Membrane Science,* **2006**, 269, 15–34.

Alvaro, M.; Cojocaru, B.; Ismail, A. A.; Petrea N.; Ferrer B.; Harraz, F.A.; Parvulescu, V. I.; Garcia, H. Visible-light photocatalytic activity of gold nanoparticles supported on template-synthesized mesoporous titania for the decontamination of the chemical warfare agent Soman. *Applied Catalysis B: Environmental*, **2010**, 99, 191–197.

An, G.; Yang, C.; Zhou, Y.; Zhao, X. Plasmon-enhanced photoluminescence from TiO_2:Sm_3R: Au nanostructure. *Physica Status Solidi A*, **2012**, 209 (12), 2583–2588.

Androzzi, R.; Caprio, V.; Insola, A. Kinetics and Mechanism of polyethyleneglycol fragmentation by ozone in aqueous solution. *Water Research*, 2000, 30, 2955-2960.

Attar, A. S.; Ghamsari., M. S.; Hajiesmaeilbaigi, F.; Mirdamadi, S.; Katagiri, K.; Baetzold, R. C. *Journal of the American Chemical Society*, **2008**, *103*, 6116.

Balamurugan, B.; Maruyama, T. Evidence of an enhanced interband absorption in Au nanoparticles: Size-dependent electronic structure and optical properties. *Applied Physics Lett*ers, **2005**, 87, 143105-3.

Balasubramanian, G.; Dionysiou, D. D.; Suidan, M. T.; Baudin, I.; Jean-Michel Laine, J. M. Evaluating the activities of immobilized TiO_2 powder films for the photocatalytic degradation of organic contaminants in water. *Applied Catalysis B: Environmental*, **2004**, 47, 73–84.

Banerjee, S.; Dionysiou, D. D.; Pillai, S. C. Self-cleaning applications of TiO_2 by photo-induced hydrophilicity and photocatalysis. *Applied Catalysis B: Environmental*, **2015**, 396–428.

Barakat, N. A. M.; Kanjwal, M. A.; Al-Deyab, S. S.; Chronakis, I. S.; Kim, H. Y. Influences of Silver-Doping on the Crystal Structure, Morphology and Photocatalytic Activity of TiO_2 Nanofibers. *Materials Sciences and Applications*, **2011**, 2, 1188-1193.

Berdahl, P. Pigments to reflect the infrared radiation from fire. *Journal of Heat Transfer*, **1995**, 117, 2, 355-358.

Bharathi, S.; Fishelson, N.; Lev, O. Direct Synthesis and Characterization of Gold and Other Noble Metal Nanodispersions in Sol-gel Derived Organically Modified Silicates. *Langmuir*, **1999**, 15 (6), 1929–1937.

Blanco-Galvez, J.; Fernandez-Ibanez, P.; Malato-Rodriguez, S. Solar photocatalytic detoxification and disinfection of water: recent overview. *Journal of Solar Energy Engineering*, **2007**, 129 (1), 4-15.

Blossey, R. Self-cleaning surfaces-virtual realities, *Nature Materials*, **2003**, 2, 301-306.

Brezova, V.; Blaskova, A.; Borsova, E.; Ceppan, M.; Fiala, R. The influence of dissolved metal ions on the photocatalytic degradation of phenol in aqueous TiO_2 suspensions. *Journal of Molecular Catalysis A-Chemical*, **1995**, 98 (2), 109－116.

Brojcin, M. G.; Scepanovic, M. J.; Mitrovic, Z. D.; Hinic, I.; Matovic, B.; Stanisic, G.; Popovic, Z. Infrared study of laser synthesized anatase TiO_2 nanopowders. *Journal of Physics D: Applied Physics*, **2005**, 38, 1415–1420.

Bryan, J. D.; Gamelin, R. D. Doped Semiconductor Nanocrystals: Synthesis, Characterization, Physical. *Progress in Inorganic Chemistry*, **2005**, *54*, 47-126.

Byranvand, M. M., Kharat, A. N., Fatholahi, L., Beiranvand, Z. M. A Review on Synthesis of Nano-TiO_2 via Different Methods. *Journal of Nanostructures*, **2013**, 1-9.

Buffat, P.; Borel, J. P. Size effect on the melting temperature of gold particles. *Physical Review*, **1976**, *13*, 2287–2298.

Burda, C.; Lou, Y.; Chen, X.; Samia, A. C. S.; Stout, J.; Gole, J. L. Enhanced Nitrogen Doping in TiO_2 Nanoparticles. *Nano Letters*, **2003**, 3 (8), 1049-1051.

Calla, O. P. N.; Mishra, S. K.; Bohra, D. Design a tunable cavity resonator for complex permittivity measurement of low-loss material at L band. *Indian Journal of Pure and Applied Physics*, **2008**, 46, 134-138.

Carp, O.; Huisman, C. L.; Reller, A. Photoinduced reactivity of titanium dioxide. *Progress in Solid State Chemistry*, **2004**, *32*, 33–177.

Chan, G. H.; Zhao, J.; Hicks, E. M.; Schatz, G. C.; Van Duyne, R. P. Plasmonic Properties of Copper Nanoparticles Fabricated by Nanosphere Lithography. *Nano Letters*, **2007**, 7 (7), 1947-1952.

Chaves, A.; Katiyan, K. S.; Porto, S. P. S. Coupled modes with A_1 symmetry in tetragonal BaTiO3. *Physical Review*, **1974**, *10*, 3522-3533.

Chen, X.; Zhu, H. Y.; Zhao, J. C.; Zheng, Z. F.; Gao, X. P. Visible-light-driven oxidation of organic contaminants in air with gold nanoparticle catalysts on oxide supports. *Angewandte Chemie International Edition*, **2008**, 47, 5353–5356.

Chen, D.; Ray, A. K. Photo-degradation kinetics of 4-nitrophenol in TiO_2 suspension. *Water Research,* **1998**, 32 (11), 3223–3234.

Chen, S.; Wang, L. W. Thermodynamic Oxidation and Reduction Potentials of Photocatalytic Semiconductors in Aqueous Solution. *Joint Center for Artificial Photosynthesis*, **2012**, 1-5.

Choi, J.; Park H.; Hoffmann, M. R. Effects of Single Metal-Ion Doping on the Visible-Light Photoreactivity of TiO_2. *Journal of Physical Chemistry* C, **2010**, 114 (2), 783–792.

Choi, W. Y.; Termin, A.; Hoffmann, M. R. The role of metal ion dopants in quantum-sized TiO_2: correlation between photoreactivity and charge carrier recombination dynamics. *Journal of Physical Chemistry,* **1994**, 84, 13669–13679.

Chong, M. N.; Jin, B.; Chow, C. W. K.; Saint, C. Recent developments in photo-catalytic water treatment technology: A review. *Water Research,* **2010**, 44, 2997-3027.

Chong, M. N.; Vimonses, V.; Lei, S.; Jin, B.; Chow, C.; Saint, C. Synthesis and characterisation of novel titania impregnated kaolinite nano-photocatalyst. *Microporus and Mesoporus Materials*, **2009**, 117, 233-242.

Choquette-Labbe, M.; Shewa, W. A.; Lalman, J. A. Shanmugam, S. R. Photo-catalytic Degradation of Phenol and Phenol Derivatives Using a Nano-TiO_2 Catalyst: Integrating Quantitative and Qualitative Factors Using Response Surface Methodology. *Water*, **2014**, 6, 1785-1806.

Cong, Y.; Zhang, J.; Chen, F.; Anpo, M. Synthesis and Characterization of Nitrogen-Doped TiO_2 Nanophotocatalyst with High Visible Light Activity. *Journal of Physical Chemistry C*, **2007**, 111 (19) 6976–6982.

Corma, A.; Garcia, H. "Zeolite-based photo-catalysts", *Chemical Communications*, **2004**, 10, 1443-1459.

Cushing, B. L., Kolesnichenko, V.L., O'Connor, C.J.: Recent advances in the liquid-phase syntheses of inorganic nanoparticles. *Chemical Reviews*, **2004**, 104, 3893–3946.

Cushing, S. K.; Li, J.; Meng, F.; Senty, T. R.; Suri, S., Zhi, M.; Li, M.; Bristow, A. D.; Wu, N. Q. Photo-catalytic activity enhanced by plasmonic resonant energy transfer from metal to semiconductor. *Journal of American Chemical Society*, **2012**, 134, 15033-41.

Cushing, S. K.; Wu, N. Plasmon-Enhanced Solar Energy Harvesting. *The Electrochemical Society Interface.* Summer, **2013**, 63-67.

Dang, T. M. D.; Nguyen, T. M. H.; Nguyen, H. P. The preparation of nano-gold catalyst supported on iron doped titanium oxide. *Advances in Natural Sciences: Nanoscience and Nanotechnology*, **2010**, *1*, 1-7.

Dang, T. M. D.; Le T. T. T.; Fribourg-Blanc, E.; Dang, M. C. Synthesis and optical properties of copper nanoparticles prepared by a chemical reduction method. *Advances in Natural Sciences: Nanoscience and Nanotechnology*, **2011**, 2, 1-6.

Dhananjeyan M. R.; Kandavelu V.; Renganathan R. An investigation of the effects of Cu^{2+} and heat treatment on TiO_2 photo-oxidation of certain pyrimidines. *Journal of Molecular Catalysis: Chemical*, **1997**, 158, 577-582.

Dijkra , M. F. J.; Buwalda, H.; De Jong, A. W. F.; Michorius, A.; Winkelman, J. G. M.; Beenackers, A. A. C. M. Experimental comparison of three reactor design for photo-catalytic water purification. *Chemical Engineering Science*, **2001**, 56, 547-562.

Ding, Z.; Zhu, H. Y.; Lu, G. Q.; Greenfield, P. F. Photo-catalytic Environmental Remediation involving clay surfaces. *Encyclopedia of Surface and Colloid Science*, **2006**, 6 (2), 4525-4537.

Di Paola, A.; Garcia-Lopez, E.; Ikeda, S.; Marci, G.; Ohtani, B.; Palmisano, L. Photo-catalytic degradation of organic compounds in aqueous systems by transition metal doped polycrystalline TiO_2. *Catalysis Today,* **2002**, 75, 87-93.

Diwald, O.; Thompson, T. L.; Zubkov, T.; Walck, T. D.; Yates, J. T. Photochemical Activity of Nitrogen-Doped Rutile TiO_2 (110) in Visible Light. *Journal of Physical Chemistry B*, **2004**, 108 (19), 6004-6008.

Djerdj, I.; Tonej, A. M.; Bijelic, M.; Vranesa, V.; Turkovic, A. Transmission electron microscopy studies of nanostructured TiO_2 films on various substrates. *Vacuum*, **2005**, 80, 371-378.

Dvorak, B. I.; Skipton, S. O. Drinking water treatment, Activated carbon filtration, University of Nebraska-Lincoln Extension, Institute of Agriculture and Natural Resources, *Binco*, **2008**, 1, 2-4.

El-Sayed, M. A. Some Interesting Properties of Metals Confined in Time and Nanometer Space of Different Shapes. *Accounts of Chemical Research*, **2001**, 34, 257–264.

Emeline, A. V.; Kuznetsov, V. N.; Rybchuk, V. K.; Serpone, N. Visible-Light-Active Titania Photo-catalysts: The Case of N-Doped TiO_2. Properties and Some Fundamental Issues. *International Journal of Photoenergy*, **2008**, 1-19.

EPA (United States Environmental Protection Agency). Drinking Water Contaminants, **2009**. http://water.epa.gov/drink/contaminants/. Accessed on the 28th of August 2015.

EPA. (1997). Environmental Protection Agency, Washington, USA. *Profile of the textile industry*

EPA (1999). Alternative Disinfectants and Oxidants Guidance Manual. United States Environmental Protection Agency. Office of Water (4607) EPA 815-R-99-014, **1999**

Escobedo Morales, A.; Sanchez Mora, E.; Pal, U. Use of diffuse reflectance spectroscopy for optical characterization of un-supported nanostructures. *Revista Mexicana de Fisica* S, **2007**, *53* (5), 18–22.

Eustis, S.; El-Sayed, M. A. Why gold nanoparticles are more precious than pretty gold: Noble metal surface plasmon resonance and its enhancement of the radiative and nonradiative properties of nanocrystals of different shapes. *Chemical Society Reviews*, **2006**, 35, (209), 209–217.

Fan, W.; Zhang, Q.; Wang, Y. Semiconductor-based nanocomposites for photocatalytic H_2 production and CO_2 conversion. *Physical Chemistry Chemical Physics*, **2013**, 15, 2632-2649.

Feng, C.; Khulbe, K. C.; Matsuura, T.; Tabe, S.; Ismail, A. F. Preparation and characterization of electro-spun nanofiber membranes and their possible applications in water treatment. *Separation and Purification Technology*, **2013**, 102, 118–135.

Feng, Q. L.; Wu, J.; Chen, G. Q.; Cui, F. Z.; Kim, T. N.; Kim, J. O. A mechanistic study of the antibacterial effect of silver ions on Escherichia coli and Staphylococcus aureus. *Journal of Biomedical Materials Research*, **2008**, 52, 662–668.

Fernhndez, A.; Lassaletta, G.; Jimknez, V. M.; Justo, A.; GonzSlez-Elipe, A. R.; Herrmann, J. M.; Tahiri, H.; Ait-Ichou, Y. Preparation and characterization of TiO_2 photocatalysts supported on various rigid supports (glass, quartz and stainless steel). Comparative studies of photocatalytic activity in water purification. *Applied Catalysis B: Environmental*, **1995**, 7, 49-63.

Fischer, K.; Fries, E.; Korner, W.; Schmalz, C.; Zwiene, C. New developments in the trace analysis of organic water pollutants. *Applied Microbiology and Biotechnology*, **2012**, 94, 11-28.

Foger, K.; Anderson, J. R. Thermally stable SMSI supports: Iridium supported on TiO_2-Al_2O_3 and on Ce-stabilized anatase. *Applied Catalysis,* **1986**, *23*, (1), 139-155.

Fogler, H. S., 1999. Elements of Chemical Reaction Engineering: Chapter 10: *Catalysis and Catalytic Reactors*. Prentice-Hall PTR Inc,. 581-685.

Franch, . M. I.; Peral, J.; Domènech, X.; Howe, R. F.; Ayllon, J. A. Enhancement of photo-catalytic activity of TiO_2 by adsorbed aluminium (III). *Applied Catalysis B: Environmental,* **2005**, 55, 105-113.

Fricker, S. P. Medicinal chemistry and pharmacology of gold compounds. *Transition Metal Chemistry,* **1996,** 21, 377–383.

Fujishima, A.; Honda, K. Electrochemical photolysis of water at a semiconductor electrode. *Nature*, 1972, 37-38.

Fujishima, A., Zhang, X. Titanium dioxide photocatalysis: present situation and future approaches. *Comptes Rendus Chimie*, **2006**, 9, 750–760.

Funston, A. M.; Novo, C.; Davis, T. M.; Mulvaney, P. Plasmon Coupling of Gold Nanorods at Short Distances and in Different Geometries. *Nano Letters*, **2009**, 9 (4), 1651-1658.

Furlong, D. N.; Wells, D.; Sasse, W. H. F. Colloidal semiconductors in systems for the sacrificial photolysis of water: Sensitization of titanium dioxide by adsorption of ruthenium complexes. *Journal of Physical Chem*istry, **1986**, 90 (6) 1107–1115.

Gao, E. Q.; Zhang, L; Yang, M. Z.; Cai, S. M. Preparation of TiO_2 Nanoparticles by Hydrothermal Method and its Application for Photoelectrochemical Cell. *Acta Physico Chimica Sinica*, **2001**, 17 (2), 177-180.

Gaya, U. I.; Abdullah, A. H. Heterogeneous photocatalytic degradation of organic contaminants over titanium dioxide: a review of fundamentals, progress and

problems. *Journal of Photochemistry and Photobiology C: Photochemistry Reviews*, **2008**, *9*, 1-12.

Gautron, J.; Lemasson, P.; Marucco, J. M. Correlation between the non-stoichiometry of titanium dioxide and its photoelectrochemical behaviour. *Faraday Discussions of the Chemical Society*, **1981**, 70, 81–91.

Gerhardt, P.; R. G. E.; Murray, W. A.; Wood, N. R. Krieg**.** 1994. "Methods for General and Molecular Bacteriology." *ASM Press*, Washington, D.C.

Ghoneim, D.; Hafez, F. M.; El-Sayed, S.N.; Mohsen, N. A.; Mahmoud, A. M. A. Optical properties of amorphous cugaxin25-xte74 films and effect of annealing on these properties. *International Journal of Recent Research and Applied Studies*, **2012**, 12, 263-279.

Gondal, M.A.; Dastageer, M. A.; Rashid, S. G.; Zubair, S. M.; Ali, M. A.; Anjum, D. H.; Lienhard, J. H.; McKinley, G. H.; Varanas, K. Plasmon Resonance Enhanced Photocatalysis Under Visible Light with Au/Cu-TiO_2 Nanoparticles : Removal of Cr (VI) from Water as a Case Study. *Science of Advanced Materials*, **2013**, 5, 1–8.

Gopidas, K. R.; Bohorquez, M.; Kamat, P. V. Photophysical and photochemical aspects of coupled semiconductors: charge-transfer processes in colloidal cadmium sulphide-titania and cadmium sulfide-silver (I) iodide systems. *Journal of Physical Chemistry* **1990**, *94*, 6435-6440.

Goss, C. A.; Charych, D. H.; Majda, M. Application of (3-Mercaptopropyl) trimethoxysliane as a Molecular Adhesive in the Fabrication of Vapor-Deposited Gold Electrodes on Glass Substrates. *Analytical Chemistry,* **1991**, 63 (1), 85-88.

Grozescu, I.; Segneanu, A. E.; Orbeci, C.; Lazau, C.; Sfirloaga, P.; Vlazan P.; Bandas C. Waste Water Treatment Methods. *InTech Publishing*, **2013**, 53-80.

Gunawan, C.; Teoh, W. Y.; Marquis, C. P.; Lifia, J.; Amal, R. Reversible Antimicrobial Photoswitching in Nanosilver. *Small*, **2009**, 5, 341-344.

Gupta, S. M, Tripathi, M. A review of TiO_2 nanoparticles. *Chinese Science Bulletin*, **2011**, 56, 1639−1657.

Guzman, M. G.; Dille, J.; Godet, S. Synthesis of silver nanoparticles by chemical reduction method and their antibacterial activity. *International Journal of Chemical and Biological Engineering*, **2009**, 2 (3), 104-111.

Hadjltaiefa, H. B., Zinaa, M. B., Galvezb, M. E., Da Costab, P. Photocatalytic degradation of methyl green dye in aqueous solution over natural clay-supported ZnO–TiO_2 catalysts. *Journal of Photochemistry and Photobiology A: Chemistry*, **2016**, 315, 25–33.

Haizel, G. R. Optical properties and photocatalytic activities of titania nanoflowers synthesized by microwave irradiation. *International Journal of Innovative Research in Science, Engineering and Technology*, **2013**, 2 (6), 2175-2181.

Hanaor, D. A. H.; Sorrell, C. C. Review of the anatase to rutile phase transformation. *Journal of Material Science*, **2011**, 46, 855–874.

Hanaor, D. A. H., Sorrell, C. C. Sand supported mixed-phase TiO_2 photo-catalysts for water decontamination applications. *Advanced Engineering Materials*, **2014**, 16, (2), 248-254.

Hanel, A., Moren, P., Zaleska, A., Hupka, J. Photo-catalytic activity of TiO_2 immobilized on glass beads. *Physicochemical Probems of Mineral Processing*, **2010**, 45, 49-56.

Hao, E.; Schatz, G. C.; Hupp, J. T. Synthesis and Optical Properties of Anisotropic Metal Nanoparticles. *Journal of Fluorescence*, **2004**, 14, (4), 331-341.

Hao, E.; Schatz G. C. Electromagnetic fields around silver nanoparticles and dimers. Journal of Chemical Physics, **2004**, 120 (1), 357-366.

Hao, O.J.; Kim, H.; Chang, P.C. Decolorization of wastewater. *Critical Reviews in Environmental Science and Technology*, **2000**, 30, 449-505.

Harikishore, M.; Sandhyarania, M.; Venkateswarlua, K.; Nellaippana, T. A.; Rameshbabua, N. Effect of Ag doping on Antibacterial and Photocatalytic Activity of Nanocrystalline TiO_2. *Procedia Materials Science*, **2014**, (6) 557 – 566.

Haruta, M. Size and support-dependency in the catalysis of gold. *Catalysis Today*, **1997**, 36, 153–166.

Hashimoto, K.; Irie, H.; Fujishima, A. TiO_2 photo-catalysis: A historical overview and future prospects. *Japanese Journal of Applied Physics*, 2005, 44, 12, 8269-8285.

He, Z.; Que W. Surface scattering and reflecting: the effect on light absorption or photocatalytic activity of TiO_2 scattering microspheres. *Physical Chemistry Chemical Physics*, **2013**, 15, 16768-16773.

He, X.; Cai, Y.; Zhang, H.; Liang, C. Photocatalytic degradation of organic pollutants with Ag decorated free-standing TiO_2 nanotube arrays and interface electrochemical response. *Journal of Materials Chemistry*, **2011**, 21, 475–480.

Hedayati M. K.; Faupel F.; Elbahri M. Review of Plasmonic Nanocomposite Metamaterial Absorber. *Materials* **2014**, 7, 1221-1248.

Heller, A.; Brock, J. R.; Helz, G. R.; Zepp, R. G.; Crosby, D. G, editors. Aquatic and surface photochemistry. Orlando: *Lewis Publication*; **1994**, p. 427.

Herron, M. M.; Herron, S.; Charsky, A.; Akkurt, R. Diffuse reflectance infrared fourier transform spectroscopy for characterization of earth materials. *US20130046469 A1*, **2013**.

Hintsho, N.; Petrik, L., Nechaev, A.; Titinchi, S.; Ndungu, P. Photo-Catalytic Activity of Titanium Dioxide Carbon Nanotube Nano-composites Modified with Silver and

Palladium Nanoparticles., *Applied Catalysis B, Environmental*, **2014**, 156-157, 2715-2725.

Hirano, K.; Suzuki, E.; Ishikawa, A.; Moroi, T.; Shiroishi, H.; Kaneko, M. Sensitization of TiO_2 particles by dyes to achieve H_2 evolution by visible light. *Journal of Photochemistry and Photobiology A: Chemistry*, **2000**, 136, 157–161.

Hong, Y.; Huh, Y. M.; Yoon, D. S.; Yang, J. Nanobiosensors Based on Localized Surface Plasmon Resonance for Biomarker Detection. *Journal of Nanomaterials*, **2012**, 9, 1-13.

Hopkins, P. E. "Influence of Inter- and Intraband Transitions to Electron Temperature Decay in Noble Metals After Short-Pulsed Laser Heating," *Journal of Heat Transfer*, **2010**, 132 (12), 122402-6.

Hornaner, H.; Vancea, J.; Reiss, G.; Hoffmann, H. Thickness dependence of the work function in double-layer metallic films. *Zeitschrift für Physik B - Condensed Matter*, 1989, 77, 399-407.

Hou, W.; Cronin, S. B. A review of Surface Plasmon Resonance–Enhanced Photocatalysis. *Advanced Functional Materials*, **2013,** 23 (13), 1612-1619.

Hou, W., Hung, W. H.; Pavaskar, P.; Goeppert, A.; Aykol, M.; Cronin, S. B. Photocatalytic Conversion of CO_2 to Hydrocarbon Fuels via Plasmon-Enhanced Absorption and Metallic Interband Transitions. *American Chemical Society*, *Catalysis*, **2011**, 1 (8), 929–936.

Hou, X.; Jones, B. T. Inductively Coupled Plasma/Optical Emission Spectrometry. Encyclopedia of Analytical Chemistry. R. A. Meyers (Ed.) John Wiley & Sons Ltd, Chichester, **2000**, 9468 – 9485.

Hu, C.; Tang, Y. H.; Jiang, Z.; Hao, Z. P.; Tang, H. X.; Wong, P. K. Characterization and photocatalytic activity of noble-metal-supported surface TiO_2/SiO_2. *Applied Catalysis A,* **2003**, 253 (2), 389-396.

Huang, D., S. Liao, J. Liu, Z Dang, and L. Petrik. Preparation of visible-light responsive N–F-codoped TiO_2 photocatalyst by a sol–gel-solvothermal method. *Journal of Photochemistry and Photobiology A: Chemistry*, **2006**, 184 (3), 282-288.

Huang, X.; El-Sayed, M. A. Gold nanoparticles: Optical properties and implementations in cancer diagnosis and photothermal therapy. *Journal of Advanced Research*, **2010**, 1, 13–28.

Huh, A. J.; Kwon, Y. J. ‘‘Nanoantibiotics’’: a new paradigm for treating infectious diseases using nanomaterials in the antibiotics resistant era. *Journal of Controlled Release*, **2011**, 156, 128–145.

Hutter, E.; Fendler J. C. Exploitation of localised surface plasmon resonance. *Advanced Materials*, **2004**, *16* (19), 1685-1706.

IAEA (Internation Atomic Energy Agency). Instrumentation for PIXE and RBS, 2000 p. 5.

Ihara, T.; Miyoshi, M.; Triyama, Y.; Marsumato, O.; Sugihara, S. Visible-light-active titanium oxide photo-catalyst realized by an oxygen-deficient structure and by nitrogen doping. *Applied Catalysis B,* **2003**; 42, 403-409.

Jensen, T.; Kelly, L.; Lazarides, A.; Schatz G. C. Electrodynamics of Noble Metal Nanoparticles and Nanoparticle Clusters. *Journal of Cluster Science*, **1999**, 10, 295.

Jeong, S. H.; Yeo, S. Y.; Yi, S. C. The effect of filler particle size on the antibacterial properties of compounded polymer/silver fibers. *Journal of Materials Science*, **2005**, 40, 5407-5411.

Jiang, Z.; Lv, X.; Jiang, D.; Xie, J.; Mao, D. Natural leaves-assisted synthesis of nitrogen-doped, carbon-rich nanodots-sensitized, Ag-loaded anatase TiO_2 square nanosheets

with dominant {001} facets and their enhanced catalytic applications. *Journal of Materials Chemistry A*, **2013**, 1, 14963- 14972.

Jones, M. R.; Osberg, K. D.; Macfarlane, R. J.; Langille, M. R.; Mirkin, C. A. Templated Techniques for the Synthesis and Assembly of Plasmonic Nanostructures. *Chemistry Reviews*, **2011**, 111, 3736–3827.

Karunakaran, C.; Dhanalakshmi, R.; Gomathisankar P.; Manikandan G. Enhanced phenol-photo-degradation by particulate semiconductor mixtures: Interparticle electron-jump. *Journal of Hazardous Materials*, **2010**, 176, 799–806.

Kefeng, Y.; Yang, T.; Tatsuma, T. Size effects of gold nanoparticles on plasmon-induced photocurrents of gold–TiO_2 nanocomposites. *Physical Chemistry Chemical Physics*, **2006**, *8*, 5417–5420.

Khan, S. J.; Reed, R. H.; Rasul, M. G. Thin-film fixed-bed reactor (TFFBR) for solar photocatalytic inactivation of aquaculture pathogen *Aeromonas hydrophila*. *BioMed Central Microbiology*, **2012**, 12 (5), 1-11

Khang, N. C.; Khoi, N. T. Nano-Particles of Co Doped TiO_2 Anatase: Raman Spectroscopy and Structural Studies. *Journal of the Korean Physical Society*, **2008**, 52 (5), 1629-1632.

Kikuchi, Y., Sunada, K., Iyoda, T., Hashimoto, K., Fujishima, A. Photocatalytic bactericidal effect of TiO_2 thin films; dynamic view of the active oxygen species responsible for the effect. *Journal of Photochemistry and Photobiology A: Chemistry*, **1997**, 106, 51-6.

Kim, S.; Hyeong-Seon, L.; Deok-Seon, R.; Soo-Jae, C.; Dong-Seok, L. Antibacterial Activity of Silver-nanoparticles against *Staphylococcus aureus* and *Escherichia coli*. *Korean Journal of Microbiology and Biotechnology*, **2011**, 39 (1), 77–85.

Kiwi, J.; Pulgarin, C.; Peringer, P.; Gratzel, M. Beneficial effects of homogenous Photo-Fenton pretreatment upon the biodegradation of anthraquinone sulfonate in waste water treatment. *Applied Catalysis B: Environmental,* **1993**, 3, 85-89.

Klare, M.; Scheen, J.; Vogelsang, K.; Jacobs, H.; Broekaert. J. A. C. Degradation of short-chain alkyl- and alkanolamines by TiO_2- and Pt/TiO_2-assisted photo-catalysis**.** *Chemosphere,* **2000**, 41, 353-362.

Kolwas, K.; Derkachova, A.; Shopa, M. Size characteristics of surface plasmons and their manifestation in scattering properties of metal particles. *Journal of Quantitative Spectroscopy & Radiative Transfer,* **2009**, 110, 1490–1501.

Konstantinou, K .I.; Sakellarides, T. M.; Sakkas, V. A.; Albanis, T. A. Photocatalytic degradation of selected s-triazine herbicides and organophosphorus insecticides over aqueous TiO_2 suspensions. *Environmental Science and Technology*, **2001**, 35, 398–405.

Kowalska, E.; Mahaney, O. O. P.; Abea, R.; Ohtania, B. Visible-light-induced photocatalysis through surface plasmon excitation of gold on titania surfaces. *Physical Chemistry Chemical Physics*, **2010**, 12, 2344–2355.

Kreibig, U.; Vollmer, M. Optical Properties of Metal Clusters. *Springer Series in Materials Science*, *Berlin*, **1995**, 532. DM 98.00, ISBN 3-540-57836-6.

Kreibig, U.; Genzel, L. Optical absorption of small metallic particles. *Surface Science*, **1985**, 156, 678-700.

Kumar**,** G. S. Azo Functional Polymers: Functional Group Approach in Macromolecular Design. *CRC Press*, **1992.**

Kuvarega, A. T.; Krause, R. W. R.; Mamba B. B. Nitrogen/Palladium Co-doped TiO_2 for Efficient Visible Light Photocatalytic Dye Degradation. *Journal of Physical Chemistry* C, **2011,** 115, 22110–22120.

Kuznetsov, V. N.; Serpone, N. Visible light absorption by various titanium dioxide specimens. *Journal of Physical Chemistry B,* **2006**, 110, 25203-25209.

Larson, S. A.; Falconer, J. L. Initial steps in photo-catalytic oxidation of aromatics. *Catalysis Letters*, **1997**, 44, 57-65.

Lazar, M. A.; Varghese, S.; Nair, S. S. Photocatalytic Water Treatment by Titanium Dioxide: Recent Updates. *Catalysts*, **2012**, *2*, 572-601.

Lee, J.; Kim, B. C.; Chao, H. J.; Lee, C. Nanobiomaterials: Development and Applications. *Environmental Applications of Nanomaterials*. Chapter 11 ISBN 13:978-1-4398-7642-8.

Lee, K. S.; El-Sayed, M. A. Dependence of the Enhanced Optical Scattering Efficiency Relative to That of Absorption for Gold Metal Nanorods on Aspect Ratio, Size, End-Cap Shape, and Medium Refractive Index. *Journal of Physical Chemistry B*, **2005**, 109, 20331-20338.

Lia, Y.; Lib, X.; Lic, J.; Yin, J. Photo-catalytic degradation of methyl orange by TiO_2-coated activated carbon and kinetic study. *Water Research*, **2006**, 40, 1119– 1126.

Liao, F.; Wang, Z. F.; Hu, X. Q. Shape Controllable Synthesis of Dendritic Silver Nanostructures at Room Temperature. *Colloid Journal*, **2011**, 73, (4), 504–508.

Li, M.; Feng, Z. C.; Yong, P. L.; Xin, Q.; Li, C. Phase transformation in the surface region of zirconia and doped zirconia detected by UV Raman spectroscopy. *Physical Chemistry Chemical Physics*, **2003**, 5, 5326-5332.

Li, Y.; Peng, S.; Jiang, F.; Lu, G.; Li, S. Effect of doping TiO_2 with alkaline-earth metal ions on its photocatalytic activity. *Journal of the Serbian Chemical Society*, **2007**, 72 (4) 393–402.

Lima E., Guerra R., Lara V., Guzmán A. Gold nanoparticles as efficient antimicrobial agents for *Escherichia coli* and *Salmonella typhi*. *Chemistry Central Journal*, **2013**, 7, 11.

Lin, H. Y.; Chou, Y. Y.; Cheng, C. L.; Chen, Y. F. Giant enhancement of band edge emission based on ZnO/TiO_2 nanocomposites. *Optics Express*, **2007**, 15, 13832–7.

Linsebigler, A. L.; Lu, G. Q.; Yates, J. T. (Jr). Photocatalysis on TiO_2 surfaces: Principles, Mechanisms and Selected Results. *Chemical Reviews*, **1995**, 95, 735-758.

Liu, B.; Wang M. Electrodeposition of Dendritic Silver Nanostructures and Their Application as Hydrogen Peroxide Sensor. *International Journal of Electrochemical Science,* **2013**, 8, 8572 – 8578

Liu, E.; Kang, L.; Yang, Y.; Sun, T.; Hu, X.; Zhu, C.; Hanchen, L. H.; Wang, Q.; Li, X.; Fan, J. Plasmonic Ag deposited TiO_2 nano-sheet film for enhanced photocatalytic hydrogen production by water splitting. *Nanotechnology*, **2014**, 25, 1-10.

Liu S. X.; Qu, Z. P.; Han, X. W.; Sun, C. L. A mechanism for enhanced photocatalytic activity of silver-loaded titanium dioxide. *Catalysis Today*, **2004**, 93, (95), 877–884.

Liu, Z.; Hou, W.; Pavaskar, P.; Aykol, M.; Cronin, S. B. Plasmon Resonant Enhancement of Photo-catalytic Water Splitting Under Visible Illumination. *Nano Letters*, **2011**, 11 (3), 1111–1116.

Lowell, S.; Shields, J. E.; Thomas, M. A.; Thommes, M. Characterization of Porous Solids and Powders: Surface Area, Pore Size and Density. *Kluwer Academic Publishers, The Netherlands*, **2004**.

Lu, Q.; Zhang, Z. B.; Dong, C. Q.; Zhang, X. Y.; Cui, F. M.. Improved Visible-light Photocatalytic Activity of Bi-crystalline Mesoporous Titania Codoped with Carbon and Silver. *Journal of Inorganic Materials*, **2014**, 29, (12), 1333-1338.

Ma, Y.; Wang, X.; Jia, Y.; Chen, X.; Han, H.; Li, C. Titanium Dioxide-Based Nanomaterials for Photocatalytic Fuel Generations. *Chemical Reviews,* **2014**, 114, 9987−10043.

Malinsky, M, D.; Kelly, K, L.; Schatz, G. C.; Van Duyne, R. P. Chain Length Dependence and Sensing Capabilities of the Localized Surface Plasmon Resonance of Silver

Nanoparticles Chemically Modified with Alkanethiol Self-Assembled Monolayers. *Journal of the American Chemical Society*, **2001**, 123, 1471-1482.

Malekshahi Byranvanda, M.; Nemati Kharata, A.; Fatholahib, L.; Malekshahi Beiranvandc, Z. A Review on Synthesis of Nano-TiO_2 via Different Methods. *Journal of nanostructures*, **2013**, 3, 1-9.

Marcus Schmelzeisen, M.; Austermann, J.; Kreiter, M. Plasmon mediated confocal dark-field microscopy. *Optical Society of America*, **2008**, 16 (22), 17826-17841.

Markelonis, A. R.; Wang, J. S.; Ullrich, B.; Wai, C. M.; Brown, G. J. Nanoparticle film deposition using a simple and fast centrifuge sedimentation method. *Applied Nanoscience*, **2015**, 5, 457–468.

Masahiro, Y.; Yoshiyuki, K.; Ariffin, R.; Kazunori, T.; Shinji, K.; Akira, M.; Lee, S. H.; Hong, Y. K.; Shin, S. Y. *Seidenki Gakkai Koen Ronbunshu*, **1999,** 47.

Matthews, R. W.; McEnvoy, S. R. Photocatalytic degradation of phenol in the presence of near-UV illuminated titanium dioxide. *Journal of Photochemistry and Photobiology A: Chemistry*, **1992**, 64, 231.

McCullagh, C.; Robertson, J.; Bahnemann, D.; Robertson, P. The application of TiO_2 photocatalysis for disinfection of water contaminated with pathogenic micro-organisms: a review. *Research on Chemical Intermediates*, **2007**, 33, (3), 359-375.

McFarland, J. The nephelometer: an instrument for estimating the numbers of bacteria in suspensions used for calculating the opsonic index and for vaccines. *The Journal of the American Medical Association*, **1907**, 49, 1176-1178.

Mie, G. Contributions to the optics of diffuse media, especially colloid metal solutions. *Annals of Physics*, **1908**, 25, 377–445.

Minabe, T.; Tryk, D. A.; Sawunyama, P.; Kikuchi, Y.; Hashimoto, K.; Fujishima, A. TiO_2-mediated photo-degradation of liquid and solid organic compounds. *Journal of Photochemistry and Photobiology A: Chemistry*, **2000**, 137, 53-62.

Minero, C.; Catozzo, F.; Pelizzetti, E. Role of adsorption in photo-catalyzed reactions of organic molecules in aqueous TiO_2 suspensions. *Langmuir,* **1992**, 8, 481-486.

Mohan, R.; Drbohlavova, J.; Hubalek, J. Water-dispersible TiO_2 nanoparticles via a biphasic solvothermal reaction method. *Nanoscale Research Letters,* **2013**, 8:503, 1-4.

Moreno-Herrero, F.; Colchero, J.; Gómez-Herrero, J.; Baró, A. M. Atomic force microscopy contact, tapping, and jumping modes for imaging biological samples in liquids. *Physical Review E*, **2004**, 69, (3), 031915-9.

Mock, J. J.; Barbic, M.; Smith, D. R.; Schultz, D. A., Schultz, S. Shape effects in plasmon resonance of individual colloidal silver nanoparticles. *Journal of Chemical Physics,* **2002**, 116, (15), 6755–6759.

Mozia, S. Photocatalytic membrane reactors (PMRs) in water and wastewater treatment. A review. *Separation and Purification Technology*, **2010**, 73, (2), 71-91.

Muggli, D. S.; Ding, L. Photo-catalytic performance of sulfated of TiO_2 and Degussa P-25 TiO_2 during oxidation of organics. *Applied Catalysis B: Environmental,* **2001**, 32, 181-194.

Mukherjee, D.; Barghi, S.; Ray, A. K. Preparation and Characterization of the TiO_2 Immobilized Polymeric Photocatalyst for Degradation of Aspirin under UV and Solar Light. *Processes,* **2014**, 2, 12-23.

Mukhopadhyay, S. M. Sample preparation for microscopic and spectroscopic characterization of solid surfaces and films. *Department of Mechanical and Materials Engineering, Wright State University, Dayton, Ohio*. Chapter 9 p. 380.

Munekwa, S. Application of X-ray diffraction techniques to the semiconductor field. *The Rigaku Journal,* **1988**, 5, (2), 31-34.

Mungondori, H. H.; Tichagwa, L. Photo-catalytic activity of carbon/nitrogen doped TiO_2-SiO_2 under UV and visible light irradiation *Materials Science Forum,* **2013**, 734, 226-236.

Murakami, H.; Ohki, Y.; Yoshida, N.; Watanabe, T. A Plasmonic Photo-catalyst Consisting of Silver Nanoparticles Embedded in Titanium Dioxide. *Journal of the American Chemical Society*. **2008**, 130, 1676-1680.

Najafabadi, A. T.; Taghipour, F. Physicochemical impact of zeolites as the support for photo-catalytic hydrogen production using solar-activated TiO_2-based nanoparticles. *Energy Conversion and Management*, **2014**, 82, 106–113.

Nakajima, A.; Koizumi, S.; Watanabe, T.; Hashimoto, K. Effect of repeated photo-illumination on the wettability conversion of titanium dioxide. *Journal of Photochemistry and Photobiology A,* **2001**, *146*, 129-132.

National Water Resource Strategy (NWRS). First Edition, September **2004** http://www.wrc.org.za/Knowledge%20Hub%20Documents/Other/NWRA%20Sept04.pdf. Accessed on the 24th of August 2015.

Naya, S. I.; Inoue, A.; Tada, H. Self-assembled heterosupramolecular visible light photocatalyst consisting of gold nanoparticle-loaded titanium (IV) dioxide and surfactant. *Journal of the American Chemical Society*, **2010**, 132, (18) 6292–6293.

Neville, E. M.; Mattle, M. J.; Loughrey, D., Rajesh, B.; Rahman, M.; MacElroy, J. M. D.; Sullivan, J. A.; Thampi, K. R. Carbon-doped TiO_2 and carbon, tungsten co-doped TiO_2 through sol−gel processes in the presence of melamine borate: reactions through photo-catalysis. *Journal of Physical Chemistry C,* **2012**, 116, 16511−16521.

Nel, P.; Lau, D. Hay, D.; Wright, N. Non-destructive micro-X-ray diffraction analysis of painted artefacts: Determination of detection limits for the chromium oxide–zinc oxide matrix. *Nuclear Instruments and Methods in Physics Research B,* **2006**, 251, 489–495.

Ni, M.; Leung, M. K. H.; Leung, D. Y. C.; Sumathy, K. A review and recent developments in photocatalytic water-splitting using TiO_2 for hydrogen production. *Renewable and Sustainable Energy Reviews*, **2007**, 11, 401–425.

Nowotny, J.; Bak T.; Sheppard, L. R.; Sorrell, C. C. Effect of Oxygen Activity on Niobium Segregation in Niobium-Doped Titanium Dioxide. *Journal of the Australian Ceramic Society*, **2008**, 44, (2), 42-44.

Nyamukamba, P.; Tichagwa, L.; Greyling, C. The influence of carbon doping on TiO_2 nanoparticle size, surface area, anatase to rutile phase transformation and photocatalytic activity. *Materials Science Forum,* **2012**, 712, 49-63.

Oakes, J.; Gratton, P. Kinetic investigations of the oxidation of Methyl Orange and substituted arylazonaphthol dyes by peracids in aqueous solution. *Journal of the Chemical Society, Perkin Transactions,* **1998**, 2, 2563–2568.

Ochiai, T.; Nakata, K.; Murakami, T.; Fujishima, A.; Yao, Y.; Tryk, D. A.; Kubota Y. Development of solar-driven electrochemical and photocatalytic water treatment system using a boron-doped diamond electrode and TiO_2 photo-catalyst, *Water Research,* **2010**, 44, 904-910.

Ojha, A. K.; Forster, S.; Kumar, S.; Vats, S.; Negi, S.; Fischer I. Synthesis of well–dispersed silver nanorods of different aspect ratios and their antimicrobial properties against gram positive and negative bacterial strains. *Journal of Nanobiotechnology*, **2013**, 11, 42, 1-7.

Overnstone, J.; Yanagisawa, K. Effect of hydrothermal treatment of amorphous titania on the phase change from anatase to rutile during calcinations. *Chemical Materials,* **1999**, 11, 2770-2774.

Pablos, C.; van Grieken, R.; Marugán J.; Moreno B: Photo-catalytic inactivation of bacteria in a fixed-bed reactor: mechanistic insights by epifluorescence microscopy. *Catalysis Today*, **2011**, 161, (1), 133-139.

Paez, L. R.; Matousek, J. Properties of sol-gel TiO_2 layers on glass substrate. *Ceramics – Silikáty*, **2004**, 48, (2), 66-71.

Palanivelu, K.; Sun Im, J.; Lee, Y. S. Carbon Doping of TiO_2 for Visible Light Photo Catalysis - A review. *Carbon Science*, **2007**, 8, (3), 214-224.

Panyala, N.; Pena-Mendze, E.; Havel, J. Silver or silver nanoparticles: a hazardous threat to the environment and human health? *Journal of Applied Biomedicine,* **2008**, 6, 117–129.

Parra, S.; Olivero, J.; Pulgarin, C. Relationships between physicochemical properties and photoreactivity of four biorecalcitrant phenylurea herbicides in aqueous TiO_2 suspension. *Applied Catalysis B: Environmental*, **2002**, 36: 75–85.

Park, S. H.; Im, J. H.; Im J. W.; Chun, B. H.; Kim, J. H. Adsorption Kinetics of Au and Ag Nanoparticles on Functionalized Glass Surfaces. *Microchemical Journal*, **1999**, 63**,** 71–91.

Pavia, D. L.; Lampman, G. M.; Kriz, G. S. Introduction to spectroscopy: A guide for students of organic chemistry. *Thomson Learning, Inc*, **2001**, (3), 353-358.

Pichat, P. In: Schiavello M, editor. Photocatalysis and environment: trends and applications, NATO advanced study institute on new trends and applications. *Dordrecht, Boston: Kluwer Academic Publishers*; **1993**, p. 339

Plueddemann, E. P. Silane adhesion promoters in coatings. *Progress in Organic Coatings*, **1983**, *11*, 297-308.

Poirier, G. E. Characterization of Organosulfur Molecular Monolayers on Au 111 using Scanning Tunneling Microscopy. *Chemical Reviews*, **1997**, 97, 1117–1127.

Pozzo, R. L.; Baltanas, M. A.; Cassano, A. E. Supported titanium oxide as photo-catalyst in water decontamination: state of the art. *Catalysis Today*, **1997**, 39, 219-231.

Prabhu, S.; Poulose, E. K. Silver nanoparticles: mechanism of antimicrobial action, synthesis, medical applications, and toxicity effects. *International Nano Letters*, **2012**, 2, 1-32.

Primo, A.; Corma, A.; Garcısa, H. Titania supported gold nanoparticles as photocatalyst. *Physical Chemistry Chemical Physics*, **2011**, 13, 886–910.

Qu, X.; Alvarez, P. J. J.; Li, Q. Applications of nanotechnology in water and wastewater treatment. *Water Research*, **2013**, 47, (12), 3931-3946.

Qu, Y.; Li X.; Chen, G.; Zhang, H.; Chen, Y. Synthesis of Cu_2O nano- whiskers by a novel wet-chemical route. *Materials Letters*, **2008**, 62, 886.

Raffi, M.; Mehrwan, S.; Bhatti, T.; Akhter, J.; Hameed, A.; Yawar, W.; Hasan, M. Investigations into the antibacterial behavior of copper nanoparticles against *Escherichia coli Ann*. *Microbiology*, **2010**, 60, 75–80.

Ramamoorthy, M.; Vanderbilt, D.; King-Smith, R. D. First-Principles Calculations of the Energetics of Stoichiometric TiO_2 Surfaces. *Physical Reviews B*, **1994**, 49, 16721–16727.

Rammohan, G.; Nadagouda, M. N. Green photocatalysis for degradation of organic contaminants; a review. *Current Organic Chemistry*, **2013**, 17, 2338–2348.

Rahulan, K. M.; Ganesan, S.; Aruna, P. Synthesis and optical limiting studies of Au-doped TiO_2 nanoparticles. *Advances in Natural Sciences: Nanoscience Nanotechnolgy*, **2011**, 2, 1-6.

Rengifo-Herrera, J. A.; Pulgarin, D. Photo-catalytic activity of N, S codoped and N-doped commercial anatase TiO_2 powders towards phenol oxidation and E-coli inactivation under simulated solar light irradiation. *Solar Energy*, **2010**, 84, 37-43.

Robert, E. A. Liquid Chromatography–Mass Spectrometry: An Introduction. John Wiley & Sons, Ltd. ISBNs, **2003**: 0-471-49799-1 (HB).

Rockafellow, E. M.; Stewart, L. K.; Jenks, W. S. Is sulfur-doped TiO_2 an effective visible light photocatalyst for remediation? *Applied Catalysis B: Environmental*, **2009**, 91, 554–562.

Ru, E. L.; Etchegoin, P. Principles of Surface-Enhanced Raman Spectroscopy: and related plasmonic effects, **2009**, p. 531, ISBN: 978-0-444-52779-0.

Ryu, W. H., Park, C.J., Kwon, H. S. Synthesis of highly ordered TiO_2 nanotube in malonic acid solution by anodization. *Journal of Nanoscience and Nanotechnology*, **2008**, 8, 1–4.

Saehana, S.; Prasetyowati, R.; Hidayat, M. I.; Arifin, P.; Khairurrijal, Abdullah, M. Efficiency improvement in TiO_2-particle based solar cells after deposition of metal in spaces between particles. *International Journal of Basic & Applied Sciences*, **2011**, 11 (6), 15-28.

Salavati-Niasari, M.; Davar, F. Synthesis of copper and copper (I) oxide nanoparticles by thermal decomposition of a new precursor. *Materials Letters*, **2009**, *63*, 441–443.

Sambrook, J.; D. W. Russell. 2001. "Molecular Cloning, a Laboratory Manual." *Cold Spring Harbor Laboratory Press, Cold Spring Harbor*, NY.

Samuel, U.; Guggenbichler, J. P. Prevention of catheter-related infections: The potential of a new nano-silver impregnated catheter. *International Journal of Antimicrobial Agents*, **2004**, 23, 75–78.

Santamarina, J. C.; Klein, K. A.; Wang, Y. H.; Prencke, E. Specific surface: determination and relevance. *Canadian Geotechnical Journal*, **2002**, 39, 233–241.

Saquib, M.; Muneer, M. TiO_2-mediated photocatalytic degradation of a triphenylmethane dye (gentian violet), in aqueous suspensions. *Dyes and Pigments*, **2003**, 56, 37-49.

Sarantopoulos, C., Puzenat, E., Guillard, C., Herrmann, J. M., Gleizes, A. N., Maury, F. Microfibrous TiO_2 supported photocatalysts prepared by metal-organic chemical vapor infiltration for indoor air and waste water purification. *Applied Catalysis B: Environmental*, **2009**, 91, 225–233.

Sathish, M.; Viswanathan, B.; Viswanath, R. P.; Gopinath, C. S. Synthesis, Characterization, Electronic Structure, and Photo-catalytic Activity of Nitrogen-Doped TiO_2 Nanocatalyst. *Chemistry of Materials*, **2005**, 17, (25), 6349–6353.

Savithramma, N.; Linga Rao, M.; Rukmini, K.; Suvarnalatha devi, P. Antimicrobial activity of Silver Nanoparticles synthesized by using Medicinal Plants. *International Journal of ChemTech Research*, **2011**, 3, (3), 1394-1402.

Setiawati, E.; Kawano, K. Stabilization of anatase phase in the rare earth; Eu and Sm ion doped nanoparticle TiO_2. *Journal of Alloys and Compounds*, **2008**; 451 (12), 293-296.

Shah, S. I.; Li, W.; Huang, C. P.; Jung, O.; Ni, C. Study of Nd^{3+}, Pd^{2+}, $Pt^{4+,}$ and Fe^{3+} dopant effect on photoreactivity of TiO_2 nanoparticles. *Proceedings of the National Academy of Sciences*, **2002**, 99 (2), 6482–6486.

Shah, Z. H.; Wang, J.; Ge, Y.; Wang, C.; Mao, W.; Zhang, S.; Lu, R. Highly enhanced plasmonic photocatalytic activityof Ag/AgCl/TiO_2 by CuO co-catalyst. *Journal of Materials Chemistry. A*, **2015**, 3, 3568–357.

Shahverdi, A.; Fakhini , A.; Shahverdi, H. R.; Minaian, S. M. S. Synthesis and effect of silver nanoparticles on the antibacterial activity of different antibiotics against

Staphylococcus aureus and *Escherichia coli*. *Nanomedicine: Nanotechnology, Biology and Medicine***, 2007,** 3, (2), 168-171.

Shan, A. Y.; Ghazi, T. I. M.; Rashid, S. A. Immobilisation of Titanium Dioxide onto Supporting Materials in Heterogeneous Photocatalysis: A Review. *Applied Catalysis A: General*, **2010**, 389, (1-2), 1-8.

Shao, Z.; Tian, Z.; Pang, J.; Feng, G.; Guo, B.; Zeng, C.; Yang, Y.; Liu, S.; Wang, Q. Optically modulated charge transfer in TiO_2-Au nanocomplexes. *Materials Research Express*, **2014**, 1, 1-20.

She, Z. W.; Liu, S.; Low, M.; Zhang, S. Y.; Liu, Z.; Mlayah, A.; Han, M. Y. Janus Au-TiO_2 Photocatalysts with Strong Localization of Plasmonic Near-Fields for Efficient Visible-Light Hydrogen Generation. *Advanced Materials*, **2012**, 24, 2310–2314.

Solomon, S. D.; Bahadory, M.; Jeyarajasingam, A. V.; Rutkowsky S. A.; Boritz C. Synthesis and Study of Silver Nanoparticles. *Journal of Chemical Education*, **2007**, 84, 322-325.

Singh, S.; Singh, P. K.; Mahalingam, H. A novel and effective strewn polymer-supported titanium dioxide photocatalyst for environmental remediation. *Journal of Materials and Environmental Science*, **2015**, 6, (2), 349-358.

Song, K. Y.; Park, M. K.; Kwon, Y. T. Preparation of transparent particulate MoO_3/TiO_2 and WO_3/TiO_2 films and their photo-catalytic properties. *Chemistry of Materials*, **2001**, 13, 2349–2355.

Stoneham, A. M.; Gavartin, J.; Shluger, A. L.; Kimmel, A. V.; Ramo, D. M.; Rønnow, H. M.; Aeppli, G.; Renner, C. "Trapping, self-trapping and the polaron family," *Journal of Physics: Condensed Matter*, **2007**, 19, 255208, 1-22.

Su, K. H.; Wei Q. H.; Zhang, X.; Mock J. J.; Smith, D. R.; Schultz, S. Interparticle Coupling Effects on Plasmon Resonances of Nanogold Particles. *Nano Letters*, **2003**, 3, (8), 1089-1090.

Suarez, S.; Carballa, M.; Omil, F.; Lema, J. M. How are pharmaceutical and personal care products (PPCPs) removed from urban wastewaters? *Reviews in Environmental Science and Biotechnology*, **2008**, 7, 125-138.

Sunada, K.; Kikuchi, Y.; Hashimoto, K.; Fujishima, A. Bactericidal and detoxification effects of TiO_2 thin film photocatalysts. *Environmental Science and Technology*. **1998**, 32, 726–728.

Sunada, K.; Watanabe, T.; Hashimoto, K. Studies on photokilling of bacteria on TiO_2 thin film. *Journal of Photochemistry and Photobiology: Chemistry*, **2003**, 156, 227–233.

Sun, Q.; Li, H.; Niu, B.; Hu, X.; Xu, C.; Zheng, S. Nano-TiO_2 immobilized on diatomite: characterization and photocatalytic reactivity for Cu^{2+} removal from aqueous solution. *Procedia Engineering*, **2015**, 102, 1935 – 1943.

Suteu, D.; Zaharia, C.; Bilba, D.; Muresan, A.; Muresan, R.; Popescu, A. Decolorization wastewaters from the textile industry – physical methods, chemical methods. *Industria Textila*, **2009**, 60 (5), 254-263.

Suteu, D.; Zaharia, C.; Muresan, A.; Muresan, R.; Popescu, A. Using of industrial waste materials for textile wastewater treatment. *Environmental Engineering and Management Journal*, **2009**, 8 (5), 1097-1102.

Tan, Y. N.; Wong, C. L.; Mohamed, A. R. An Overview on the Photo-catalytic Activity of Nano-Doped-TiO_2 in the Degradation of Organic Pollutants. *International Scholarly Research Notices: Materials Science*, **2011**, 211, 1-18.

Tang, W. Z.; An, H. UV/TiO_2 photocatalytic oxidation of commercial dyes in aqueous solutions, *Chemosphere*, **1995**, 31, 4158–4170.

Tennakone, K.; Tilakaratne, C. T. K.; Kottegoda, I. R. M. Photo-catalytic degradation of organic contaminants in water with TiO_2 supported on polythene films. *Journal of Photochemistry and Photobiology A: Chemistry*, **1995**, 87, (2), 177–17.

Tayade, R. J.; Surolia, P. K.; Kulkarni, R. G.; Jasra, R.V. Photo-catalytic degradation of dyes and organic contaminants in water using nanocrystalline anatase and rutile TiO_2. *Science and Technology of Advanced Materials*, **2007**, 8, (6), 455-462.

Thill, A.; Zeyons, O.; Spalla, O.; Chauvat, F.; Rose, J.; Auffan, M.; Flank, A. M. Cytotoxicity of CeO_2 nanoparticles for *Escherichia coli*. Physico-chemical insight of the cytotoxicity mechanism. *Environmental Science and Technology*, **2006**, 40, 6151–6156.

UNICEF - Joint Monitoring Program Report : Progress on Drinking Water & Sanitation **2012**, http://www.unicef.org/media/files/JMPreport2012.pdf.

Valentin, C. D.; Pacchioni, G.; Selloni, A.; Livraghi, S.; Giamello, E. Characterization of Paramagnetic Species in N-Doped TiO_2 Powders by EPR Spectroscopy and DFT Calculations. *Journal of Physical Chemistry B,* **2005,** 109, 11414-11419.

Venczel, L. V.; Arrowood, M.; Hurd, M.; Sobsey, M. D. Inactivation of Cryptosporidium parvum oocysts and Clostridium perfringens spores by a mixed-oxidant disinfectant and by free chlorine. *Applied Environmental Microbiology*, **1997**, 63, 1598-1601.

Verbruggen, V. W.; Keulemans, M.; Filippousi, M.; Flahaut, D.; Van Tendeloo, G.; Lacombe, S.; Martens, J. A.; Lenaerts, S. Plasmonic gold–silver alloy on TiO_2 photocatalysts with tunablevisible light activity. *Applied Catalysis B: Environmental*, **2014**, 156–157, 116–121.

Verdier, T.; Coutand, M.; Bertron, A.; Roques, C. Antibacterial Activity of TiO_2 Photo-catalyst Alone or in Coatings on *E. coli*: The Influence of Methodological Aspects. *Coatings*, **2014**, 4, (3), 670-686.

Verma, V. C.; Singh, S. K.; Solanki, R.; Prakash, S. Biofabrication of Anisotropic Gold Nanotriangles Using Extract of Endophytic Aspergillus clavatus as a Dual Functional Reductant and Stabilizer. *Nanoscale Research Letters,* **2011**, 6, (16), 1-7.

Vinodgopal, K.; Bedja, I.; Kamat, P. V. Nanostructured semiconductor films for photocatalysis. Photoelectrochemical behavior of SnO_2/TiO_2 composite systems and its role in photocatalytic degradation of a textile azo dye. *Chemistry of Materials,* **1996**, 8, 2180–2187.

Vinodgopal, K.; Hotchandani, S.; Kamat, P. V. Electrochemically assisted photocatalysis, TiO_2 particulate film electrodes for photocatalytic degradation of 4-Chlorophenol. *Journal of Physical Chemistry*, **1993**, 97, 9040-9044.

Wang, C.; Shao, C.; Zhang, X. SnO_2 Nanostructures-TiO_2 nanofibers heterostructures: Controlled fabrication and high photocatalytic properties. *Inorganic Chemistry*, **2009**, 48, 7261–7268.

Wang, S.; Peng, Y. Natural zeolites as effective adsorbents in water and wastewater treatment. *Chemical Engineering Journal*, **2010**, 156, 11–24.

Wang, X.; Meng, S.; Zhang, X.; Wang, H.; Zhong, W.; Du, Q. Multi-type carbon doping of TiO_2 photocatalyst. *Chemical Physics Letters*, **2007**, 444, 292–296.

Wang, Y.; Zhang, R.; Li, J.; Li, L.; Lin, S. First-principles study on transition metal-doped anatase TiO_2. *Nanoscale Research Letters*, **2014**, 9, 46, 1-8.

Wei, T. Y.; Yang, Y. Y.; Wan, C. C. Kinetics of photo-catalytic oxidation of phenol on TiO_2 surface. *Journal of Photochemistry and Photobiology A: Chemistry,* **1992**, 69, (2), 241-249.

WHO Guidelines for Drinking-water Quality first addendum to third edition Volume 1, Recommendations. 3rd edition, **2006,** 1, (3).

WHO, Guidelines for Drinking-water Quality, Geneva **2008**. Third edition Volume 1, ISBN 978 92 4 154761 1. http://www.who.int/water_sanitation_health/dwq/fulltext.pdf

Willets, K. A.; Van Duyne, R. P. Localized Surface Plasmon Resonance Spectroscopy and Sensing. *Annual Review of Physical Chemistry*, **2007**, 58, 267–297.

Wu, J. M.; Zhang, T. W.; Zeng, Y. W.; Hayakawa, S.; Tsuru, K.; Osaka, A. Large-scale preparation of ordered titania nanorods with enhanced photocatalytic activity. *Langmuir*, **2005**, 21, 6995-6999.

Xin, W.; Zhu, D.; Liu, G.; Hua, Y.; Zhou, W. Synthesis and Characterization of Mn–C–Codoped TiO_2 Nanoparticles and Photocatalytic Degradation of Methyl Orange Dye under Sunlight Irradiation. *International Journal of Photoenergy*, **2012**, 1-7.

Xu, J.; Xiao, X.; Stepanov, A. L.; Ren, F.; Wu, W.; Cai, G.; Zhang, S.; Dai, Z.; Mei, F.; Jiang, C. Efficiency enhancements in Ag nanoparticles-SiO_2-TiO_2 sandwiched structure via plasmonic effect-enhanced light capturing. *Nanoscale Research Letters*, **2013**, *8* (73), 1-5.

Xu, Q. A.; Zhang, J.; Feng, Z. C.; Ma, Y.; Wang, X.; Li, C. Surface Structural Transformation and the Phase Transition Kinetics of Brookite TiO_2. *Asian Journal of Chemistry*, **2010**, 5, 2158-2161.

Yadav, H. M.; Otari, S. V.; Bohara, R. A.; Mali, S. S.; Pawar, S. H.; Delekar, S. D. Synthesis and visible light photocatalytic antibacterial activity of nickel-doped TiO_2 nanoparticles against Gram-positive and Gram-negative bacteria. *Journal of Photochemistry and Photobiology A*, **2014**, 294, 130–136.

Yan, X. M.; Kang, J. L.; Gao, L.; Xiong, L.; Mei, P. Solvothermal synthesis of carbon coated N-doped TiO_2 nanostructures with enhanced visible light catalytic activity. *Applied Surface Science*, **2013**, 265, 778-783.

Yang, J.; Bai, H.; Jiang, Q.; Lian, J. Visible-light photocatalysis in nitrogen–carbon-doped TiO_2 films obtained by heating TiO_2 gel–film in an ionized N_2 gas. *Thin Solid Films*, **2008**, 516, 1736–1742.

Yang, X.; Cao, C.; Ericksona, L.; Hohna, K.; Maghirang R., Klabunde K. Synthesis of visible-light-active TiO_2-based photocatalysts by carbon and nitrogen doping. *Journal of Catalysis*, **2008**, 260, 128–133.

Yeshchenk, O. A. Temperature effects on the surface Plasmon resonance in copper nanoparticles. *Journal of Physics*, **2013**, 58, (3), 249-259.

Yu, B.; Leung, K. M.; Guo, Q.; Lau, W. M.; Yang, J. Synthesis of Ag–TiO_2 composite nano thin film for antimicrobial application Nanotechnology, **2011**, 115603, (22), 1-9.

Yu, C.; Wei, L.; Li, X.; Chen, J.; Fan, Q.; Yu, J. C. Synthesis and characterization of Ag/TiO_2-B nanosquares with high photocatalytic activity under visible light irradiation. *Materials Science and Engineering B*, **2013**, 178, 344– 348.

Yuranova, T.; Rincon, A. G.; Bozzi, A.; Parra, S.; Pulgarin, C.; Albers, P.; Kiwi, J. Antibacterial textiles prepared by RF-plasma and vacuum-UV mediated deposition of silver. *Journal of Photochemistry and Photobiology A*, **2003**, 161, 27–34.

Zaharia, C.; Suteu, D.; Muresan, A.; Muresan, R.; Popescu, A. Textile wastewater treatment by homogenous oxidation with hydrogen peroxide. *Environmental Engineering and Management Journal*, **2009**, 8, (6), 1359-1369.

Zainal, N.; Lee, K. H.; Hussein, M. Z.; Taufiq-Yap, Y. H.; Abdullah, A. H.; Ramli, I. Removal of dyes using immobilized titanium dioxide illuminated by fluorescent lamps. *Journal of Hazardous Materials*, B125, **2005**, 113–120.

Zainudin, N. F.; Abdullah, A. Z.; Mohamed, A. R. Development of supported TiO_2 photocatalyst based adsorbent for photo-catalytic degradation of phenol. International Conference on Environment, **2008,** (ICENV 2008), 1-7.

Zhang, F.; Zheng, Z.; Ding, X.; Mao, Y.; Chen, Z.; Yang, S.; Liu, X. Highly oriented rutile-type TiO_2 films synthesized by ion beam enhanced deposition. *Journal of Vacuum Science and Technology*, **1997**, 15, 1824-1827.

Zhang, H.; Banfield, J. F. Understanding polymorphic phase transformation behavior during growth of nanocrystalline aggregates: insights from TiO_2. *Journal of Physical Chemistry*, **2000**, 104, 3481-3487.

Zhang, S.; Song, L. Preparation of visible-light-active carbon and nitrogen co-doped titanium dioxide photocatalysts with the assistance of aniline. *Catalysis Communications*, **2009**, 10, 1725–1729.

Zhang, X.; Chen, Y. L.; Liu, R.; Tsai, D. P. Plasmonic photocatalysis. *Reports on Progress in Physics*, **2013**, 76, 1-41.

Zhang, J.; Li, M.; Feng, Z.; Chen, J.; Li, C. UV Raman Spectroscopic Study on TiO_2. Phase Transformation at the Surface and in the Bulk. *Journal of Physical Chemistry B*, **2006**, 110, 927-935.

Zhang, J.; Xu, Q.; Feng, Z.; Li, M.; Li, C. Importance of the relationship between surface phases and photo-catalytic activity of TiO_2. *Angewandte Chemie International Edition*, **2008**, 47, 1766-1769.

Zhang, T. H.; Piao L. Y.; Zhao, S. L.; Xu , Z.; Wu, Q.; Kong, C. Application of TiO_2 with different structures in solar cells. *Chinese Physics* B, **2012**, 21, (11), 118401-118405.

Zhao, L.; Jiang, Q.; Lian, J. Visible-light photocatalytic activity of nitrogen-doped TiO_2thin film prepared by pulsed laser deposition. *Applied Surface Science*, **2008**, 254, 4620–4625.

Zheng, L.; Xu, M.; Xu, T. TiO_{2-x} thin films as oxygen sensor. *Sensors and Actuators B: Chemical*, 2000, 66, (1-3), 28-30.

Zhou, M.; Zhang, J.; Cheng, B.; Yu, H. Enhancement of Visible-Light Photocatalytic Activity of Mesoporous Au-TiO_2 Nanocomposites by Surface Plasmon Resonance. *International Journal of Photoenergy*, **2012**, 1-10.

Zhu, C.; Wang, L.; Kong, L.; Yang, X.; Wang, L.; Zheng, S.; Chen, F.; MaiZhi, F.; Zong, H. Photocatalytic degradation of AZO dyes by supported TiO_2 + UV in aqueous solution. *Chemosphere*, **2000**, 41, 303-309.

Zhu, H.; Chen X.; Zheng, Z.; Ke, X.; Jaatinen, E.; Zhao J.; Guo, C.; Xied, T.; Wangd, D. Mechanism of supported gold nanoparticles as photocatalysts under ultraviolet and visible light irradiation. *Chemical Communications*, **2009**, 7524–7526.

APPENDIX A

Effect of other contaminants on methyl orange photo-degradation

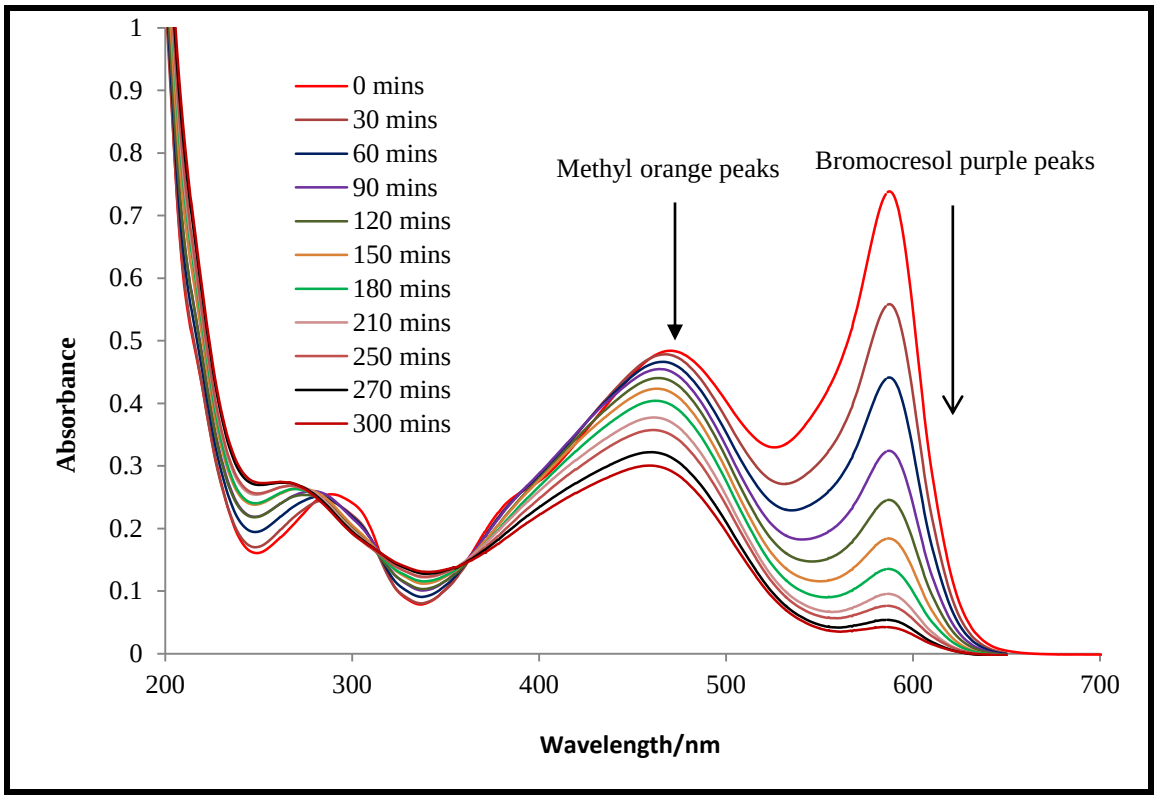

Figure A.1: Photo-degradation absorption spectra of a mixture of methyl orange and bromocresol purple using TiO_2 photo-catalyst deposited on trimetallic layer (Au, Cu and Ag) under UV light at 25 °C and pH 7.

APPENDIX B

Characterization of carbon/plasmon metal co-doped TiO_2 photo-catalyst.

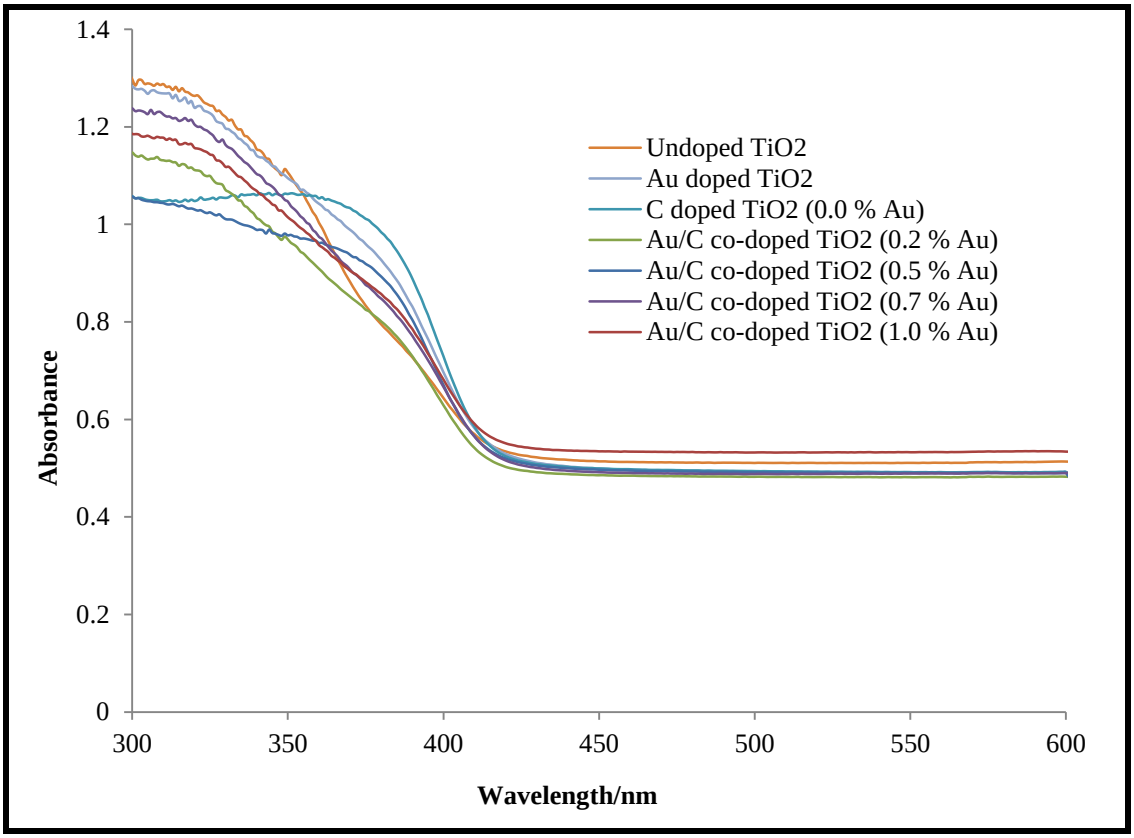

Figure B.1: Absorbance spectra of Au/C co-doped TiO_2 photo-catalyst.

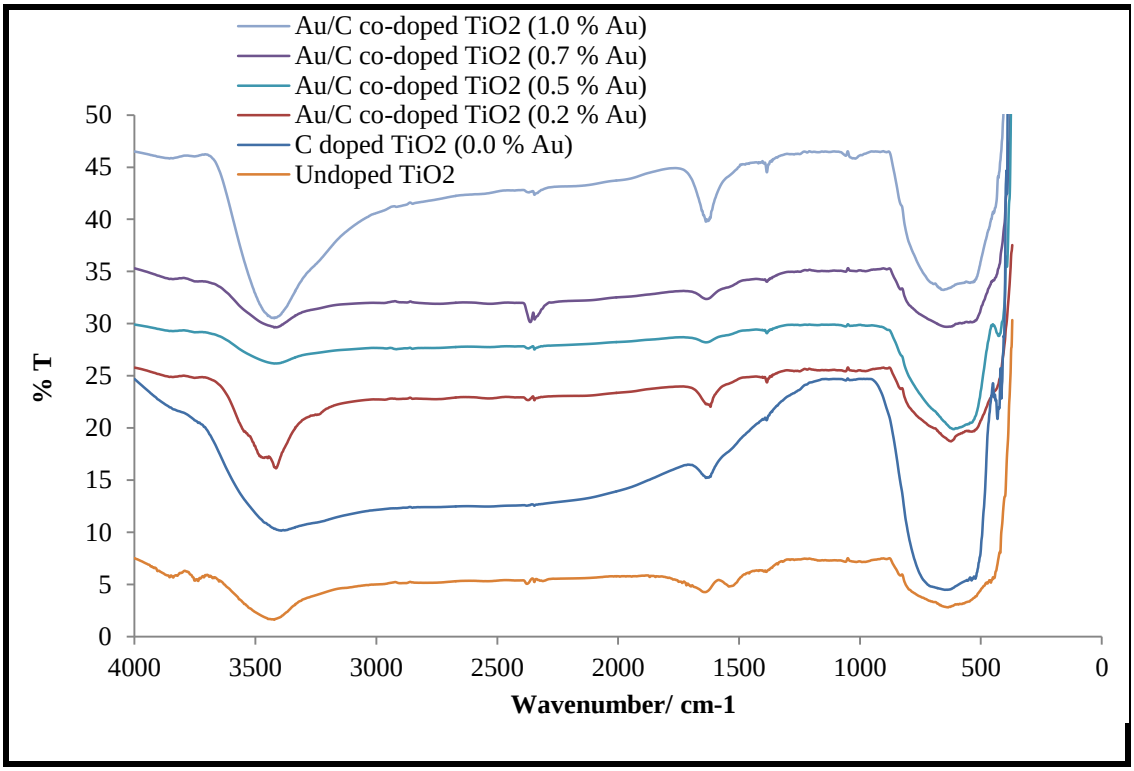

Figure B.2: FTIR spectra of Au/C co-doped TiO_2 with different contents of Au.

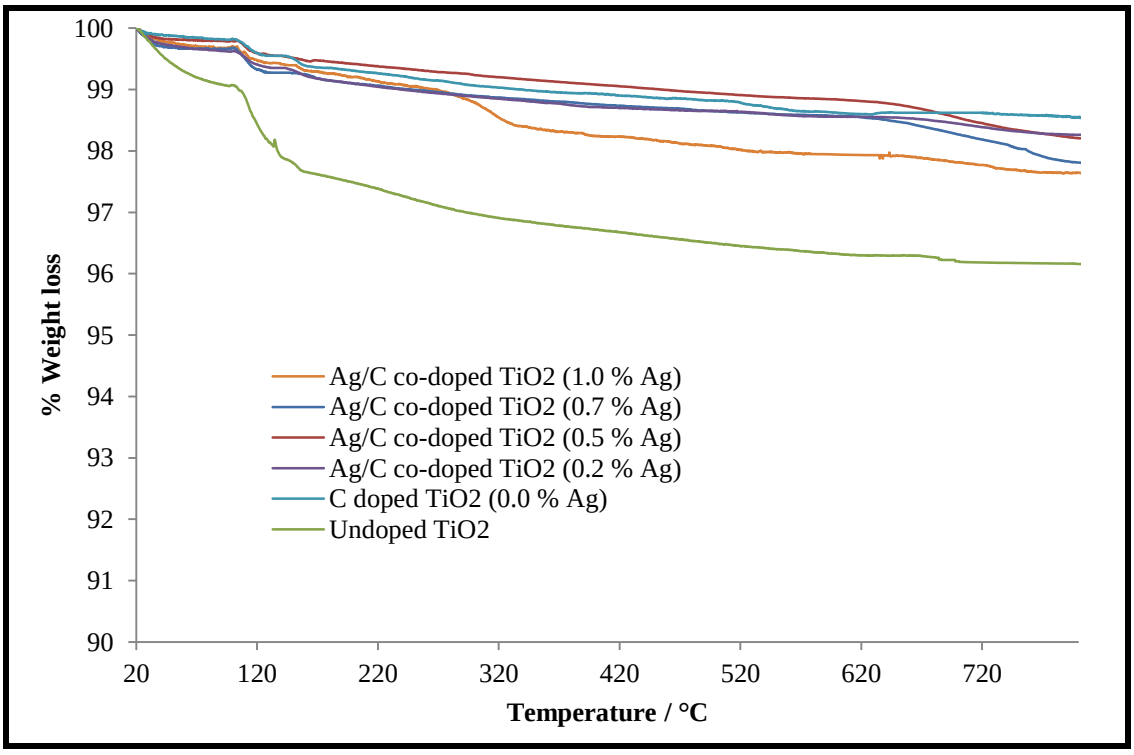

Figure B.3: Thermograms of carbon and gold doped TiO_2 photo-catalysts.

Appendix C

Characterization and photo-degradation results of TiO_2/plasmon metal composite photo-catalysts.

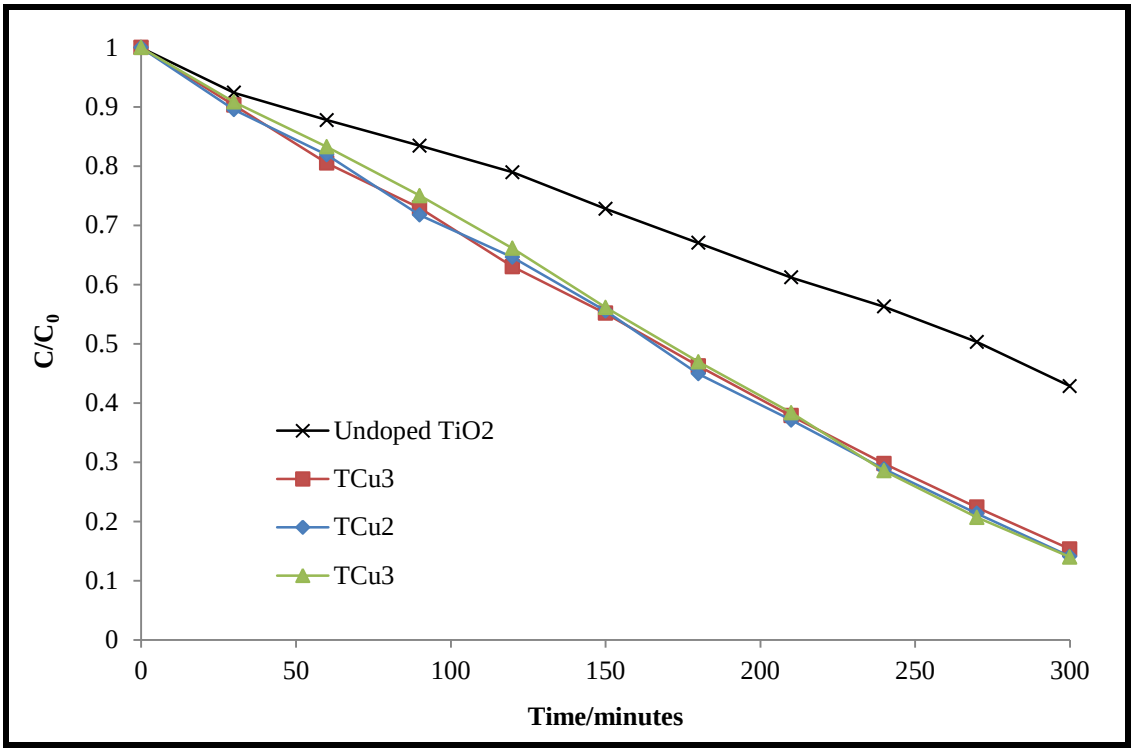

Figure C.1: Photo-degradation curves of methyl orange using Cu/TiO_2 composites at 25 °C and pH 7 under UV light.

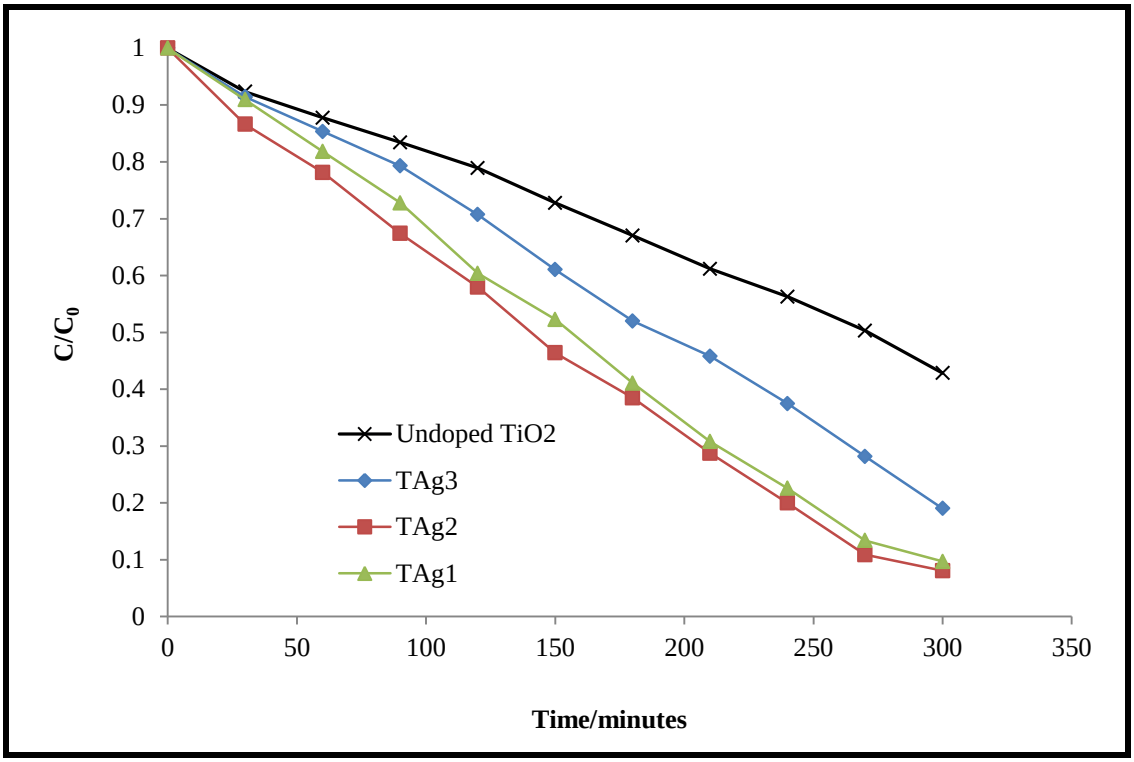

Figure C.2: Photo-degradation curves of methyl orange using Ag/TiO_2 composites at 25 °C and pH 7 under UV light.

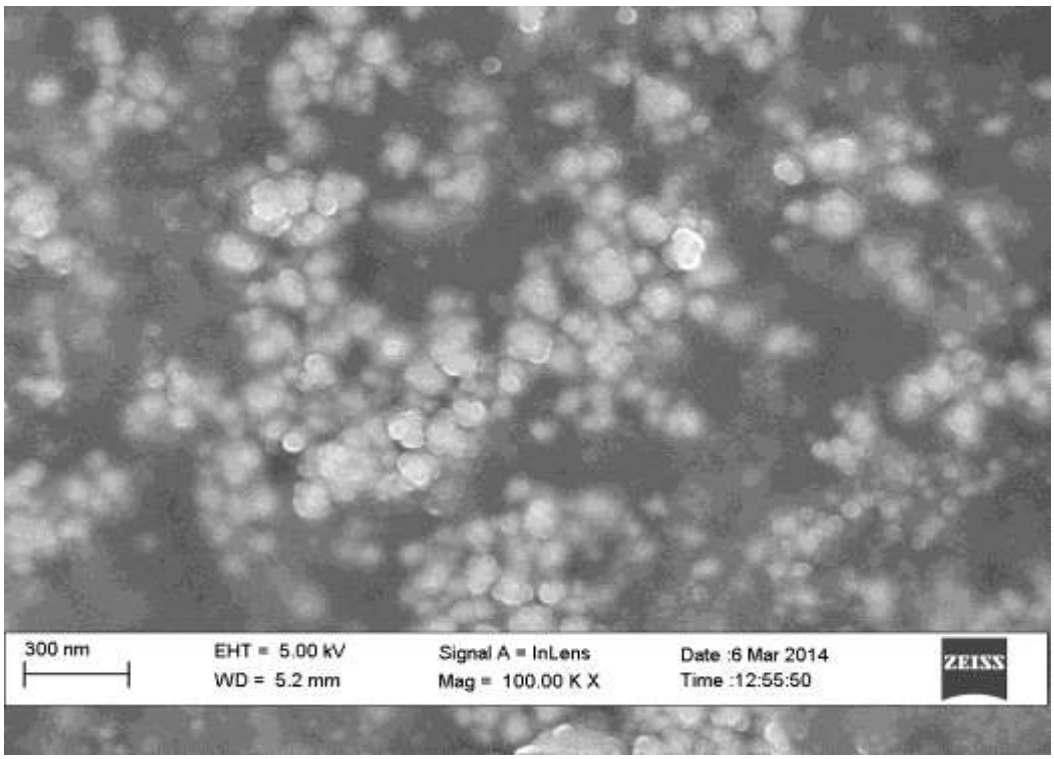

Figure C.3: HRSEM image of TAu1 composite on quartz support.

Appendix D

Research outputs associated with the work

D1: Research outputs published in conference proceedings

Nyamukamba, P.; Tichagwa, L, Mamphweli, S.; Petrik, L. Plasmon metal enhanced titanium dioxide photo-catalyst nanoparticles for the removal of organics in water. *Journal of Nanomedicine and Nanotechnology*, **2015**, 6:6 http://dx.doi.org/10.4172/2157-7439.C1.026

D2: Research papers presented at national conferences

Nyamukamba, P.; Tichagwa, L, Mamphweli, S.; Petrik, L. Preparation of titanium dioxide nanoparticles immobilized on carbon nanofibres for the removal of organic contaminants in water. *5th IUPAC Green Chemistry Conference*, Durban, South Africa, 17-21 August **2014**.

D3: Research papers presented at international conferences

Nyamukamba, P.; Tichagwa, L, Mamphweli, S.; Petrik, L. Plasmon metal enhanced titanium dioxide photo-catalyst nanoparticles for the removal of organics in water. *5th International Conference on Nanotek & Expo*, November 16-18, **2015** San Antonio, USA.

Nyamukamba, P.; Tichagwa, L, Mamphweli, S.; Petrik, L. Plasmon decorated TiO_2 photo-catalytic thin films for the photo-degradation of bromocresol purple and methyl orange. *9th IWA International Conference and Exhibition on Water Reuse*, 27-31 October **2013**, Windhoek in Namibia.